Gerald Raab, BSc.

„Magmatic, Metamorphic and Tectonic Evolution of the Seckau Complex in the Area of the Sonntagskogel Mountain (Triebener Tauern, Province of Styria)"

MASTER'S THESIS

to achieve the university degree of

Master of Science

Master's degree programme: Earth Sciences

submitted to

Graz University of Technology

Supervisor

Univ.-Prof. Dr.rer.nat. Walter Kurz

Institute of Earth Sciences

Ao.Univ.-Prof. Dr.rer.nat. Christoph Hauzenberger

Graz, October 2015

AFFIDAVIT

I declare that I have authored this thesis independently, that I have not used other than the declared sources/resources, and that I have explicitly indicated all material which has been quoted either literally or by content from the sources used. The text document uploaded to TUGRZonline is identical to the present master‘s thesis dissertation.

Date

Signature

Thank you note

I contribute my thanks first of all to my parents who have supported me in difficult times throughout my studies, and of course my grandmother, who has given me unforgettable times of wisdom which I will honour throughout my life. But also my sisters and there endless phone-talks, and even if we do not share a lot of time together, I say thanks. But of course I do not forget my roommates (Andi, Flo, Martin, Didi, Gregor, Theresa, Magda…) which have changed over the years but always have shared their thoughts, laughs and dinners. I am thanking all my friends in the scout movement (Mario, Babsi, Tschosi, Bossi, Klaus, Enzi, Babsi, Konrad, Simon, Lukas, Tobias, Flo, Erich, Clemens, Benny, Kathi, Magdi, Daniel, Mathias, Julia, Corni, Felix, Julia, Stephan, Hannes, Michael, Raffi, Reinhard, Alpha, Hiasi, Leo etc.) for the wonderful times and keeping me off-balance when I needed it!, and of course our Gilde (Ecki, Gernot, Fred, Beat, Robert etc.). I am also grateful for all the colleagues of the Red Cross I have spent my time with, for being understanding if I cannot split myself to be in Graz and in Steyr. Even if I know I will not be able to cover all the people who have enriched my life in the last years I still do not forget my biologists Flo and Alex, as well as my ERASMUS colleagues (Michela, Paula, Daniela, Samu, Giorgia, Bruno, Ng, Fabrizio, Cris, Menel, Pavel, Jon, Sergio, Alvaro etc.). Not to forget, I am thanking my girlfriend for being there for me, supporting me, and showing some interest “in those stupid rocks of mine” ☺ !, and also her parents who supplied me with freshly home gardened vegetables so often. To the end I am appreciating my student fellows (Andi, Andi, Max, Kathi, Kathi, Theresa, Stefan, Tobi, Flo, Katica, Sandra, Julia, Nunu, Marlene, Marlene, Evelyn, Anna, Doria, Sylvia, Sorger, Sara, Toni, Simon, Felix, Fede, Manu, Christian, Jürgen, Marko, Mirjam, Isa, Pevo, Markus, Mike, Amon etc.) who know my “insanity”, and with which I have not only shared numerous pictures of memories but also great times by having just a couple of beers. Last but not least I thank Walter Kurz for his quick and precise amendment, Christoph Hauzenberger for his critical advices and Jürgen Neubauer together with Karl Ettinger and Magdalena Mandl for their technical support! For those I have not mentioned, I am sure a beer makes up for it!

Abstract

The Seckau Complex within the Seckauer Tauern is part of a remapping project with the purpose of contributing new data about the magmatic, metamorphic and tectonic evolution including radiometric dating. This thesis provides, beside an all-embracing summary of the hitherto existing literature, this new data, regarding the area of the “Sonntagskogel” and “Triebener Törl” south of Trieben in Styria, Austria. The methods used during the research included areal mapping, optical microscoping of self-prepared thin-sections and description of minerals, microstructures as well as quartz textures analysis by photometer. Further, geochemical analyses of selected samples and zircon separations and preparations for radiometric dating were part of it. The results indicate a clear west-north-west linear stretching of the diverse orthogneisses with observed plagioclase richness and paragneisses with partly high mica content. The evaluated temperature of deformation has been set between 300 °C and 400 °C based on optical petrography and quartz textures analysis by LPO measurements. The chemical petrography revealed a clear trend in most major oxides and a strong peraluminous character. The melting series has been clearly defined as potassium rich calc-alkaline whereby the source type varies between S, I and A type granitoids which have been assigned to certain geotectonic positions. Those positions range from late-orogenic, post-collisional uplift to pre-plate collision and syn-collision, whereby all are grouped as a volcanic arc setting. Zircons of eight samples were separated, mounted, polished and analysed by the scanning electron microscope, due technical difficulties with the LA-ICP-MS no measurement could have been executed, but the zircon shape correlates strongly with geochemical data. The correlation between the newly gathered information and literature pointed out that the study area is very likely a northern volcanic island arc and active continental margin of the Cadomian terranes north of Gondwana, whereby a successful measuring of the prepared zircons could substantiate the Cadomian theory for the Seckauer Tauern.

Table of Content

1. Introduction

1.1. Objective and Purpose

The cause for this thesis is the remapping of the old map sheets “ÖK 130” and “ÖK 131” of the federal geology institute of Austria, which covers the area of Trieben and Kalwang in the province Styria, Austria. Therefore several master students have been working on this project in different areas (Fig. 1), collected rock samples, geochemical data and mapped a certain part of a requested district of one of the older maps.

This thesis belongs to the stated remapping project and has the purpose of contributing new data to the magmatic, metamorphic and tectonic evolution of the Seckau complex, with focus of structural and petrological analyses (kinematic of nappe stacking, metamorphic conditions) and U-Pb dating of zircons in the area of the Triebener Tauern.

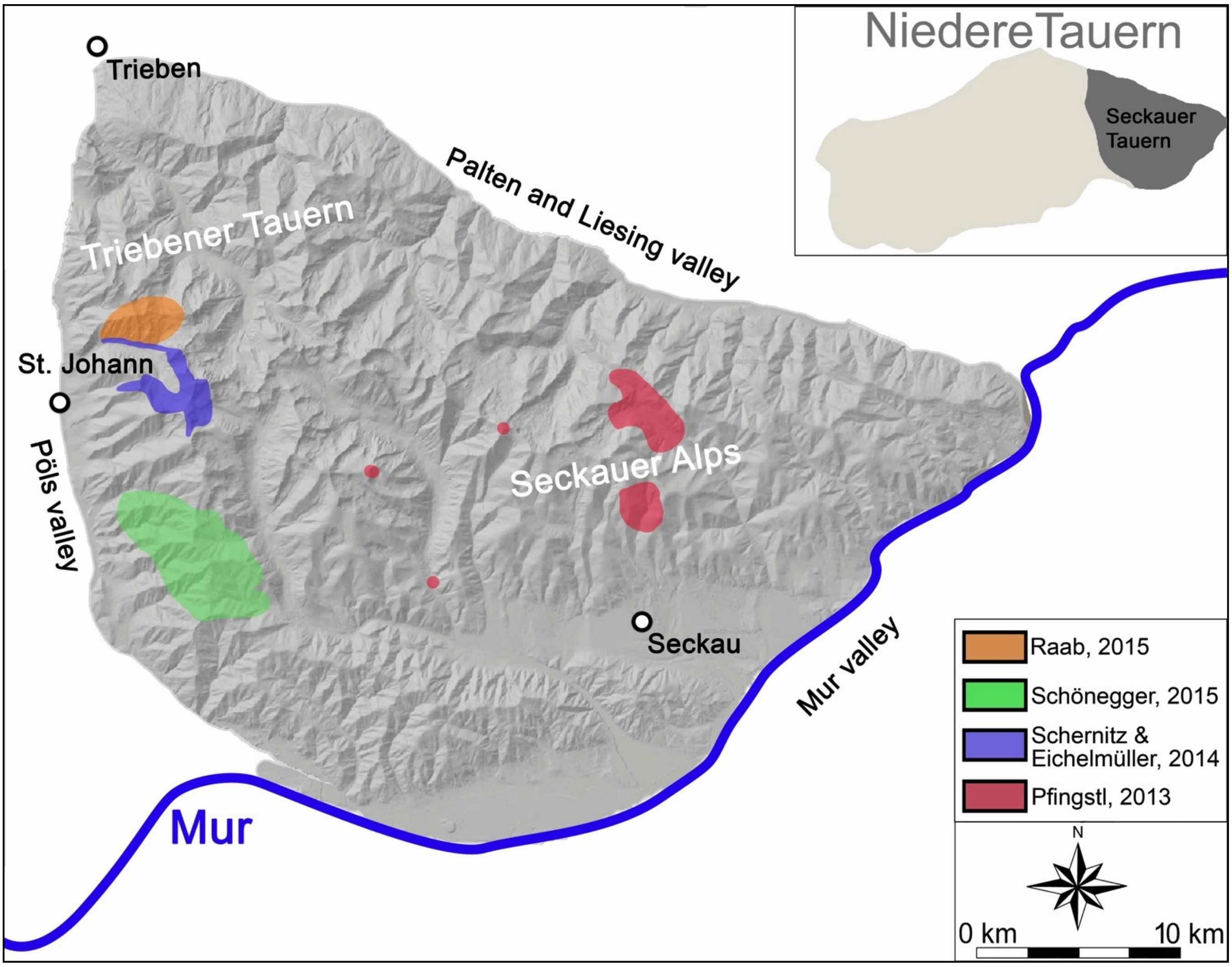

Fig. 1: Locations of former and current study and mapping areas transferred to a laser scan of GIS-Styria.

Therefore the local granitoids should be geochemically characterized and the intrusion sequence and the intrusion age should be determined by radiometric age dating of zircons. Not only newly collected samples through this thesis should be used for analysing, also prepared and semi-prepared samples which haven’t been fully investigated of a previous thesis.

1.1.1. Geographic Position of the Working Area

The Eastern Alps are commonly divided into four major groups, “Northern Calcareous Alps”, “Central Eastern Alps”, “Southern Calcareous Alps” and “Western Calcareous Alps”. The Niedere Tauern are positioned in the north of the Central Eastern Alps as it is seen in the following (Fig. 2) (Grassler, 1984). The Niedere Tauern in Styria is divided into four separate parts. From west to east these parts are named as follow “Radstädter Tauern”, “Schladminger Tauern”, “Rottenmanner and Wölzer Tauern” and “Seckauer Tauern” (Grassler, 1984)-. All subareas belong to Styrian province of Austria (Fig. 3), except for the Radstädter Tauern which is part of the Salzburg province.

The focus of the study is within the northern range of the Seckauer Tauern, the so called “Triebener Tauern” (Fig. 1). Further all of the former and current thesis areas are also clearly in this figure represented. The field of this thesis continues north of the anterior thesis of “Eichelmüller & Schernitz” from 2014. The core target of the mapping is the 2,229 m high and so called “Sonntagskogel” which hasn’t been mapped since 1976 by Karl Metz (Metz, 1976). and is located near St. Johann.

The Sonntagskogel is surrounded by several valleys. The southern valley is the previous mentioned Bären valley, the one in the northeast is called “Bärengraben”, the “Fratten” borders it in the southeast and the last in the west is named “Weingruber”. In the following (Fig. 4) are the related lowlands presented. The graphic further illustrates the extent of the working area. It spreads from the Fratten valley across the Sonntagskogel to the Weingruber valley and from the Bären valley over the” Triebener Törl” to the Bärengraben valley.

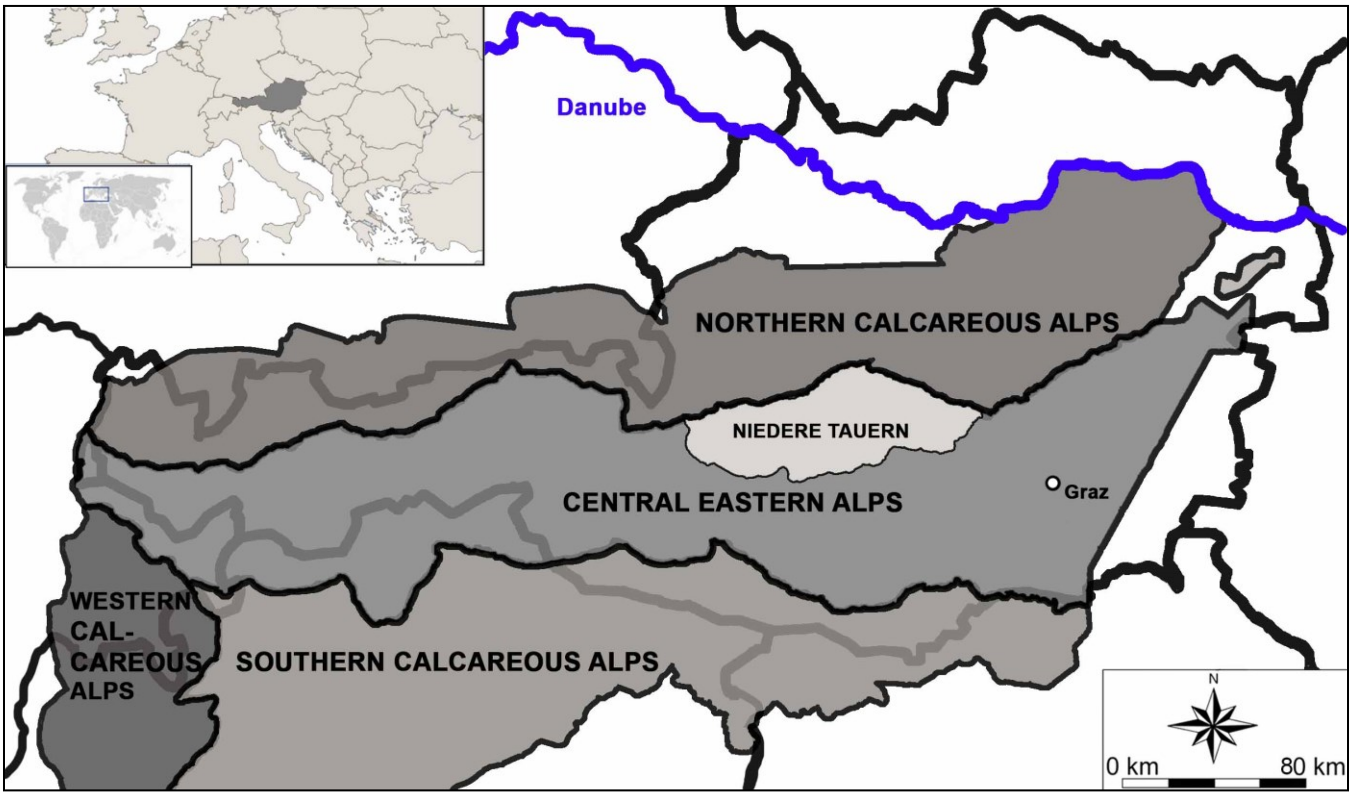

Fig. 2: Position of the Niedere Tauern in Austria based on the Alpine Club classification of the Eastern Alps (Grassler, 1984).

Fig. 3: Geographical overview and subdivision of the Niedere Tauern in Styria, Austria (Grassler, 1984).

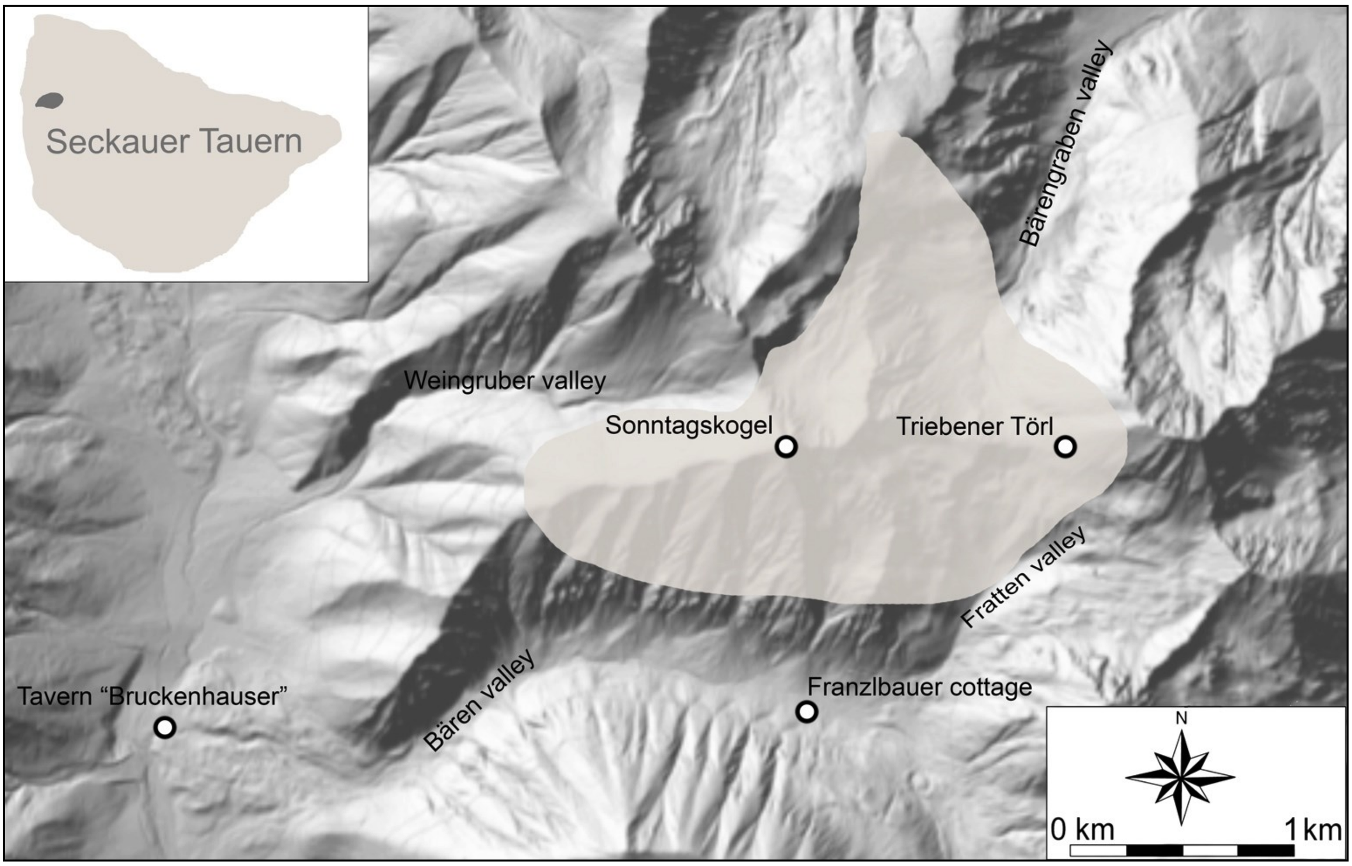

Fig. 4: Overview of the thesis research area in the Triebener Tauern projected onto a laser scan of GIS-Styria. Regional landmarks include the tavern “Bruckenhauser“ and the Franzlbauer cottage.

2. Geological Overview of the Eastern Alps

The Alpine orogeny resulted from collision of two tectonic plates, the European and Adriatic plate (or “Apulian plate”), which have collided after subduction of intervening ocean basins, which are presented on page 14. The Alps are subdivided into four super units (Fig. 5) the “South-Alpine” and the other three super units which are named “Helvetic”, “Penninic” and “Austro-Alpine”, whereby the Austro-Alpine builds the upper most part as illustrated (Fig. 6). The Austro-Alpine is represented mostly in the eastern Alps (Austria) with several nappe systems and forms the major land mass in this European region (Froitzheim, 2011; Janoschek & Matura, 1980). During the orogeny flysch sediments, and on top of it molasse sediments, have been deposited and formed the nowadays “Foreland”.

These super units have been incorporated at different stages in the Alpine orogenesis and they consist nowadays of basement and cover nappes (Froitzheim, 2011). A schematic drawing of the nowadays stacking design of the Alps is illustrated on page 12, where the several major units and their tectonic position within the stacked system can be seen. It provides also a schematic design of the tectonic situation of the Alps and displays the sequential arrangement of the Alpine super units especially the difference of the Austro-Alpine and the south-directed reverse faults and thrusts of the South-Alpine (Froitzheim, 2011). Further the differentiated basement and cover units as well as the major fault systems of the Alps are drawn at their nowadays geographical position.

The Permo-Mesozoic metasedimentary cover still overlies most of the Alpine basement units in the north and south, which are mainly uncovered in the central area (Fig. 5). The Tauern Window (TW) and Engadine Window (EW) are situated in the Austro-Alpine of the Eastern Alps, and are rare locations where the Helvetic and Penninic units forced their way through the Austro-Alpine, as it is seen in Fig. 6. Further, these windows provide an insight into the complex orogenesis and stacking of the super units and are the only locations, except for the slim area north of the Austro-Alpine, where Penninic and Helvetic units appear. Also the Seckauer Tauern are located in the Eastern Alps as it can be seen in previous introduction chapter, and belong to a nappe stack which will be explained in the following “Palaeogeography and Tectonostratigraphy of the Eastern Alps”.

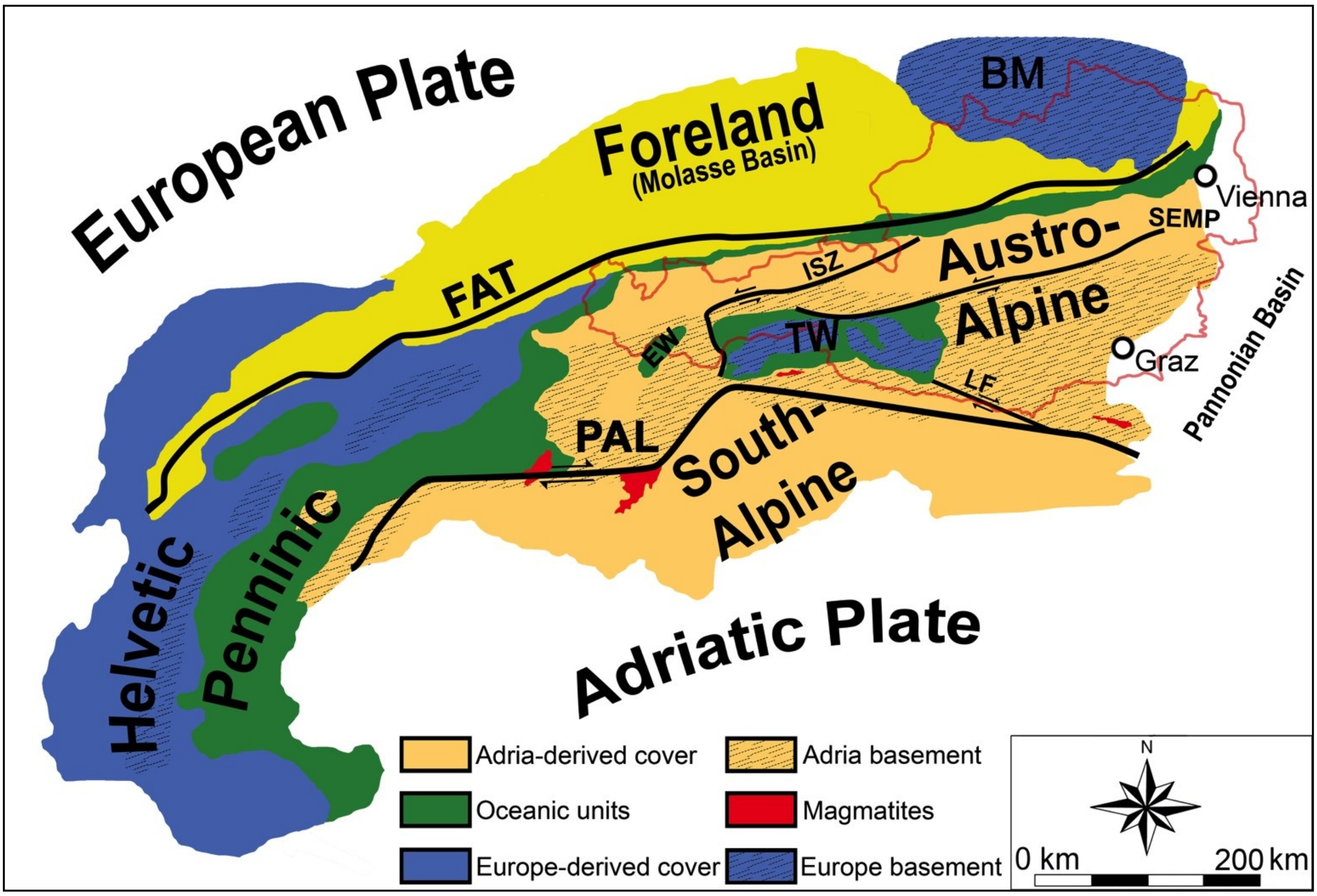

Fig. 5: Schematic overview of the geological super units of the Alps and their subdivision of basement and cover. LF = Lavanttal Fault system, ISZ Inntal Sutur Zone, SEMP = Salzachtal-Ennstal-Mariazell-Puchberg fault system, EW = Engadine Window, TW = Tauern Window, PAL = Periadriatic Lineament, FAT = Frontal Alpine Thrust Fault. After Ortner et al. (2015).

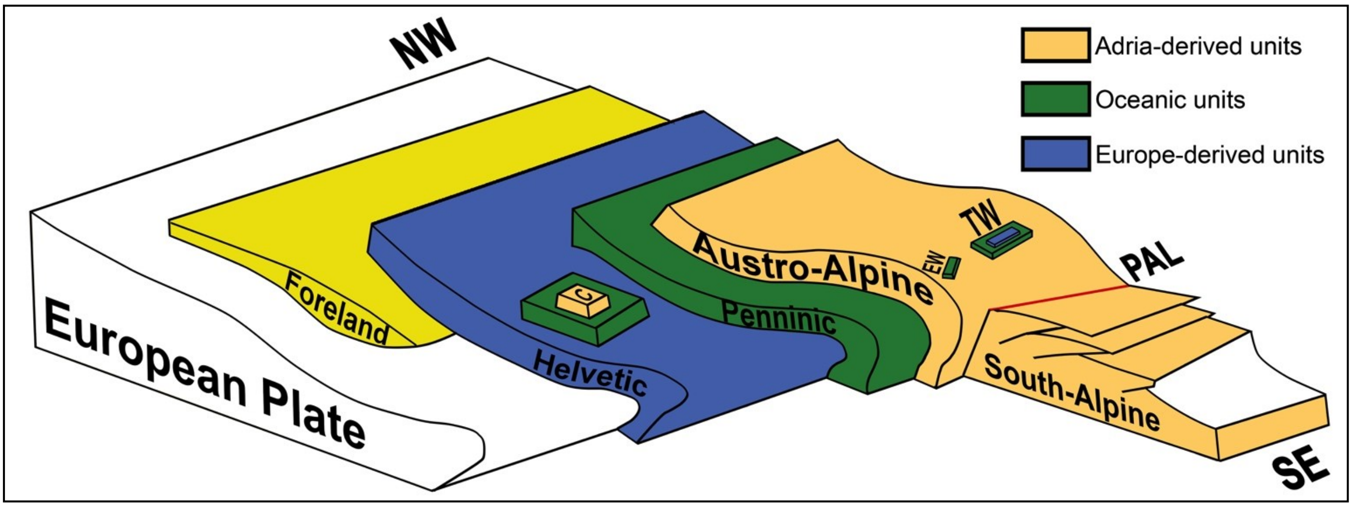

Fig. 6: Schematic illustration of the tectonic stacking of the geological super units of the Alps. The Tauern Window (TW) and the Engadine Window (EW) belong to the Penninic and Helvetic and do not represent an upper geological unit, instead the display their special feature as single occurrence of Penninic and Helvetic within the upper most unit, the Austro-Alpine. C= Cervinia, PAL = Periadriatic Lineament, NW = Northwest, SE = Southeast. After Marthaler (2001).

2.2. Palaeogeography and Tectonostratigraphy of the Eastern Alps

The Alps are geographically divided from southwest to northeast in “Western Alps”, “Central Alps”, “Southern Alps” and “Eastern Alps”. The Eastern Alps are separated from the Southern Alps through the Periadriatic Lineament (PAL) (Fig. 6). In the west of the Eastern Alps runs the boundary to the Central Alps through the “Rhine Valley”, “Splügen Pass” and “Lago di Como”. In the Austrian literature the Central Alps are mostly seen as part of the Western Alps, which makes the previous mentioned boundary between Eastern Alps and Central Alps the actual boundary to the Western Alps (Froitzheim, 2011). The North and East of the Eastern Alps are bounded by the Molasse Basin (Foreland), the external Variscan massif (Bohemian Massif) and the Pannonian basin in the east (Fig. 5). As it has been illustrated (Fig. 5) the Eastern Alps consist mainly of the Austro-Alpine super unit and show only a minor amount of Penninic and Helvetic. The new alpine classification of Schmid et al. (2004) declares that the Helvetic, Ultrahelvetic and Subpenninic nappes are paleogeographically seen representatives of the Mesozoic to Paleogene European continent. Further, the Upper and Lower Penninic nappes are counted as remains of the “Piedmont-Ligurian Ocean” and the “Valais Ocean”, together also known as “Penninic Ocean” or “Alpine Tethys”. They are also seen accountable for the formation of the Rhenodanubian Flysch and the Penninic nappes of the Tauern Window, Rechnitz Window and Engadine Window. Further, the ancient “Iberian-Briançonnais” land mass (microcontinent) is nowadays represented through the Middle Penninic nappes. This microcontinent was positioned in the Alpine Tethys, and splitted it into the previous mentioned southern Piedmont-Ligurian Ocean and the northern Valais Ocean.

The Austro-Alpine and South-Alpine are still considered as derivatives of the Adriatic plate. On top of it within selected areas of the Eastern Alps occur relicts of the “Neotethys Ocean” which are named in the literature “Meliata Ocean”, “Hallstatt Ocean” and “Vardar Ocean” (Schmid et al., 2004). These distinct continental and oceanic basements with their sedimentary covers (Fig. 5) collided in two stages. During the first phase, in the Cretaceous, the Neotethys has been subducted through the South Alpine while in the second stage, in the Paleogene the Alpine Tethys has been subducted through the Austro-Alpine followed by lateral extrusion in the Neogene. The metamorphism of the primary tectonic event is only seen in rocks of the Austro-Alpine and called “Eo-Alpine Metamorphism”, and is distinguishable from the secondary collision through different metamorphic peaks (Fig. 8) (Schuster & Stüwe, 2010). The figure on page 14 displays the various units with a schematic palaeogeographical cross section and the according palaeogeographic units of the Alps.

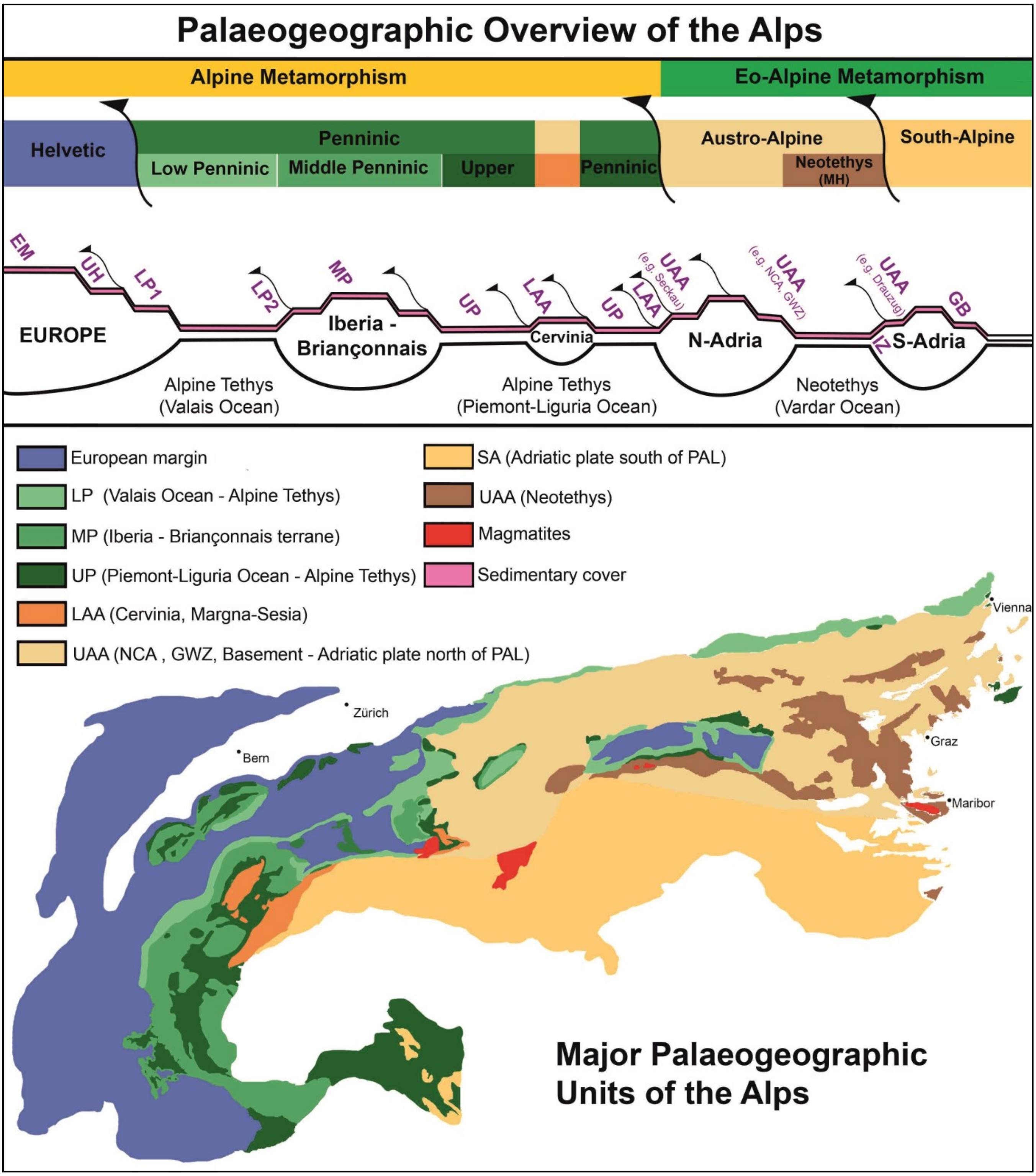

Fig. 7: Schematic overview of the major palaeogeographic relicts of the presented ancient landmasses to their nowadays geographical position after the Eo-Alpine- and Alpine-Metamorphism of the Alps, including a palaeogeographical cross-section illustrating all land masses and oceans which have occurred and are representatives of nowadays geological units. The cross-section does not represent a specific time period event. The sedimentary cover involves mainly Permo-Mesozoic metasediments. Categorisation has been done after Schmid et al. (2004). LP = Lower Penninic nappes, MP = Middle Penninic nappes, UP = Upper Penninic nappes, LAA = Lower Austro-Alpine nappes, UAA = Upper Austro-Alpine, NCA = Northern Calcareous Alps, GWZ = Greywacke Zone, PAL = Periadriatic Line, MH = Meliata-Hallstatt Ocean, GB = Gosau Basin, IZ = Ivrea Zone, EM = External Massif, UH = Ultra-Helvetic.

Description of the Super Units of the Alps

Helvetic and Ultrahelvetic

The structurally lowest Helvetic and Ultrahelvetic super unit, also named “Dauphiné”, which is nowadays the northernmost one, derived from the ancient European plate margin of the Mesozoic to Paleogene European continent (Fig. 7) (Neubauer & Raumer, 1993). It consists of a detached Mesozoic and Cenozoic sedimentary cover and a crystalline basement which includes deeply eroded Variscan rocks of Late Devonian to Carboniferous age. Due alpine deformation and partial uplift, the basement has been brought to the surface. (Neubauer & Raumer, 1993). The thin and discontinuous Ultrahelvetic nappes overlay the Permian to Paleogene sedimentary rocks of the Helvetic nappes and cover the Variscan basement. The direct derivative of the distal European continental margin is named Subpenninic (e.g. Venediger nappe) (Froitzheim, 2011).

Penninic

In contrary to the subjacent Helvetic, the Penninic represents the southernmost margin of the ancient European plate margin and encloses the ophiolitic suture between the Alpine foreland plus the Helvetic super unit and the Austro-/ South-Alpine units (Neubauer & Raumer, 1993). This includes the Alpine Tethys (“Valais Ocean” and “Piedmont-Ligurian Ocean”) the Iberian-Briançonnais microcontinent and forms together with the Helvetic complex north-vergent folded thrust sheets (Neubauer & Raumer, 1993). These oceans and land masses are divided after Schmidt et al. (2004) into three sub-devisional nappes.

The Piedmont-Liguria Ocean is assigned to “Upper Penninic Nappes” and contains the South-Penninic ophiolites such as “Bündnerschiefer” and “Schist Lustrés”. The terrains of the Briançonnais belong to the “Middle Penninic Nappes” which includes sedimentary covers of Middle Penninic basement nappes, the basement itself, detaches Middle Penninic cover nappes and the Permo-Carboniferous sediments and their Mesozoic cover (Froitzheim, 2011).

The Valais Ocean or also named “Valais trough” belongs with its Tertiary flysch, North Penninic ophiolites and Bündnerschiefern (including Rhenodanubian flysch) to the “Lower Penninic” nappes (Schmid et al., 2004). The Penninic in the Eastern Alps is covered by the Austro-Alpine. Hence, the Penninic occurs in Austria only in exceptional windows, such as Tauern and Engadine Window, and along the northern limit of the Austro-Alpine.

Austro-Alpine

The Austro-Alpine is the highest tectonic unit in the Eastern Alps and contains several thrust systems of pre-Alpine basements and their Late Palaeozoic and Mesozoic covers of sediments (Neubauer & Raumer, 1993). Further, it overlies the Penninic and contains relicts of the southern margin of the Piedmont-Liguria Ocean (Schmid et al., 2004). The Austro-Alpine is derived from the continental crust of the Adriatic plate and is geologically separated due the Periadriatic Lineament (PAL) from the South Alpine. An ophiolitic suture of the Piedmont-Ligurian Ocean separates the Austro-Alpine from the Helvetic and Penninic basement (Neubauer & Raumer, 1993). Further the Austro-Alpine shows in comparison to the Helvetic and Penninic a subdivision of the Eo-Alpine and Alpine metamorphic overprint. These two stages are separated by extension during the Late Cretaceous (Schmid et al., 2004).

The Austro-Alpine nappe stack of crustal material is subdivided into “Lower and Upper Austro-Alpine” (LAA & UAA). The “Northern Calcareous Alps” (NCA) and “Grauwackenzone” (GWZ) are also included in the Upper Austro-Alpine as the upper most units. The “Cervinia” microcontinent, also named “Margna-Sesia fragment”, which occurs only as relicts in the Western and Central Alps, and is according to Froitzheim et al. (1996) a small fragment of the Apulian margin, is also seen as the lowest unit of the LAA. The sequence of the Mesozoic cover (NCA) comprises the “Juvavic”, “Tirolian” and “Bavarian” nappes, which overly the GWZ (Schmid et al., 2004). The former subdivision of the “Middle Austro-Alpine” (MAA) with the “Koriden” and “Muriden” (Tollmann, 1977), has been revised by Schmidt et al. (2004), where the MAA has been newly organised and is now part of the UAA as nappe systems. The UAA includes from top to bottom the following nappe systems, the “Drauzug-Gurktal”, the “Ötztal-Bundschuh”, the “Koralpe-Wölz“ high pressure nappe system and the “Silvretta-Seckau” which is also the topic of this thesis main unit, the “Seckauer Tauern”. The LAA includes the Lower Austro-Alpine nappes e.g. “Radstädter Tauern” and “Wechsel” nappe.

South Alpine

The south of the PAL located South Alpine (Southern Alps) origins similar to the Austro-Alpine from the Adriatic plate, but shows in contrast to it a south-vergent reverse faults and thrusts, which are of a more limited extent than the Austro-Alpine. The South Alpine retro wedge originated dominantly in the Miocene and consists of upper crustal slices. Integral parts of the South Alpine are the Dolomites, which build a retro-wedge of the upper plate, from which the PAL separated the South Alpine (Schmid et al., 2004).

The Southern Alps are classified after Schmidt et al. (2004) into the “Lower crust of the Southern Alps” which includes the “Ivrea Zone” (Fig. 7), the “Upper crustal basement of the Southern Alps”, the “Post-Variscan volcanic and sedimentary cover of the Southern Alps” and the “Adriatic micro-plate”. The several fault systems of the Eo-Alpine Metamorphism of the South Alpine were mainly reactivated during the Alpine Metamorphism (Bernoulli, 2007).

Metamorphic Evolution of the Eastern Alps

An Overview of the crystalline nappe stacks of the Eastern Alps and its metamorphic evolution and differentiation of metamorphic character is presented in the following graphics.

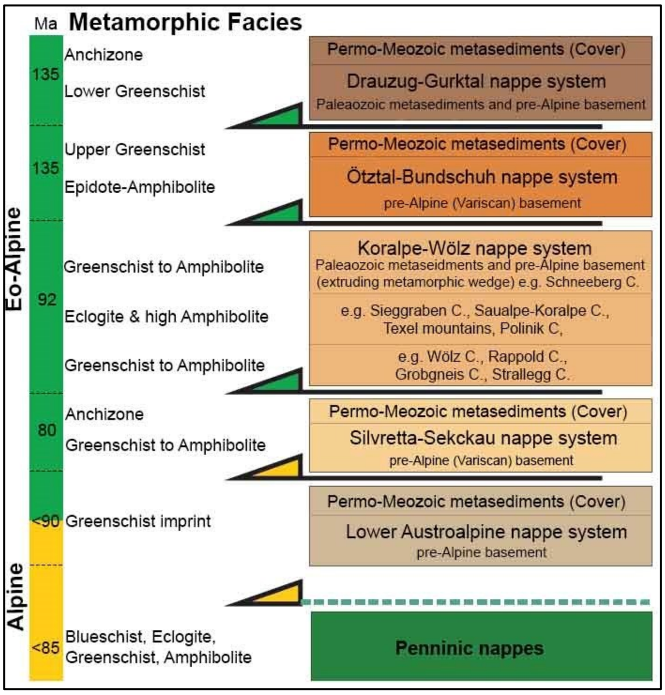

Fig. 9: Schematic sketch of the crystalline nappe stack and metamorphic evolution of the Eastern Alps, including the orogenic incorporation age and the differentiation of the Eo-Alpine Metamorphism and Alpine Metamorphism (Schuster et al., 2004).

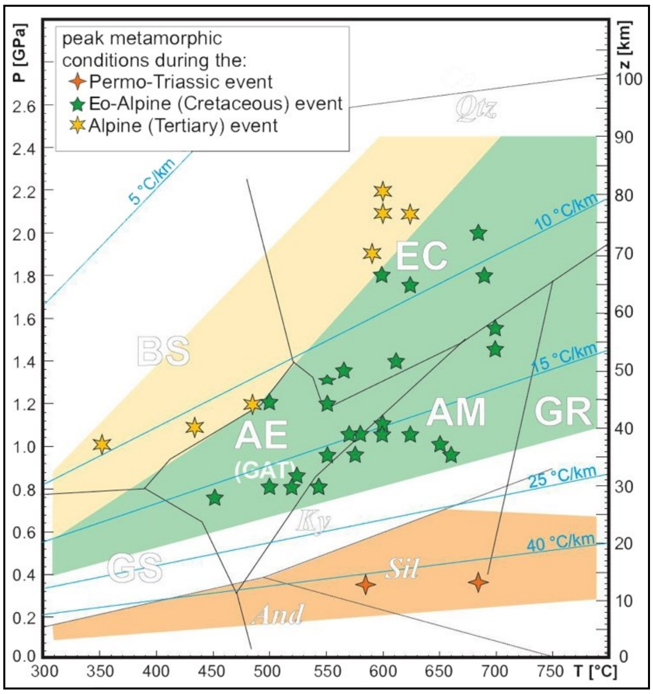

Fig. 8: Peak metamorphic P-T data and geothermal gradients (Schuster et al., 2004). GS = Greenschist, AE = Epidote-Amphibolite, AM = Amphibolite, GR = Granulite, EC = Eclogite, BS = Blueschist, Qtz = Quartz, Ky = Kyanite, Sil = Sillimanite, And = Andalusite.

Variscan Collisional Event

The Variscan orogeny occurred from Devonian (419 Ma) to Triassic (252 Ma). Beginning with the accretion of the Pangea supercontinent during the collision of Gondwana and Laurussia in the Upper Devonian to Carboniferous (Kroner & Romer, 2013). Imprints of low temperature and high pressure (LT/HP) happened prior to 350 Ma, the typical cooling age of the Variscan is around 310 Ma, after the thermal metamorphic peak at 340 Ma (Miller & Thöni, 1997; Neubauer et al., 1999). The Drauzug-Gurktal crystalline underwent a high pressure and low temperature metamorphism, which ranges between greenschist and granulite facies, in comparison to the South-Alpine which records only a greenschist overprint (Schuster et al., 2004). After the collapse of the Variscan orogeny an extension event followed.

Permian-Triassic Extensional Event

The extension within the Austro-Alpine and South-Alpine was caused due anticlockwise rotation of Africa including the southern part of the Adriatic plate with respect to Eurasia and the northern part of the Adriatic plate extension (Schuster et al., 2004) (Fig. 28). This developments included thinning of the lithosphere and therefore imprints of high temperature metamorphism which affected pre-Permian rocks e.g. Drauzug-Gurktal nappe system and part of the western Silvretta-Seckau nappe System of the UAA (Schuster et al., 2001). The Koralpe-Wölz nappe system also went through a low pressure and high temperature metamorphism during those times, accompanied by mafic intrusions, through the thinning of the basement in north-south direction.

Eastern Alpine Collisional Events

The evolution of this basement-cover relationship started in the early Permian (299 Ma). The metamorphic situation and stacking of the super units during regional compressional deformation, is the result of two independent plate tectonic events, as mentioned in the paragraph “Austro-Alpine” (Schuster et al., 2004). The Eo-Alpine metamorphic event of the Cretaceous is related to the continental collision, closure and embayment of the Neotethys (Vardar Ocean), which was closed during Upper Jurassic to Lower Cretaceous times. The continental collision of the Austro-Alpine, which formed the lower plate, and the South-Alpine, which acted as the upper plate during collision, evolved because of an intra-continental subduction zone between the nowadays Koralpe-Wölz nappe system and the Ötztal-Bundschuh nappe system around 145 Ma (Kurz & Fritz, 2003; Schmid et al., 2004). The metamorphic peak of the Eo-Alpine event has been dated to 100 Ma, whereby the youngest cooling age reaches 65 Ma (Frank et al., 1987). This consumption of the Adriatic plate and it’s in between ocean continued until the South-Penninic (Alpine Tethys - Piedmont-Ligurian Ocean) started to subduct during the Upper Cretaceous (Froitzheim et al., 2008).

The Alpine metamorphic event of the Paleogene occurred due the closer of the Alpine Tethys and the embedding of it and the Iberian-Briançonnais land mass (Western and Central Alps include also Cervinia land mass), due the re-arrangement of the border-zone of Penninic and Austro-Alpine from a passive to an active continental margin, which has started at about 120 Ma. Oceanic lithosphere and fragments of the northern margin of the LAA have been subducted below the UAA. Areas around the Tauern Window show eclogite facies whereby Mesozoic part of the Penninic and parts of the LAA reached blueschist facies (Schuster et al., 2004). The thermal peak has been dated at about 30 Ma (Blanckenbur et al., 1989).

2.3. The Niedere Tauern in Styria

The area of Styria is covered by the Eastern Alps and the “Styrian Basin”, whereby the Alpine part consists of poly-phase deformed and metamorphosed sedimentary and crystalline rocks of the Austro-Alpine. In contrast to the overlying Styrian Basin, which consists of unmetamorphosed and weakly deformed sediments, the stacked nappe systems of the Austro-Alpine in Styria are either separated by flat-lying shear zones, or by major steep strike-slip faults from each other. The GWZ and the NCA are exposed north of the “Rax–Aflenz–Leoben–Schoberpass-Ennsvalley–Line”, and low to high grade Palaeozoic and Mesozoic metamorphic rocks of the Crystalline basement are exposed south of it (Gasser et al., 2009). A tectonostratigraphic map (Fig. 11) and a schematic nappe stack of Styria (Fig. 10) is provided.

The Crystalline basement can be separated into several nappe systems as it has been stated previously. The lowest unit (Semmering-Wechsel nappe system) of the LAA is only exposed in north-eastern Styria in the area of the Semmering Pass and Wechsel Mountains and contains mostly paragneisses and phyllitic micaschists, but also of orthogneisses, greenschists, amphibolites and quartzites. The Permo-Mesozoic cover of carbonaceous, siliciclastic and volcanoclastic metasediments are folded into the crystalline basement and partly overly it (Gasser et al., 2009).

The Silvretta-Seckau nappe system (SSN), the lowest unit of the UAA, builds just a small region in the area of the Schladminger, Rottenmanner and Seckauer Tauern (see introduction) and the Gleinalpe, as well as at the elongated region north of the Mürz valley and is an essential part of the Niedere Tauern. The SSN consists of mica schists and biotite-plagioclase gneisses, amphibolite, orthogneisses and hornblende gneisses, whereby migmatites and ultramafics occur only locally, like the residuals of the Permo-Mesozoic cover, which included siliciclastic, volcanoclastic and carbonaceous sediments. The SSN has a widely distributed Variscan tectonics and metamorphism, but it has no records of Permo-Triassic Metamorphism within the Niedere Tauern, as stated in the previous chapter. The SSN is mostly overprinted by greenschist facies, but also shows an amphibolite facies of the Eo-Alpine, as presented (Fig. 9) (Gasser et al., 2009; Schuster et al., 2004).

In the western Niedere Tauern the Koralpe-Wölz nappe system, which builds the largest parts of Styria, is situated, as well as in the Seetaler Alpen, the Koralpe and the Fischbacher Alpen. It does not have a Permo-Mesozoic cover and consists of micaschists and paragneisses, pegmatites and orthogneisses, whereby marbles, amphibolites and eclogites can locally occur.

Two imprints are seen in the Koralpe-Wölz nappe system, one is the Permo-Triassic with amphibolite facies and local anatexis, accompanied by Permian gabbros, granites and volcanic rocks. The second imprint is caused by the Eo-Alpine metamorphism, which includes greenschist, epidote-amphibolite facies and eclogite facies (Gasser et al., 2009; Schmid et al., 2004; Schuster et al., 2004).

The next nappe system of the UAA is the Ötztal-Bundschuh nappe system, which is only exposed in the south-westernmost part of the Niedere Tauern, and consists of biotite-plagioclase gneisses, mica schist, orthogneisses and amphibolites. There are only few remnants of the cover present. Further, in this nappe system occurred a epidote-amphibolite facies during the Variscan, which has been overprinted by the Eo-Alpine with greenschist and amphibolite facies (Gasser et al., 2009; Schmid et al., 2004; Schuster et al., 2004).

The uppermost unite of the UAA is the Drauzug-Gurktal nappe system. It occurs only in areas of the central Styria in the north of Graz, the Palaeozoic of Graz and the Gurktal nappe in the region of Murau. All consist of a low-grade metamorphic Palaeozoic sedimentary rocks, including relics of the Permo-Mesozoic cover within in the Gurktal nappes system (Gasser et al., 2009).

The Greywacke Zone also occurs in the north of the Niedere Tauern and includes Palaeozoic rocks between the NCA and the medium- to high-grade metamorphosed units of Styria (e.g. Silvretta-Seckau, Koralpe-Wölz and Ötztal-Bundschuh nappe system). It consists of several tectonic sub-nappes, namely Veitsch, Silbersberg, Kaintaleck and Noric nappe which also were stacked on top of each other (Neubauer & Handler, 1994).

The elongated thrust belt from the Rhein valley to the west of Vienna, which is located north of the GWZ and south of the Penninic flysch zone are the Northern Calcareous Alps. The NCA builds together with the GWZ the north of Styria, whereby only the GWZ builds a minor extent in the north of the Niedere Tauern, and contains Permo-Mesozoic sediments which have withstood several metamorphic and tectonic events, and are subdivided into the “Upper Bavaric”, “Tirolic”, “Ultra Tirolic” units with “Hallstatt Melange” and an imbricated belt which is part of the last division (Frisch & Gawlick, 2003).

The “Neogene” and “Intermontane Basins” are characterized by sediments of the Plio- / Pleisto- and Holocene. Whereby the Styrian Basin is the largest basin and is also the representative of the western-most part of the Pannonian Basin (Gasser et al., 2009).

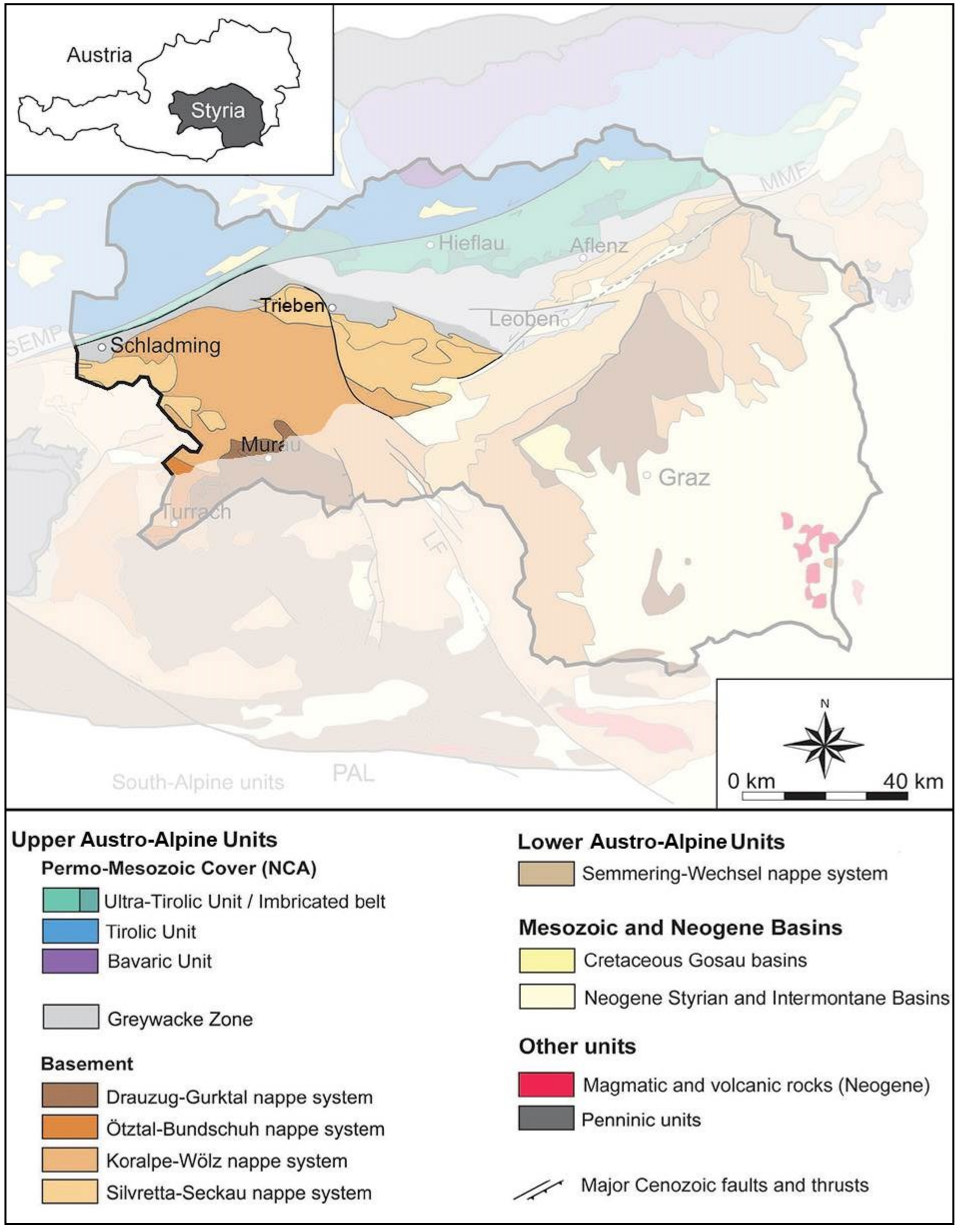

Fig. 11: Tectonic overview map of Low Tauern in Styria, after Schmid et al. (2004) and Frisch & Gawlick (2003), drawn after Gasser et al. (2009). Northern NCA = Calcareous Alps, SEMP = Salzachtal-Ennstal-Mariazell-Puchberg fault system, MMF = Mur-Mürz Fault system, LF = Lavanttal Fault system, PAL = Periadriatic Lineament.

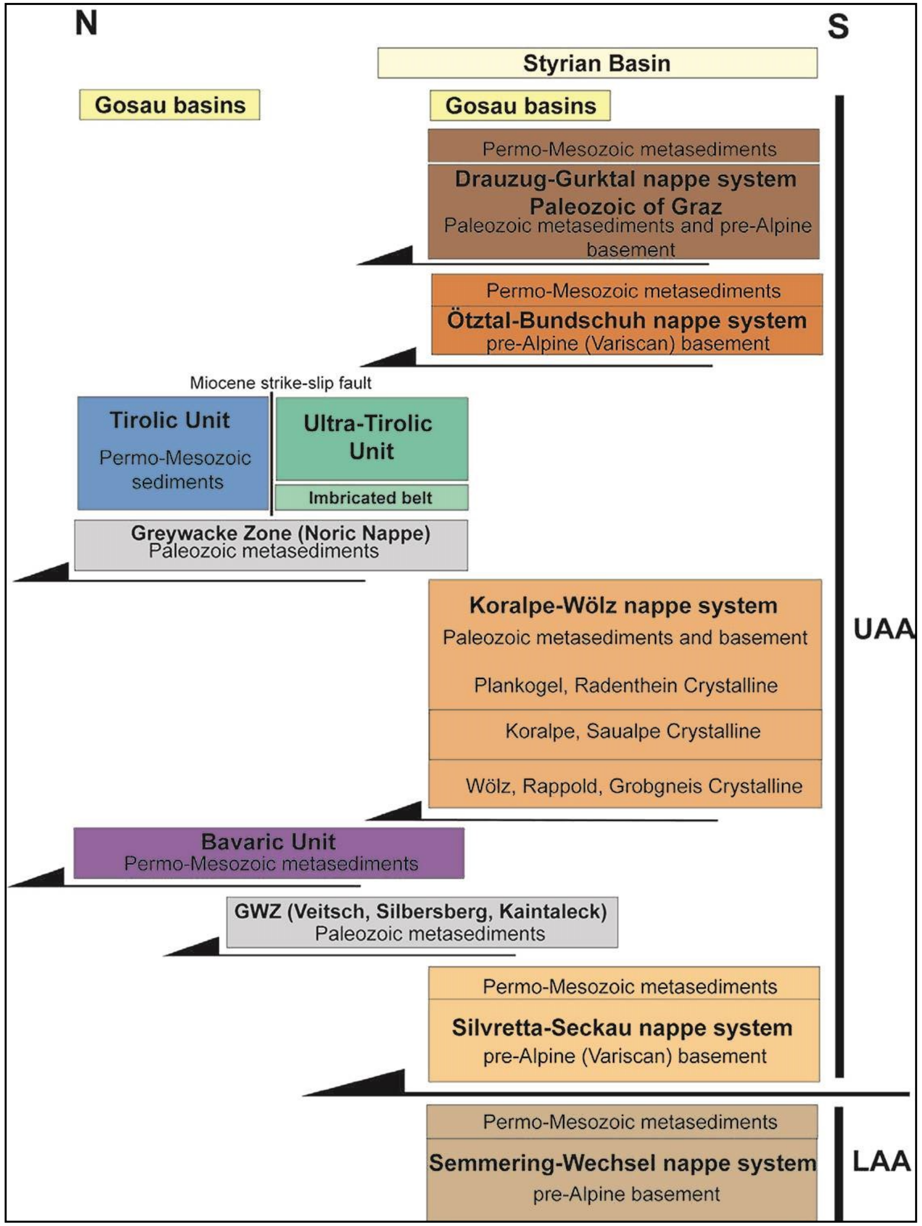

Fig. 10: Tectonostratigraphic relationships of Styria after Frisch & Gawlick (2003), Schmid et al. (2004) and Froitzheim et al. (2008) drawn by Gasser et al., (2009). UAA = Upper Austro-Alpine Units, LAA = Lower Austro-Alpine Units, GWZ = Greywacke Zone.

As forecited, there are three major units of the Upper Austro-Alpine and a minor unit within the area of the Niedere Tauern present. The Greywacke Zone in North, the Koralpe-Wölz nappe system in the west and the Silvretta-Seckau nappe system (SSN) in the east are the three master units, whereby the last two units predominate each of the mentioned cardinal directions. The Neogene Styrian and Intermontane Basins cover, only occurs at a minor area in the south-east. These units underwent different metamorphic developments during different geological periods as previously described. In the following graphic, the summarized geodynamic evolution of Styria is presented according to their geological nappe system (Fig. 12).

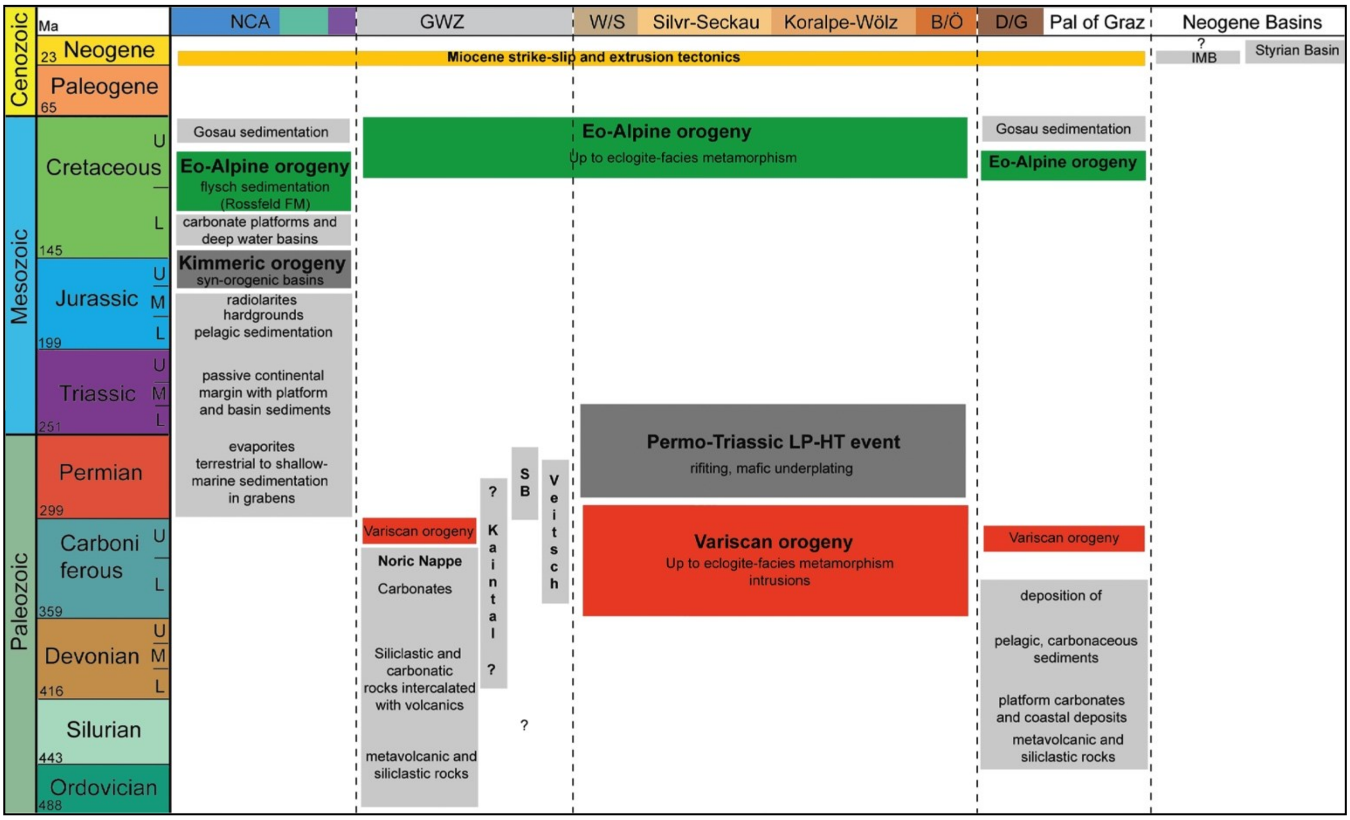

Fig. 12: Time relation of sedimentary and tectonic processes of Styria. Sediment accumulation of important events is coloured in light grey, deformation and metarmophic events are painted in dark grey, whereby the Variscan orogeny (red) and the Eo-Alpine orogeny (green) are marked separately (Gasser et al., 2009). The stratigraphic table follows the colour code of the "international comission of stratigraphy" (ICS), "L", "M" and "U" stands for "Lower", "Middle" and "Upper". IB = Intermontane Basins, NCA = Northern Calcareous Alps, GWZ = Greywacke Zone, W/S = Semmering-Wechsel Nappe, B/Ö = Ötztal-Bundschuh Nappe, Pal = Palaeozoic (Pal), SB =Silbersberg.

3. Seckauer Tauern

3.1. Tectonic Setting and Lithology

The Austro-Alpine basement east of the Tauern Window is divided into different lithotectonic units (Neubauer & Frisch, 1993). Within this division the Core Complex, Speik Complex and Micaschist-Marble Complex (Fig. 13) build up the area of the Seckauer Tauern, which is part of the Seckau nappe, as it is part of the SSN (Silvretta-Seckau nappe). Remains of the Permo-Mesozoic (metasediments), which are overlain by the Veitsch nappe of the Greywacke Zone, provide the cover of the Seckauer Tauern. The Seckauer Tauern is bounded in the north by the Greywacke Zone and in the west, south and east by the Koralpe-Wölz nappe System (KWN), whereby the KWN makes up the south-west region of the Seckauer Tauern (Metz, 1965; Schuster, 2013). The subunits of the SSN (Fig. 14) include the Bösenstein nappe and Pletzen nappe of the Seckau nappe. The Seckau Complex, Amering Complex and Speik Complex together with the Permo-Mesozoic cover build up the Seckau nappe and therefore the Seckauer Tauern. Boundaries of the complexes are not well defined (Pfingstl et al., 2015).

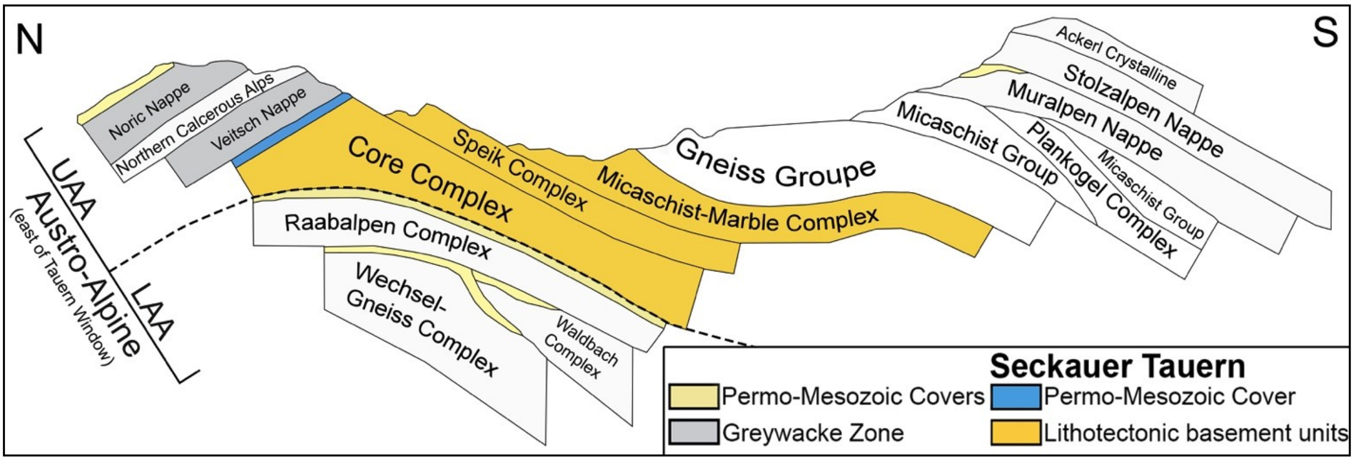

Fig. 13: Schematic Alpine structure east of the Tauern Window based on Franz Neubauer (1988), modified according to Schmid et al. (2004). UAA = Upper Austro-Alpine, LAA = Lower Austro-Alpine, N = north, S= south.

Micaschist-Marble Complex

This complex, positioned above the Speik complex remembers fossiliferous Silurian and Devonian sedimentary sequence. The metamorphic development is therefore assumed to be younger than Devonian. The upper portion of the sequence is dominated by siliceous and pure marbles, which are also intercalated with biotite amphibolites, some garnet micaschists and sheet-like pegmatites (Becker, 1981; Metz, 1976a; Neubauer, 1988b). The transition to the lower carbonates is characterized by calc-silicate rocks, dolomitic marbles and sometimes by scheelite-bearing tourmalinites (Neubauer & Raumer, 1993; Neubauer, 1988b).

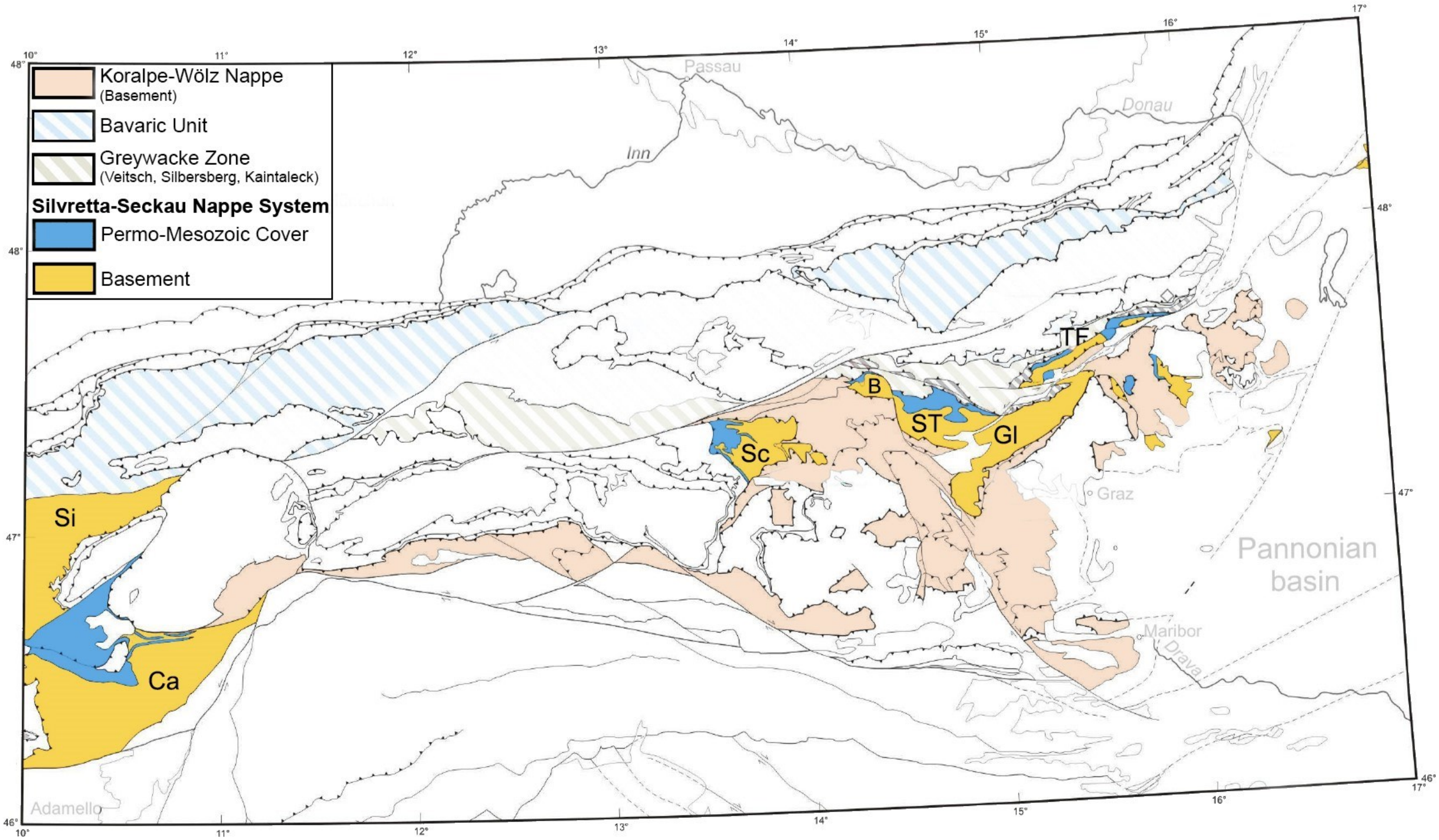

Fig. 14: Subdivision of the Seckau-Silvretta nappe system and its overlying units. Si = Silvretta nappe with Silvretta complex, C = Campo nappe, Sc = Schladminger Nappe, Se = Seckauer nappe including Bösenstein nappe and Seckauer Tauern, Gl= Gleinalm, TF = Troiseck-Floning nappe.

Speik Complex

This complex inherits a package of several hundred meter thick garnet amphibolites, metabasaltic rocks (banded amphibolites), garnet-zoisite and metagabbro rocks, plagioclase amphibolites, thin serpentinite or augen gneiss lenses with a length of up to 20 km. It contains all necessities of an ophiolite, whereby ultramafic rocks are mainly exposed at Hochgrössen and Kraubath (Neubauer & Raumer, 1993). In general it is exposed along south and north of the Gleinalm. Geochemical patterns of the southern Gleinalm show floor basalt and back-arc basin character (Neubauer, 1989) and a low $^{87}Sr/^{86}Sr$ ratio of 0.7044 from a plagioclase-rich orthogneiss, which leads to the interpretation of a bimodal volcanic suit. There are still uncertainties about the interpretation of the pre-Alpine ophiolites of the Speik Complex and Plankogel Complex (Neubauer & Raumer, 1993).

Core Complex

The lowest lithotectonic unit of the Upper Austro-Alpine appears in structural domes and cores. It consists of a strongly foliated biotite plagioclase paragneisses pile which forms the ground rocks of the other lithological units. Further, plagioclase orthogneisses appear in large domes (e.g. Gleinalm, Gr. Grießstein) surrounded by biotite plagioclase paragneiss. Grand masses of the most common banded amphibolite type and other various amphibolites are confined by orthogneiss and paragneiss (Becker, 1981; Frisch et al., 2003; Neubauer et al., 1987; Haiss, 1991; Neubauer & Raumer, 1993; Neubauer, 1988a; Schedl, 1981). Further, there are layered metatonalite complex's which are often accompanied by ultramafic rocks and metagabbros. The last lithological unit of the Core Complex are major plutons of tonalitic, granitic or granodioritic character in dome structures. The hanging wall of the Core Complex forms sheet-like "augen gneiss". Radiogenic Sr isotopic composition shows crust-derived magma but Archean and Early Proterozoic memories in magmatic zircons indicate a presence of an old continental crust which should underlie the Core Complex (Neubauer & Raumer, 1993).

Core Complex inherits the Amering Complex and the Seckau Complex (Bösenstein Massif, Pletzen nappe and the Troiseck-Floning). The Amering Complex formed by biotite-plagioclase paragneisses and some intercalations of orthogneisses differs from the Seckau Complex with its feldspar variations of orthogneisses, magmatic paragneisses, paragneisses, and amphibolites (Faryad & Hoinkes, 2001; Metz, 1976b; Pfingstl et al., 2015). The working area "Sonntagskogel" of this thesis is positioned in the north of the Pletzen nappe of the Seckau Complex and borders the Permo-Mesozoic metasediments.

Permo-Mesozoic metasediments

The metasediments, named “Rannach Formation”, include coloured quartz conglomerate, also known as “Alpine Verrucano”, sericite quartzite and phyllite, crystalline limestone and sericite schist (Fig. 15) after Metz (1976b) and Tollmann (1977), are overlain by the Greywacke Zone.

Greywacke Zone

Within the Seckauer Tauern are two nappes of the Greywacke Zone present, the Veitsch nappe and the Noric nappe. The Veitsch nappe has continuous stratigraphic section, including fossil bearing Early to Late Carboniferous formations (Neubauer et al., 1994; Ratschbacher, 1987). Further, it has been newly divided (Fig. 15) by Neubauer et al. (1994) into “Steilbachgraben”, “Triebenstein”, “Sunk” and “Grasschnitz” formations which inherit clastic and minor carbonates, carbonates and greenschists, quartz conglomerates and anthracite/graphite deposits, brownish to reddish sandstone and phyllites each respectfully. Ages vary from Carboniferous (Early Visean) to Perm (Scathian). The Noric nappe north of the Rannach Formation is divided into “Gerichtsgraben Formation”, “Blasseneck Porphyroid” and “Rad Phyllite”. Those units include phyllites and sandstones, acidic metatuff, shales and sandstones and show ages from Ordovician to Lower Devonian (Ratschbacher, 1987).

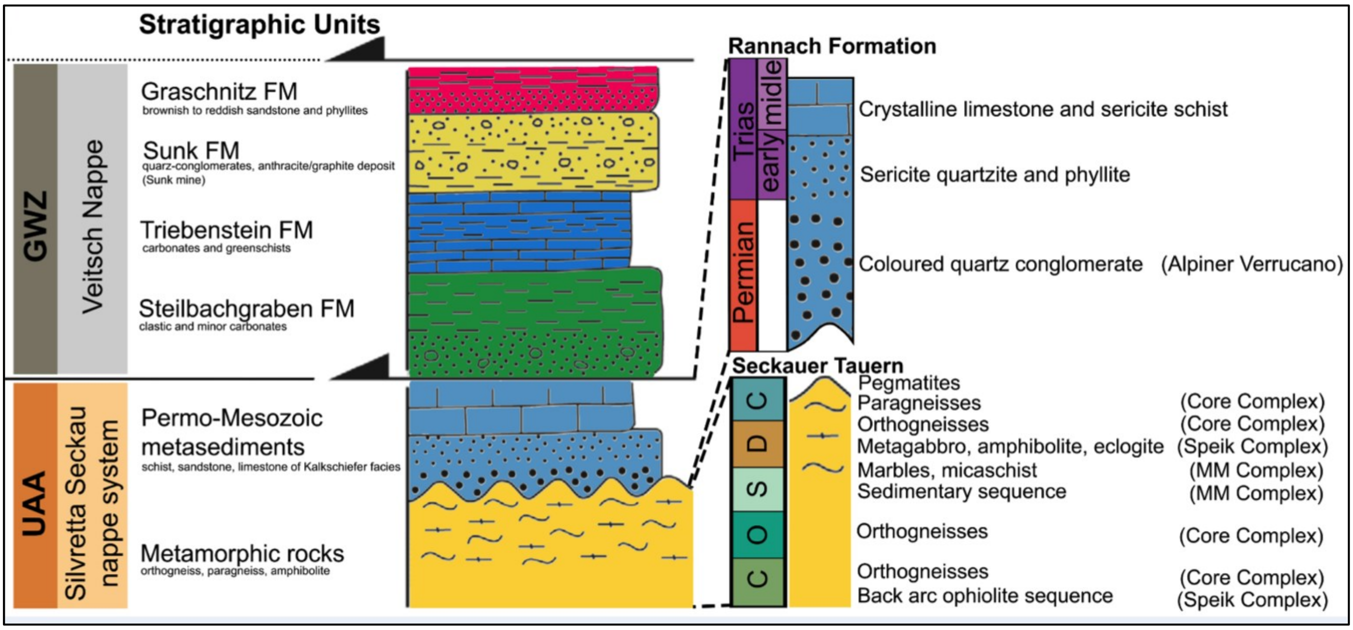

Fig. 15: Stratigraphic evolvement of the Silvretta-Seckau Nappe System and Greywacke Zone (Neubauer et al., 1994; Schmid et al., 2004; Tollmann, 1977) and division of the Seckauer Tauern (Faryad & Hoinkes, 2001; Faryad et al., 2002; Melcher, 2004; Neubauer & Raumer, 1993; Scharbert, 1981). C = Cambrian, O = Ordovician, S = Silurian, D = Devonian, C = Carboniferous, MM = Mica-Marble.

Based on the descripted unites above (Neubauer, 1988b) and new divisions within the Seckau nappe (Pfingstl et al., 2015), following domain distribution has been created (Fig. 16).

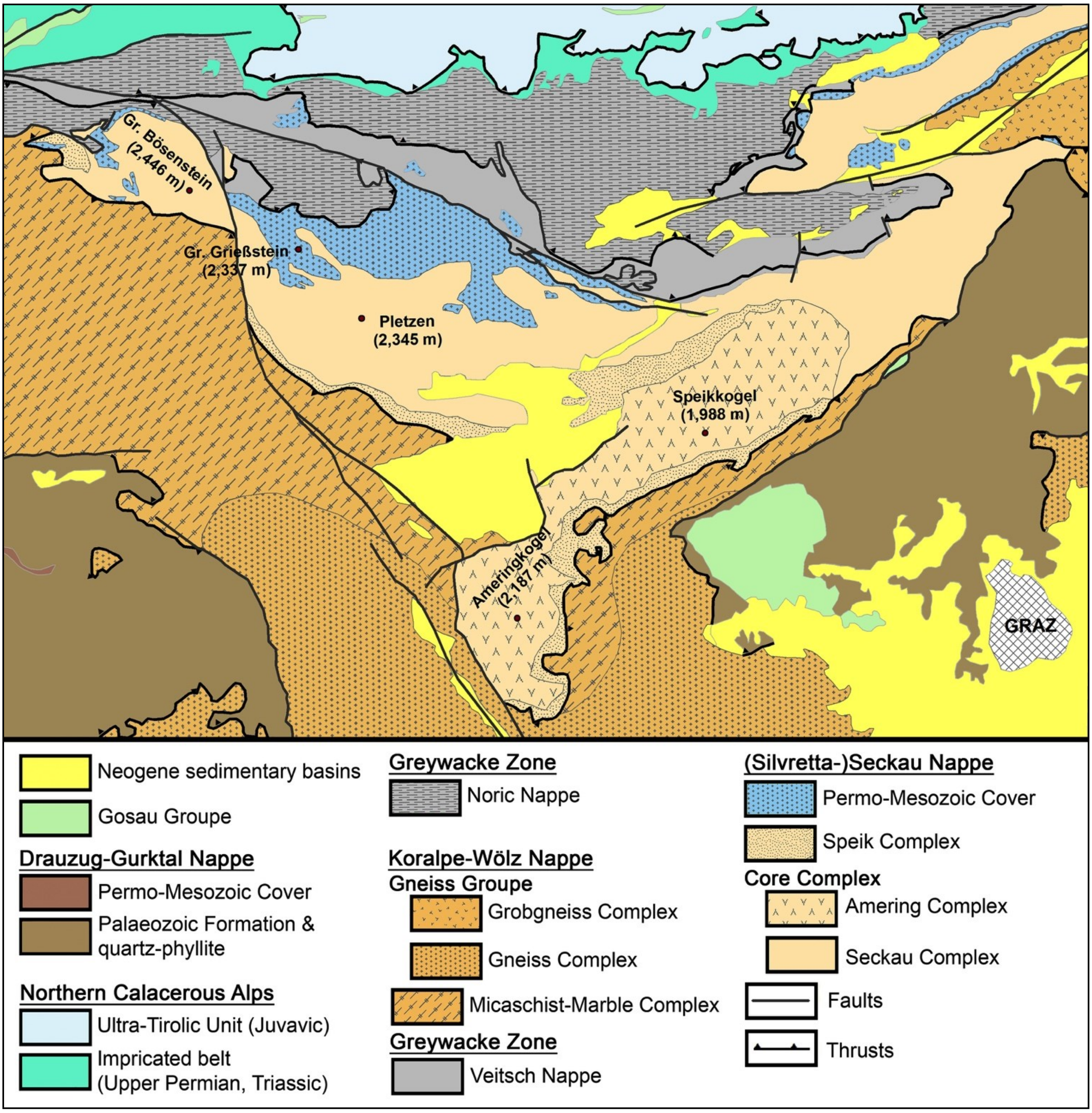

Fig. 16: Division of the Austro-Alpine domains in upper Styria, with focus on the Seckauer Tauern. (Neubauer & Raumer, 1993; Neubauer, 1988b; Pfingstl et al., 2015).

Fault Systems

The Seckau nappe is transected by several fault systems (Fig. 17). The “Mur-Mürz fault”, which has developed during lateral extrusion in the Miocene (Neubauer et al., 2000; Ratschbacher et al., 1991), is the north-east trending lineament that separates parts of the Seckau Complex. Between those faults and extent of the Mur-Mürz fault, the “Trofaichach fault”, reaches in (Pfingstl et al., 2015). Between the northern sinistral “Palten fault” and the dextral north-west to south-east trending dextral strike-slip “Pöls fault”, which separates the Bösenstein area form the Seckauer Alps (Metz, 1976a) a “Central Block” can be interpreted. The “Lavanttal fault” builds the south-western boarder (Metz, 1962, 1976b, 1978).

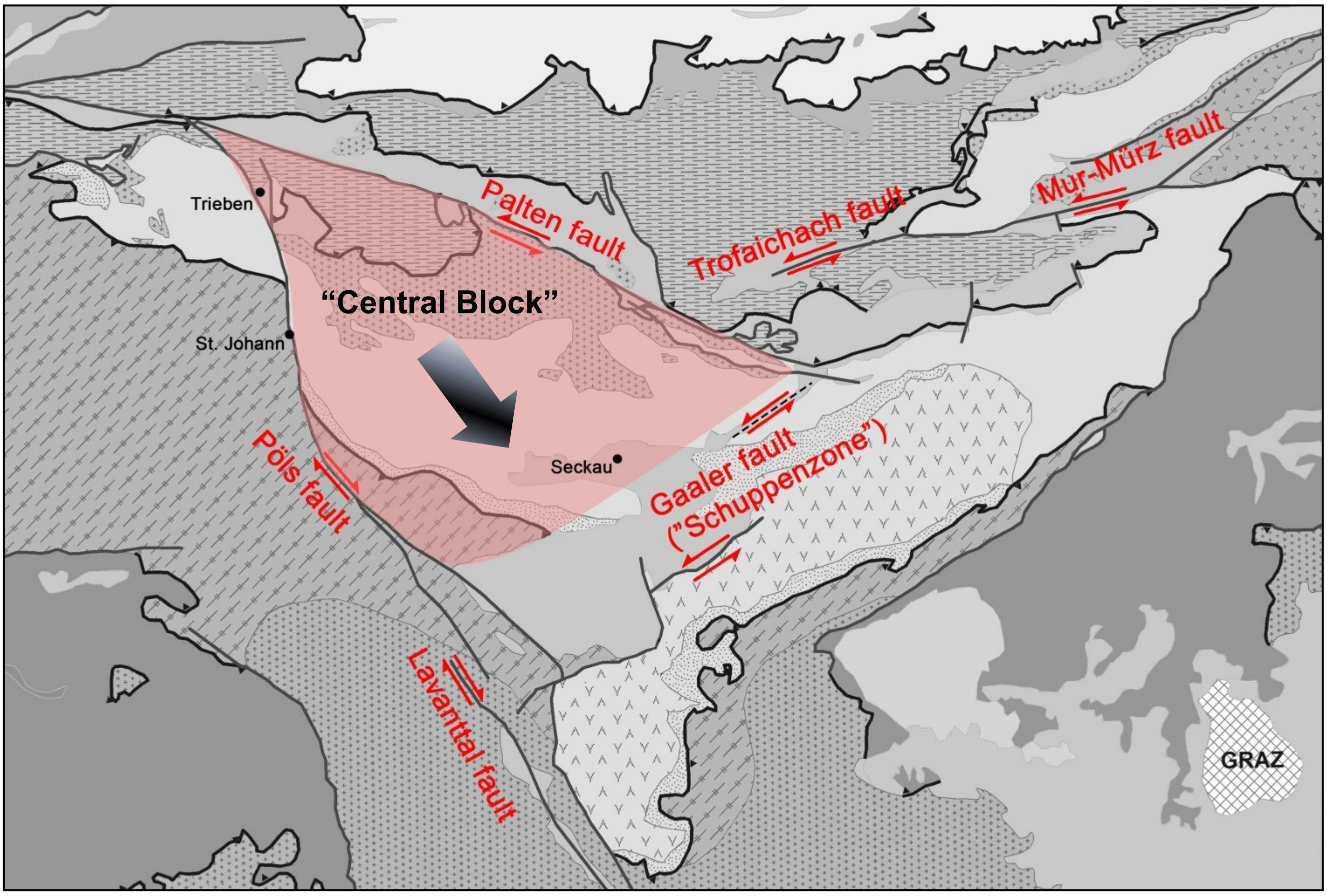

Fig. 17: Major fault systems within the Seckau nappe (Metz, 1962, 1976b, 1978, 1971; Pfingstl et al., 2015). The marked area between the Pöls and Palten fault is concluded as south-east moving "Central Block".

Seckau Complex

The Seckau Complex consists of the Bösenstein nappe, Pletzen nappe and the Mugel-Rennfeldzug of the Troiseck-Floning nappe (Fig. 16) (Faryad & Hoinkes, 2001; Pfingstl et al., 2015; Tollmann, 1977). The Permo-Mesozoic Cover is made up of quartz-conglomerate (Alpine Verrucano), sericite quartzite, phyllites, crystalline limestone and sericite. After Metz (1976) there are mostly mica poor "Flaser" (flaked) granite-gneisses and mica granitoids (Fig. 18). After Neubauer (2002) the basement comprises of orthogneisses and partly magmatic paragneisses with intermediate layers of amphibolites, micaschists, quartzites, gneisses with hornblende and occurrences of eclogites and serpentinites. The majority of orthogneisses and amphibolites evolved from magmatic rocks during the Cambrian and Ordovician and have been interpreted as reflections of the pre-Cambrian to Ordovician collision event (Fig. 21) (Neubauer, 2002). Schermaier et al. (1997) assumed, based on the age of Scharbert (1981) and the chemically similar tonalites of the eastern Hohe Tauern, that the large masses of tonalites and granodiorites of the Seckau-Bösenstein terrain may well be late Carboniferous and are related to dome structures. The Seckau Complex in the north east is named Mugel-Rennfeldzug (Tollmann, 1977) or Rennfeld Crystalline (Franz Neubauer, 1988a) and consists of biotite-plagioclase rich and also quartz rich gneisses, which are intercalated by decimetre to

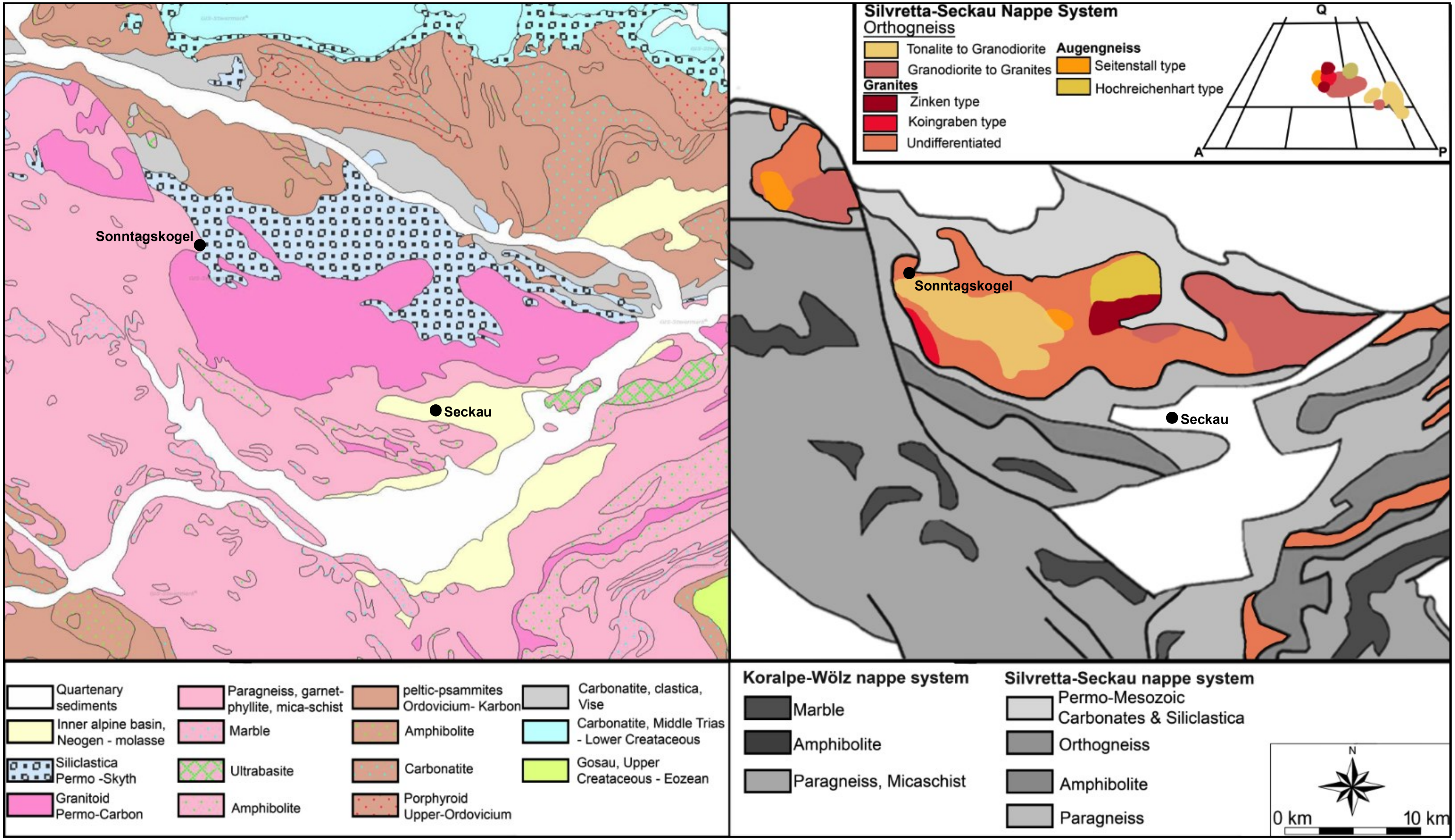

Fig. 18: Geological map after GIS-Steiermark (left) and an classification of different granitoids types(K. Metz, 1976a; Scharbert, 1981; Schermaier et al., 1997; Schermaier et al., 1992) printed on a geological overview map after Gasser et al. (2009) (right). Q = Quartz, A = Alkali feldspar, P = Plagioclase.

meter thick amphibolites layers. If the Seckauer Tauern and the Gleinalm (Amering Complex) represent a continuous nappe sheet or independent ones is still an open question (Pfingstl et al., 2015). The “Gaaler Schuppenzone” or Gaaler fault system, comprised mostly of the Speik Complex, is considered as the southern border of the Seckau Complex (Metz, 1971).

Quaternary Sediments

During the “Würm” glaciation (115 Ka to 10 Ka), the Seckauer Tauern were partly glaciated (Fig. 19). The area has not been fully covered, but the valleys of Hagenbach, Gaal, Ingering, Feistritz und Liesing valley received great parts of their nowadays shape. Further valley shapes, moraine sediments, and cirque of the higher peaks e.g. Gr. Grießstein, Sonntagskogel or Pletzen are relicts of this time period (Nagl, 1976). The area of the Sonntagskogel and Gr. Grießstein show a significant imprint of this glaciation event.

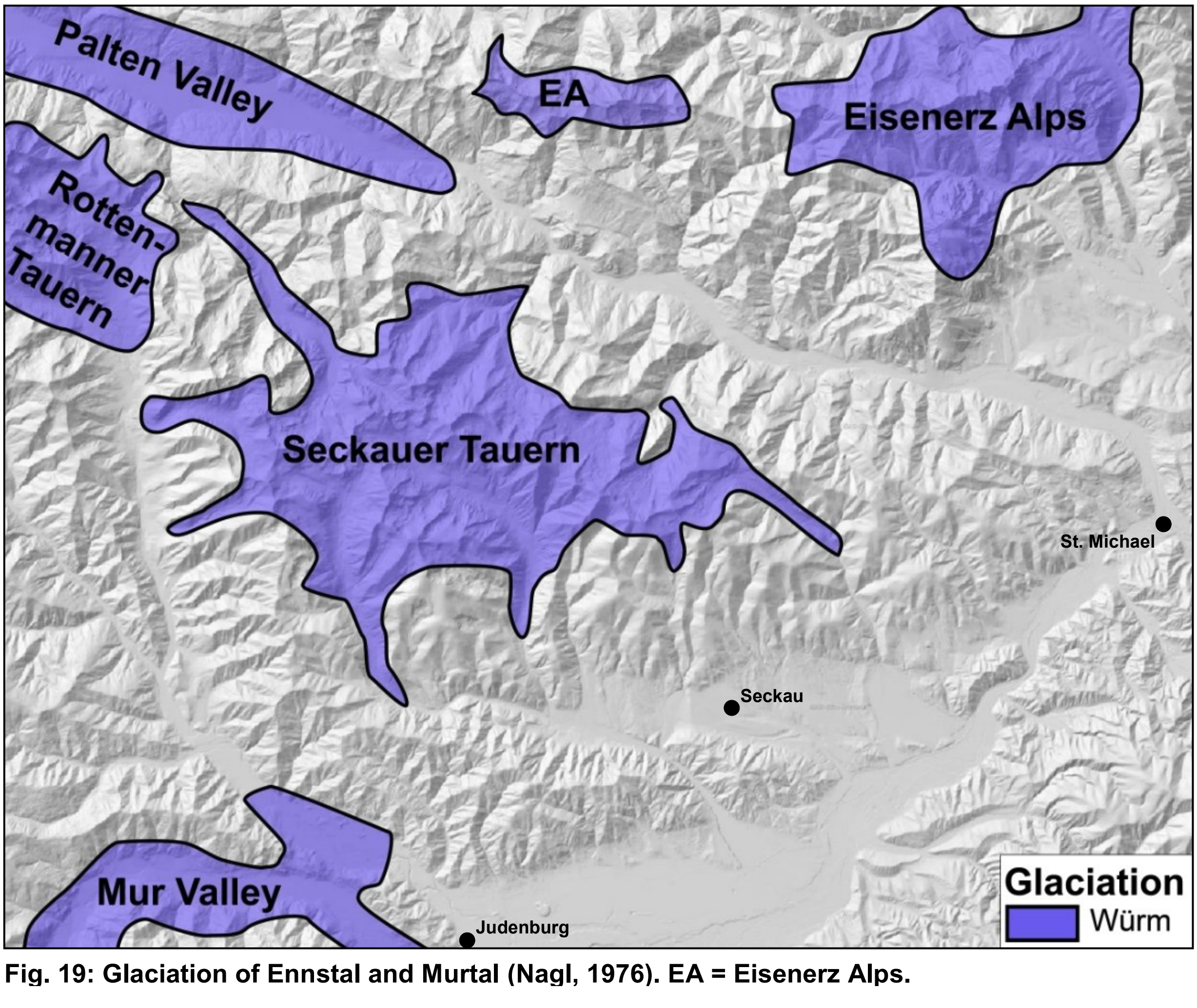

Fig. 19: Glaciation of Ennstal and Murtal (Nagl, 1976). EA = Eisenerz Alps.

3.1.1. Ancient mappings

On the following page, two cross-sections of the study area Sonntagskogel and surrounding is provided, including a space distribution and gneiss classification based on geographical references (Fig. 20).

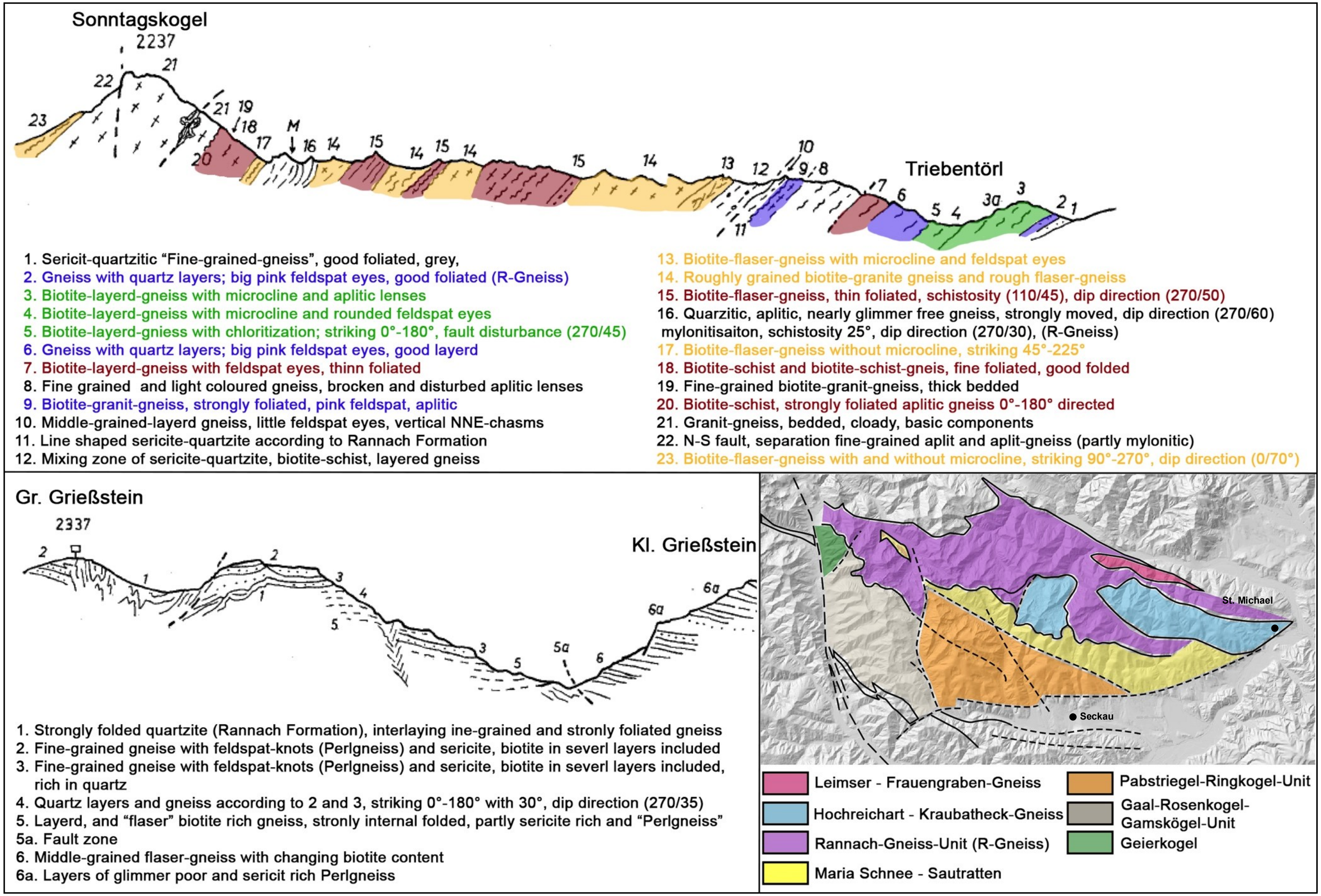

1. Sericit-quartzitic “Fine-grained-gneiss”, good foliated, grey,
2. Gneiss with quartz layers; big pink feldspat eyes, good foliated (R-Gneiss)
3. Biotite-layerd-gneiss with microcline and aplitic lenses
4. Biotite-layerd-gneiss with microcline and rounded feldspat eyes
5. Biotite-layerd-gneiss with chloritization; striking 0°-180°, fault disturbance (270/45)
6. Gneiss with quartz layers; big pink feldspat eyes, good layerd
7. Biotite-layerd-gneiss with feldspat eyes, thinn foliated
8. Fine grained and light coloured gneiss, brocken and disturbed aplitic lenses
9. Biotite-granit-gneiss, strongly foliated, pink feldspat, aplitic
10. Middle-grained-layerd gneiss, little feldspat eyes, vertical NNE-chasms
11. Line shaped sericite-quartzite according to Rannach Formation
12. Mixing zone of sericite-quartzite, biotite-schist, layered gneiss
13. Biotite-flaser-gneiss with microcline and feldspat eyes
14. Roughly grained biotite-granite gneiss and rough flaser-gneiss
15. Biotite-flaser-gneiss, thin foliated, schistosity (110/45), dip direction (270/50)
16. Quarzitic, aplitic, nearly glimmer free gneiss, strongly moved, dip direction (270/60) mylonitisaiton, schistosity 25°, dip direction (270/30), (R-Gneiss)
17. Biotite-flaser-gneiss without microcline, striking 45°-225°
18. Biotite-schist and biotite-schist-gneis, fine foliated, good folded
19. Fine-grained biotite-granit-gneiss, thick bedded
20. Biotite-schist, strongly foliated aplitic gneiss 0°-180° directed
21. Granit-gneiss, bedded, cloady, basic components
22. N-S fault, separation fine-grained aplit and aplit-gneiss (partly mylonitic)
23. Biotite-flaser-gneiss with and without microcline, striking 90°-270°, dip direction (0/70°)

1. Strongly folded quartzite (Rannach Formation), interlaying ine-grained and stronly foliated gneiss
2. Fine-grained gneise with feldspat-knots (Perlgneiss) and sericite, biotite in severl layers included
3. Fine-grained gneise with feldspat-knots (Perlgneiss) and sericite, biotite in severl layers included, rich in quartz
4. Quartz layers and gneiss according to 2 and 3, striking 0°-180° with 30°, dip direction (270/35)
5. Layerd, and “flaser” biotite rich gneiss, stronly internal folded, partly sericite rich and “Perlgneiss”

5a. Fault zone

6. Middle-grained flaser-gneiss with changing biotite content

6a. Layers of glimmer poor and sericit rich Perlgneiss

🟥 Leimser - Frauengraben-Gneiss
🟦 Hochreichart - Kraubatheck-Gneiss
🟪 Rannach-Gneiss-Unit (R-Gneiss)
🟨 Maria Schnee - Sautratten
🟧 Pabstriegel-Ringkogel-Unit
⬜ Gaal-Rosenkogel-Gamskögel-Unit
🟩 Geierkogel

Fig. 20: Maps and cross-section of the Sonntagskogel and Gr. Grießstein after Metz (1976) and an older space distribution of the tectonic units within the Seckauer Tauern (Metz, 1976b). The cross-section of the Sonntagskogel includes also a colour-cluster of similar rock types and does not refer to the space distribution on the bottom right corner.

3.2. Radiometric Dating

Plagioclase orthogneisses of the Gleinalm have been whole rock dated with Rb-Sr (Frank et al., 1976; Neubauer, 1988a) and produced an errorchrone of 518 ± 50 Ma. Augen gneisses of the Gleinalm yielded Rb-Sr ages of 330 ± 30 Ma (Frank et al., 1983). Nearly concordant U-Pb zircon ages (Haiss, 1991) of tonalite gneisses with 500 Ma of age are seen as the minimum formation time and correlates with the whole rock data of Frank et al. (1976). Metatonalite within the Core Complex dated to 356 ± 5 Ma by zircons (Neubauer et al., 1993), is considered as age of the Variscan metamorphism.

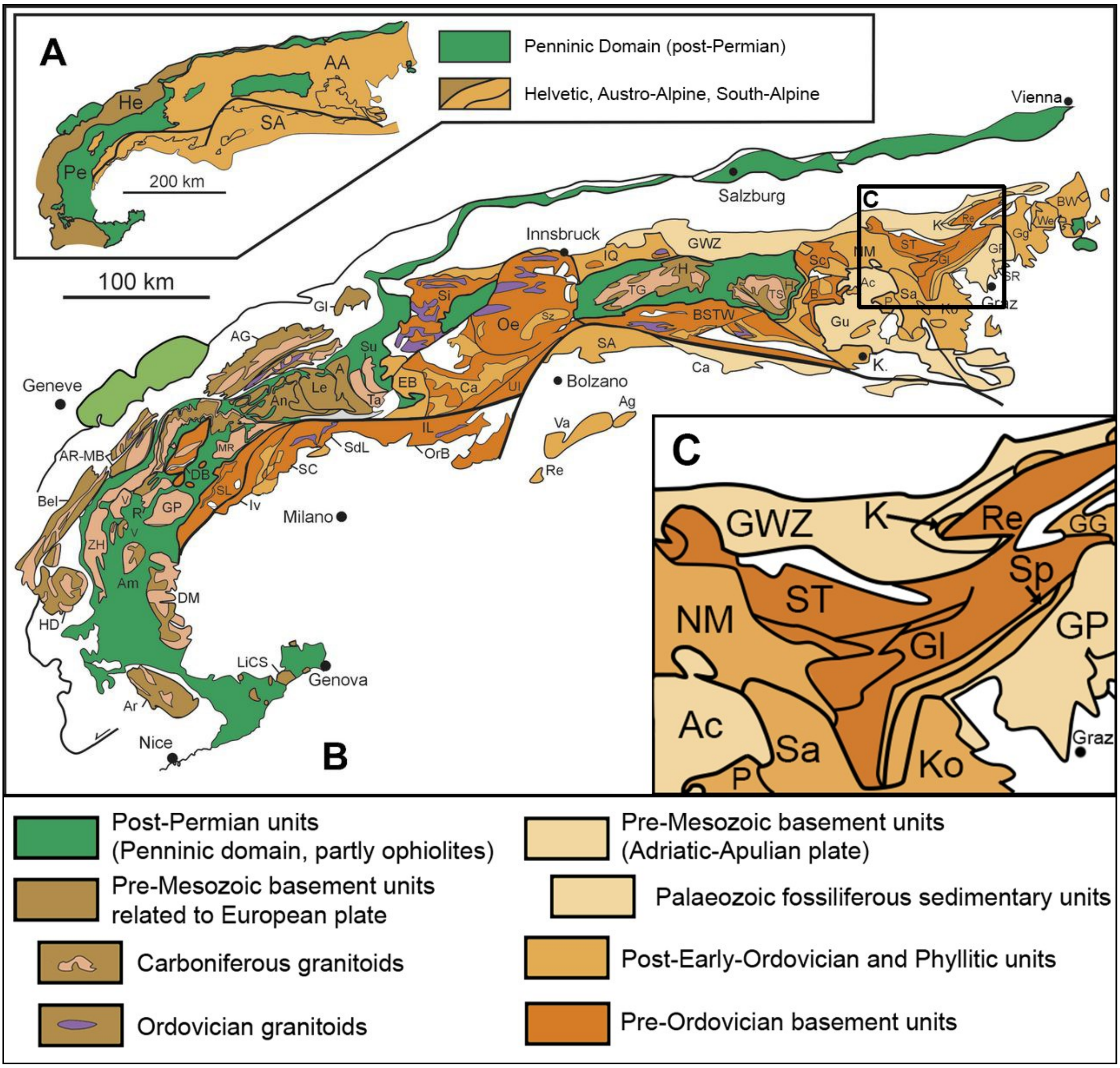

Fig. 21: Geological and geochronological map of the Alps. A = Domains of the Alps, B = Pre-Mesozoic basement units in the Alps, C = Section of the Seckau nappe; Ac = Ackerl Crystalline; Gg = Grobgneiss Complex; GP = Grazer Palaeozoic; Gl = Gleinalm; GWZ = Greywacke zone; K = Kaintaleck slices; Ko = Koralpe; NM = Niedere Tauern and Micaschist-Marble Complexes; P = Plankogel; Re = Rennfeld; Sa = Saualpe, Sp = Speik Complex, ST = Seckauer Tauern (Schulz, 2008; Raumer et al., 2013).

The upper intercepts of the metatonalite measured by U-Pb reached 3 Ga, and augen gneisses yielded 2.25 Ga, this ages have been seen as contamination of Archaean and Proterozoic zircons from continental crust during the melt rise of magmas (Neubauer et al., 1993; Neubaue et al., 2003). Orthogneisses of the Seckau Complex, yielded Rb-Sr ages of 432 ± 16 Ma (Scharbert, 1981).

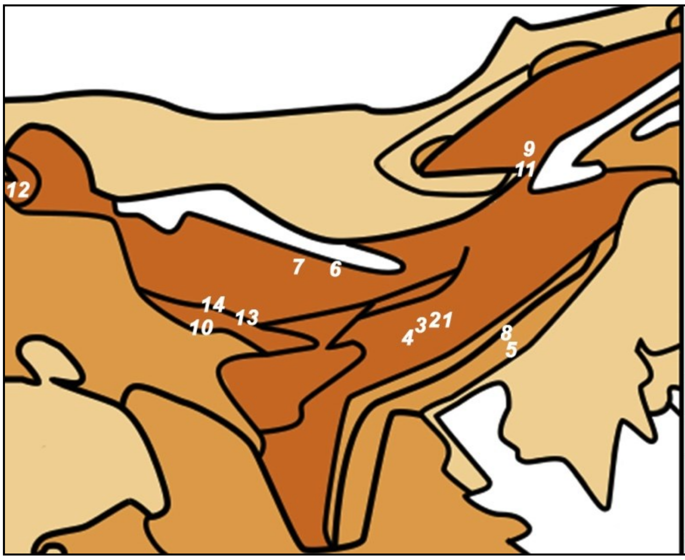

1: 745±44 Ma; Sm-Nd, Peridotite (Melcher, 2004)
2: 554±37 Ma; Sm-Nd, Orthopyroxenite (Melcher, 2004)
3: 550±17 Ma; Re-Os, Orthopyroxenite (Melcher, 2004)
4: 519±13 Ma; Re-Os, Orthopyroxenite (Melcher, 2004)
5: 518±50 Ma; Rb-Sr; Plagioklasgneiss (Neubauer, 1988)
6: 517±16 Ma; Rb-Sr, Granites, Granodiorites (Pfingstl, 2015)
7: 507±60 Ma, Rb-Sr, Granites, Granodiorite (Pfingstl, 2015)
8: 500±45 Ma; Rb-Sr, Plagioklasgneiss (Frank, 1976)
9: 433±28 Ma; U-Pb, Augengneiss (Neubauer, 2003)
10: 432±16 Ma; Rb-Sr, Orthogneiss (Scharbert, 1981)
11: 406±62 Ma; U-Pb, Paragneiss (Neubauer, 2003)
12: 397±7.8 Ma, Ar-Ar, Amphibolite from eclogite (Hoinkes, 2002)
13: 354±16 Ma; Rb-Sr, Two-mica metagranite (Scharbert, 1981)
14: 340±110 Ma;Rb-Sr, Flasergneiss (Scharbert, 1981)

Fig. 22: Geochronological overview of previous dated areas within the Seckau nappe based on publications, where also the location of sampling was known. Colour code is identical to the antecedent figure (Fig. 21). (Faryad et al., 2002; Frank et al., 1976; Melcher, 2004; Neubauer et al., 2003; Neubauer, 1988a; Pfingstl et al., 2015; Scharbert, 1981).

The oldest ages within the Speik Complex, of the Seckau nappe, are dated with orthopyroxenite at 550 ± 17 Ma (Melcher, 2004) further ages within Kraubath has shown a crystallisation age of 554 ± 37 Ma with a Sm-Nd isochron. The peridotite host rock provided an errorchrone Re-Os age of 745 ± 44 Ma (Melcher, 2004). The existence of these Cambrian and Proterozoic magmatic protoliths is explained by ocean and back-arc basins. Relicts of eclogite facies of the Hochgrössen massif (Speik Complex) are derived from ocean-floor basalts with the affinities to back-arc basin basalts and mid-ocean ridge basalts (Faryad et al., 2002). Ages of the Amering Complex (Core-Complex), measured with Rb-Sr, provided an isochron age of 500 ± 45 Ma and its volcanic origin (Frank et al., 1976) correlate with the Speik complex. During the Late Ordovician to Early Carboniferous, the protolith of the Micaschist-Marble Complex must have evolved, based on correlations with fossil-bearing sequences. Further it is presumed, that the micaschists arose during the Late Ordovician and Early Devonian age, whereby the marbles are mainly Middle Devonian (Becker, 1981; Neubauer & Raumer, 1993). The mineralization of several pegmatite's categorize them to a highly fractionated melt which have derived from a major granite (Koller et al., 1983) and are part of the later development within the Austro-Alpine (Raumer et al., 2013).

The Seckau Complex within the Core Complex dates a metagranite with Rb-Sr at 331 ± 25 Ma and an orthogneiss at 432 ± 16 Ma, which has been corrected based on field observations to 350 Ma (Scharbert, 1981). Calculations of whole rock isochron of granitic and granodioritic rocks presented an age of 517 ± 61 Ma, with a $^{87}Sr/^{86}Sr$ ratio of 0.7045 (Pfingstl et al., 2015). The evaluated ages correlate with the U-Pb ages 523 ± 3 Ma, 522 ± 6 Ma and 524 ± 5 Ma of the Silvretta nappe (Schaltegger et al., 1997).

3.3. Magmatic Development and Geochemistry

The magmatic evidences show an active margin dominated setting since the early Cambrian along the northern Gondwana margin (Stampfli et al., 2011). Pre-Cambrian events during mantle mobilization are suggested to be the first magmatic events within the Austro-Alpine and therefore the earliest possible sources for the Seckau nappe (Raumer et al., 2013). Whole-rock errorchrone of a peridotite host rock dated 745 ± 44 Ma by Melcher et al. (2004) supports this time period. Several magmatic pulses occurred after the Neoproterozoic and Early Cambrian (Fig. 23) and are seen as result of the Neoproterozoic breakup of the Gondwana margin and the Palaeozoic active and passive margin settings (Raumer et al., 2013). Also the Seckau nappe is considered to be fed by this magmatism’s, so evidence of zircon contamination (3 Ga - 2.25 Ga) and orthogneiss dating (568 Ma – 425 Ma) has proven as described in the previous chapter. Further granites, tonalites, mafic and ultramafic events occurred during the Upper Devonian to Lopingian (Permian) which are related to collisional and post-collisional stages strongly connected to the Variscan orogeny (420 Ma – 200 Ma). Pegmatite intrusions occurred during 375 Ma and 282 Ma (Handler et al., 1999; Hejl, 1984).

There are deformed, syn-collisional S-type granitoids which are assumed to have built during the Variscan (Scharbert, 1981). Eichelmüller and Schernitz (2014) concluded in the Seckauer Tauern also different intrusions. The study of Pfingstl (2013) has shown a calc-alkaline trend as well as a distribution of A-type, I-type and S-type plutonism, whereby biotite-orthogneisses and porphyry rocks are the product of the I-type intrusions, the muscovite-orthogneisses and two-mica-orthogneisses are the result of the S-type intrusions. Trace element analyses have yielded an island-arc tectonic setting. Further there are less deformed pre-plate collision, post-collision uplift and late-orogenic I-type granitoids, which are considered to be younger than the S-Type granitoids, and are accounted to be a secondary intrusion event, after the Variscan orogeny (Eichelmüller & Schernitz, 2014; Ratschbacher, 1986). The chemical data of the I-type suite of the Seckauer Tauern is similar to the Schladminger Tauern (Schermaier et al., 1997). The I-type suites of Schermaier et al. (1997), Pfingstl (2013) and Eichelmüller and

Schernitz (2014) comprised of metaluminous to peraluminous composition, whereby the samples of the last two have primary peraluminous character, contrary to Schermaier et al. (1997), who defined the Seckau-Bösenstein area as metaluminous and only slightly peraluminous. The calc-alkaline trend and tectonic setting of Pfingstl (2013) in the east has been confirmed by similar data in the west of the Seckauer Tauern by Eichelmüller and Schernitz (2014). Further, high K_2O concentration in the majority of samples fits the study of Schermaier et al. (1997) for the Schladminger Tauern and Seckauer Tauern. Considering the different sampling sites (page 7), this areas seem strongly connected and experienced the same development over time, in contrary to the south-western part of the Seckauer Tauern (Schönegger, 2015), which shows mostly a continent-continent collisional trace element signature. The largest masses of tonalite are especially situated in the western Seckauer Tauern (Fig. 18), interjacent of the Ringkogel-Pletzen massif and the Bären valley, including the study area of this thesis.

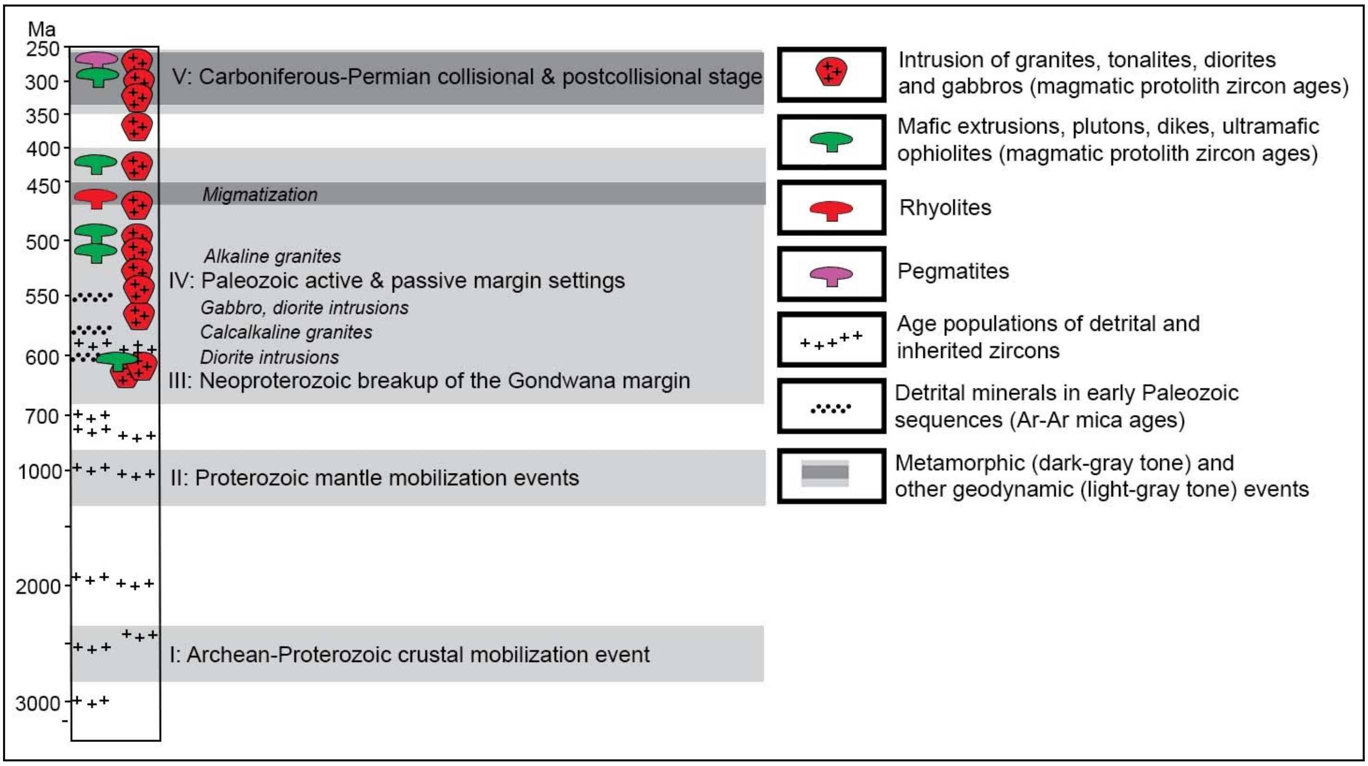

Fig. 23: Precambrian and Palaeozoic events in the Austro-Alpine basement domain (Handler et al., 1997; Neubauer, 2002; Raumer et al., 2013; Schulz, 2008). Events during 500 Ma to 418 Ma and 370 Ma to 320 Ma are seen as the main events within the Seckau nappe (Neubauer, 1988a).

The Cambrian island arc setting constrained through the above cited data correlates with the Silvretta nappe (Schaltegger et al., 1997) and builds therefore a new connection between the Silvretta nappe and Seckau nappe. The $^{87}Sr/^{86}Sr$ ratios e.g. 0.7047 (Scharbert, 1981), 0.705 (Schermaier et al., 1997), 0.7045 (Pfingstl et al., 2015), 0.7044 (Frank et al., 1976) and 0.7058 (Frank et al., 1983) of whole rock analyses are seen as unrealistic for granitic rocks (Mandl et al., 2014; Scharbert, 1981; Schermaier et al., 1997) but they could also indicate a highly evolved melt of a typical volcanic arc and batholithic core zone (White, 2015).

3.4. Metamorphic Evolution

Based on the radiometric data and the reasoned magmatic development the metamorphic development probably reaches back to the Neoproterozoic, earliest high-grade metamorphism event occurred between 490 Ma and 470 Ma (Neubauer et al., 2002), but no evidences for previous events have been presented so far. Therefore it is considered that the basement of the Seckau nappe is dominated by Variscan metamorphism. Tectonics and metamorphism of the Variscan is widely distributed within this nappe (Mandl et al., 2014). Transgressive Permian to Lower Triassic metasediments are considered as upper greenschist facies by the assemblage of muscovite-chloritoide-chlorite-quartz and suggest facies conditions of 520 °C at 0.9 GPa (Faryad & Hoinkes, 2001). The crystalline underneath e.g. Seckau complex and Amering complex, underwent an Eo-Alpine epidote-amphibolite metamorphism whereby the metamorphic peak was estimated in the Campanian (80 Ma) (Schuster, 2013), than set to the Santonian (85 Ma) (Mandl et al., 2014) and is now being estimated at 90 Ma to 100 Ma (Pfingstl et al., 2015).

In comparison, the Gleinalm shows higher metamorphic conditions based on the assemblages garnet-staurolite-kyanite from mica-schist and from amphibolite with garnet-amphibolite-plagioclase (Faryad & Hoinkes, 2001). Therefore the Eo-Alpine event has imprinted on the Seckauer Tauern differently, which is also seen in the increase of the metamorphic grade towards the south (Fig. 24). The whole nappe can be seen as overprinted by greenschist to epidote-amphibolite facies during the Cretaceous (Faryad & Hoinkes, 2001; Faryad et al., 2002; Gasser et al., 2009). The Seckauer nappe stacking process was directed west-north-west and it is assumed that it has been completely moved prior to Gosau sedimentation from a former easterly position along the Mur-Mürz line (Metz, 1978). During this movement a north-south directed compressional phase occurred, which led to an east-south-east directed normal fault during the Alpine evolution after the decreasing of the compressional forces (Eichelmüller & Schernitz, 2014).

The study of 2015 in the southwest of the Seckauer Tauern (Schönegger, 2015, provides two generation of fluid inclusions which are interpreted as separate metamorphic events. The first formation condition was upper greenschist (300-400°C and 3-5 kbar), the second lower greenschist (300-400°C and 1-2 kbar). The decreasing pressure and constant temperature are assumed to be related and can be assign to a time of 85 Ma after Pfingstl et al. (2015).

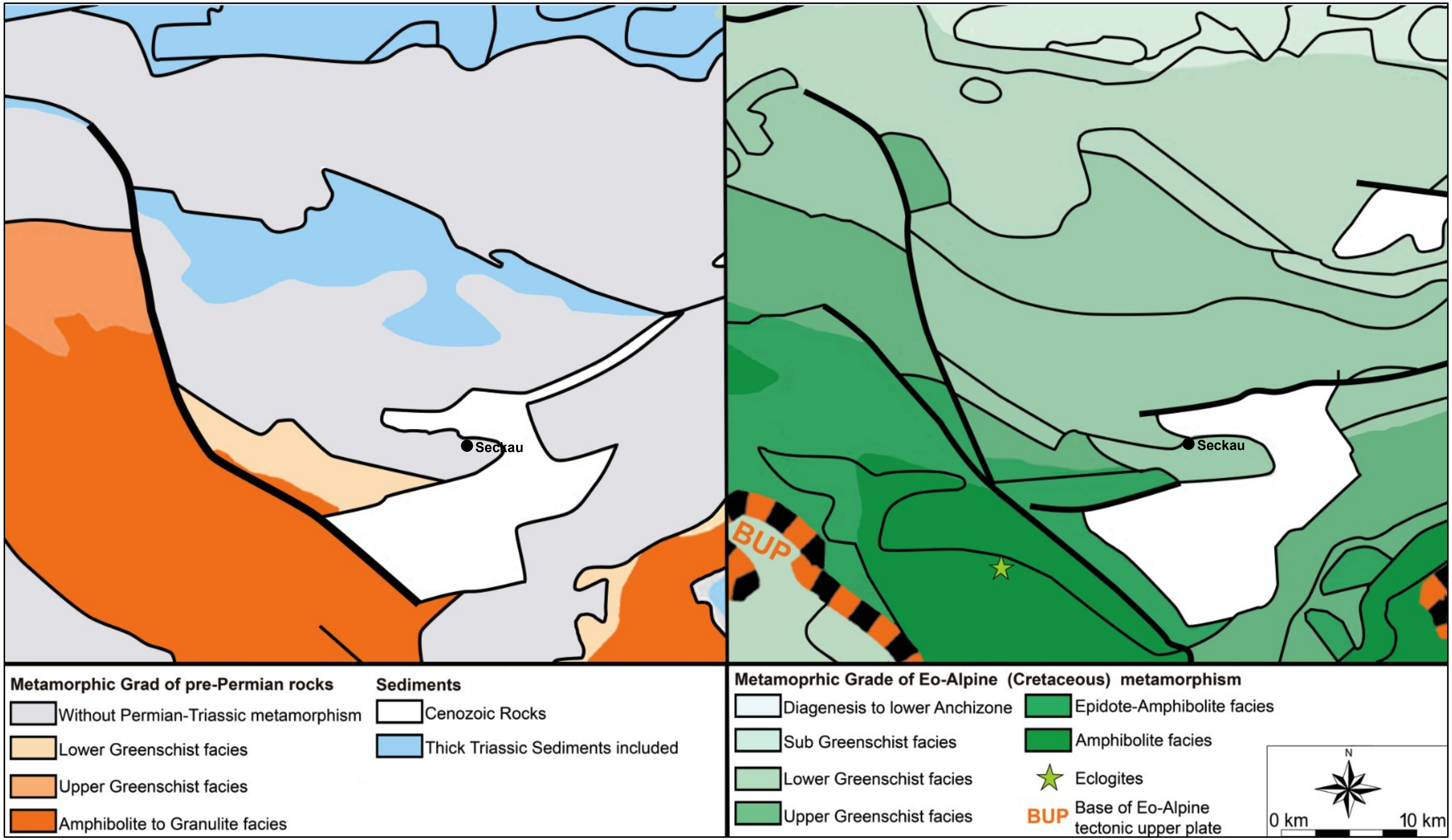

Fig. 24: Metamorphic maps presenting pre-Permian (left) and Eo-Alpine (right) peak metamorphic grades of the Seckau nappe (Gasser et al., 2009; Schuster, 2013).

3.4.1. Cooling

After the Eo-Alpine metamorphic peak (95 Ma) the T-t paths of Gleinalm and Seckauer Tauern have developed differently. The peak conditions vary (Fig. 24), whereby an increase from north to south has been documented and seen in the difference of the Gleinalm (about 500 °C) to the lower peak conditions of the Seckauer Tauern. Further it has to be stated, that the northern region of the Seckau nappe cooled earlier compared to the south (Pfingstl et al., 2015). Scharbert (1981) yielded through Rb-Sr biotite measurement ages ranging from 70 Ma to 77 Ma. Apatite fission track ages from Hejl (1997) with 60 Ma to 44 Ma, lead to the conclusion of a nearly constant temperature during the Late Cretaceous until the late Oligocene and suggested a fast cooling until the Miocene extrusion event, where slow cooling has occurred (Hejl, 1997). The suggested flat cooling path for the Seckauer Tauern by Hejl (1997) has been revised by Pfingstl et al. (2015) according to new Rb-Sr biotite cooling ages, and the conclusion that the Seckau Complex cooled below 300 ± 50°C at about 85 Ma. The fission track data from the Gleinalm on titanite (94 Ma), zircon (65 Ma) and apatite (34 Ma) (Dunkl et al., 2005; Neubauer et al., 1995) were also included. This newly introduced cooling path correlates now strongly with the cooling of the northern Koralpe-Wölz nappe System after Hejl (1997). Further, the Seckau Complex and the Permo-Triassic sedimentary unit above were heated prior to the Eo-Alpine metamorphic peak (Pfingstl et al., 2015) and the north cooled 25-30 Ma earlier than the south (Mandl et al., 2014).

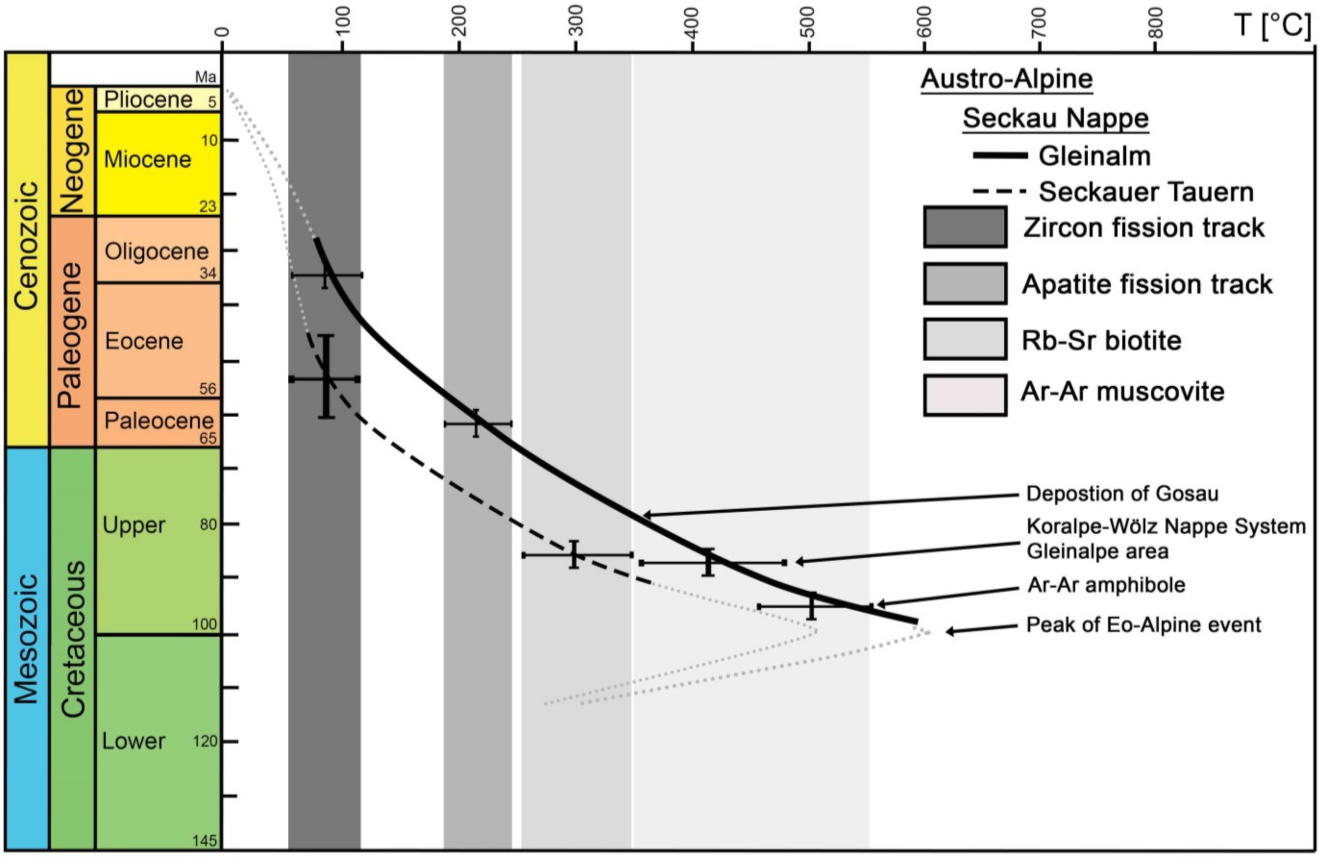

Fig. 25: T-t path of Gleinalm and Seckauer Tauern after Pfingstl et al. (2015). Grey dotted lines are estimates of the cooling development.

3.5. Palaeogeographic Evolution

The palaeogeographic evolution of the „Proto-Alps“ is still hottly debated. New zircon ages should itemise the time frames of development. In the following the paleogeographic evolution of different viewpoints is graphically displayed.

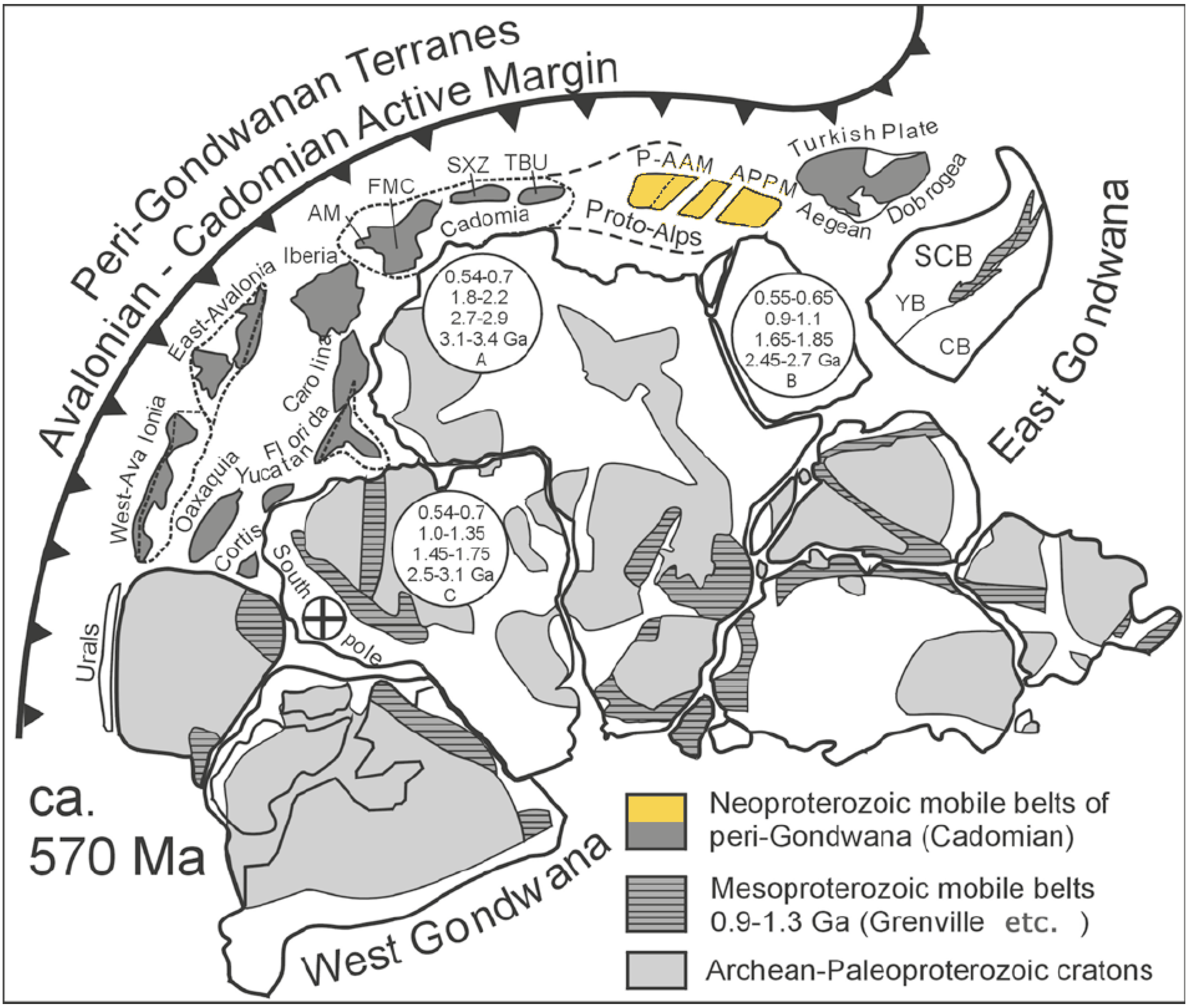

Fig. 26: Early-Palaeozoic paleogeography at ~570 Ma. AM = Armorican Massif, APPM = Austro-Alpine Palaeozoic Passive Margin, CB = Cathaysia Block, FMC = French Massif Central, P-AAM = Penninic-Austro-Alpine Active Margin (yellow), SCB = South China Block, SXZ = Saxo-Thuringian Zone (part of the Bohemian Massif), TBU = Teplá-Barrandium unit (part of the Bohemian Massif), YB = Yangtze Block (Heinrichs et al., 2012; Raumer & Stampfli, 2008).

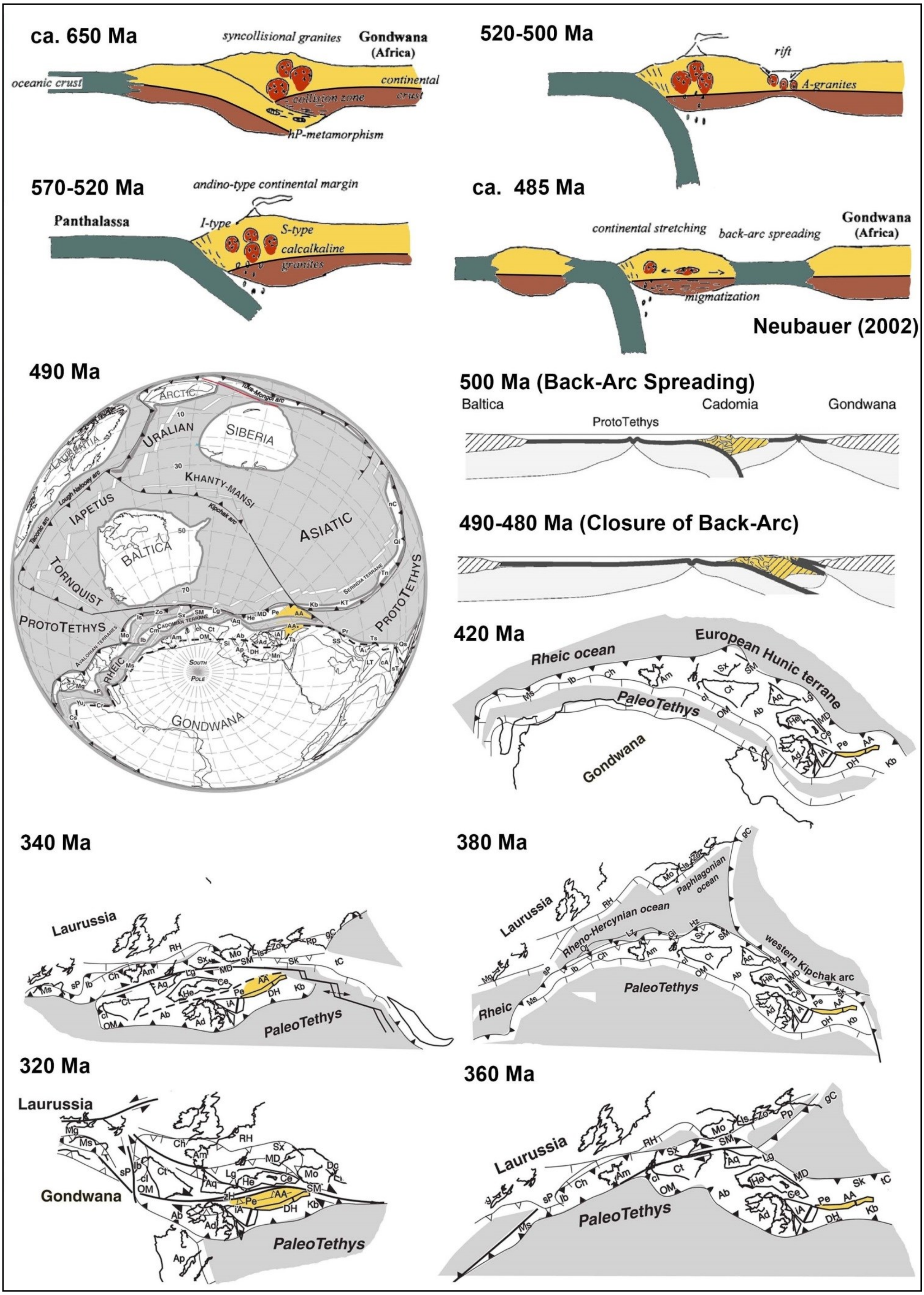

Fig. 27: Based on the previous chapters the following assumptions concerning the evolutionary steps of the Seckauer Tauern have been made. Figures are extractions of several papers (Golonka & Gawęda, 2012; Neubauer, 2002, 2014; Stamp & Borel, 2002; Stampfli et al., 2011). AA = Austro Alpine.

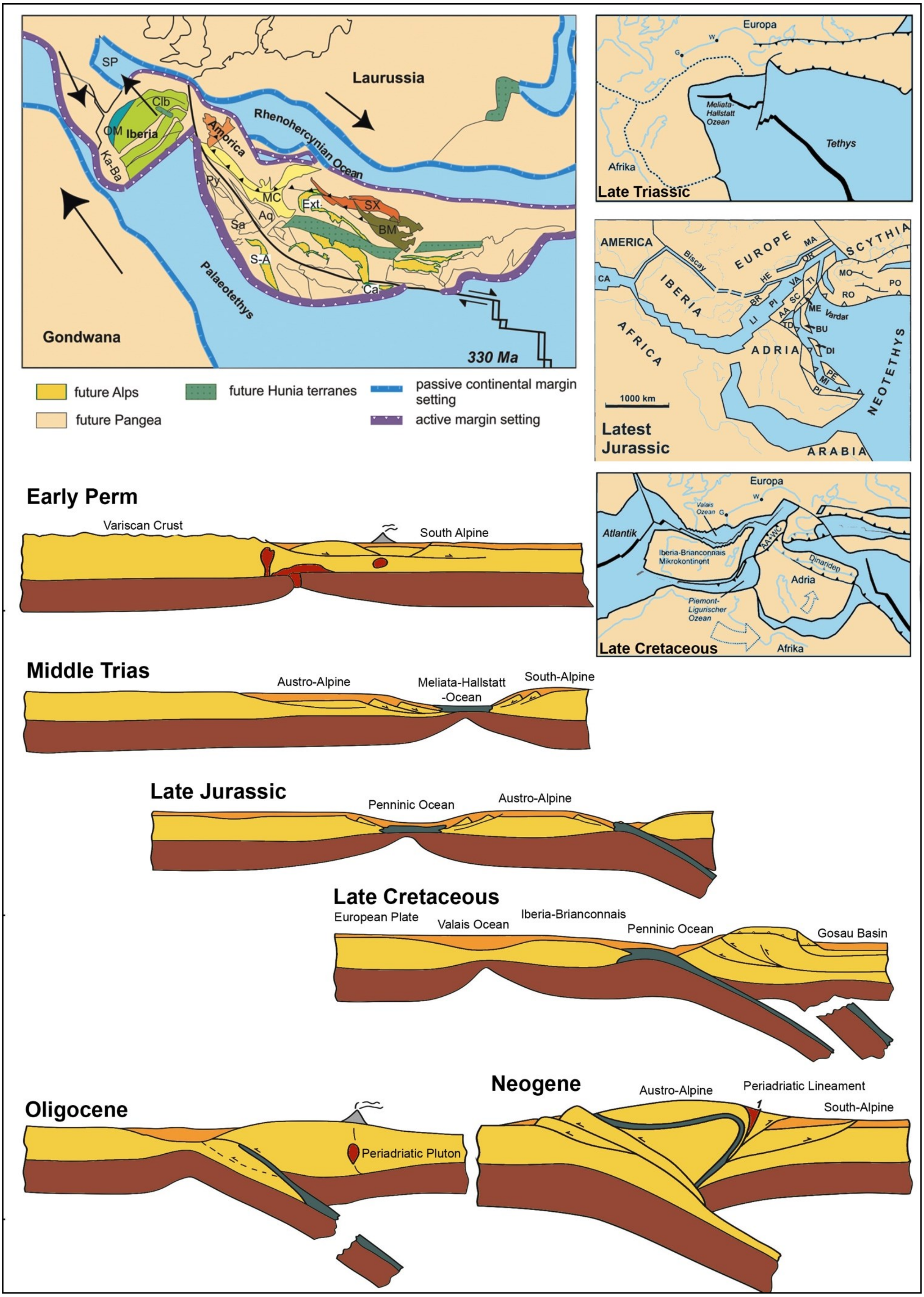

Fig. 28: Based on the previous chapters (Tectonic Setting and Lithology; Radiometric Dating; Magmatic Development and Geochemistry; Metamorphic Evolution) the following assumptions concerning the evolutionary steps of the Seckauer Tauern have been made. Figures are extractions of several papers (Golonka & Gawęda, 2012; Neubauer, 2002, 2014; Stamp & Borel, 2002; Stampfli et al., 2011).

4. Material and Methods

The following listed methods and used materials for sample preparation and analyses provide an overview of the necessary tasks during this research to obtain the in chapter 5 presented results.

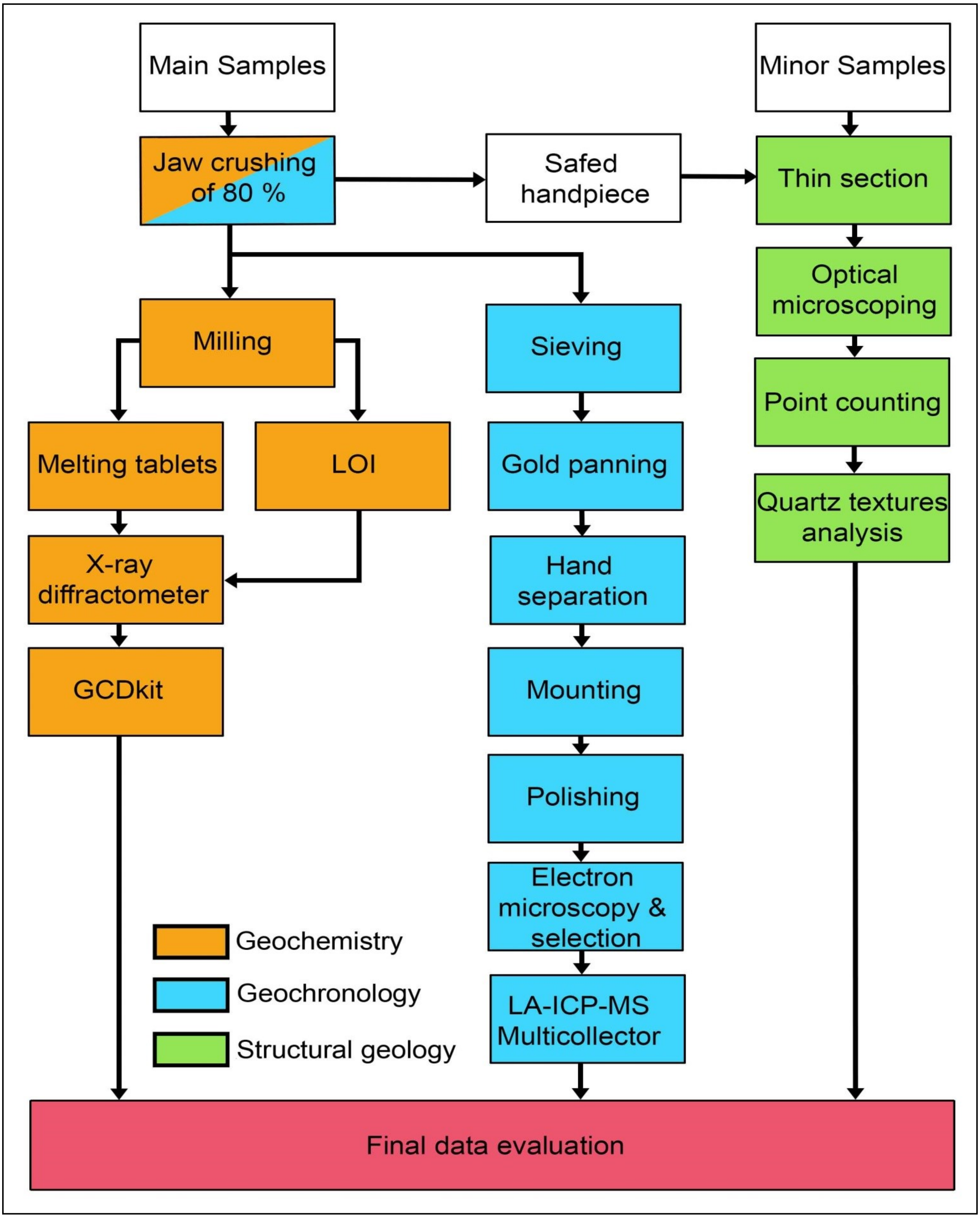

Fig. 29: Workflow design.

4.1. Optical Microscopy

Polarisation microscopes, “Olympus BX50”,”Olympus BH2”, and reflected-light microscopes “Olympus SZX12”, “Zeiss Discovery V8”, “Wild Heerbrugg”, have been used for thin-section description by minerals and microstructures. Further a “Point Counter” and a photometer “Crystal Imaging System G50 Fabric Analyser” from Russell-Head Instruments were used during the study.

4.1.1. Point Counter Analysis

Point counter analysis was used as an impartial and quantitative method for rock description. The instrument “Prior James Swift – England” was used for non-geochemical analysed samples, so they could also be classified as a rock type according to Streckeisen (1974). The “GCDkit” was used as plotting software.

4.1.2. Quartz Textures Analysis

Deformation of rocks is influenced by several processes and further depends on internal factors (intergranular fluids, mineralogy, grain size, lattice-preferred orientation, porosity, permeability) and external factors (temperature, differential stress, fluid pressure, lithostatic pressure, strain rate) (Blenkinsop, 2000; Passchier & Trouw, 2005).

<u>Rheological Characterisations - (Recrystallization)</u>

Grains are formed by separation of other grains of different or same minerals e.g. quartz. Because of this boundary they have different lattice-preferred orientation. Grain boundaries of quartz are used to determine deformation by temperature, whereby visible structures within are named intracrystalline deformation structures (Fig. 30) (Passchier & Trouw, 2005).

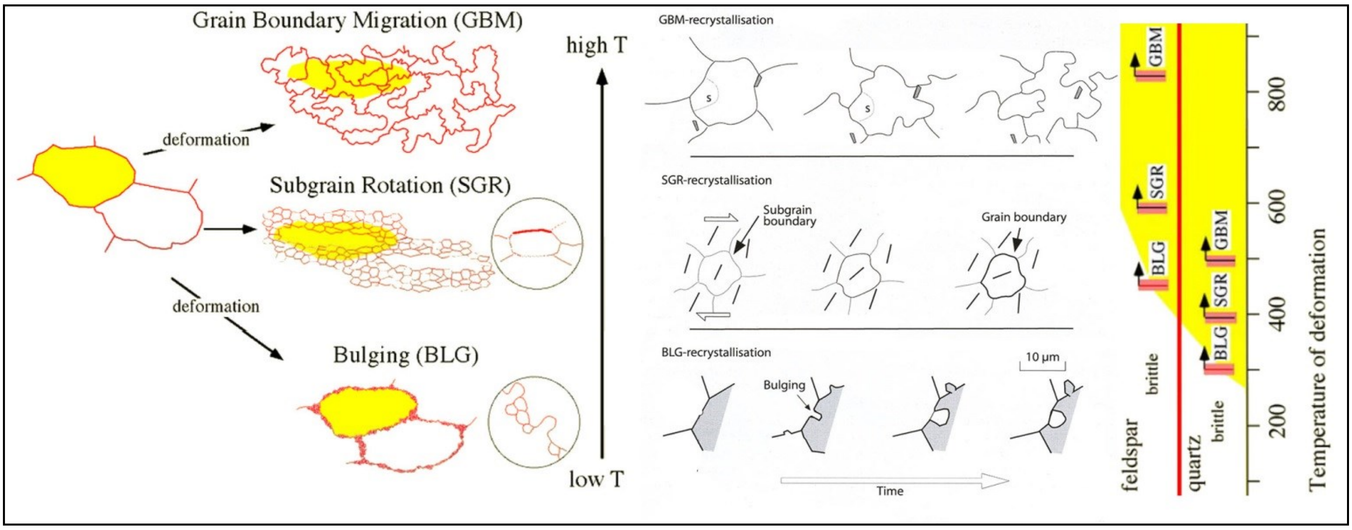

Fig. 30: The three mechanisms of dynamic recrystallization on the grain scale (Passchier & Trouw, 2005).

These recrystallization patterns are divided into bulging (BLG), sub-grain rotation (SGR) and grain-boundary migration (GBM). Further stages, e.g. diffusion creep, follow but are difficulty to examine under the microscope. This grain boundary mobility is temperature and material depending, and therefore used in this thesis for temperature estimation by the most common minerals quartz and feldspar (Passchier & Trouw, 2005).

Lattice-Preferred Orientation - LPO

The lattice orientation of quartz crystals it not randomly distributed, instead it is arranged in systematic way. Quartz can be checked for it by inserting a gypsum plate under crossed polars, where blue or yellow colour indicate the LPO, or by using a photometer (Passchier & Trouw, 2005). The last named instrument uses a polarisation microscope with two polarizers, whereby in-between the thin section is positioned. The emitting light of eight different LEDs, which are equally circular positioned by an inclination of 20°, emit the light, while one diode is positioned along the optical axes, and the two polarizers rotate synchronously with a step size of 11,25° between 0° and 90°. Eighteen pictures were taken by an CCD camera of each LED, by the GIGE Vision (type: GE2040C) and the software “Crystal Imaging System Investigator G50v5.9”, which are used to create an axe-distribution analysis with the software “Investigator v5.8” (Wilson et al., 2007). The orientation of the quartz c-axes are afterwards plotted by the software “Fabric 8” (Wallbrecher, 2012).

This orientation data is normally presented in an orientation distribution function diagram (ODF), where the orientation, of each crystal axes (a, b, c) according to every single quartz crystal, is plotted as a point (Passchier & Trouw, 2005). For easier reading, only the c-axis of quartz has been plotted on polar diagrams. The LPO data in the polar diagrams varies from point maxima, small circles, great circle or connected as crossed girdles patterns, whereby the crossed girdles appear either as type I or type II (Lister, 1977; Passchier, 1983).

Those different patterns (Fig. 31 and Fig. 32) provide a good base for further interpretations, by showing the influence of finite strain and flow type on the geometry of c-axis, by coaxial progressive deformation at low, medium- and high-grade metamorphism. Those interpretations include temperature estimation during the deformation processes as well as kinematics. It is differentiated into single girdles, crossed girdle type I, crossed girdle type II, cleft girdle and centred, whereby slightly asymmetric type I crossed girdles and inclined single girdles are the most common (Passchier & Trouw, 2005).

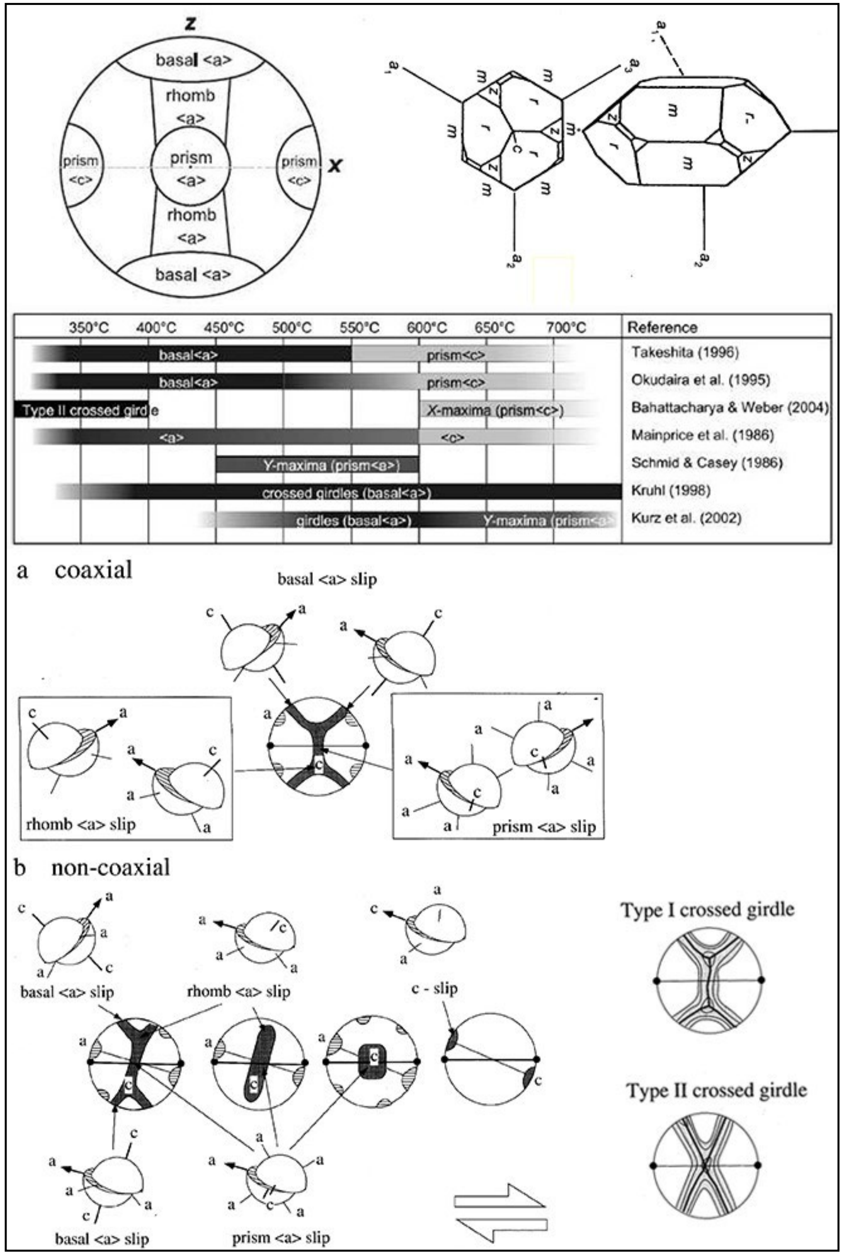

Fig. 32: a = Quartz c-axes within LPO diagrams; b = Slip system types of quartz; c = orientation of quartz crystals in a reference frame defined by lineation (Lr), foliaiton pole, and foliation (Sr); d = example of the the two types of crossed girdles (Lister, 1977; Passchier & Trouw, 2005; Toy et al., 2008).

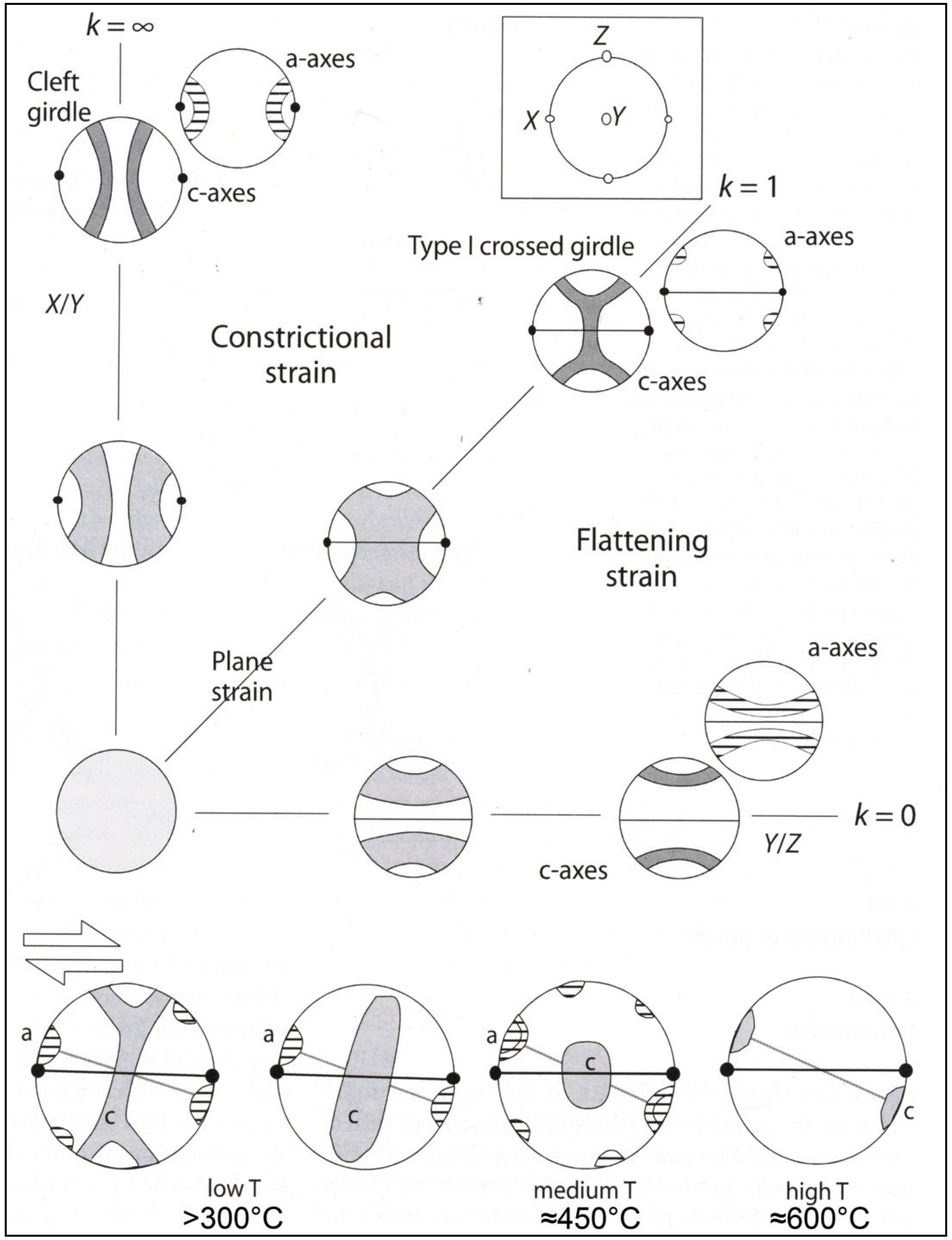

Fig. 31: Flinn diagram illustrating the relation of geometry of LPO patterns of quartz c-axes (grey contours) and a-axes (striped ornaments) with strain in the case of coaxial progressive deformation (Lister & Hobbs, 1980; Passchier & Trouw, 2005).

4.2. X-Ray Fluorescence Spectroscopy (XRF spectroscopy)

The x-ray fluorescence spectroscopy (XRF) yield the generation of geochemical data set of specific rock samples. To obtain this data a sample has to go through a variety of steps, which will be explained in the following.

Fresh and non-altered rock samples, which were cut out of the centre of main samples, were used. In the next step these centrepieces were powdered by a vibrating disc mill with a tungsten carbide milling unit (Retsch RS1 & Retsch RS200), than dried in a drying oven at 105 °C for 24 h and afterwards cooled in a desiccator. To assure good final results, the milling unit was cleaned after every sample with tab water, air pressure and ethanol. These preparations were necessary to create the finally measured objects of the XRF, melting tablets.

These tablets were made by combining 1 g of the powdered sample material with 7 g of lithium tetraborate (Fluxana) both weighted in with an accuracy of +/- 0.0005 g, and then melted together in a platinum crucible at 1,200 °C and forming a tablet by casting it into a platinum plate. For this procedure the Vulcan 2M (VAA 2M) was used. The platinum crucible was rinsed with distilled water and afterwards cleaned in a HCL (37 %) containing ultrasonic water quench after every melting process. Sample material which contained sulphide, metallic iron or carbon had to be annealed prior in an annealing furnace.

The annealing furnace is also used to receive the loss of ignition (LOI), by annealing 1g of the previous dried powdery sample for 1 hour at 1,200 °C, cooling it afterwards for 20 minutes in a desiccator with an open valve, 1 hour with a closed valve and calculating the relatively difference of the weight before and after the annealing. The LOI value (see appendix) is needed to estimate the amount of organic components for each sample with XRF.

The XRF spectrometry uses photons form an excitation source which interacts with the elements of the melting tablet. During this interaction the photons cause ejections of inner shell electrons of the sample atoms, so the electrons of the outer shells then fall back into these vacancies, thereby x-rays are released which are characteristic of the certain element. The measured intensity of the rays is compared with standards and in further consequence a measure of the element amount which is present in the melting table (Beckhoff et al., 2006). During this thesis a “Bruker Pioneer S4” was used. The generated data were then evaluated and interpreted by plots produced by the software “GCDkit”.

4.3. GeoChemical Data Toolkit (GCDkit)

The GCDkit is a tool for geochemical analysis (Janousek et al., 2006). It defers into two major groups of graphical display of geochemical data provided by the XRF. The first group are the “classification plots” which include plots for general discrimination, specially designed plots for volcanic rocks and as well for plutonic rocks. The second group includes “geotectonic plots” to determine the tectonic position during earth history, whereby the plot setting is distinguished for granitoids or basaltoids. For this thesis GCDkit with the version 3.0 has been used. The utilized plots are explained in the accordingly cited publication. The following plots have been used: For data evaluation of the compositional variations, Harker diagrams of major and trace elements versus SiO_2 were used. To distinguish the calc-alkaline or tholeiitic trend the AFM plot (Irvine & Barager, 1971), was used together with the plots of Miyashiro (1974), Peccerillo and Taylor (1976). Classic A/CNK versus A/NK was plotted to discriminate between metaluminous, peraluminous and peralkaline composition (Shand, 1943). Also a source type classification for the granitoids have been done, to classify between I-Type and S-Type (Chappell & White, 1974, 2001). The data were plotted into diagrams of Middlemost (1985), De la Roche et al. (1980), Debon and Le Fort (1983), Fillaseca et al. (1998). Also TAS diagram of Le Bas et al. (1986), Cox et al. (1979) and Middlemost (1994) were used to classify the rocks type. The geotectonic position was evaluated by Batcher and Bowden (1985), Maniar and Piccoli (1989) and Sylvester (1989). Other classifications were not possible, because essential values have been under the detection limit.

4.4. Scanning Electron Microscopy

The scanning electron microscopy (SEM) yields images with a very high spatial resolution (< 1 nm). Thereby an electron beam is created by an electron gun (e.g.Tungsten filament), inside of an evacuated chamber. It is accelerated and focused by magnetic lenses and scanning coils before it traces over an object and interacts with the sample. During these interactions secondary electrons get dislodged and can be analysed by a secondary electron detector and an image showing different levels of brightness is obtained. The secondary electron image is dominated by the topography contrast, but also the phase contrast and charging effects have an influence. To reduce these charging effects, non-conductive samples like most rocks and thin-sections have to be coated by noble metals (Goldstein & Newbury, 1997). For this thesis the samples were sputtered by a “Bal Tec MCS 010” coating system with carbon at $5*10^{-5}$ mbar at 180 °C and investigated with the “JEO JSM-6310”. Two pictures of each acceptable zircon were made, a cathodoluminescence picture to see rims and zonings, and a back-scatter-electron (BSE) picture for material contrast. BSE are surface reflected beam electrons by elastic scattering which depends on the atomic number of the material, therefore the distribution of different chemical materials can be seen, and further to see if the laser beam of the LA-ICP-MS will interfere with other materials than the zircon (Reed, 2010).

4.5. LA-ICP-MS Multicollector

The laser ablation inductively coupled plasma mass spectrometry with multicollector was used to determine the U and Pb content of the previous prepared, microscoped and selected zircons (Fig. 29) and there according isotopes. The principles of the LA-ICP-MS are briefly introduced.

Interactions between a laser beam and the sample material vaporises most of the exposed area of the zircon in our case. The ablated material is carried away with an argon beam to the ICP-MS unit. The aerosol is than introduced into the ICP torch, where it is completely dissolved and converted first into gaseous atoms and then ionized with around 5,727 °C to 9,727 °C. In an electromagnetic field atoms are separated by their mass to charge ratio. The Lorentz force affects the charged ions according to the equation

$$F = F_E + F_B = q(E + vB) \tag{1}$$

The F_E is the electric and the F_B is the magnetic component of the Lorentz force, q represents the charge of the ions, v their velocity and B the magnetic field. Secondly the ions are affected by a gravitational force as a result to their mass and according to Newton’s second law of motion,

$$F = ma \tag{2}$$

predicative that a force F, accelerates a mass m, to a certain acceleration a (Taylor, 2001b). Balancing these equations results in

$$\left(\frac{m}{Q}\right) a = E + vB \tag{3}$$

This connotes that for every mass to charge ration (m/Q) at given electromagnetic conditions (E and B) and a given velocity of an entering ion, v, the direction of flight is influenced by a particular acceleration a. This leads to separation of the ions according to their mass to charge ratio. Interferences of ions with the same ration must be considered (Taylor, 2001a). Most elements have different isotopes, which results in different mass to charge ratios. For the analysation, the samples had to be cleaned of the sputtered carbon (see chapter 4.4) and inserted into the vacuum chamber of the LA-ICP-MS “Nu Plasma II Multi-Collector”. Calibrations and standards were done accordingly to the producer’s manual. A laser beam with 15 µm and 20 µm in diameter was chosen, depending on the size of the zircon.

4.6. Radiometric Dating

To determine the formation age, the mineral zircon ($ZrSiO_4$) was separated for U-Pb dating. Therefore field samples between 5-8 kg were collected and selected by their geographical location and zirconium content based on the XRF (4.2) results. The first step of preparation was to jaw crush the selected field samples to gain a rough to fine powder for the subsequent sieving. Based on the average size of zircon minerals (0.1-0.3 mm), the sieving has been set to gain a grain-size fraction between <500 µm and >63 µm. This fraction was further separated by gold panning. Zircons were than separated by hand from the residual amount under the microscope. Those hand-picked zircons were than embedded in epoxy resin of a standard sample ring – “Mount”. The Mount had to be polished until the zircons have been on the surface so they could be analysed by the SEM (4.4) for the further selection process. The final chosen zircons were than measured by the ICP-MS (4.5).

4.6.1. U-Pb - Zircon

The concentrations of U^{4+} and Th^{4+} ranges in zircon from a few hundred to a few thousand parts per million (ppm). Average values reach 550 ppm and 1,350 ppm respectively. These elements are attributed in zircon to isomorphous replacement of Zr^{4+} through their similar ionic radii or through inclusions of thorite ($ThSiO_4$). These substitutions are limited by their ionic radii differences therefore U^{4+} and Th^{4+} are admitted into the zircon crystals in contrary to Pb^{2+} which is excluded because of its larger radius and its lower charge. From this follows that zircon contains very little Pb^{2+} during the time of formation and therefore high U^{4+}/Pb^{2+} and Th^{+4}/Pb^{2+}. This fact, and it’s closing temperature of 850±50 °C, enhances its sensitivity as a geochronometer and the reason it is used for crystallisation dating of magmatic rocks, which starts crystallising at about <800 °C, by U-Th-Pb isotopic methods (Doe, 1970; Faure & Mensing, 2005).

Uranium occurs as ^{238}U, ^{235}U and ^{234}U, thorium as ^{232}Th and five additional short-living intermediate daughters, whereby ^{234}U plays only a minor role. Each of these parents, followed by a chain of radioactive daughters, ends with the stable isotopes of Pb (^{206}Pb, ^{207}Pb, ^{208}Pb). The decay chain resulting from the successive emission of α- and β-particles is presented in the following, whereby the parameter Q represents the sum of the decay energies of the entire series, the He represents the α-particles and the β-particle represents electrons:

$$^{238}U \rightarrow {}^{206}Pb + 8\ {}^{4}He + 6\ \beta^{-} + Q$$

$$^{235}U \rightarrow {}^{207}Pb + 7\ {}^{4}He + 4\ \beta^{-} + Q$$

$$^{232}Th \rightarrow {}^{208}Pb + 6\ {}^{4}He + 4\ \beta^{-} + Q$$

Each of these isotopes follows a different decay chain, all together 43 isotopes of 12 elements are formed as intermediate daughters during these decay series (excluding ^{4}He), but each belongs only to one series, therefore the end all with a final decay product of a different stable Pb form. The half-life's (Table 1) of ^{238}U, ^{235}U and ^{232}Th are all longer than those of the respective daughters. From this it follows that these decay series fulfil the prerequisite condition for a secular equilibrium, which means that with increasing time, the rate of decay of the unstable daughter becomes at some point equal to that of its parent. So, the production rate of stable daughters at the end of the decay chain (e.g. ^{206}Pb, ^{207}Pb, ^{208}Pb) is equal to the rate of its parent, if it is a mineral of a closed system where a secular equilibrium is established.

As a consequence the growth of the radiogenic isotopes Pb by decay of their respective parents can be described by the law of radioactivity. The law of radioactivity includes the number of atoms (N), time (t), whereby N = N_0 represents the condition when t=0, and the proportionality constant or also named decay constant (λ), which is characteristic of the particular radionuclide (Table 1) and describes the probability that an atom will decay within a stated time (Faure & Mensing, 2005):

$$N = N_0 \; e^{-\lambda t} \tag{4}$$

The decay constant (λ) is connected to its half-life ($T_{1/2}$), which expresses the time required of a radionuclide to decay one half of a given number of atoms, therefore,

$$\frac{1}{2} N_0 = N_0^{-\lambda T_{1/2}} \tag{5}$$

from which it follows

$$T_{1/2} = \frac{ln2}{\lambda} = \frac{0.693}{\lambda} \tag{6}$$

or as another parameter, the mean life or decay constant (τ), which is the reciprocal of the decay constant (Faure & Mensing, 2005).

$$\tau = \frac{1}{\lambda} \tag{7}$$

Table 1: Abundances, half-life's and decay constants of principal naturally occurring isotopes of U and Th. Decay constants fixed by the IUGS subcommission on geochronology. (Faure & Mensing, 2005; Lide & Frederikse, 1995; Steiger & Jäger, 1977).

Isotope	Abundance (%)	Half-life (years)	Decay Constant (y^{-1})
^{238}U	99.2743	4.489×10^{9}	1.55125×10^{-10}
^{235}U	0.7200	0.7038×10^{9}	9.8485×10^{-10}
^{234}U	0.0055	2.45×10^{5}	2.829×10^{-6}
^{232}Th	100.00	14.010×10^{9}	4.9475×10^{-11}

The law of radioactivity can be combined with the growths of radiogenic daughters, which describes a radionuclide (N) decays in a closed system a number of stable daughters (D*), whereby these daughters accumulate in a unit weight of the rock or in the mineral zircon of this thesis, equally to the number of parent atoms that have decayed (Faure & Mensing, 2005):

$$D^* = N_o - N \tag{8}$$

from which it follows that

$$D^* = N_o(1 - e^{-\lambda t}) \tag{9}$$

The equations of the radiogenic Pb are written ratios because ^{204}Pb is the only stable non-radiogenic. The variable λ_1, λ_2 and λ_3 are the according decay constant of ^{238}U, ^{235}U and ^{232}Th, the subscript “i” refers to the initial values of the Pb ratios, the ^{238}U/^{204}Pb, ^{235}U/^{204}Pb and ^{232}Th/^{204}Pb are the calculated ratios based on the measured concentration of U, Th and Pb (Faure & Mensing, 2005):

$$\frac{^{206}Pb}{^{204}Pb} = \left(\frac{^{206}Pb}{^{204}Pb}\right)_i + \frac{^{238}U}{^{204}Pb}\left(e^{\lambda_1 t} - 1\right) \tag{10}$$

$$\frac{^{207}Pb}{^{204}Pb} = \left(\frac{^{207}Pb}{^{204}Pb}\right)_i + \frac{^{235}U}{^{204}Pb}\left(e^{\lambda_2 t} - 1\right) \tag{11}$$

$$\frac{^{208}Pb}{^{204}Pb} = \left(\frac{^{208}Pb}{^{204}Pb}\right)_i + \frac{^{232}U}{^{204}Pb}\left(e^{\lambda_3 t} - 1\right) \tag{12}$$

Age Determination

For the age determination of U containing minerals, the concentration of U and Pb are measured by an analytical technique (see chapter 4.5) and the isotope composition of Pb has to be determined. The U-Pb date is calculate by means of the previous stated equations ((10),(11),(12)), by using an assumed value of the initial isotope ratio of Pb by the following equation

$$t_6 = \frac{1}{\lambda_1} ln\left(\frac{\left(^{206}Pb/^{204}Pb\right) - \left(^{206}Pb/^{204}Pb\right)_i}{^{238}U/^{204}Pb}\right) \tag{13}$$

If ^{235}U and ^{232}Th have also been measured, the equations (11) and (12) are solved similar as equation (10) in equation (13). Minerals with high U/Pb ratios are not significantly affected by the initial Pb ratios because their ratio reaches high values. Therefore the following initials are used (Faure & Mensing, 2005):

$$\frac{^{206}Pb}{^{204}Pb} = 17.21 \qquad \frac{^{207}Pb}{^{204}Pb} = 15.78$$

$$\frac{^{208}Pb}{^{204}Pb} = 37.43 \qquad \frac{^{238}U}{^{235}U} = 137.88$$

To minimize the effect of Pb loss on U-Pb dates the calculation can either be based on the $^{207}Pb/^{206}Pb$ ratio which is insensitive to recent Pb loss, if the Pb loss of a mineral had the same isotope composition as the Pb that remained (e.g. no isotope fractionation):

$$\frac{^{207}Pb/^{204}Pb-\left(^{207}Pb/^{204}Pb\right)_i}{^{206}Pb/^{204}Pb-\left(^{206}Pb/^{204}Pb\right)_i}=\frac{^{235}U}{^{238}U}\left(\frac{e^{\lambda_2 t}-1}{e^{\lambda_1 t}-1}\right) \tag{14}$$

or on a graphical procedures (Ahrens, 1955; Faure & Mensing, 2005; Wetherill, 1956, 1963). One of these graphical evaluations is the "Wetherill's Concordia Diagram" for the interpretation of U bearing minerals (e.g. zircon), where the ratios $^{206}Pb/^{238}U$ and $^{207}Pb/^{235}U$ are plotted against each other (Fig. 33). Therefore the following equations are needed:

$$\frac{^{206}Pb^*}{^{238}U}=e^{\lambda_{238}t}-1 \tag{15}$$

$$\frac{^{207}Pb^*}{^{235}U}=e^{\lambda_{235}t}-1 \tag{16}$$

The concordia diagram is based on the mentioned secular equilibrium during the growth of daugthers. Therefore the parent (N_1, e.g. ^{238}U and ^{235}U) of a decay chain shows a longer half-life than its unstable or stable daughter (N_2, e.g. ^{206}Pb and ^{207}Pb) (Faure & Mensing, 2005).

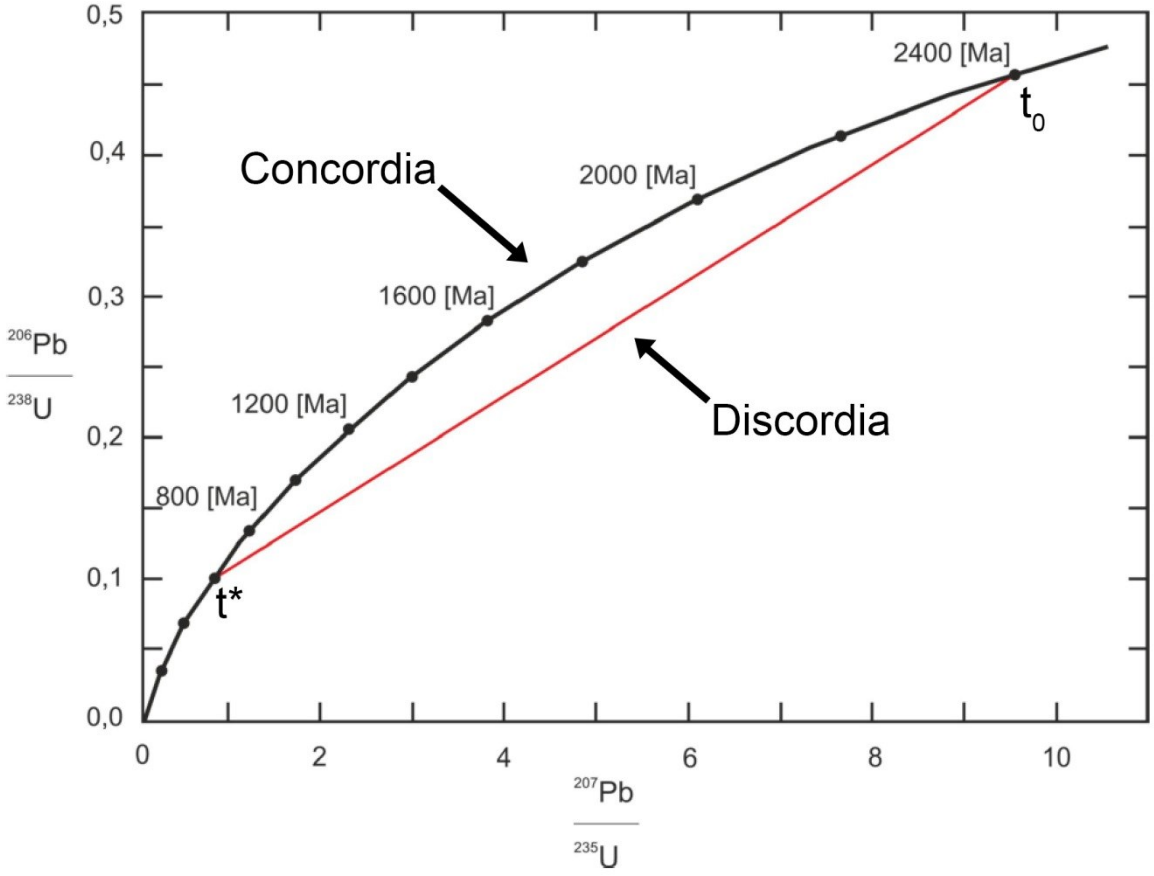

Fig. 33. Concordia diagram after Wetherill to interpret the loss of radiogenic Pb of U-bearing minerals and yielded discordant dates (Faure & Mensing, 2005; Wetherill, 1963).

It is stated, that the rate of the daughter production is equal to the rate of decay of the parent, hence the intermediate unstable daughter can be erased and so the number of stable daughters (D*) has to be equal to the number of parent atoms in a unit weight of a rock or in this case of the mineral zircon (Faure & Mensing, 2005).

This is only valid as long as the system stayed closed. If it did, the measured values have to be on the concordia line and the age of origin is determined. If it plots under it, a so called discordia is created, where on the on end the last change of the system (t*) (e.g. metamorphism) and on the other end its origin formation age (t_0) (e.g. last crystallisation) can be determined (Wetherill, 1963).

5. Results

5.1. Mapping

The mapping has revealed normal faults and different lithologies. Granite, granite-gneiss, granodiorite-gneiss, tonalite, tonalite-gneiss and amphibolite as well as different paragneisses have been distinguished. All units strike more or less north/northwest to south/south-east and have a westerly dip-direction and a dip-angle of ~25° (see appendix). All units have a strong weathered crust with a thickness of up to four centimetres.

The tonalitic units with their distinct withe appearance and dark biotite flakes, which are either randomly (tonalite) or orientated (tonalite-gneiss), differ strongly from the other units. The granite, granite-gneiss and granodiorite-gneiss vary in their mica content, and can be mainly discriminated by the size of their feldspar components, whereby the granitic units have a higher tendency to be coarse grained (>5 mm). The paragneisses are overall tighter laminated and show additionally either very high mica of over 50% (e.g. paragneisses with high mica) or high amount of clastic components (e.g. grained paragneisses). Quartzite was occasionally found as elongated quartz bars (Fig. 34) and occurred often as discordant veins (dykes <1 m) (Fig. 35) whereby the dip-direction of the quartz veins varies between east and west. All unites except the paragneisses and quartzites show roughly concordant bedding (see Structural Maps), whereby the granodiorite-gneiss alternates either with the granite-gneiss or the tonalitic units (see Lithological Map). The paragneisses seem to overlie the orthogneisses, whereby partly conjoint tectonic forces have influenced them, especially the intervening paragneisses within the granite-gneiss, which show a very dense foliation. The coarse grained paragneisses are further seen as part of the Rannach-Formation as described on page 26.

Within one trench fault gouge material (Fig. 36 and Fig. 38) and also step joints in the westerly part were recorded and interpreted as normal faults. The profile on page 59 is based on the anticline indicating z-shaped fold (Fig. 37), found in the north-west of the study area, whereby other indications (e.g. further fold axes) have not been found within the sketched lithologies and the profile is therefore highly visionary. The resulting maps are provided on the following pages the basic information about lithology (5.1.1), preferred orientations (Fig. 40), stretching lineation (Fig. 40) and LPO patterns (Fig. 58) are presented.

It has to be stated that the weathered crust makes the identification of rock types in field rather difficulty, and classification had to be rechecked by OP (page 62) and geochemistry (page 86).

Fig. 37: Assumed disharmonic secondary z-fold. Dip direction and angle are: A = 230/25, B = 242/28, C = 242/30, D = 324/10, E = 212/45 at N 47°23.760', E 014°30.406'.

Fig. 38: West directing step joint. Dip direction and dip are 270/15 at N 47°23.049', E 014°30.352.

Fig. 34: Parallel-bedding veins (PBV) of different quartz laminae. Lineation 280/25, dip direction and angle 235/40. Found at N 47°23.491', E 014°30.932'.

Fig. 35: Quartz dyke at the position N 47°23.062', E 014°30.341'.

Fig. 36: Fault gouge material found at N 47°23.049', E 014°30.352 substantiates the brittle movement of the normal fault.

5.1.1. Lithological Map

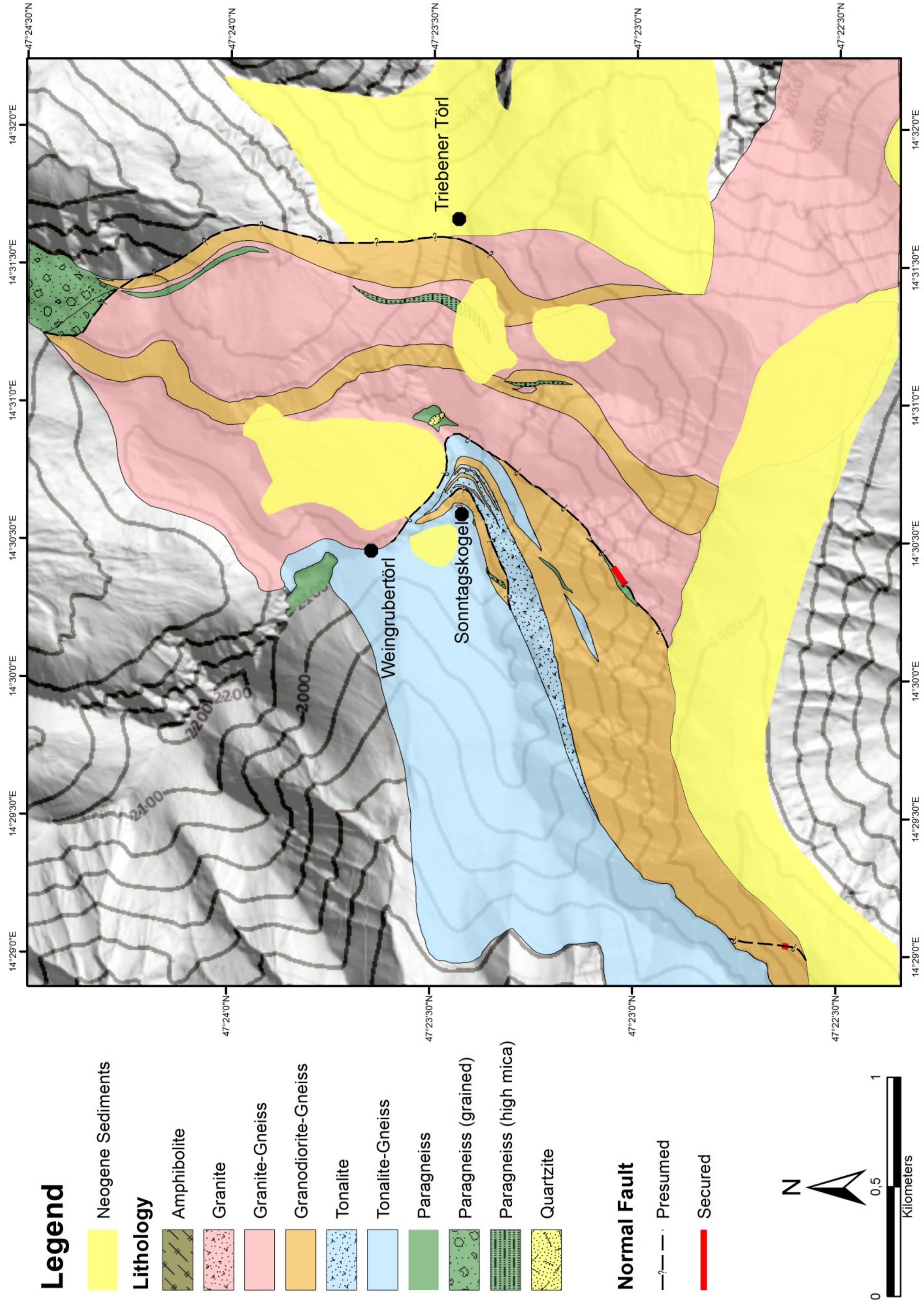

5.1.2. Structural Maps

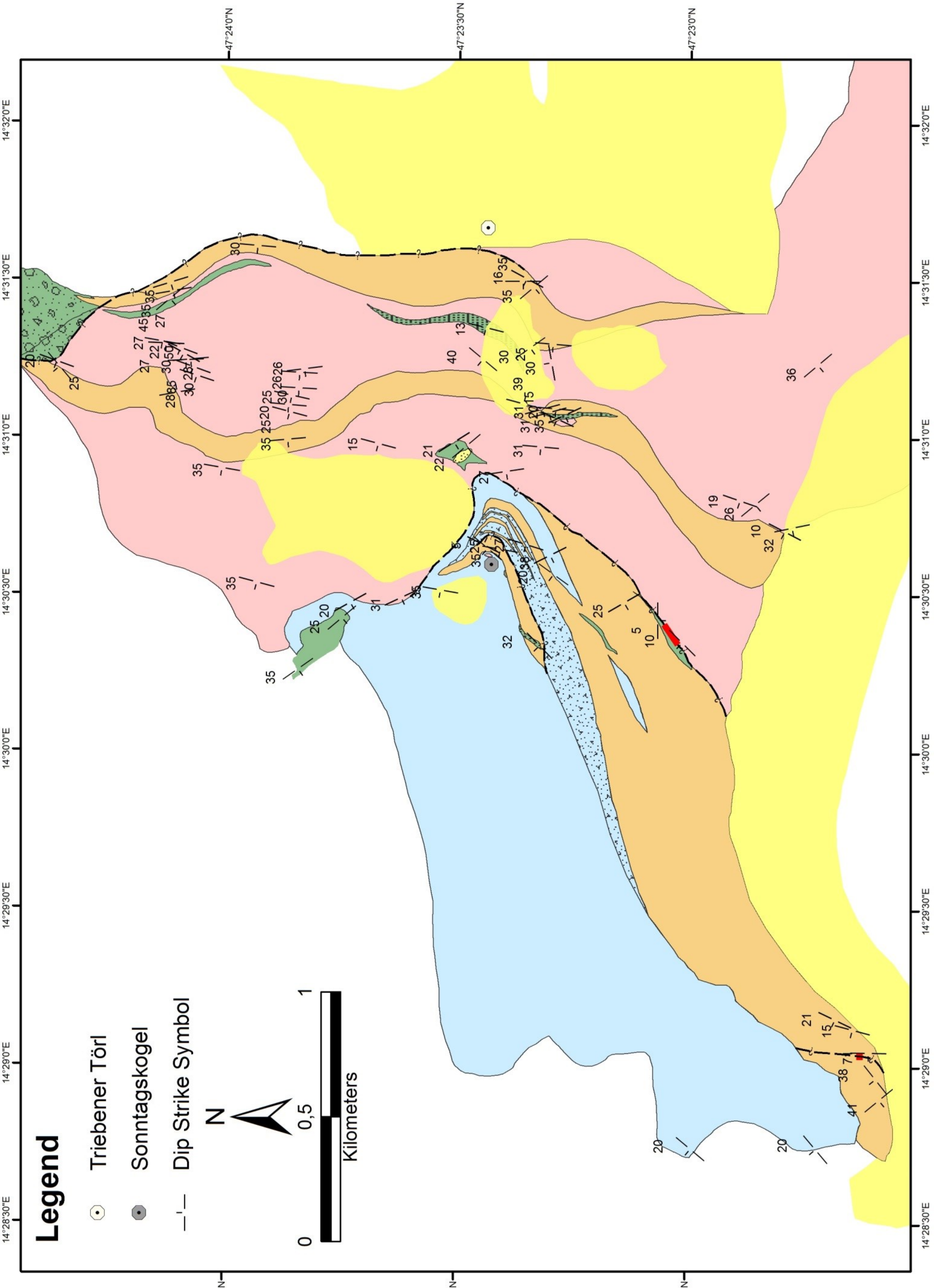

Fig. 39: Illustration of dip-direction and dip-angle (values in degrees). Legend according to page 56.

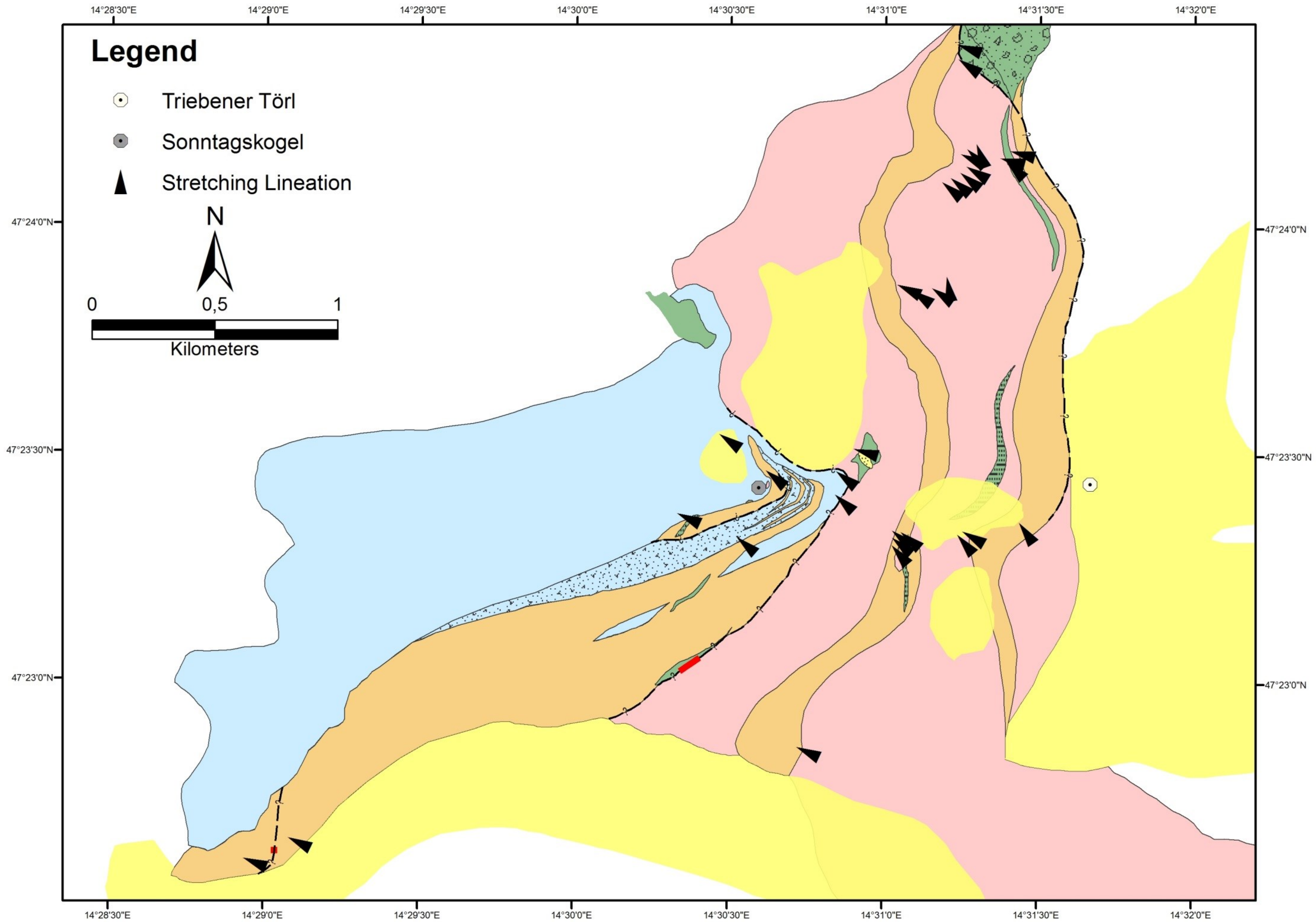

Fig. 40: Direction of stretching lineation. Point of arrow indicates the direction. Legend according to page 56.

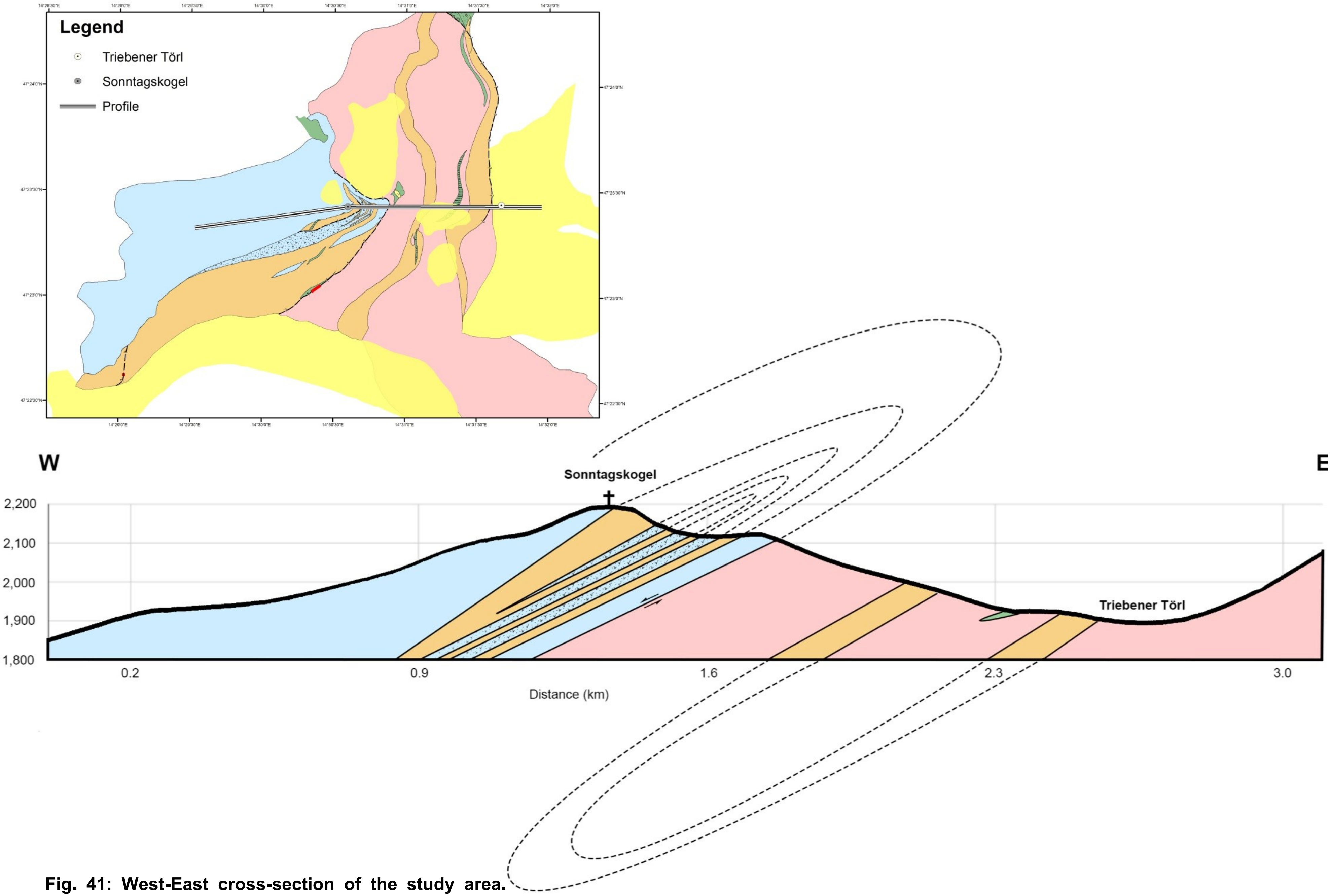

Fig. 41: West-East cross-section of the study area. Legend according to page 56.

5.1.3. Structural Data

Data have been summarized to “Granite-Gneiss”, “Granodiorite-Gneiss” and “Paragneiss”, because those provided the largest and therefore most significant amount of collected data. All measurements of the foliation were plotted as dip-direction and dip-angle, their according poles and stretching lineations are seen in the following table (Fig. 42).

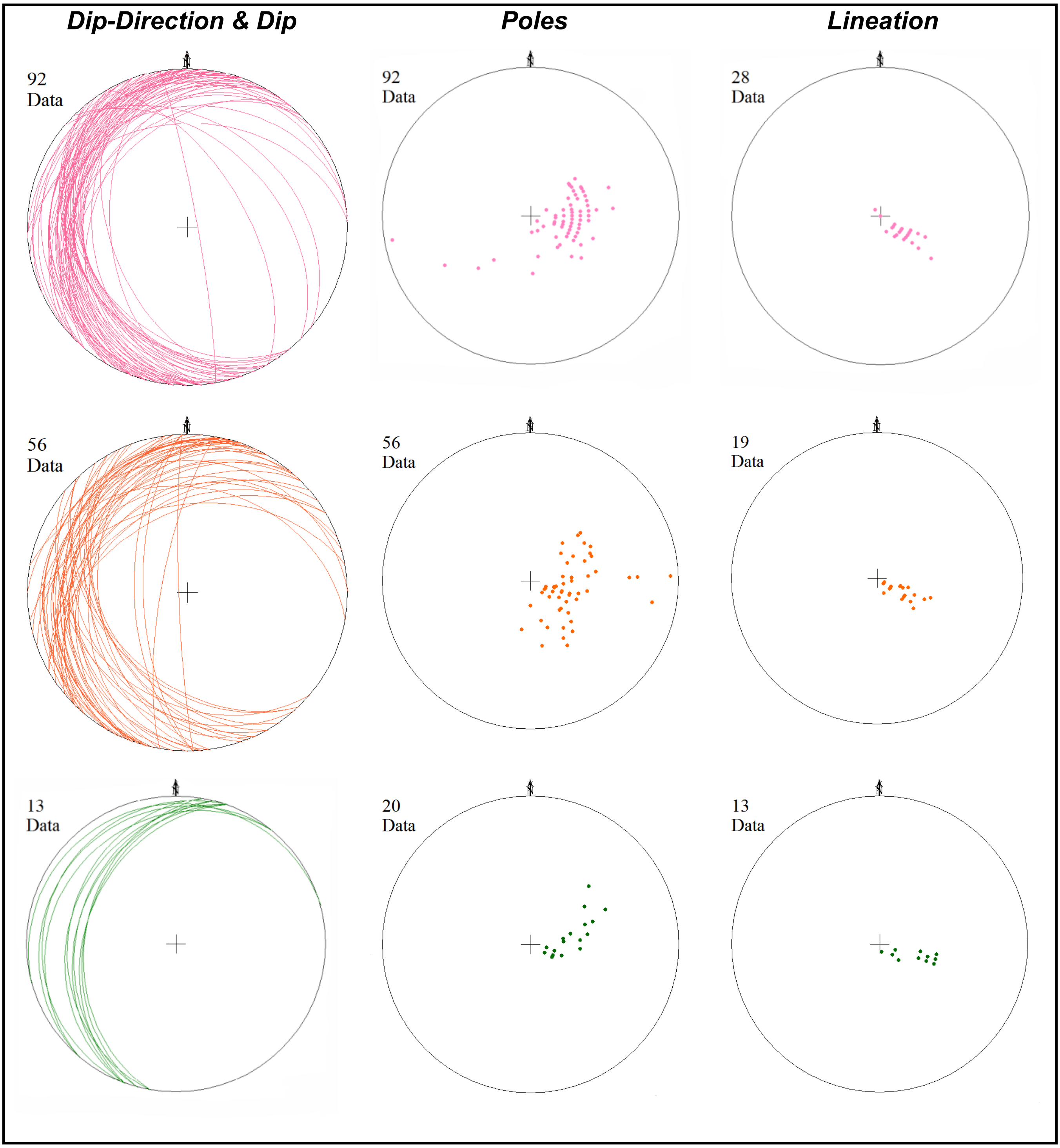

Fig. 42: Illustration of the complete structural data of foliation plains, plotted as stereographic projection on the lower hemisphere with Fabrics 8 (Wallbrecher, 2012). The colour code is equal to the lithological map, therefore granite-gneiss (pink), granodiorite-gneiss (orange), and paragneiss (green).

Further the stretching lineation was plotted separately as rose diagram, to better distinguish the lineation differences or occurring patterns of the lithologies, whereby the summarized data was plotted in full circles, the different lithologies in half circles.

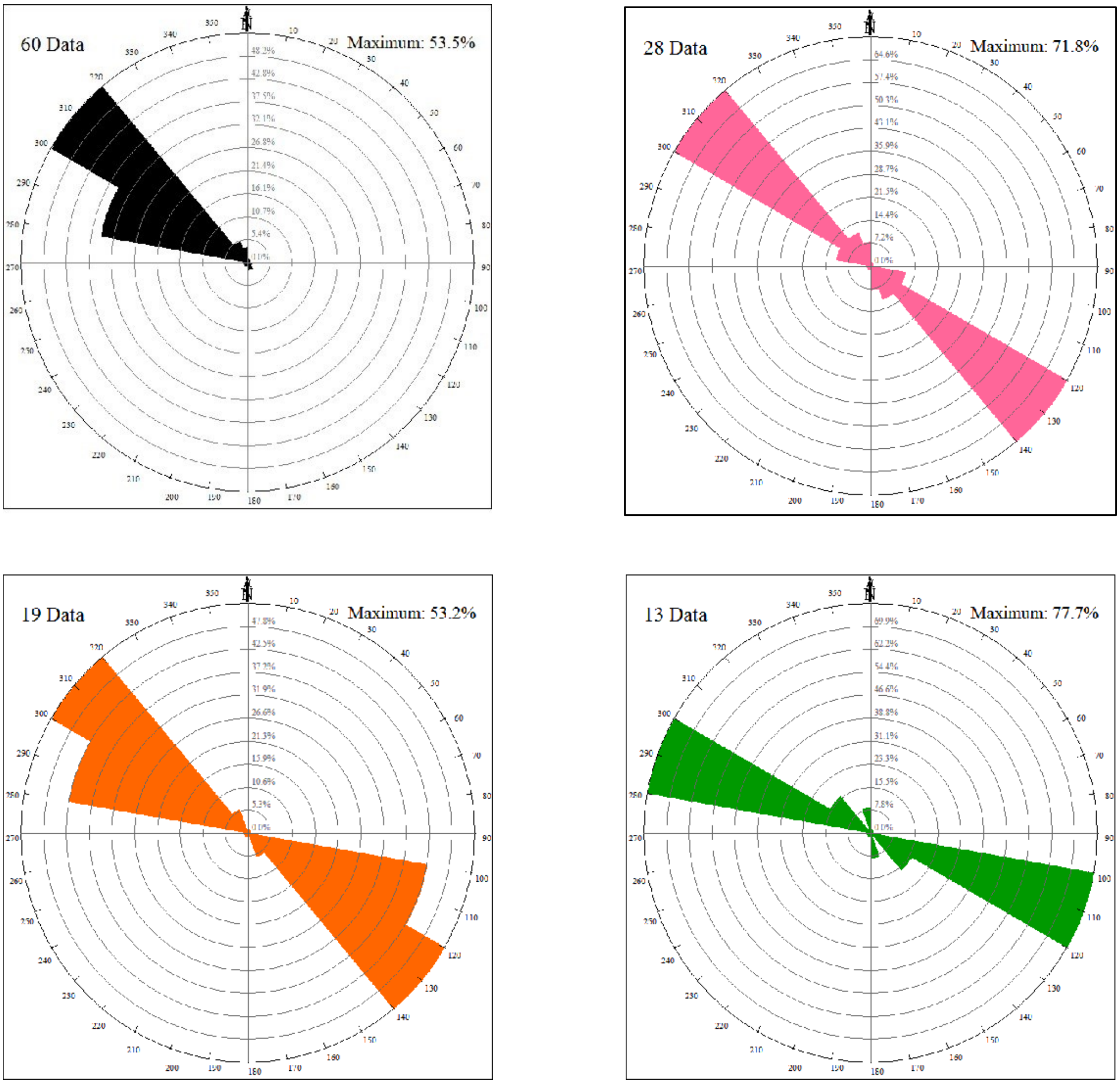

Fig. 43: Rose diagrams of stretching lineation with Fabric 8 (Wallbrecher, 2012). The colour code is equal to the lithological map, therefore granite-gneiss (pink), granodiorite-gneiss (orange), paragneiss (green), summarized data is coloured in black

As seen in the above rose diagrams, the granite-gneisses (300°-320°) defer up to 40° from the paragneisses (280°-300°), the granodiorite-gneisses (280°-320°) vary within those two lithologies. Directions and flows have also been visible in varies thin-sections, which were described by optical petrography.

5.2. Optical Petrography (OP)

Granite and Granite-Gneiss

The single granite sample SK78 (according to the final data evaluation, page 85) and the other granite-gneisses (Fig. 44, Fig. 50, Fig. 51, Fig. 54 and Fig. 55) show holo-crystalline crystallinity with a clustered granularity. The phanerocrystalline grainsize varies in absolute size and has been categorized as middle-grained (1-5 mm) and coarse-grained (>5mm). The relative size of the grains is unequally distributed and varies from seriate to an oriented trachytoidic structure. The main shape of the crystals is hypidiomorphic, whereby the distribution varies between equidimensional (isometric) to inequidimensional (anisometric) over to seriate. The general grain shape can be described as either inequigranular-interlobat to seriate-interlobate. The textures has an unequally arrangement and the grain binding is direct. The metamorphic character has been defined as hypidioblastic, whereby the foliation provided S and SC structures. Further, zoned crystals and mortar structures occurred. Feldspar shows a brittle behaviour in contrary to quartz which bulges often. A general content of plagioclase (~25 vol.%), quartz (~35 vol.%) and kalifeldspar (>15 vol.%) is characteristic.

Main minerals: Quartz, plagioclase, kalifeldspar, biotite, chlorite, muscovite, sericite
Accessories: Zircon, titanite, tourmaline, apatite, zoisite, epidote
Samples after OP: SK4, SK7, SK8.2, SK10.1, SK11, SK15.1, SK16, SK16.1, SK16.2, SK20, SK26.1, SK79, SK82, SK85, SK87.1, SK95 and SK100.

Tonalite and Tonalite-Gneiss

The tonalites (Fig. 46) shows a holo-crystalline crystallinity and a dispersed to clustered granularity with unequally, poikilitic, middle (1-5 mm) to coarse-grained (>5 mm) components. The recrystallized quartz shows bulging, whereby feldsparsw occur brittle. Further the feldspar shows an overall strong saussuritization, whereby transformations into sericite, epidote and zoisite assemble. A general content of plagioclase (>60 vol.%), quartz (<30 vol.%) and kalifeldspar (<5 vol.%) is characteristic. Also middle-grained biotite with varies chloritizations and fine muscovite can be seen. Titanite, apatite and zircon are also seen as accessories.

Main minerals: Quartz, plagioclase, kalifeldspar, biotite, muscovite, chlorite, sericite
Accessories: Titanite, apatite, zircon, zoisite, epidote
Samples after OP: SK19.1, SK93, SK96 and SK97.

Granodiorite-Gneiss

The granodiorite-gneisses (Fig. 45), strongly vary in their appearances. The crystallinity is holo-crystalline the granularity is clustered and the general grainsize is described as phanerocrystalline. The absolute size has been set to middle-grained (1-5 mm), whereby it is unequally grained. The samples show a trachytoidic orientation and the main crystal shape is hypidiomorphic. The distribution varies from seriate to inequidimensional (anisometric), whereby the grain shape is interlobate. The texture arrangement is unequally with a direct grain binding, bulging occurs on quartz. SC foliation and mortar structures as well as zones crystals occur. Feldspar has a brittle behaviour. A general content of plagioclase (35-58 vol.%), quartz (~35-56 vol.%) and kalifeldspar (<16 vol.%) is characteristic.

Main minerals: Quartz, plagioclase, kalifeldspar, chlorite, sericite, muscovite, biotite
Accessories: Titanite, tourmaline, zircon, apatite, opaque phases
Samples after OP: SK3, SK12.1, SK13.1, SK21.1, SK22.1, SK57, SK58, SK73, SK78, SK94 and SK99.

Paragneiss

Basically three types of paragneisses have been discriminated. One with clastic components (Fig. 53), which was classified as “grained”, one with very high mica content (Fig. 48) with over 50% and one which is neither grainy nor does it have a high mica content (Fig. 47). The paragneisses show holocrystalline crystallinity, and a clustered granularity. The grainsize is phanerocrystalline, whereby the components are classified as middle-grained (1-5 mm). The grainy paragneiss shows of course a very unequal distribution in relative size, compared to the other two, which are also seen as unequal but with a tendency to be equally grained. All paragneisses show an orientation which is categorized as trachytoidic. The main crystal shape is hypidiomorph, with an inequidimensional (anisotropic) grain shape and occurring bulging. The texture arrangement is unequally, whereby biotite fills most interspace. Quartz bulges, also forms aggregated shape preferred orientations (ASPO) and is definitely the main mineral besides biotite. A general content of plagioclase (>20 vol.%), quartz (>60 vol.%) and kalifeldspar (<1 vol.%) is characteristic.

Main minerals: Quartz, biotite, muscovite, feldspar
Accessories: Epidote, zoisite and opaque phases
Samples after OP: SK6, SK8, SK8.2, SK9, SK17.3, SK18, SK18.1, SK69 and SK77.1.

Amphibolite

In the study area one amphibolite (hornblende gneiss) (Fig. 49) has been found. It is holo-crystalline, its granularity is clustered, the grainsize is described as aphanitic and shows therefore equally fine-grained (<1 mm) minerals. The relative size is hypidiomorphic the crystal shape is inequigranular-interlobate with direct grain binding. It consists mainly of hornblende.

The following is valid for Fig. 44 to Fig. 55: Scale bar is in bottom right corner. Each sample is presented with pictures of parallel (left one) and crossed (right one) polarizer. The direction and angle of the stretching lineation and the sample number is printed on top of each picture. Coordinates are listed in the appendix (page 112). Rock type is based on final evaluation (Table 2). Bt = biotite, Chl = chlorite, Ep = epidote, Hbl = hornblende, Kfs = kalifeldspar, Msc = muscovite, Plg = plagioclase, Qtz = quartz, Tur = tourmaline, Zo = zoisite.

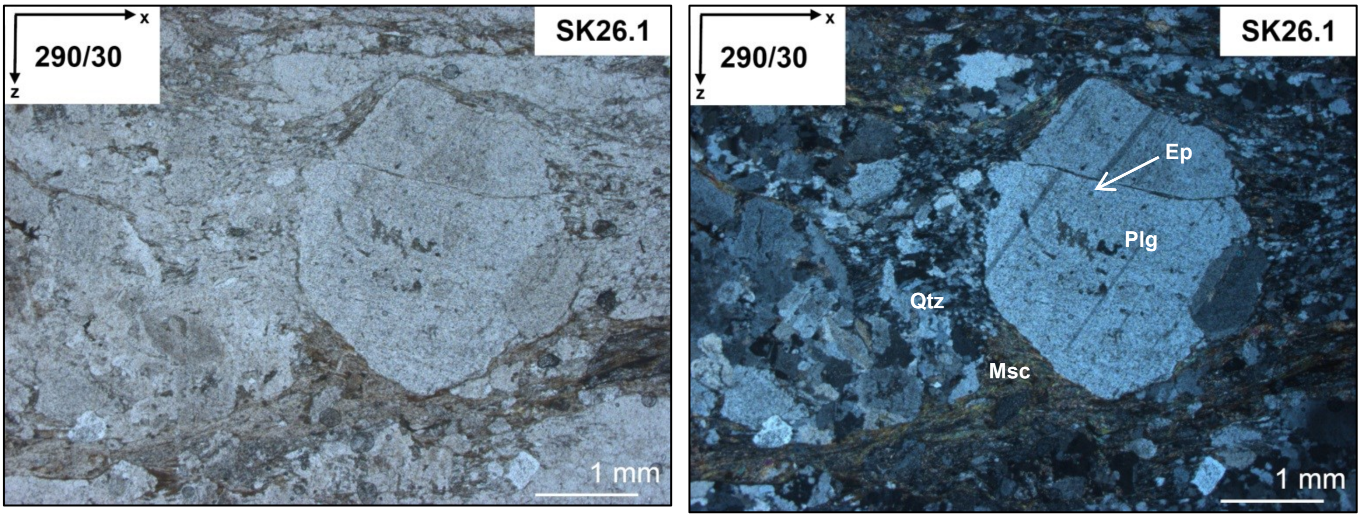

Fig. 44: The sample SK26.1, granite-gneiss, is a holo-crystalline, clustered, phanerocrystalline rock, with middle and serial unequally grained components (1-5mm). The main shape is hypidiomorph, the distribution inequidimensional, whereby the grain shape is inequigranular-interlobate. It shows direct grain binding, whereby quartz bulges and feldspars are still brittle, as it is seen above in the west-northwest sheared clast.

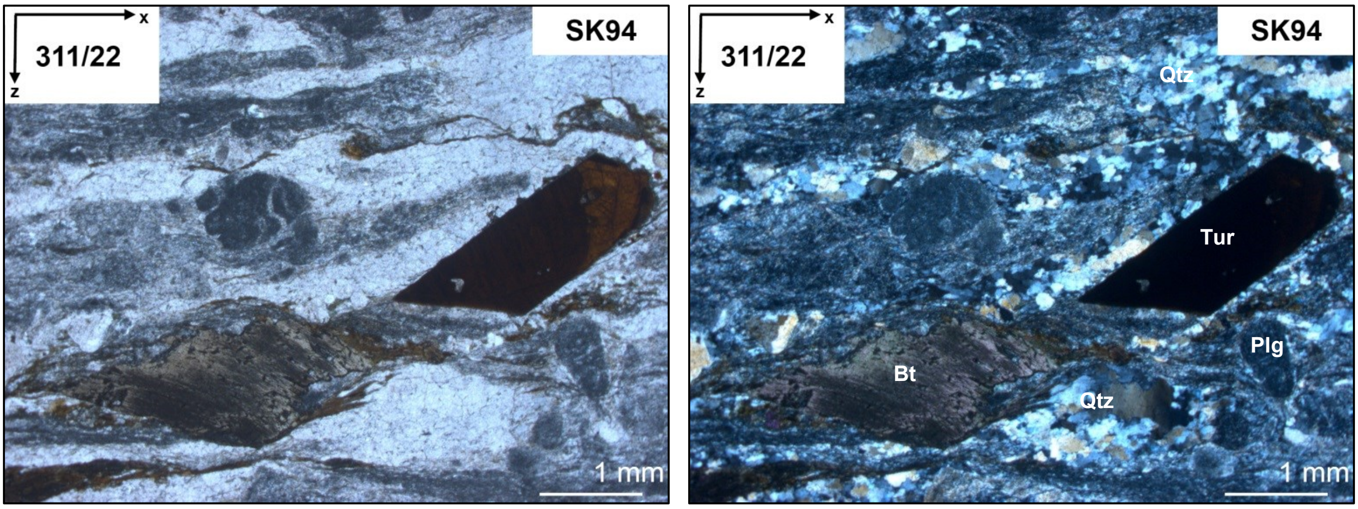

Fig. 45: The sample SK94, granodiorite-gneiss, is a holo-crystalline, dispersed, phanerocrystalline rock, with middle and trachytoidic unequally grained components (1-5 mm). The main shape is hypidiomorph the distribution is inequidimensional, whereby the grain shape is inequigranular-interlobate. It shows direct grain binding, whereby quartz bulges and feldspars are still brittle.

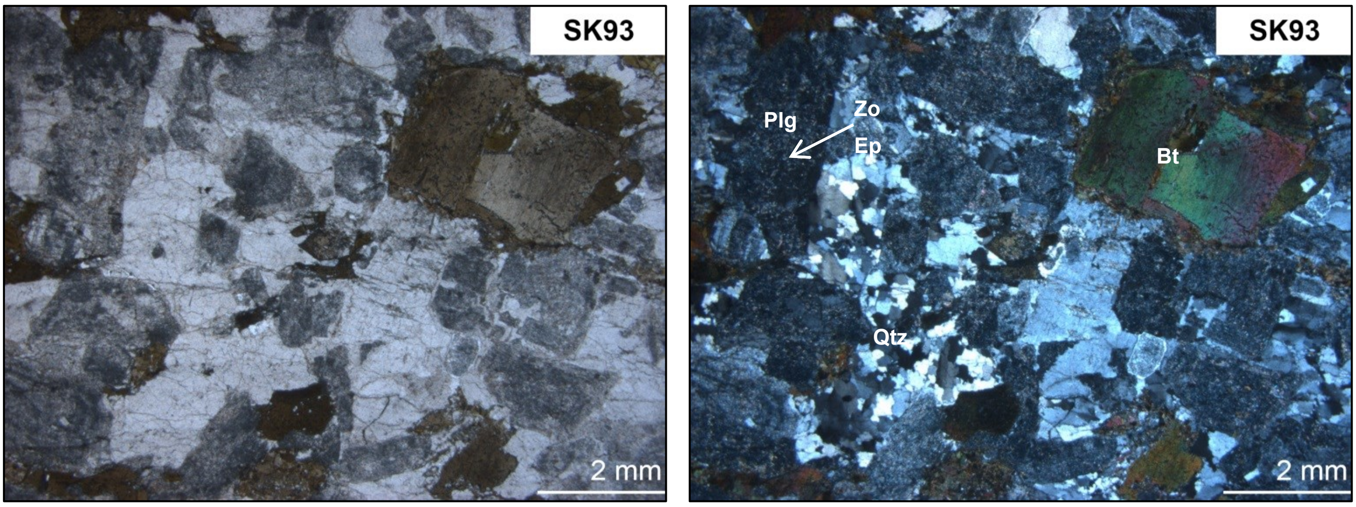

Fig. 46: The sample SK93, tonalite, is a holo-crystalline, dispersed, phanerocrystalline rock, with middle and poikilitic unequally grained components (1-5 mm). The main shape is hypidiomorph the distribution is seriate, whereby the grain shape is seriate-interlobate. It shows direct grain binding, quartz bulges.

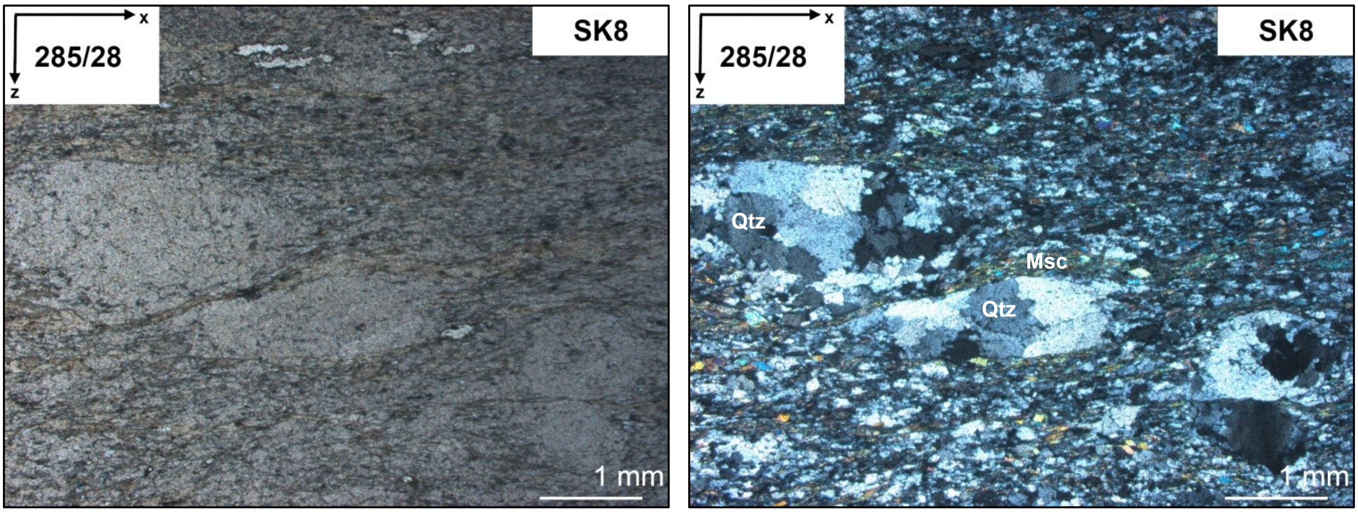

Fig. 47: The sample SK8, paragneiss, is a holo-crystalline, clustered, phanerocrystalline rock, with middle and trachytoidic unequally grained components (1-5 mm). The main shape is hypidiomorph the distribution is inequidimensional, whereby the grain shape is inequigranular-interlobate. It shows direct grain binding, wherby quartz bulges and has often an ASPO.

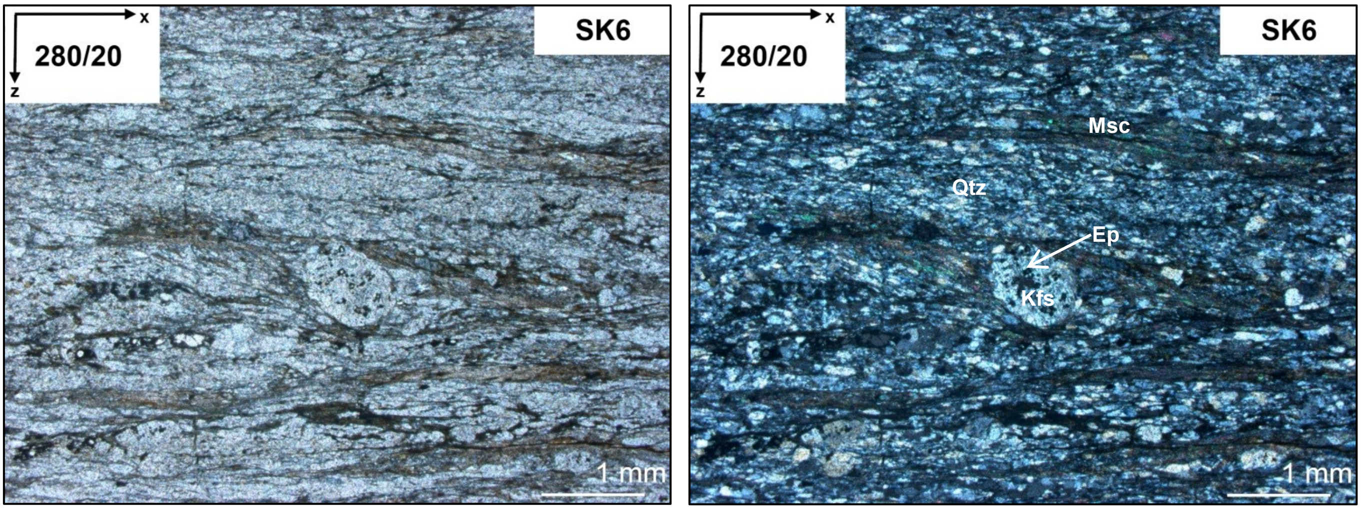

Fig. 48: The sample SK6, paragneiss, is a holo-crystalline, clustered, phanerocrystalline rock, with middle and trachytoidic unequally grained components (1-5 mm). The main shape is hypidiomorph the distribution is inequidimensional, whereby the grain shape is inequigranular-interlobate. It shows direct grain binding, wherby quartz shows bulges. Most spaces are filled by biotite.

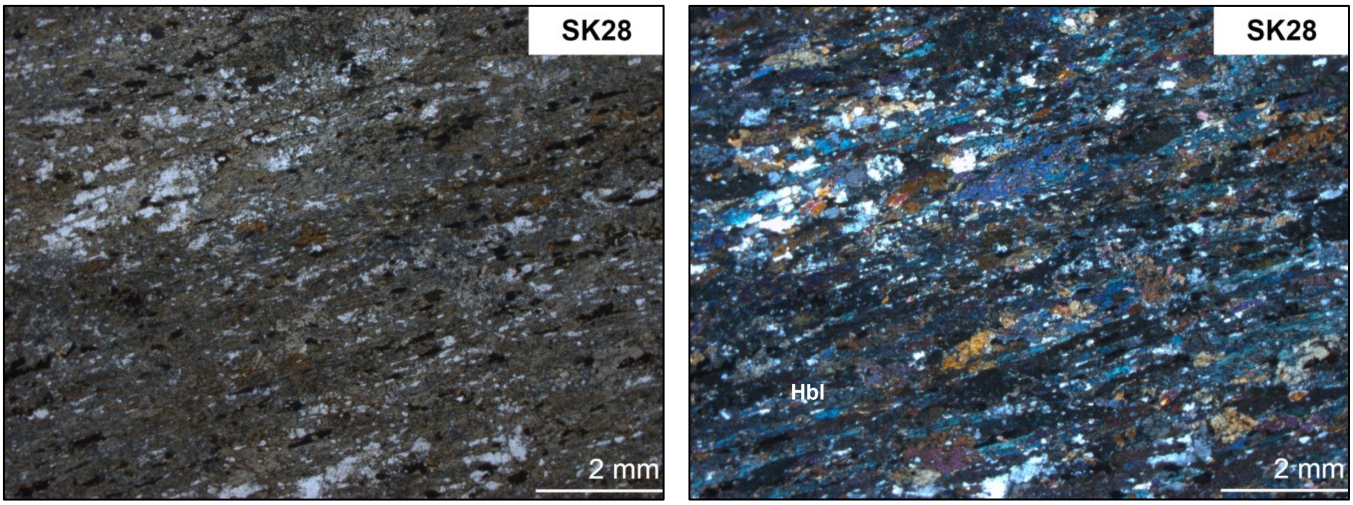

Fig. 49: The sample SK28, amphibolite is a holo-crystalline, clustered, aphanitic rock, with middle and trachytoidic equally grained components (1-5 mm). The main shape is hypidiomorph the distribution is inequidimensional, whereby the grain shape is inequigranular-interlobate. It shows direct grain binding.

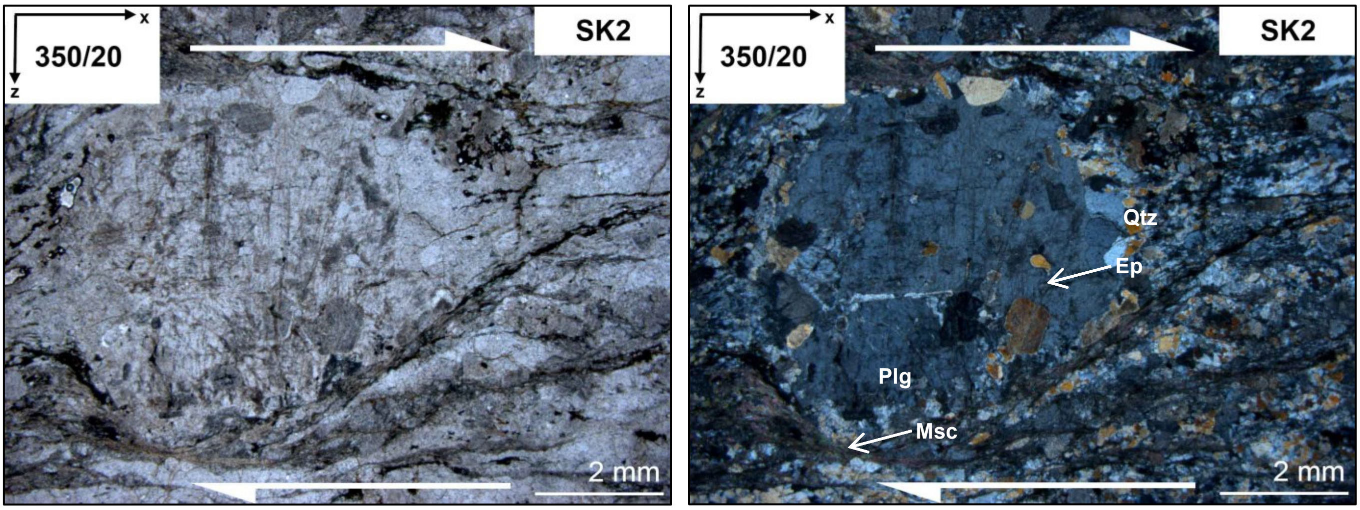

Fig. 50: The sample SK2, granite-gneiss is a holo-crystalline, clustered, phanerocrystalline rock, with coarse-grained and trachytoidic unequally grained components (>5 mm). The main shape is hypidiomorph the distribution is inequidimensional, whereby the grain shape is inequigranular-interlobate. It shows direct grain binding and a top north-west-north shear of σ-type clast.

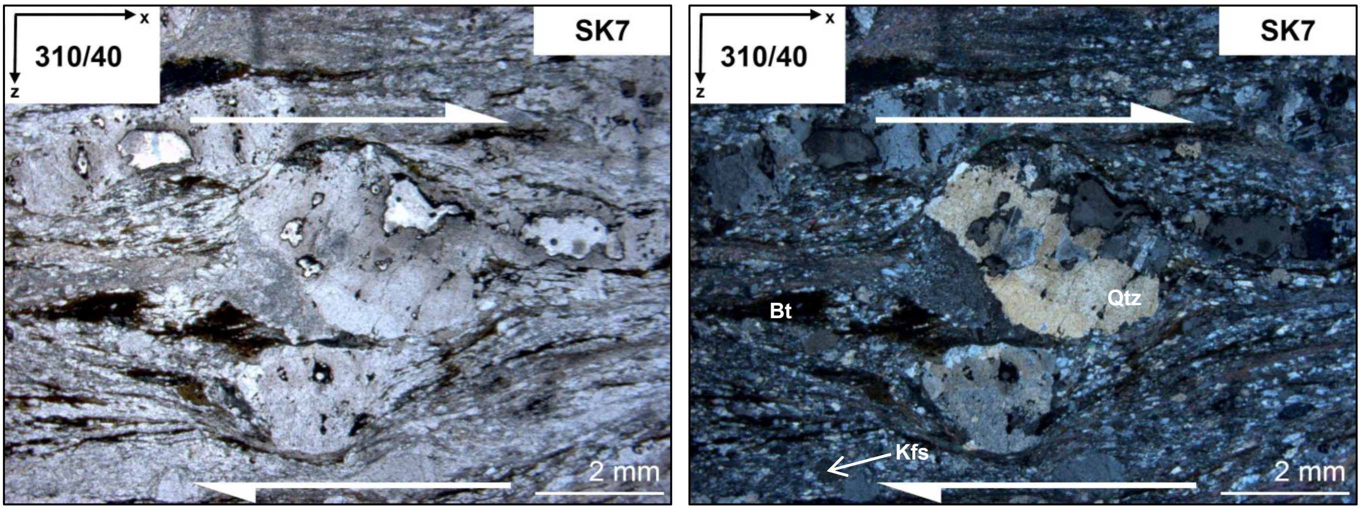

Fig. 51: The sample SK7, granite-gneiss is a holo-crystalline, clustered, phanerocrystallien rock, with middle and trachytoidic unequally grained components (1-5 mm). The main shape is hypidiomorph the distribution is inequidimensional, whereby the grain shape is inequigranular-interlobate. It shows direct grain binding and a top north-west shear of σ-type clast.

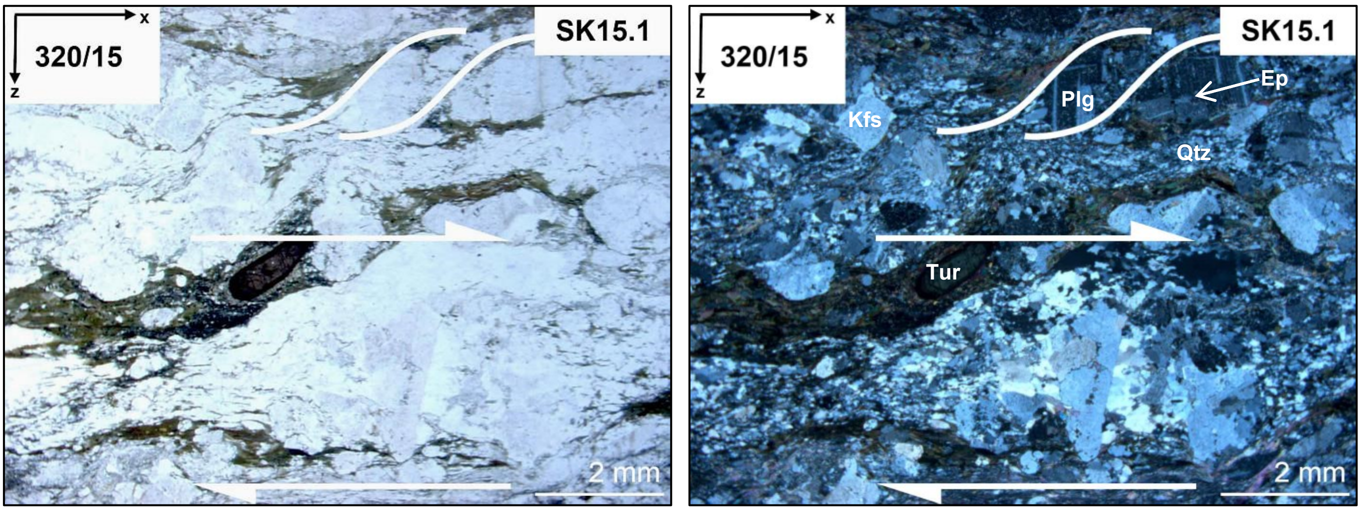

Fig. 52: The sample SK15.1, granite-gneiss is a holo-crystalline, clustered, phanerocrystallien rock, with middle and seriate unequally grained components (1-5 mm). The main shape is hypidiomorph, whereby the grain shape is seriate-interlobate. The direct grain bound has a top north-west shear and SC shear bands.

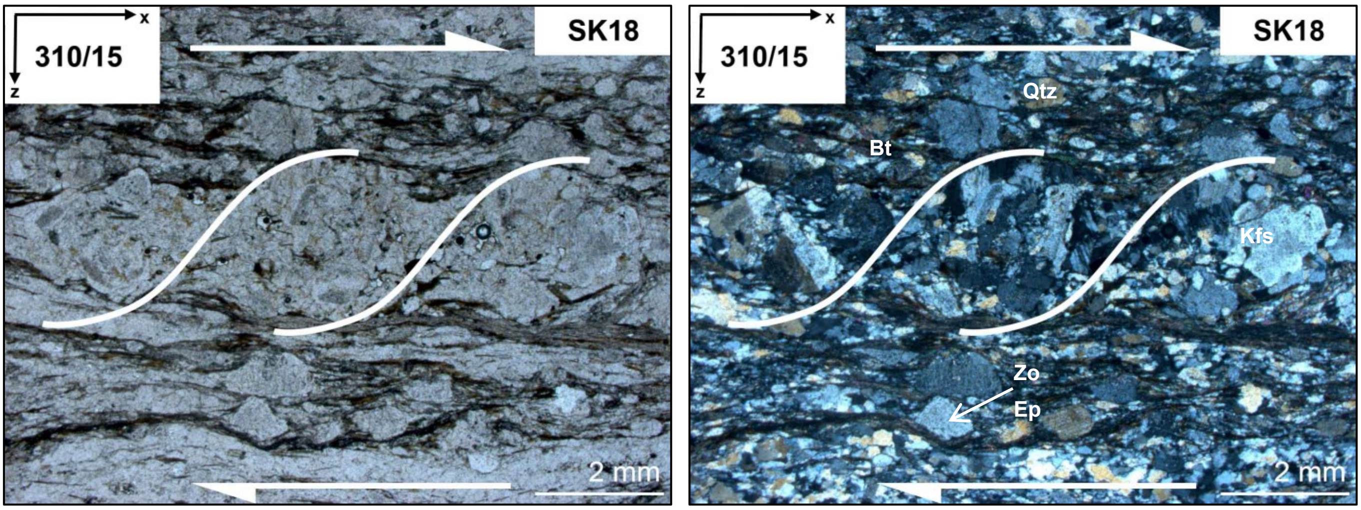

Fig. 53: The sample SK18, paragneiss is a holo-crystalline, clustered, phanerocrystallien rock, with middle and seriate unequally grained components (1-5 mm). The main shape is hypidiomorph, whereby the grain shape is seriate-interlobate. The direct grain bound has a top north-west shear and SC shear bands.

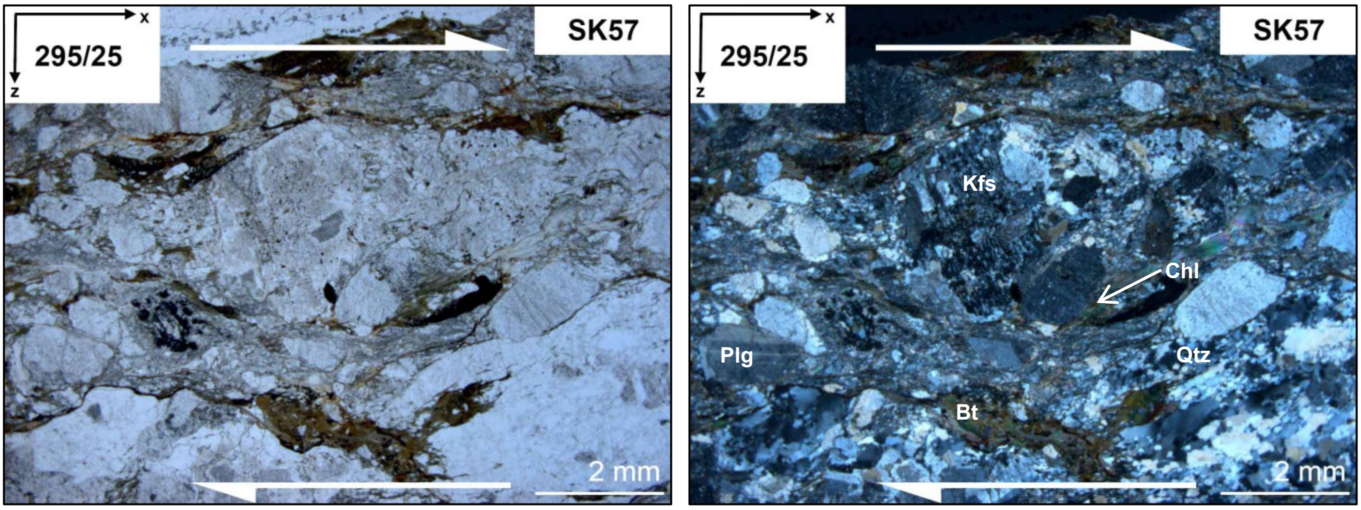

Fig. 54: The sample SK57, granite-gneiss is a holo-crystalline, clustered, phanerocrystallien rock, with middle and trachytoidic unequally grained components (1-5 mm). The main shape is hypidiomorph the distribution is inequidimensional, whereby the grain shape is inequigranular-interlobate. It shows direct grain binding, a top west-north-west shear and bulging.

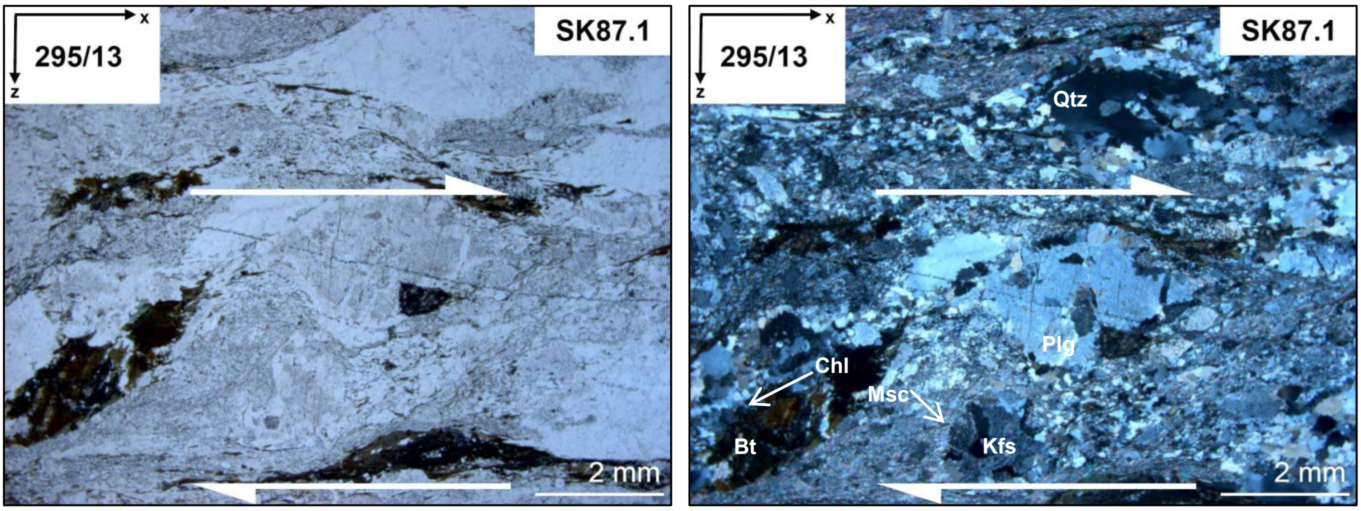

Fig. 55: The sample SK87.1, granite-gneiss is a holo-crystalline, clustered, phanerocrystallien rock, with middle and seriate unequally grained components (1-5 mm). The main shape is hypidiomorph the distribution is inequidimensional, whereby the grain shape is seriate-interlobate. It shows direct grain binding, a top west-north-west shear and bulging.

Temperature

Based on 60 analysed thin sections by microscoping 56 samples have shown bulging of quartz, two samples have even shown sub-grains (SK8.2 and SK77.1) and two did not have shown any sign of temperature influence of quartz. An amount of 34 samples had a brittle behaviour of feldspar, the rest had none. Therefore the temperature of deformation has been estimated to be between 300 °C and 400 °C (see chapter 4.1.2).

Rock Classification – Microscoping

Under the microscope it had to be differentiated primarily between paragneisses and different orthogneisses. The paragneisses variated with their mica content and clastic components and often have shown ASPO (aggregate shape preferred orientations). All samples which have not been analysed by XRF spectroscopy have been point countered as described (chapter 4.1.1). Around 500 grains have been counted per sample the result is presented in the following illustration (Fig. 56) and Table 2. Most samples plot in the quartz richer area, which is considered as a general error of the method, by defining an overall fitting mesh-width by unequally grained samples, which most of the samples are.

Table 2: Data of point counter. Only the necessary minerals according to Streckeisen (1974) are named. Qtz = quartz, Plg = plagioclase, Kfs = kalifeldspar.

Sample	Number of Grains				%			Rock Type
	Qtz	Plg	Kfs	Total	Qtz	Plg	Kfs	
SK2	253	119	46	418	61	28	11	**Quartz-rich granitoids**
SK5	255	27	1	283	90	10	0	**Quartz-rich granitoids**
SK7	210	86	29	325	65	26	9	**Quartz-rich granitoids**
SK7	200	37	90	327	61	11	28	**Quartz-rich granitoids**
SK8.1	259	51	15	325	80	16	5	**Quartz-rich granitoids**
SK8.3	210	191	31	432	49	44	7	**Granodiorite**
SK8.3	295	91	1	387	76	24	0	**Quartz-rich granitoids**
SK8.3	291	35	0	326	89	11	0	**Quartz-rich granitoids**
SK9.1	344	96	22	462	74	21	5	**Quartz-rich granitoids**
SK9.2	178	150	25	353	50	42	7	**Granodiorite**
SK9.3	186	197	32	415	45	47	8	**Granodiorite**
SK11.1	195	154	67	416	47	37	16	**Granodiorite**
SK11.2	153	235	44	432	35	54	10	**Granodiorite**
SK12	428	49	16	493	87	10	3	**Quartz-rich granitoids**
SK12	213	203	33	449	47	45	7	**Granodiorite**
SK15	205	55	66	326	63	17	20	**Quartz-rich granitoids**
SK15	178	93	69	340	52	27	20	**Monzogranite**
SK20.1	191	99	19	309	62	32	6	**Quartz-rich granitoids**
SK21	193	170	52	415	47	41	13	**Granodiorite**
SK22	248	166	28	442	56	38	6	**Granodiorite**
SK24	321	29	1	351	91	8	0	**Quartzolite**
SK24	231	225	39	495	47	45	8	**Granodiorite**
SK73	170	55	20	245	69	22	8	**Quartz-rich granitoids**
SK82	138	253	7	398	35	64	2	**Tonalite**
SK85	185	103	8	296	63	35	3	**Quartz-rich granitoids**
SK95	228	70	83	381	60	18	22	**Quartz-rich granitoids**
SK100	135	190	30	355	38	54	8	**Granodiorite**

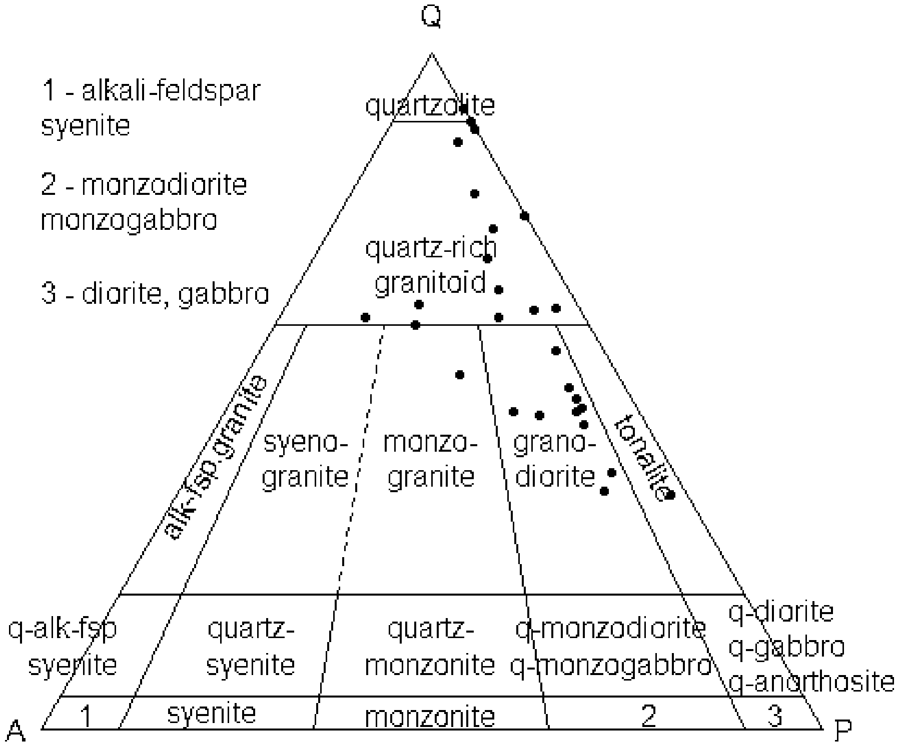

Fig. 56: Rock classification after Streckeisen (1974) of non-geochemical analysed samples.

5.2.1. LPO Data

The following pages present the graphical evaluation of the LPO measurements with the software “Fabric 8”, the according coordinates of the sampling site can be found in the appendix.

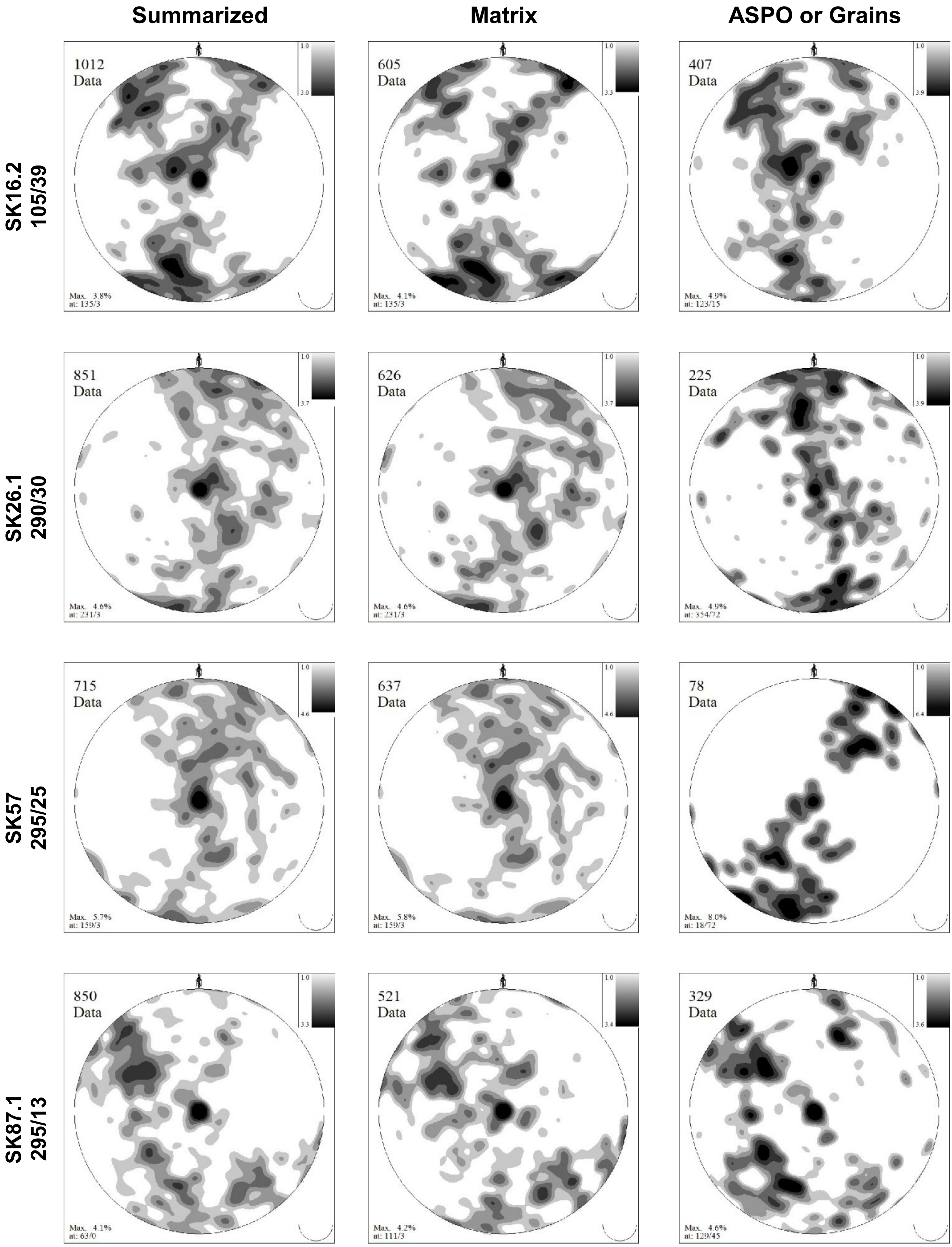

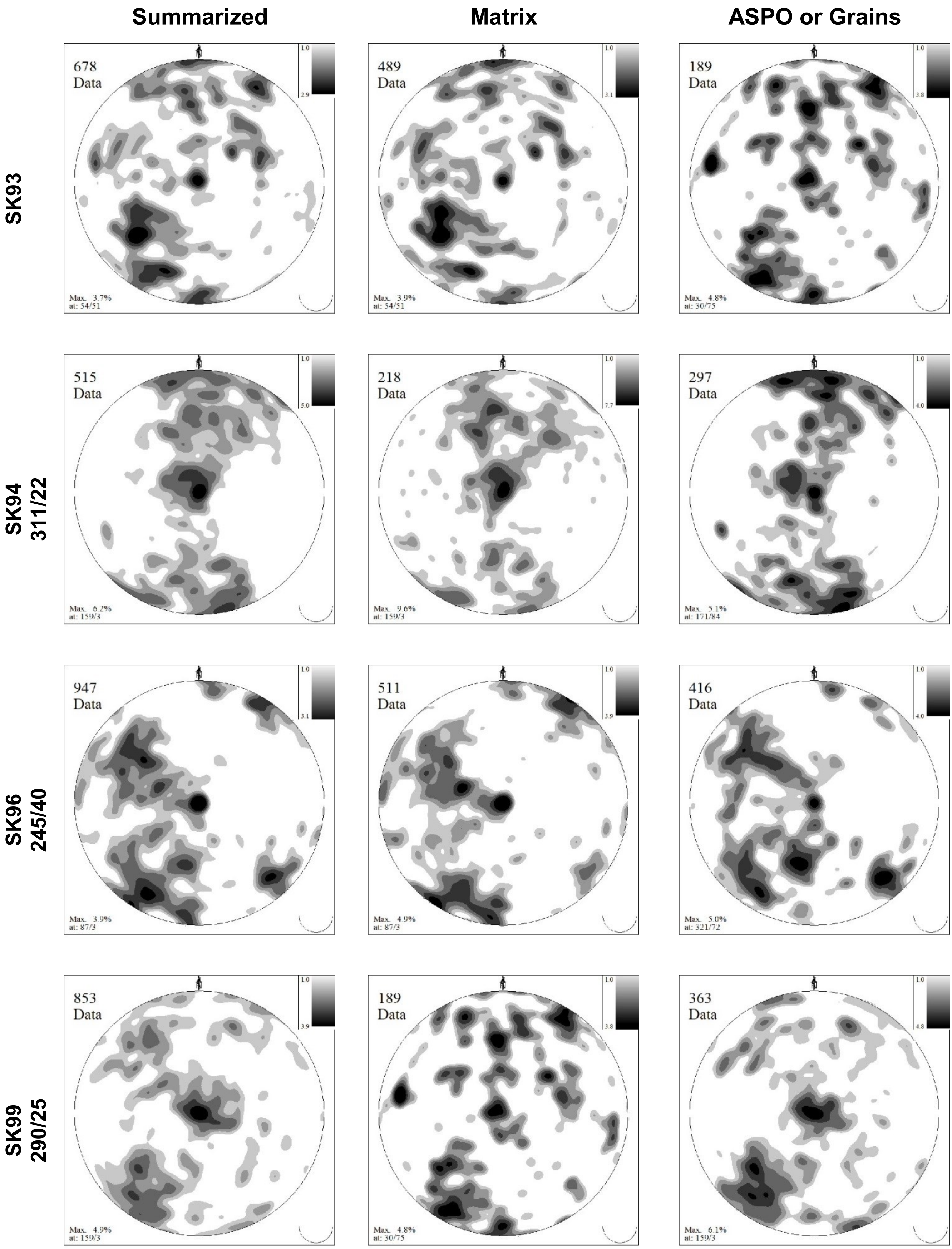
Summarized
Matrix
ASPO or Grains
SK93
678
Data
1.0
2.9
Max. 3.7%
at: 54/51
489
Data
1.0
3.1
Max. 3.9%
at: 54/51
189
Data
1.0
3.8
Max. 4.8%
at: 30/75
SK94
311/22
515
Data
1.0
5.0
Max. 6.2%
at: 159/3
218
Data
1.0
7.7
Max. 9.6%
at: 159/3
297
Data
1.0
4.0
Max. 5.1%
at: 171/84
SK96
245/40
947
Data
1.0
3.1
Max. 3.9%
at: 87/3
511
Data
1.0
3.9
Max. 4.9%
at: 87/3
416
Data
1.0
4.0
Max. 5.0%
at: 321/72
SK99
290/25
853
Data
1.0
3.9
Max. 4.9%
at: 159/3
189
Data
1.0
3.8
Max. 4.8%
at: 30/75
363
Data
1.0
4.8
Max. 6.1%
at: 159/3

Summarized **Matrix** **ASPO or Grains**

SK100
230/36

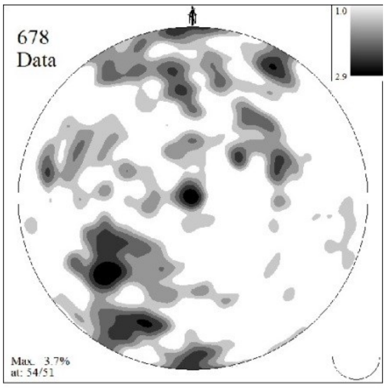

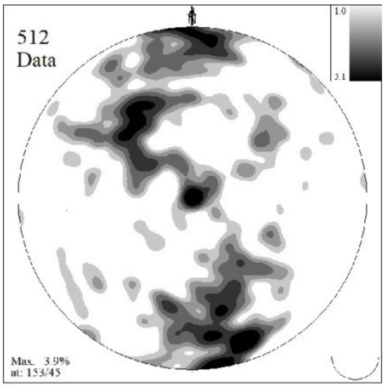

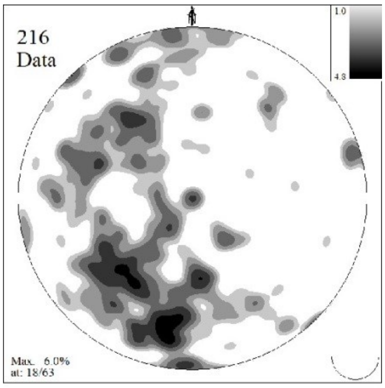

SK8
285/28

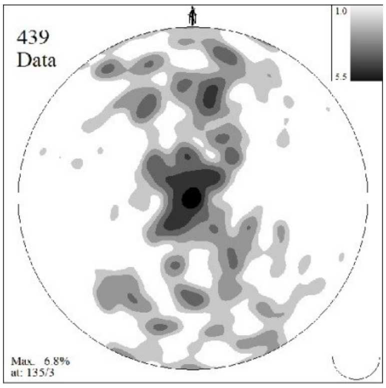

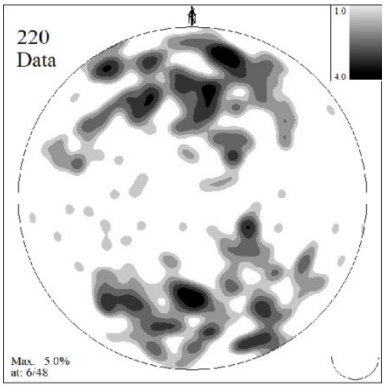

Summarized **Summarized**

SK8.2
275/30

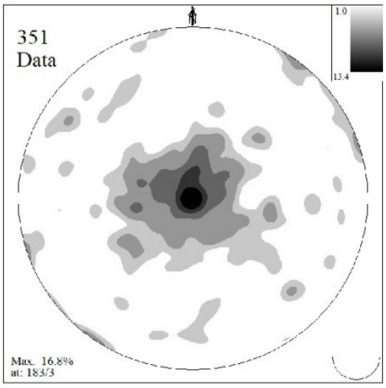

SK15.1
320/15

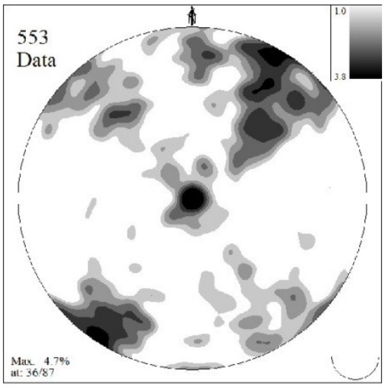

SK58
285/20

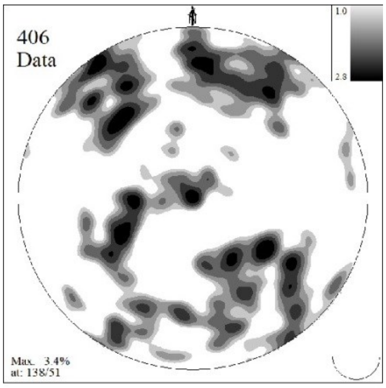

SK77.1
316/32

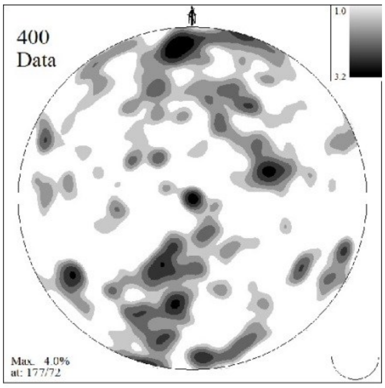

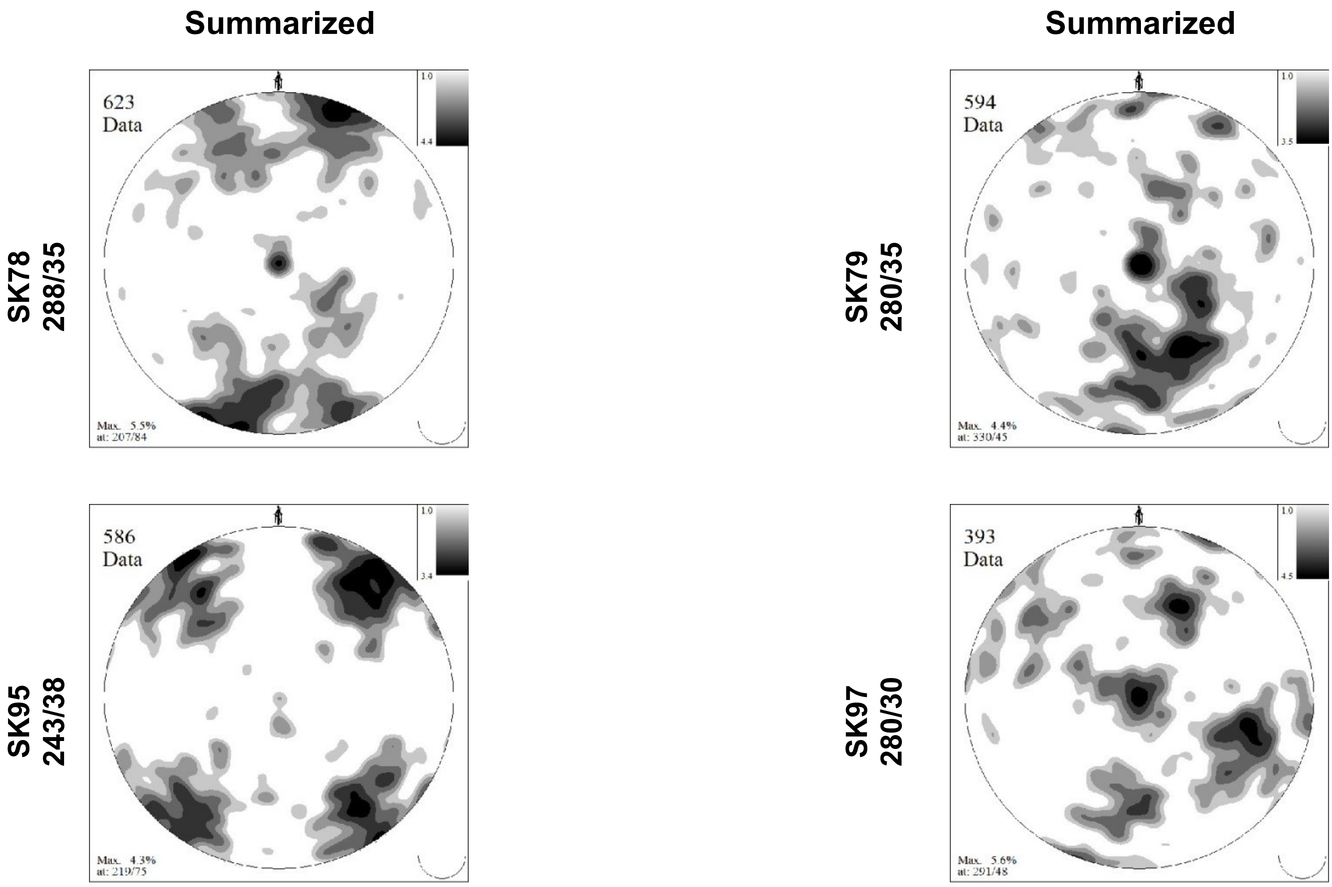

Fig. 57: The pages 70-73 present the stereographic projections, lower hemisphere, and logarithmic gradation of isolines of the LPO measurements, plotted with the software Fabric 8 with a smoothing factor of three. The samples were partly grouped and separated into matrix, grains and ASPO.

Based on Fig. 31 and Fig. 32 on page 45 of chapter 4, the type of LPO, its assumed gliding system and interpreted temperature and deformation is presented in the Table 3. All LPO analyses are seen as non-coaxial with a strong tendency to the formation of NW shearing cross girdle type I and small circles, whereby the overall deformation is considered as a plane strain within a temperature window of 300-400 °C.

This data is conclusive to the previous stated temperature estimation of the optical thin section description. As seen (Table 3) the samples SK16.2, SK93, SK94, SK96 and SK100 have the same pattern in all three categories compared to the samples SK8, SK57 and SK87.1 which have different ones. The data distribution of SK93 is randomly.

On the following figure (Fig. 58) is a map illustrated which states the position of the samples, and it’s according LPO pattern of the summarized amount of measured points.

Table 3: Representation of the assumed gliding system and type of LPO is provided according to the previous division of Fig. 57. The temperature and deformation were estimated. Empty categories mean no measurements were executed.

	Rock Type	Summarized	Matrix	Grains or ASPO	Temperature & Deformation
SK8	Paragneiss	Type II cross girdle Prism <a>	Small circles Basal <a>		Low T 300-400°C Plane strain
SK8.2	Paragneiss	Point Maximum Prism <a>			Medium T 450-550°C
SK15.1	Granite-Gneiss	Type II cross girdle Prism <a> Basal <a>			Low T 300-400°C Plane strain
SK16.2	Granite-Gneiss	Type I cross girdle Prism <a> Rhomb <a> Basal <a>	Type I cross girdle Prism <a> Rhomb <a> Basal <a>	Type I cross girdle Prism <a> Rhomb <a> Basal <a>	Low T 300-400°C Plane strain
SK26.1	Granite-Gneiss	Single girdle Prism <a> Basal <a>	Single girdle Prism <a> Rhomb <a> Basal <a>	Single girdle Prism <a> Basal <a>	Low T 300-400°C Plane strain
SK57	Granite-Gneiss	Type I cross girdle Prism <a> Rhomb <a> Basal <a>	Type I cross girdle Prism <a> Rhomb <a> Basal <a>	Single girdle Prism <a> Basal <a>	Low T 300-400°C Plane strain
SK58	Granite-Gneiss	Small circles Point maximum Prism <a> Basal <a>			Medium T 450-550°C Flattening strain
SK77.1	Granodiorite-Gneiss	Small circles Basal <a> Rhomb<a>			Medium T 450-550°C Flattening strain
SK78	Granite	Small circles Point maximum Prism <a> Basal <a>			Medium T 450-550°C Flattening strain
SK79	Granodiorite-Gneiss	Type I cross girdle Prism <a> Rhomb <a>			Medium T 300-400°C Plane strain

SK87.1	Granite-Gneiss	Type I crossed girdle Prism <a> Rhomb <a> Basal <a>	Type I crossed girdle Prism <a> Rhomb <a> Basal <a>	Small circles Prism <a> Basal <a>	Low T 300-400°C Constrictional strain
SK93	Tonalite	Type I cross girdle Prism <a> Rhomb <a> Basal <a>	Type I cross girdle Prism <a> Rhomb <a> Basal <a>	Type I cross girdle Prism <a> Rhomb <a> Basal <a>	Low T 300-400°C Plane strain
SK94	Granodiorite-Gneiss	Type I cross girdle Prism <a> Basal <a>	Type I cross girdle Prism <a> Basal <a>	Type I cross girdle Prism <a> Basal <a>	Low T 300-400°C Plane strain
SK95	Granodiorite-Gneiss	Small circles Basal <a>			Medium T 450-550°C Flattening strain
SK96	Tonalite	Type II cross girdle Prism <a> Basal <a>	Type II cross girdle Prism <a> Basal <a>	Type II cross girdle Prism <a> Rhomb <a> Basal <a>	Low T 300-400°C Plane strain
SK97	Tonalite	Type I cross girdle Prism <a> Rhomb <a> Basal <a>			Low T 300-400°C Plane strain
SK99	Granodiorite-Gneiss	Type I cross girdle Prism <a> Rhomb <a> Basal <a>	Type I cross girdle Prism <a> Rhomb <a> Basal <a>	Type I cross girdle Prism <a> Rhomb <a> Basal <a>	Low T 300-400°C Plane strain
SK100	Granite-Gneiss	Single girdle Prism <a> Rhomb <a> Basal <a>	Single girdle Prism <a> Rhomb <a> Basal <a>	Single girdle Prism <a> Rhomb <a> Basal <a>	Low T 300-400°C Plane strain

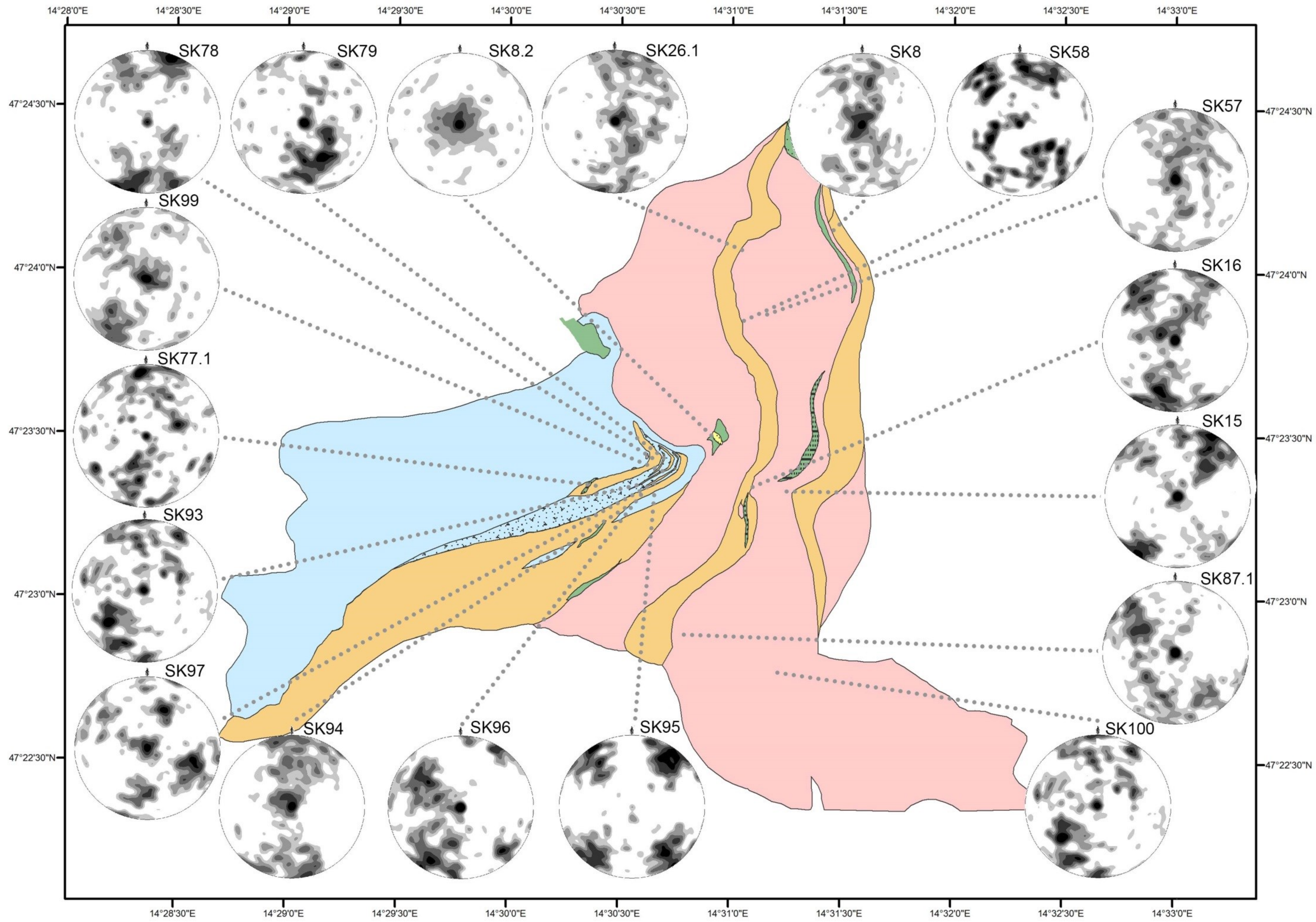
14°28'0"E
14°28'30"E
14°29'0"E
14°29'30"E
14°30'0"E
14°30'30"E
14°31'0"E
14°31'30"E
14°32'0"E
14°32'30"E
14°33'0"E
47°24'30"N
47°24'0"N
47°23'30"N
47°23'0"N
47°22'30"N
SK78
SK79
SK8.2
SK26.1
SK8
SK58
SK57
SK99
SK16
SK77.1
SK15
SK93
SK87.1
SK97
SK94
SK96
SK95
SK100

5.3. Chemical Petrography

As already described in the previous chapter “Materials and Methods”, 44 samples have been geochemically analysed. Results were compared with the optical petrography.

5.3.1. Evaluation of Chemical Data

The chemical data have been evaluated for their correct values to proof if the data set is suitable for a further chemical classification. Therefore the “Harker Diagram” was used to see if the geochemical data follow geochemical trends. First the major oxides and then the trace elements were plotted (Fig. 59). The samples SK79, SK28, SK8_2, SK90, SK88_1 and SK8 have been excluded from the plot because of their exceptional values in several plots. All the data and sample locations can be seen in the attached table in the appendix.

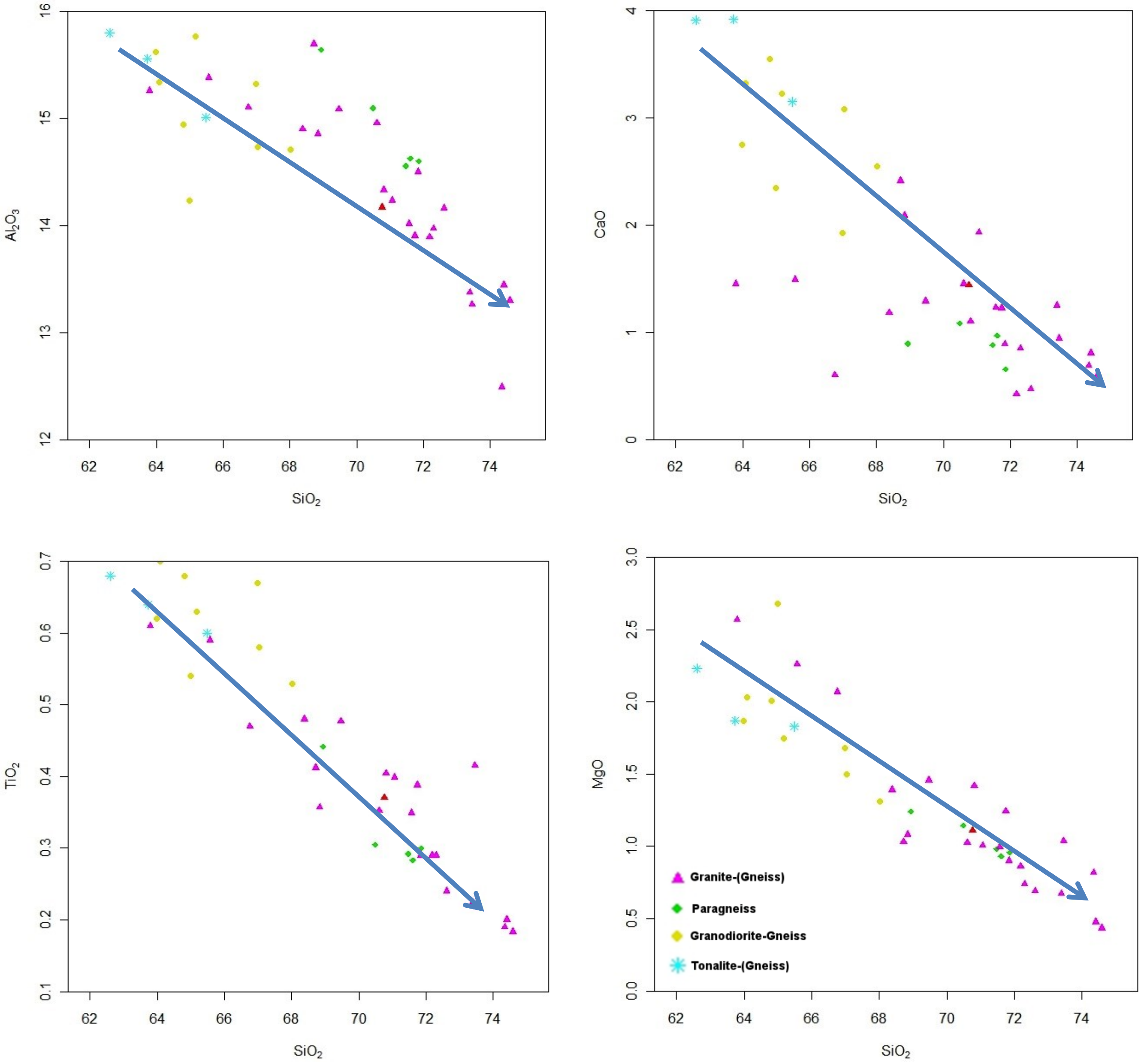

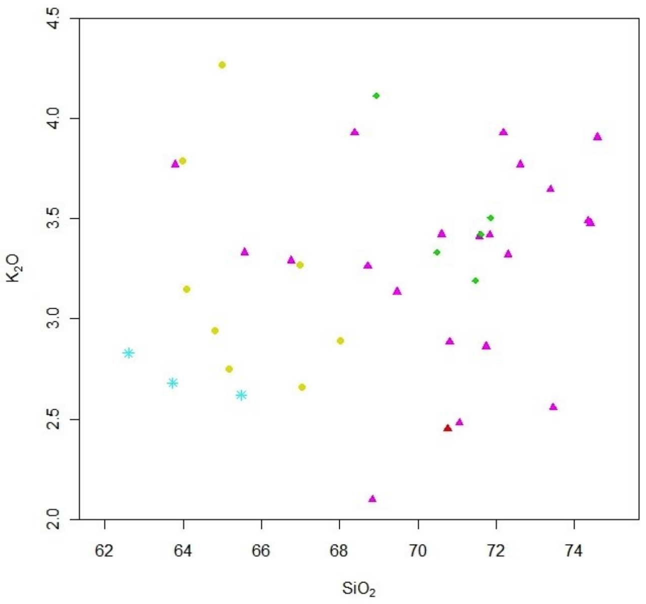
K$_2$O
2.0
2.5
3.0
3.5
4.0
4.5
62
64
66
68
70
72
74
SiO$_2$

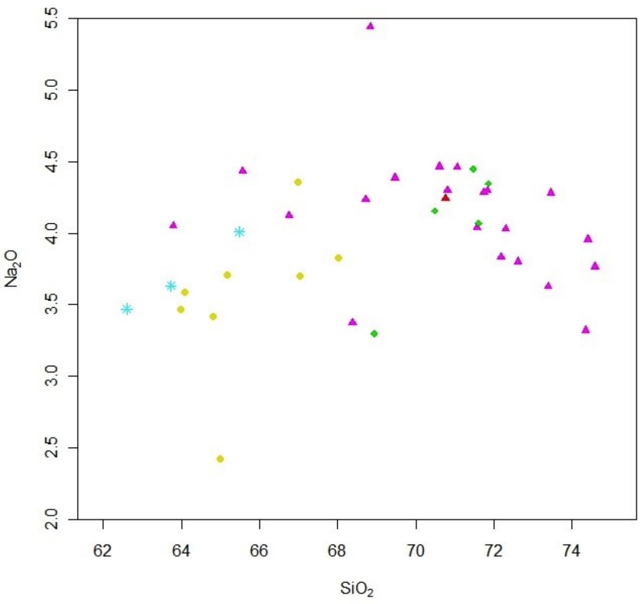
Na$_2$O
2.0
2.5
3.0
3.5
4.0
4.5
5.0
5.5
62
64
66
68
70
72
74
SiO$_2$

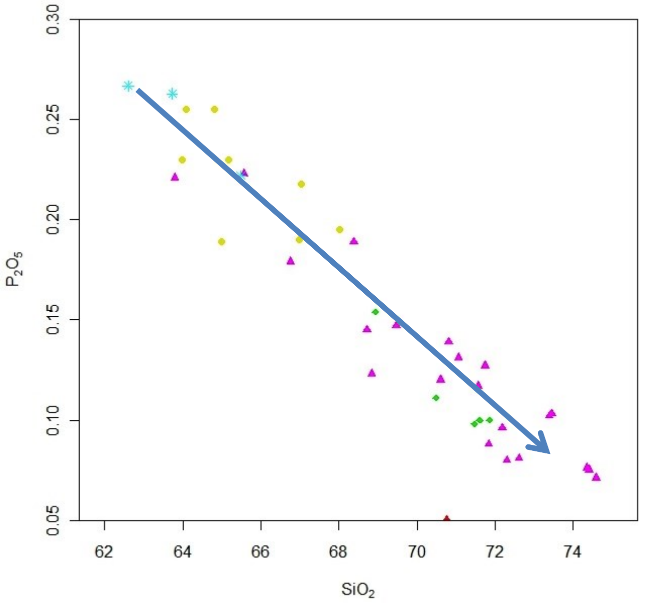
P$_2$O$_5$
0.05
0.10
0.15
0.20
0.25
0.30
62
64
66
68
70
72
74
SiO$_2$

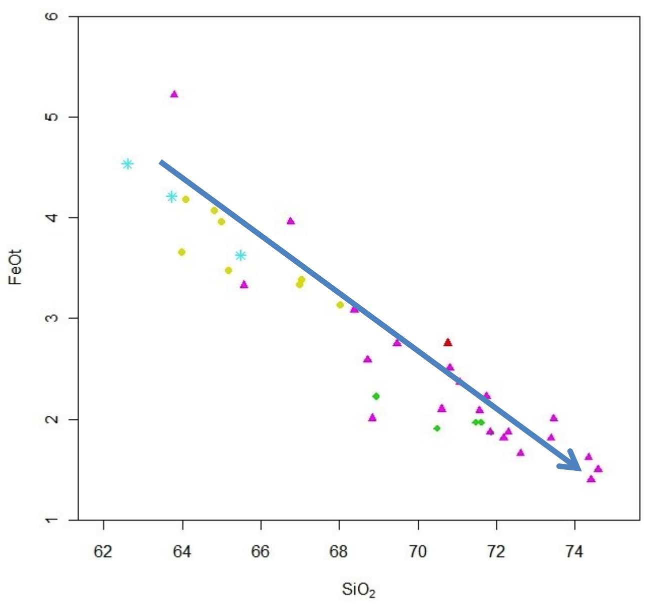
FeOt
1
2
3
4
5
6
62
64
66
68
70
72
74
SiO$_2$

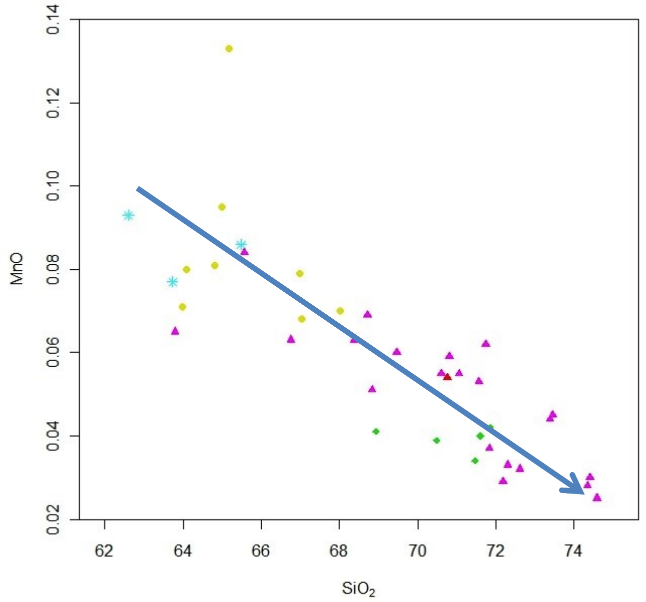
MnO
0.02
0.04
0.06
0.08
0.10
0.12
0.14
62
64
66
68
70
72
74
SiO$_2$

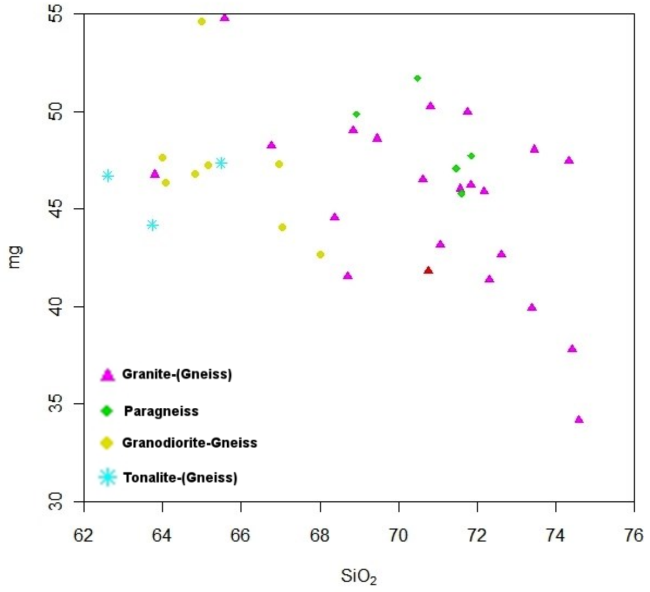
mg
30
35
40
45
50
55
62
64
66
68
70
72
74
76
SiO$_2$
Granite-(Gneiss)
Paragneiss
Granodiorite-Gneiss
Tonalite-(Gneiss)

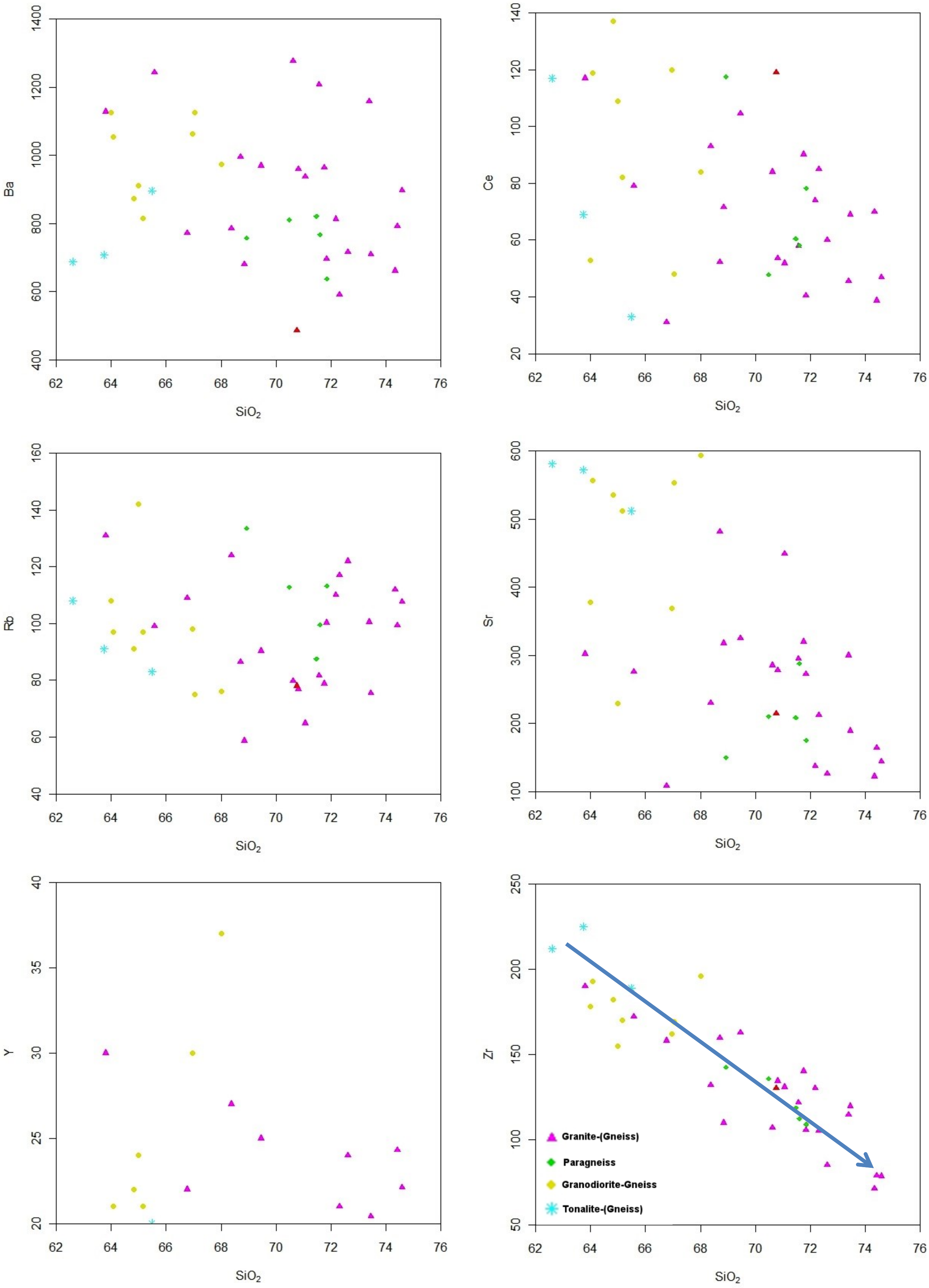
Ba
1400
1200
1000
800
600
400
Ce
140
120
100
80
60
40
20
Rb
160
140
120
100
80
60
40
Sr
600
500
400
300
200
100
Y
40
35
30
25
20
Zr
250
200
150
100
50
62
64
66
68
70
72
74
76
SiO$_2$
Granite-(Gneiss)
Paragneiss
Granodiorite-Gneiss
Tonalite-(Gneiss)

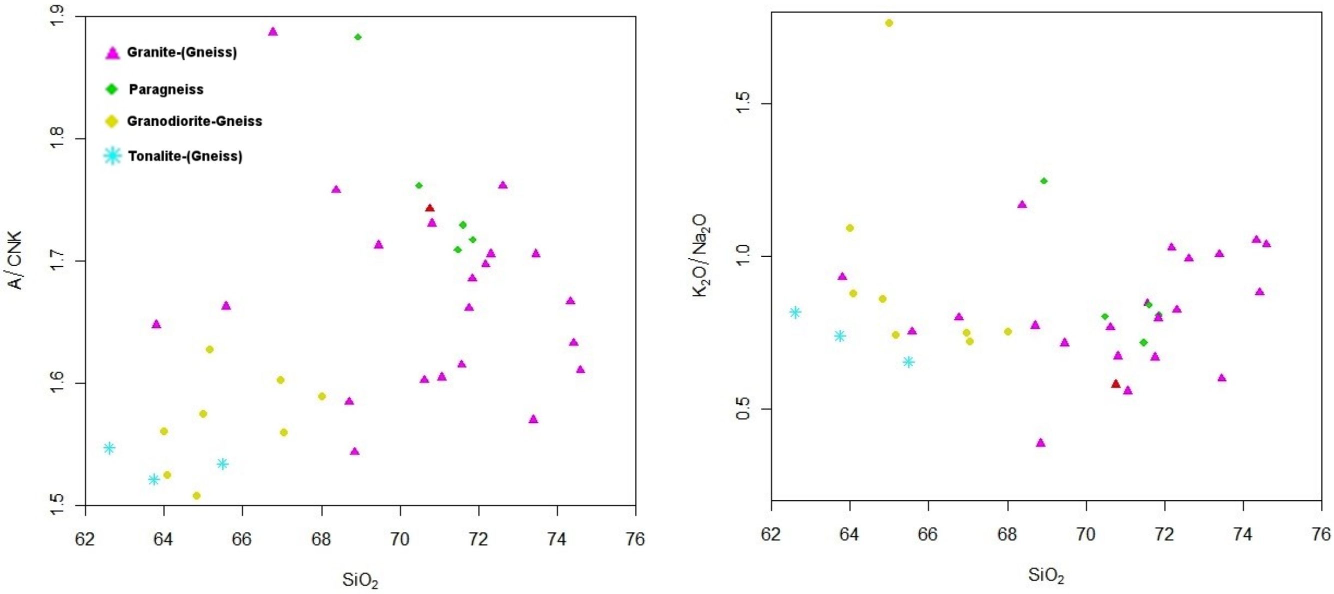

Fig. 59: The pages 77-80 present major elements plotted as wt.% and trace elements as amount in ppm.

As seen in the previous plots, the data follow within the major oxides Al_2O_3, CaO, MgO, TiO_2, P_2O_5, Fe_2O_3 and MnO the typical geochemical trend by increasing SiO_2, except for K_2O and Na_2O. The trace elements do not show any trends except for Zr.

To classify the melting series (Fig. 60) of the samples the plots of Irvine & Barager (1971), Miyashiro (1974) and Peccerillo & Taylor (1976) were chosen. The results show a pure calc-alkaline trend with various variations in the potassium content. Further all samples show a peraluminous character after Shand (1943) and a molar plot of Na_2O-Al_2O_3-K_2O, except for the samples SK9, SK79, SK82, SK93, SK94, SK95 and SK96 which have a metaluminous character after Shand (1943).

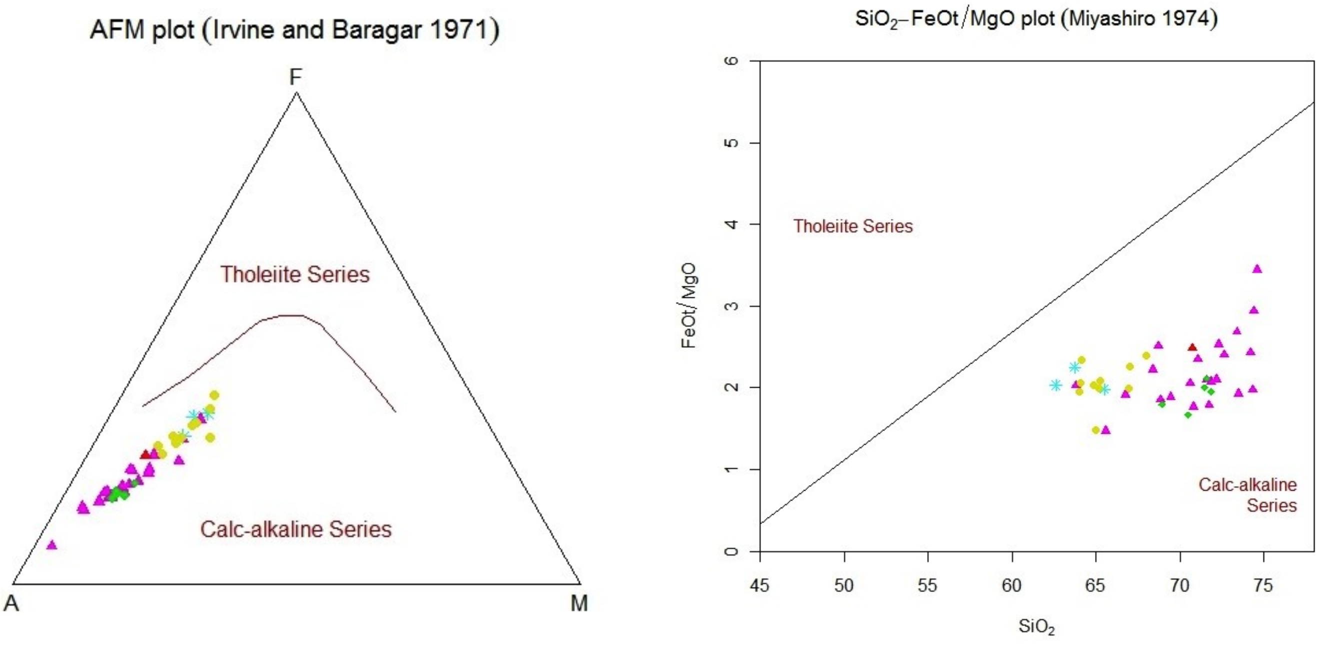

Fig. 60: Classification plots of melting series after Irvine and Baragar (1971) and Miyashiro (1974).

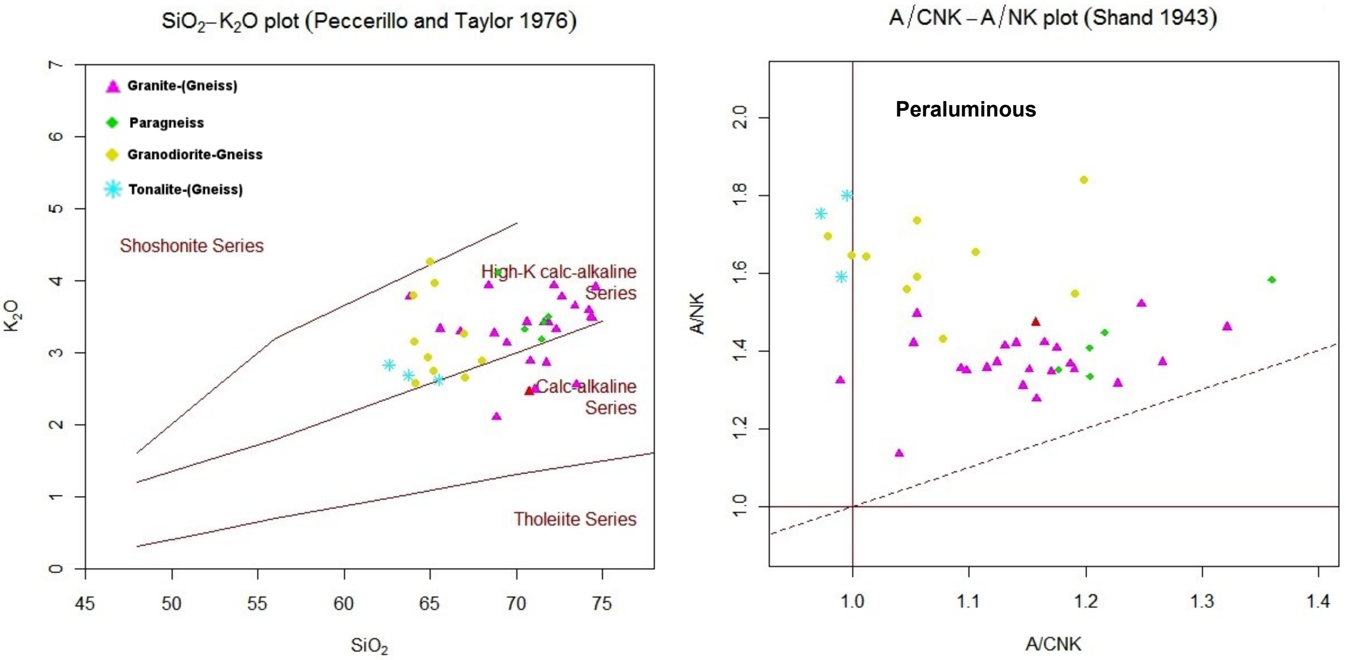

Fig. 61: Plots of the melting series (Irvine & Barager, 1971; Miyashiro, 1974; Peccerillo & Taylor, 1976; Shand, 1943), and categorization into peraluminous (Shand, 1943).

Table 4: Categorization of aluminous character.

Sample	Shand (1943)	Molar Na2O-Al2O3	Sample	Shand (1943)	Molar Na2O-Al2O3
SK3	Peraluminous	Meta-/Peraluminous	**SK26_1**	Peraluminous	Meta-/Peraluminous
SK4	Peraluminous	Meta-/Peraluminous	**SK28**	Peraluminous	Meta-/Peraluminous
SK6	Peraluminous	Meta-/Peraluminous	**SK57**	Peraluminous	Meta-/Peraluminous
SK7	Peraluminous	Meta-/Peraluminous	**SK58**	Peraluminous	Meta-/Peraluminous
SK8.2	Peraluminous	Meta-/Peraluminous	**SK69**	Peraluminous	Meta-/Peraluminous
SK9	Metaluminous	Meta-/Peraluminous	**SK73**	Peraluminous	Meta-/Peraluminous
SK10_1	Peraluminous	Meta-/Peraluminous	**SK77_1**	Peraluminous	Meta-/Peraluminous
SK11	Peraluminous	Meta-/Peraluminous	**SK78**	Peraluminous	Meta-/Peraluminous
SK12_1	Peraluminous	Meta-/Peraluminous	**SK79**	Metaluminous	Meta-/Peraluminous
SK13_1	Peraluminous	Meta-/Peraluminous	**SK82**	Metaluminous	Meta-/Peraluminous
SK15_1	Peraluminous	Meta-/Peraluminous	**SK85**	Peraluminous	Meta-/Peraluminous
SK16	Peraluminous	Meta-/Peraluminous	**SK87**	Peraluminous	Meta-/Peraluminous
SK16_1	Peraluminous	Meta-/Peraluminous	**SK87_1**	Peraluminous	Meta-/Peraluminous
SK16_2	Peraluminous	Meta-/Peraluminous	**SK90**	Peraluminous	Meta-/Peraluminous
SK17_3	Peraluminous	Meta-/Peraluminous	**SK93**	Metaluminous	Meta-/Peraluminous
SK18	Peraluminous	Meta-/Peraluminous	**SK94**	Metaluminous	Meta-/Peraluminous
SK18_1	Peraluminous	Meta-/Peraluminous	**SK95**	Metaluminous	Meta-/Peraluminous
SK19_1	Peraluminous	Meta-/Peraluminous	**SK96**	Metaluminous	Meta-/Peraluminous
SK20	Peraluminous	Meta-/Peraluminous	**SK97**	Peraluminous	Meta-/Peraluminous
SK21_1	Peraluminous	Meta-/Peraluminous	**SK99**	Peraluminous	Meta-/Peraluminous
SK22_1	Peraluminous	Meta-/Peraluminous	**SK100**	Peraluminous	Meta-/Peraluminous

Also another classification (Sylvester, 1989) has proven the calc-alkaline trend and the strong peraluminous character except for SK90 which was determined as alkaline by Sylvester (1989)

5.3.2. Source-Type Classification

The first step to do further investigation was to determine the origin of the samples if they are either orthogenetic or paragenetic. This division has already been done through microscoping and field observation. Therefore further investigations focused on the orthogenetic samples. These were divided by several plots into S-type, I-type and A-type granitoids.

Table 5: Distinction between S- and I-type granitoids (Chappell & White, 2001).

	I-Type Granitoids	**S-Type Granitoids**
CIPW Norm	C<1%	C<1%
A/CNK (Al_2O_3/(2*CaO+Na_2O+K_2O))	>1.1%	<1.1%
SiO_2	65-74%	53-76%
K_2O/Na_2O	High	Low
Chrome and Nickle	High	Low
Al rich minerals	Present	Not present
Hornblende	Not present	Present
Clinopyroxene	Not present	Present
Fe-oxides	Ilmenite	Magnetite

The geochemical distinction between orthogenetic and paragenetic origin (Fig. 62) indicates a strong orthogenetic origin, with minor A-type characteristic. All tonalitic rocks are clearly identified as an I-type origin as well as most of the granodioritic rocks, in contrary to the granitic rocks and paragneisses which plotted mainly within the S-type regime (Fig. 63 and Fig. 64). The final result of the source type classification can be seen in Table 6.

The rock classifications starting with Table 7 and continuing with Table 8 represents the results of different rock classifications used, as written in the tables. Further the magmatic fractionation plot of Imeokparia (1981) was used which indicates that most samples are anomalous granites.

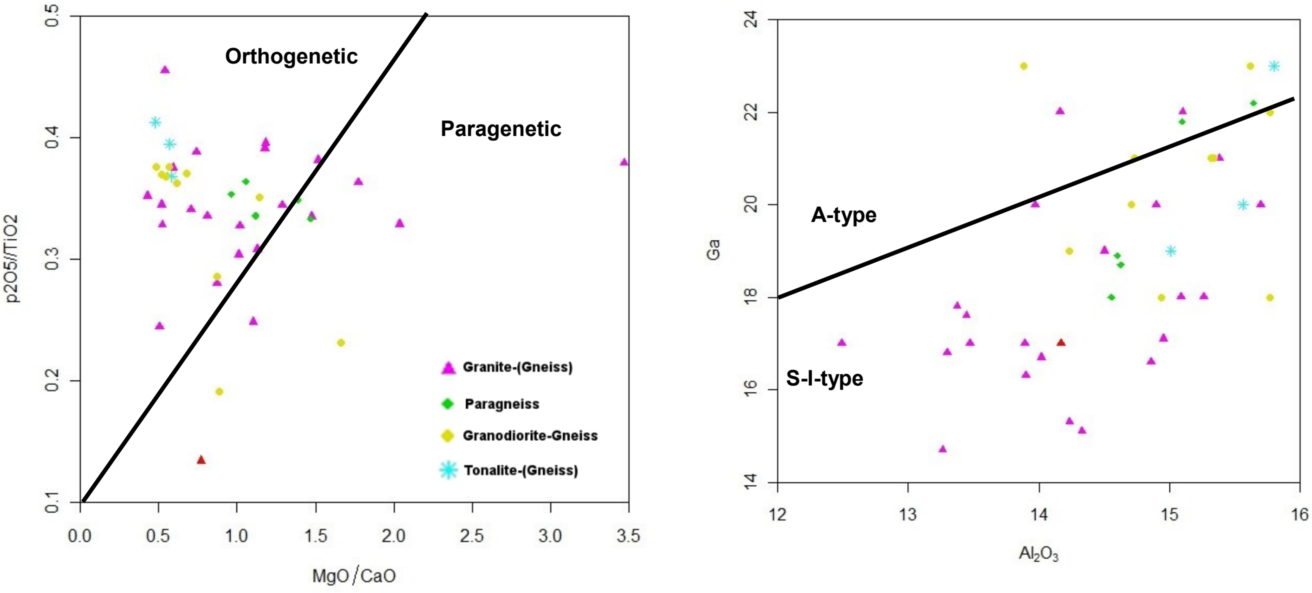

Fig. 62: Chemical distinction between orthogenetic and paragenetic origin. The value of the result is seen as minority (Werner, 1987) (left). Differentiation between A-type and S-I-type.(Collins, Beams, White, & Chappell, 1982) (right).

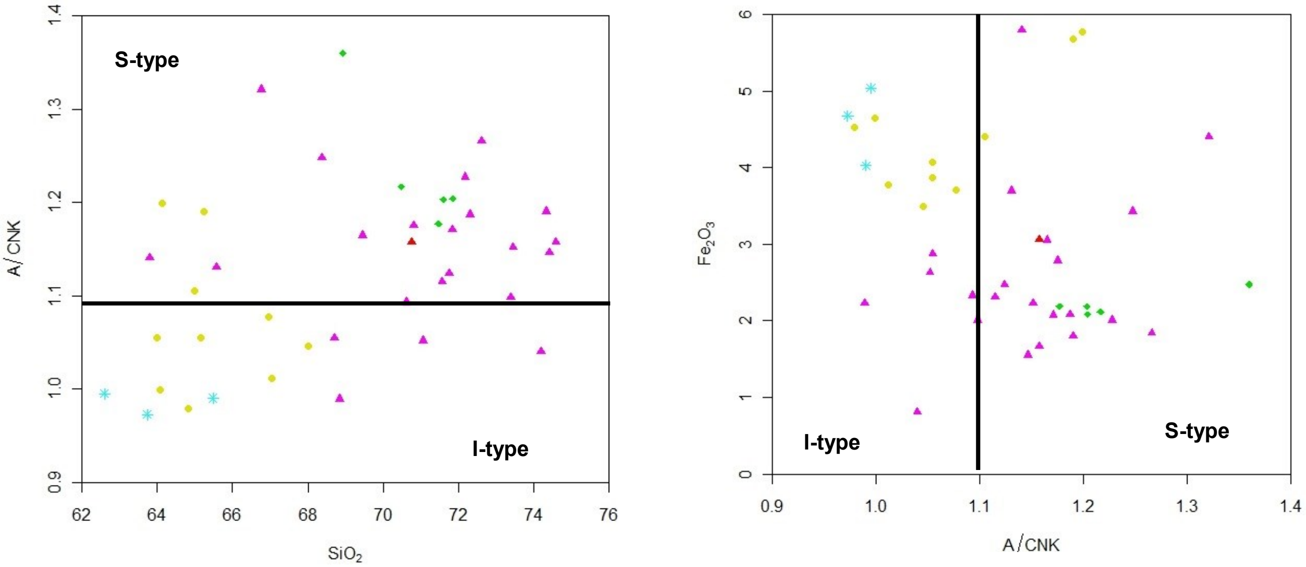

Fig. 63: Further characterisation between S- and I-type granitoids.(Chappell & White, 1974) (left). Another differentiation between S- and I-type (Norman & Leeman, 1992) (right).

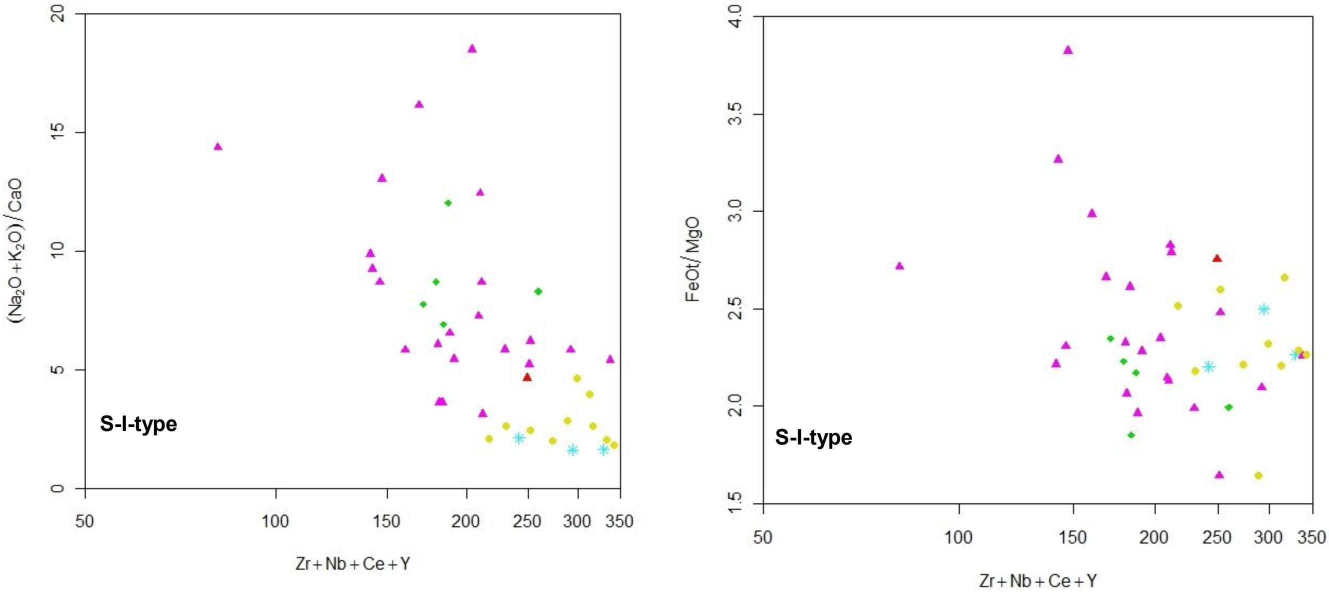

Fig. 64: Further plots to distinct the magmatic source type (Whalen, Curri, & Chappell, 1987).

Table 6: Overview of the source type classification, whereby I = I-type (igneous or meta-igneous rocks), S = S-type (meta-sedimentary), A = A-type (anorogenic and/or anhydrous).

Sample	Chappel et al. (1974)	Collins et al. (1982)	Whalen (1987)	Whalen (1987)	Norman et al. (1992)	Result
SK3	I	S/I	S/I	S/I	I	I
SK4	S	S/I	S/I	S/I	S	S
SK6	S	A	S/I	S/I	S	A
SK7	S	S/I	S/I	S/I	S	S
SK8.2	S	A	S/I	S/I	S	A
SK9	S	S/I	S/I	S/I	S	S
SK10_1	S	S/I	S/I	S/I	S	S
SK11	S	S/I	S/I	S/I	S	S
SK12_1	S	S/I	S/I	S/I	S	S
SK13_1	I	S/I	S/I	S/I	I	I
SK15_1	S	S/I	S/I	S/I	S	S
SK16	I	S/I	S/I	S/I	I	I
SK16_1	I	S/I	S/I	S/I	I	I
SK16_2	I	S/I	S/I	S/I	I	I
SK17_3	S	A	S/I	S/I	S	A
SK18	S	S/I	S/I	S/I	S	S
SK18_1	S	S/I	S/I	S/I	S	S
SK19_1	S	S/I	S/I	S/I	S	S
SK20	I	S/I	S/I	S/I	I	I
SK21_1	S	A	S/I	S/I	S	A
SK22_1	S	A	S/I	S/I	S	A
SK26_1	S	S/I	S/I	S/I	S	S
SK57	S	S/I	S/I	S/I	S	S
SK58	S	S/I	S/I	S/I	S	S
SK69	S	S/I	S/I	S/I	S	S
SK73	S	S/I	S/I	S/I	S	S
SK78	S	S/I	S/I	S/I	S	S
SK79	S	A	S/I	S/I	S	A
SK82	I	A	S/I	S/I	I	A
SK85	I	S/I	S/I	S/I	I	I
SK87	I	A	S/I	S/I	I	A
SK87_1	S	S/I	S/I	S/I	S	S
SK90	I	S/I	S/I	S/I	I	I
SK93	I	S/I	S/I	S/I	I	I
SK94	I	S/I	S/I	S/I	I	I
SK95	I	S/I	S/I	S/I	I	I
SK96	I	A	S/I	S/I	I	A
SK97	I	S/I	S/I	S/I	I	I
SK99	I	A	S/I	S/I	I	A
SK100	S	S/I	S/I	S/I	S	S

5.3.3. Rock Classification

Table 7: Rock classification part 1.

Sample	Microscopy	QAPF	O'Connor (1965)	Cox et al. (1979)	De la Roche et al. (1980)
SK3	Granodiorite-Gneiss	Granodiorite	Granite	Unclassified	Granite
SK4	Granite-Gneiss	Granodiorite	Granite	Unclassified	Granite
SK6	Paragneiss (high mica)	Monzogranite	Granite	Unclassified	Granite
SK7	Granite-Gneiss	Granodiorite	Granite	Unclassified	Granite
SK8	Paragneiss	Alk-Fsp. Granite	Granite	Unclassified	Unclassified
SK8_2	Paragneiss	Alk-Fsp. Granite	Granite	Unclassified	Unclassified
SK8.2	Granite-Gneiss	Granodiorite	Granodiorite	Granite	Granodiorite
SK9	Paragneiss (grained)	Granodiorite	Granite	Unclassified	Granite
SK10_1	Granite-Gneiss	Monzogranite	Granite	Unclassified	Granite
SK11	Granite-Gneiss	Granodiorite	Granite	Unclassified	Granite
SK12_1	Granodiorite-Gneiss	Granodiorite	Granite	Unclassified	Granite
SK13_1	Granodiorite-Gneiss	Granodiorite	Granite	Unclassified	Granodiorite
SK15_1	Granite-Gneiss	Granodiorite	Granite	Unclassified	Granite
SK16	Granite-Gneiss	Granodiorite	Granite	Unclassified	Granodiorite
SK16_1	Granite-Gneiss	Granodiorite	Granite	Unclassified	Granite
SK16_2	Granite-Gneiss	Granodiorite	Granite	Unclassified	Granodiorite
SK17_3	Paragneiss (grained)	Granodiorite	Granite	Unclassified	Granite
SK18	Paragneiss (grained)	Granodiorite	Granite	Unclassified	Granite
SK18_1	Paragneiss (high mica)	Granodiorite	Granite	Unclassified	Granite
SK19_1	Tonalite-Gneiss	Granodiorite	Granite	Unclassified	Granite
SK20	Granite-Gneiss	Granodiorite	Granodiorite	Granite	Granodiorite
SK21_1	Granodiorite-Gneiss	Granodiorite	Granite	Unclassified	Granite
SK22_1	Granodiorite-Gneiss	Granodiorite	Granite	Unclassified	Granite
SK26_1	Granite-Gneiss	Granodiorite	Granite	Unclassified	Granite
SK28	Amphibolite	Tonalite	Unclassified	Gabbro	Gabbro
SK57	Granodiorite-Gneiss	Granodiorite	Granite	Granite	Granite
SK58	Granodiorite-Gneiss	Monzogranite	Granite	Unclassified	Granite
SK69	Paragneiss (grained)	Granodiorite	Quartz monzonite	Granite	Granodiorite
SK73	Granodiorite-Gneiss	Granodiorite	Granite	Unclassified	Granite
SK77_1	Paragneiss (high mica)	Granodiorite	Granodiorite	Granite	Granodiorite
SK78	Granodiorite-Gneiss	Granodiorite	Granite	Unclassified	Granite
SK79	Granite-Gneiss	Granodiorite	Granite	Granite	Granite
SK82	Granite-Gneiss	Granodiorite	Granite	Granite	Granite
SK85	Granite-Gneiss	Granodiorite	Trondhjemite	Unclassified	Granite
SK87	Tonalite	Granodiorite	Granite	Granite	Granodiorite
SK87_1	Granite-Gneiss	Granodiorite	Granite	Unclassified	Granite
SK90	Quartzite	Granodiorite	Granite	Unclassified	Alkali Granite
SK93	Tonalite	Granodiorite	Granodiorite	Granite	Tonalite
SK94	Granodiorite-Gneiss	Granodiorite	Granodiorite	Granite	Granodiorite
SK95	Granite-Gneiss	Granodiorite	Granodiorite	Granite	Granodiorite

SK96	Tonalite	Granodiorite	Granodiorite	Granite	Tonalite
SK97	Tonalite	Granodiorite	Granodiorite	Granite	Tonalite
SK99	Granodiorite-Gneiss	Granodiorite	Quartz monzonite	Granite	Granodiorite
SK100	Granodiorite-Gneiss	Granodiorite	Granite	Granite	Granite

Table 8: Rock classification part 2.

Sample	**Middlemost (1985)**	**Debon and le Fort (1986)**	**Debeon le fort (1986)**	**Middlemost (1994)**	**Result**
SK3	Granite	Adamellite	Peraluminous with biotite > muscovite	Granite	**Granite-Gneiss**
SK4	Granite	Granodiorite	Peraluminous with biotite > muscovite	Granite	**Granite-Gneiss**
SK6	Granite	Adamellite	Peraluminous with two-mica (muscovite > biotite)	Granite	**Paragneiss**
SK7	Granite	Granodiorite	Peraluminous with biotite > muscovite	Granite	**Granite-Gneiss**
SK8	Granite	Unclassified	Peraluminous with two-mica (muscovite > biotite)	Unclassified	**Paragneiss**
SK8_2	Granite	Unclassified	Peraluminous with two-mica (muscovite > biotite)	Unclassified	**Paragneiss**
SK8.2	Granodiorite	Granodiorite	Peraluminous with biotite	Granodiorite	**Granodiorite-Gneiss**
SK9	Granite	Granodiorite	Peraluminous with biotite > muscovite	Granite	**Paragneiss**
SK10_1	Granite	Adamellite	Peraluminous with biotite > muscovite	Granite	**Granite-Gneiss**
SK11	Granite	Adamellite	Peraluminous with biotite > muscovite	Granite	**Granite-Gneiss**
SK12_1	Granite	Granodiorite	Peraluminous with biotite > muscovite	Granite	**Granite-Gneiss**
SK13_1	Granodiorite	Granodiorite	Peraluminous with biotite	Granite	**Granodiorite-Gneiss**
SK15_1	Granite	Granodiorite	Peraluminous with biotite > muscovite	Granite	**Granite-Gneiss**
SK16	Granite	Granodiorite	Peraluminous with biotite	Granite	**Granite-Gneiss**
SK16_1	Granite	Granodiorite	Peraluminous with biotite > muscovite	Granite	**Granite-Gneiss**
SK16_2	Granite	Granodiorite	Peraluminous with biotite	Granite	**Granite-Gneiss**
SK17_3	Granite	Granodiorite	Peraluminous with biotite > muscovite	Granite	**Paragneiss**
SK18	Granite	Granodiorite	Peraluminous with biotite > muscovite	Granite	**Paragneiss**

SK18_1	Granite	Granodiorite	Peraluminous with biotite > muscovite	Granite	**Paragneiss**
SK19_1	Granite	Granodiorite	Peraluminous with biotite > muscovite	Granite	**Granite-Gneiss**
SK20	Granodiorite	Granodiorite	Peraluminous with biotite	Granodiorite	**Granodiorite-Gneiss**
SK21_1	Granite	Adamellite	Peraluminous with two-mica (muscovite > biotite)	Granite	**Granite-Gneiss**
SK22_1	Granite	Granodiorite	Peraluminous with biotite > muscovite	Granite	**Granite-Gneiss**
SK26_1	Granite	Adamellite	Peraluminous with biotite > muscovite	Granite	**Granite-Gneiss**
SK28	Gabbro	Gabbro	Metaluminous with biotite +/-amphibolite +/-orthopyroxene +/-clinopyroxene	Unclassified	**Amphibolite**
SK57	Quartz monzonite	Granodiorite	Peraluminous with biotite	Granite	**Granite-Gneiss**
SK58	Granite	Adamellite	Peraluminous with biotite > muscovite	Granite	**Granite-Gneiss**
SK69	Granodiorite	granite	Peraluminous with biotite	Granodiorite	**Granodiorite-Gneiss**
SK73	Granite	Adamellite	Peraluminous with biotite > muscovite	Granite	**Granite-Gneiss**
SK77_1	Granodiorite	Granodiorite	Peraluminous with biotite	Granodiorite	**Granodiorite-Gneiss**
SK78	Granite	Granodiorite	Peraluminous with biotite > muscovite	Granodiorite	**Granit**
SK79	Granodiorite	Granite	Peraluminous with biotite	granodiorite	**Granodiorite-Gneiss**
SK82	Granodiorite	Adamellite	Peraluminous with biotite > muscovite	Granite	**Granite-Gneiss**
SK85	Granite	Tonalite	Metaluminous with biotite +/-amphibolite +/-orthopyroxene +/-clinopyroxene	Granite	**Granite-Gneiss**
SK87	Granodiorite	Granodiorite	Peraluminous with biotite	Granodiorite	**Granodiorite-Gneiss**
SK87_1	Granite	Granodiorite	Peraluminous with biotite > muscovite	Granite	**Granite-Gneiss**
SK90	Granite	Granodiorite	Peraluminous with biotite > muscovite	Granite	**Granite-Gneiss**
SK93	Granodiorite	Granodiorite	Metaluminous with biotite +/-amphibolite +/-orthopyroxene +/-clinopyroxene	Granodiorite	**Tonalite**

SK94	Granodiorite	Granodiorite	Metaluminous with biotite +/-amphibolite +/-orthopyroxene +/-clinopyroxene	Granodiorite	**Granodiorite-Gneiss**
SK95	Granodiorite	Granodiorite	Metaluminous with biotite +/-amphibolite +/-orthopyroxene +/-clinopyroxene	Granodiorite	**Granodiorite-Gneiss**
SK96	Granodiorite	Granodiorite	Metaluminous with biotite +/-amphibolite +/-orthopyroxene +/-clinopyroxene	Granodiorite	**Tonalite**
SK97	Granodiorite	Granodiorite	Metaluminous with biotite +/-amphibolite +/-orthopyroxene +/-clinopyroxene	Granodiorite	**Tonalite**
SK99	Granodiorite	Adamellite	Peraluminous with biotite	Granodiorite	**Granodiorite-Gneiss**
SK100	Quartz monzonite	Adamellite	Peraluminous with biotite	Quartz monzonite	**Granite-Gneiss**

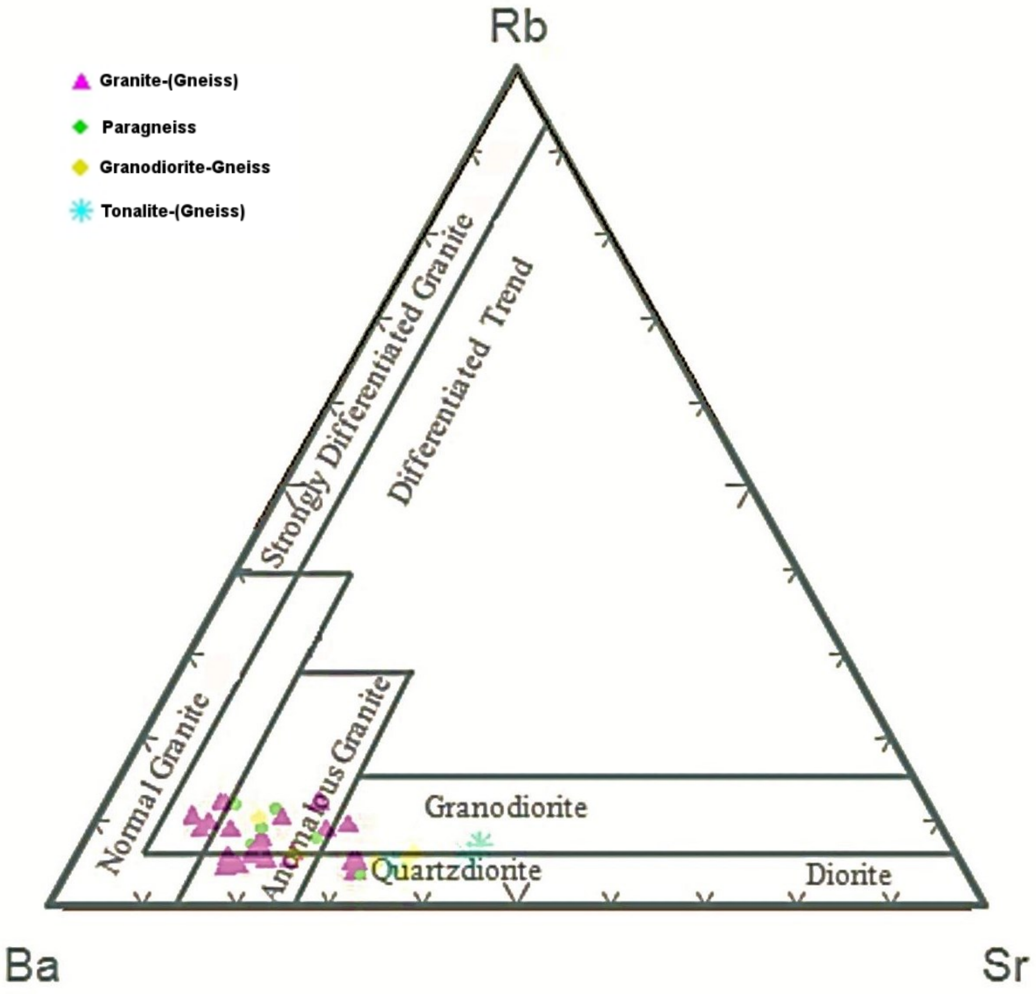

Fig. 65: Ba, Sr and Rb plot as indicator of magmatic fractionation (Imeokparia, 1981).

5.3.4. Geotectonic Positioning

To determine the difference between ORG (ocean ridge granites), WPG (within plate granites) and VAG (volcanic arc granites), syn-COLG (syn-collision granites), Nb versus SiO_2 should be plotted. Because all samples show a Nb content of <20 ppm, this plot has not been made, because they automatically are classified as VAG/syn-COLG/ORG group (Pearce, Harris, & Tindle, 1984). Therefore the data has only been plotted in a SiO_2 versus Rb/Zr plot.

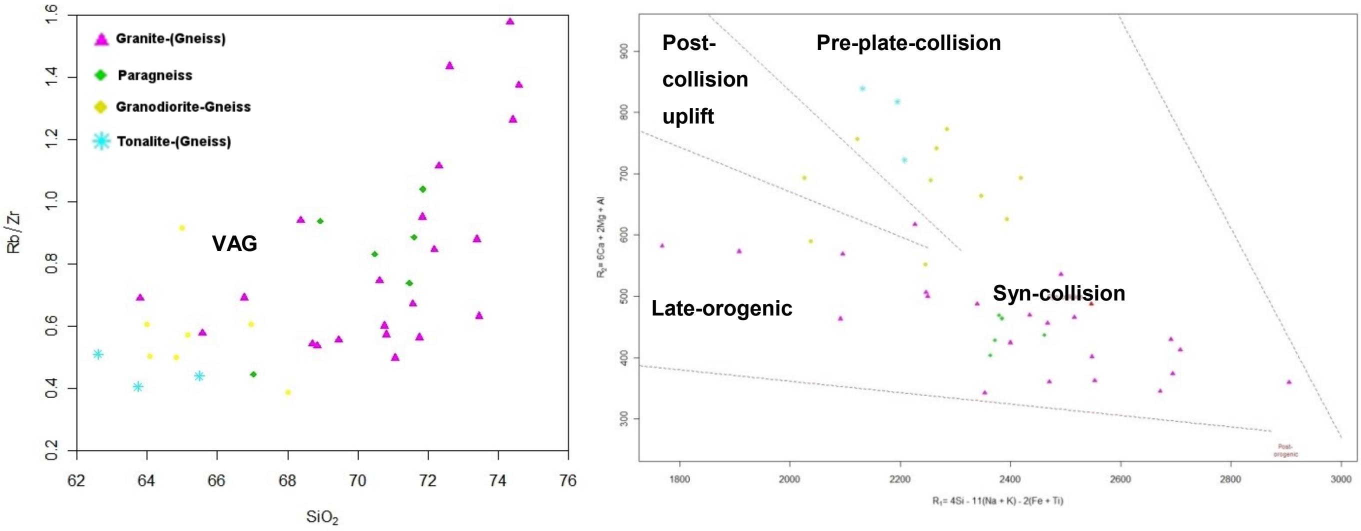

Fig. 66: Geotectonic characterisation(Harris, Pearce, & Tindle, 1986) (left) and (Batchelor & Bowden, 1985) (right). VAG =volcanic arc granites.

After the geotectonic classification plots all data is classified as volcanic arc, but they show different stages going from pre-plate-collision to late-orogenic. The individual result of each sample is seen in the following (Table 9).

Table 9: Individual results of the geotectonic classification whereby IAG = island arc granitoids, CAG = continental arc granitoids, CCG = continental collisional granitoids, RRG = rift-related granitoids, CEU = continental epeirogenic uplift granitoids, POG = post-orogenic granitoids, VAG = volcanic arc granite.

Sample	Maniar & Piccoli (1989)		Harris et al. (1986)	Batchelor et al. (1985)
	K_2O / SiO_2	AFM	Rb/Zr	R1-R2
SK3	IAG+CAG+CCG+ RRG+CEUG POG	IAG+CAG+CCG	VAG	Syn-collision
SK4	IAG+CAG+CCG+ RRG+CEUG POG	IAG+CAG+CCG	VAG	Syn-collision
SK6	IAG+CAG+CCG+ RRG+CEUG POG	IAG+CAG+CCG	VAG	Syn-collision
SK7	IAG+CAG+CCG+ RRG+CEUG POG	IAG+CAG+CCG	VAG	Syn-collision
SK8.2	IAG+CAG+CCG+ RRG+CEUG POG	IAG+CAG+CCG	VAG	Pre-plate collision

SK9	IAG+CAG+CCG+RRG+CEUG POG	IAG+CAG+CCG	VAG	Syn-collision
SK10_1	IAG+CAG+CCG+RRG+CEUG POG	IAG+CAG+CCG	VAG	Syn-collision
SK11	IAG+CAG+CCG+RRG+CEUG POG	IAG+CAG+CCG	VAG	Syn-collision
SK12_1	IAG+CAG+CCG+RRG+CEUG POG	IAG+CAG+CCG	VAG	Syn-collision
SK13_1	IAG+CAG+CCG+RRG+CEUG POG	IAG+CAG+CCG	VAG	Late orogenic
SK15_1	IAG+CAG+CCG+RRG+CEUG POG	IAG+CAG+CCG	VAG	Syn-collision
SK16	IAG+CAG+CCG+RRG+CEUG POG	IAG+CAG+CCG	VAG	Syn-collision
SK16_1	IAG+CAG+CCG+RRG+CEUG POG	IAG+CAG+CCG	VAG	Syn-collision
SK16_2	IAG+CAG+CCG+RRG+CEUG POG	IAG+CAG+CCG	VAG	Post-collision uplift
SK17_3	IAG+CAG+CCG+RRG+CEUG POG	IAG+CAG+CCG	VAG	Syn-collision
SK18	IAG+CAG+CCG+RRG+CEUG POG	IAG+CAG+CCG	VAG	Syn-collision
SK18_1	IAG+CAG+CCG+RRG+CEUG POG	IAG+CAG+CCG	VAG	Syn-collision
SK19_1	IAG+CAG+CCG+RRG+CEUG POG	IAG+CAG+CCG	VAG	Syn-collision
SK20	IAG+CAG+CCG+RRG+CEUG POG	IAG+CAG+CCG	VAG	Pre-plate collision
SK21_1	IAG+CAG+CCG+RRG+CEUG POG	IAG+CAG+CCG	VAG	Syn-collision
SK22_1	IAG+CAG+CCG+RRG+CEUG POG	IAG+CAG+CCG	VAG	Syn-collision
SK26_1	IAG+CAG+CCG+RRG+CEUG POG	IAG+CAG+CCG	VAG	Post-orogenic
SK57	IAG+CAG+CCG+RRG+CEUG POG	IAG+CAG+CCG	VAG	Late orogenic
SK58	IAG+CAG+CCG+RRG+CEUG POG	IAG+CAG+CCG	VAG	Syn-collision

SK69	IAG+CAG+CCG+ RRG+CEUG POG	IAG+CAG+CCG	VAG	Pre-plate collision
SK73	IAG+CAG+CCG+ RRG+CEUG POG	IAG+CAG+CCG	VAG	Syn-collision
SK78	IAG+CAG+CCG+ RRG+CEUG POG	IAG+CAG+CCG	VAG	Syn-collision
SK79	IAG+CAG+CCG+ RRG+CEUG POG	IAG+CAG+CCG	VAG	Late-orogenic
SK82	IAG+CAG+CCG+ RRG+CEUG POG	IAG+CAG+CCG	VAG	Late orogenic
SK85	IAG+CAG+CCG+ RRG+CEUG POG	IAG+CAG+CCG	VAG	Late-orogenic
SK87	IAG+CAG+CCG+ RRG+CEUG POG	IAG+CAG+CCG	VAG	Pre-plate collision
SK87_1	IAG+CAG+CCG+ RRG+CEUG POG	IAG+CAG+CCG	VAG	Syn-collision
SK93	IAG+CAG+CCG+ RRG+CEUG POG	IAG+CAG+CCG	VAG	Pre-plate collision
SK94	IAG+CAG+CCG+ RRG+CEUG POG	IAG+CAG+CCG	VAG	Pre-plate collision
SK95	IAG+CAG+CCG+ RRG+CEUG POG	IAG+CAG+CCG	VAG	Pre-plate collision
SK96	IAG+CAG+CCG+ RRG+CEUG POG	IAG+CAG+CCG	VAG	Pre-plate collision
SK97	IAG+CAG+CCG+ RRG+CEUG POG	IAG+CAG+CCG	VAG	Pre-plate collision
SK99	IAG+CAG+CCG+ RRG+CEUG POG	IAG+CAG+CCG	VAG	Post-collision uplift
SK100	IAG+CAG+CCG+ RRG+CEUG POG	IAG+CAG+CCG	VAG	Late-orogenic

The majority of the samples (22) have been classified as syn-collision, followed by pre-plate collision (8), late-orogenic (4), post-collision uplift (2) and one post-orogenic. The data points with their according geotectonic position were printed with ArcMap for a better display of the geographic position. The according graphic is seen on the following page (Fig. 67).

Table 10: Summary of geochemical evaluation whereby I = I-type (igneous or meta-igneous rocks), S = S-type (meta-sedimentary), A = A-type (anorogenic and/or anhydrous).

Sample	Aluminous character	Tectonic position	Source type	Rock type
SK3	Peraluminous	Syn-collision	I	**Granite-Gneiss**
SK4	Peraluminous	Syn-collision	S	**Granite-Gneiss**
SK6	Peraluminous	Syn-collision	A	**Paragneiss**
SK7	Peraluminous	Syn-collision	S	**Granite-Gneiss**
SK8.2	Peraluminous	Pre-plate collision	A	**Granodiorite-Gneiss**
SK9	Metaluminous	Syn-collision	S	**Paragneiss**
SK10_1	Peraluminous	Syn-collision	S	**Granite-Gneiss**
SK11	Peraluminous	Syn-collision	S	**Granite-Gneiss**
SK12_1	Peraluminous	Syn-collision	S	**Granite-Gneiss**
SK13_1	Peraluminous	Late orogenic	I	**Granodiorite-Gneiss**
SK15_1	Peraluminous	Syn-collision	S	**Granite-Gneiss**
SK16	Peraluminous	Syn-collision	I	**Granite-Gneiss**
SK16_1	Peraluminous	Syn-collision	I	**Granite-Gneiss**
SK16_2	Peraluminous	Post-collision uplift	I	**Granite-Gneiss**
SK17_3	Peraluminous	Syn-collision	A	**Paragneiss**
SK18	Peraluminous	Syn-collision	S	**Paragneiss**
SK18_1	Peraluminous	Syn-collision	S	**Paragneiss**
SK19_1	Peraluminous	Syn-collision	S	**Granite-Gneiss**
SK20	Peraluminous	Pre-plate collision	I	**Granodiorite-Gneiss**
SK21_1	Peraluminous	Syn-collision	A	**Granite-Gneiss**
SK22_1	Peraluminous	Syn-collision	A	**Granite-Gneiss**
SK26_1	Peraluminous	Post-orogenic	S	**Granite-Gneiss**
SK57	Peraluminous	Late orogenic	S	**Granite-Gneiss**
SK58	Peraluminous	Syn-collision	S	**Granite-Gneiss**
SK69	Peraluminous	Pre-plate collision	S	**Granodiorite-Gneiss**
SK73	Peraluminous	Syn-collision	S	**Granite-Gneiss**
SK78	Peraluminous	Syn-collision	S	**Granite-Gneiss**
SK79	Metaluminous	Late-orogenic	A	**Granodiorite-Gneiss**
SK82	Metaluminous	Late orogenic	A	**Granite-Gneiss**
SK85	Peraluminous	Late-orogenic	I	**Granite-Gneiss**
SK87	Peraluminous	Pre-plate collision	A	**Granodiorite-Gneiss**
SK87_1	Peraluminous	Syn-collision	S	**Granite-Gneiss**
SK93	Metaluminous	Pre-plate collision	I	**Tonalite**
SK94	Metaluminous	Pre-plate collision	I	**Granodiorite-Gneiss**
SK95	Metaluminous	Pre-plate collision	I	**Granodiorite-Gneiss**
SK96	Metaluminous	Pre-plate collision	A	**Tonalite**

SK97	Peraluminous	Pre-plate collision	I	**Tonalite**
SK99	Peraluminous	Post-collision uplift	A	**Granodiorite-Gneiss**
SK100	Peraluminous	Late-orogenic	S	**Granite-Gneiss**

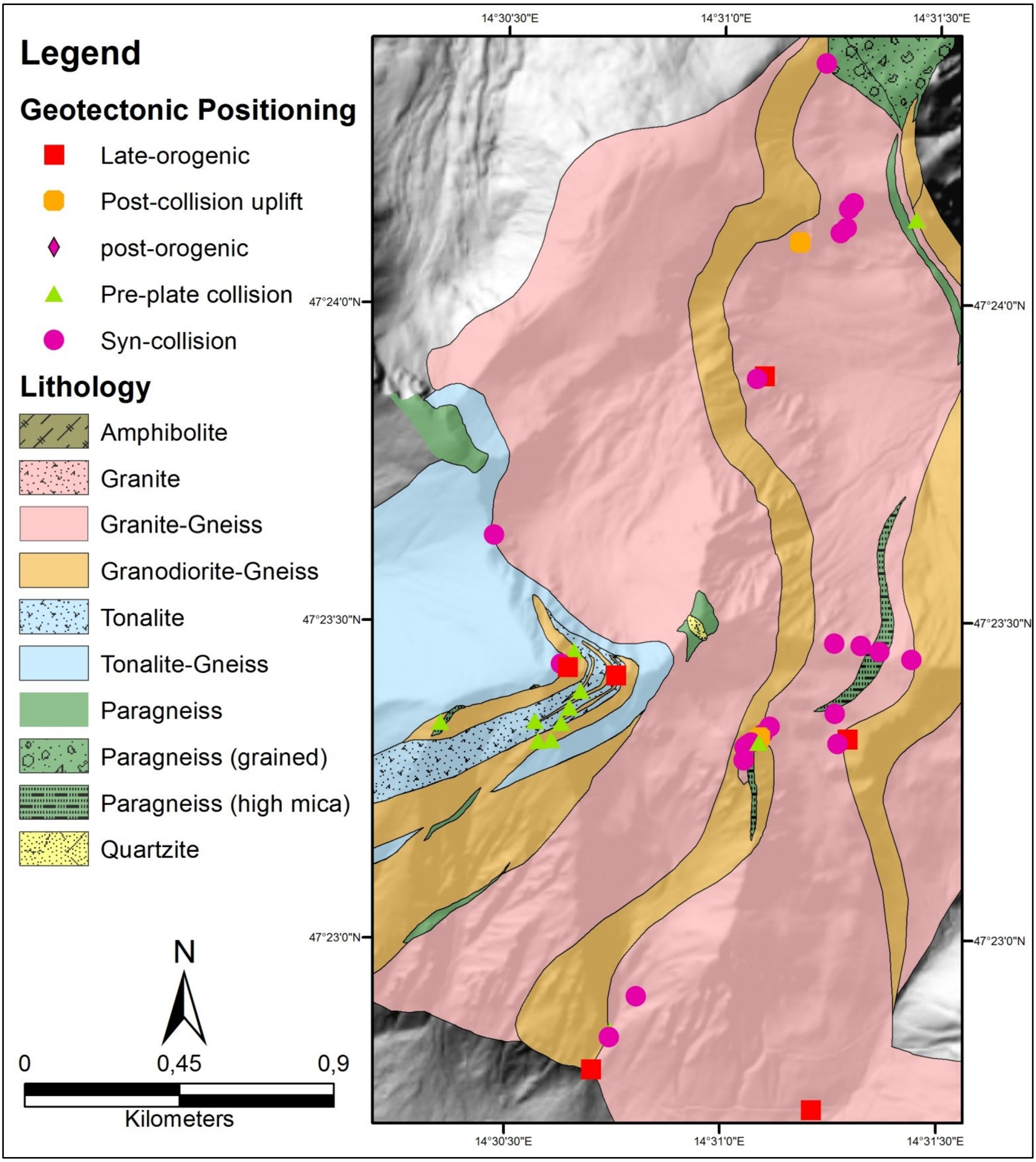

Fig. 67: Illustration of the geotectonic position results within the study area.

5.3.5. Chemical Signature of Zircon Samples

Those samples, which were used for radiometric dating, are listed separately. The following table (Table 11) and graphics show the rock type classification and the Harker diagrams.

Table 11: Overview of the zircon samples. VAG = volcanic arc granites.

Sample	Rock type	Harris et al. (1986)	Batchelor et al. (1985)
SK16_2	Granite-Gneiss	VAG	Post-collision uplift
SK79	Granodiorite-Gneiss	VAG	Late-orogenic
SK87_1	Granite-Gneiss	VAG	Syn-collision
SK95	Granodiorite-Gneiss	VAG	Pre-plate collision
SK96	Tonalite	VAG	Pre-plate collision
SK97	Tonalite	VAG	Pre-plate collision
SK99	Granodiorite-Gneiss	VAG	Post-collision uplift
SK100	Granite-Gneiss	VAG	Late-orogenic

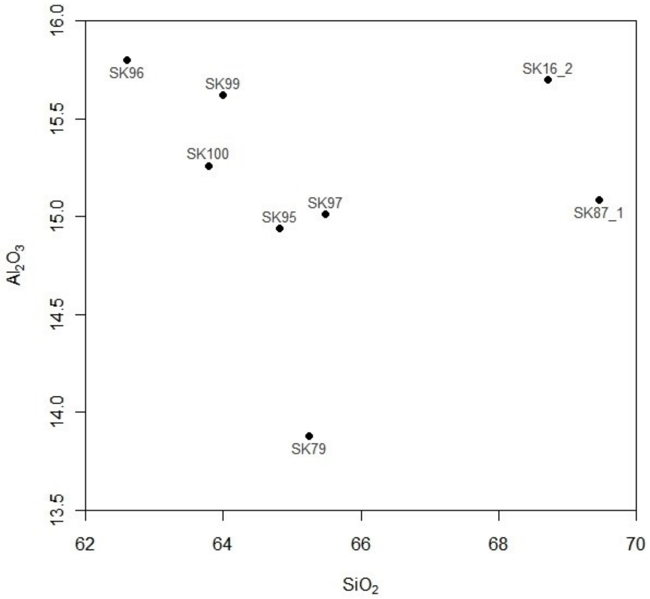

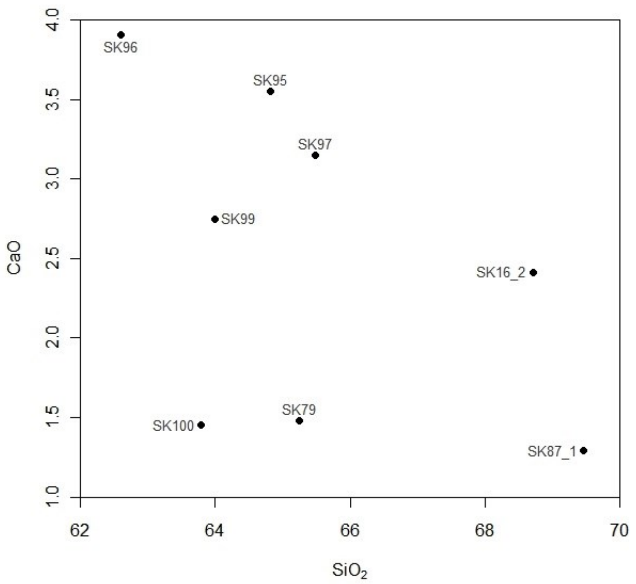

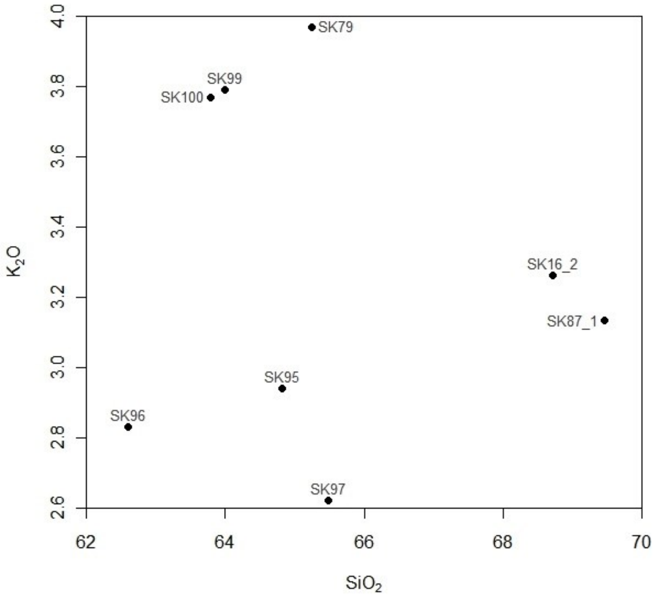

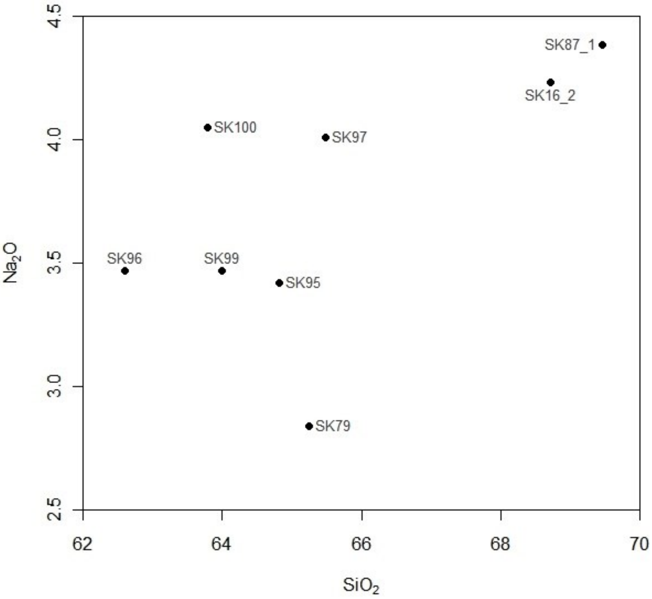

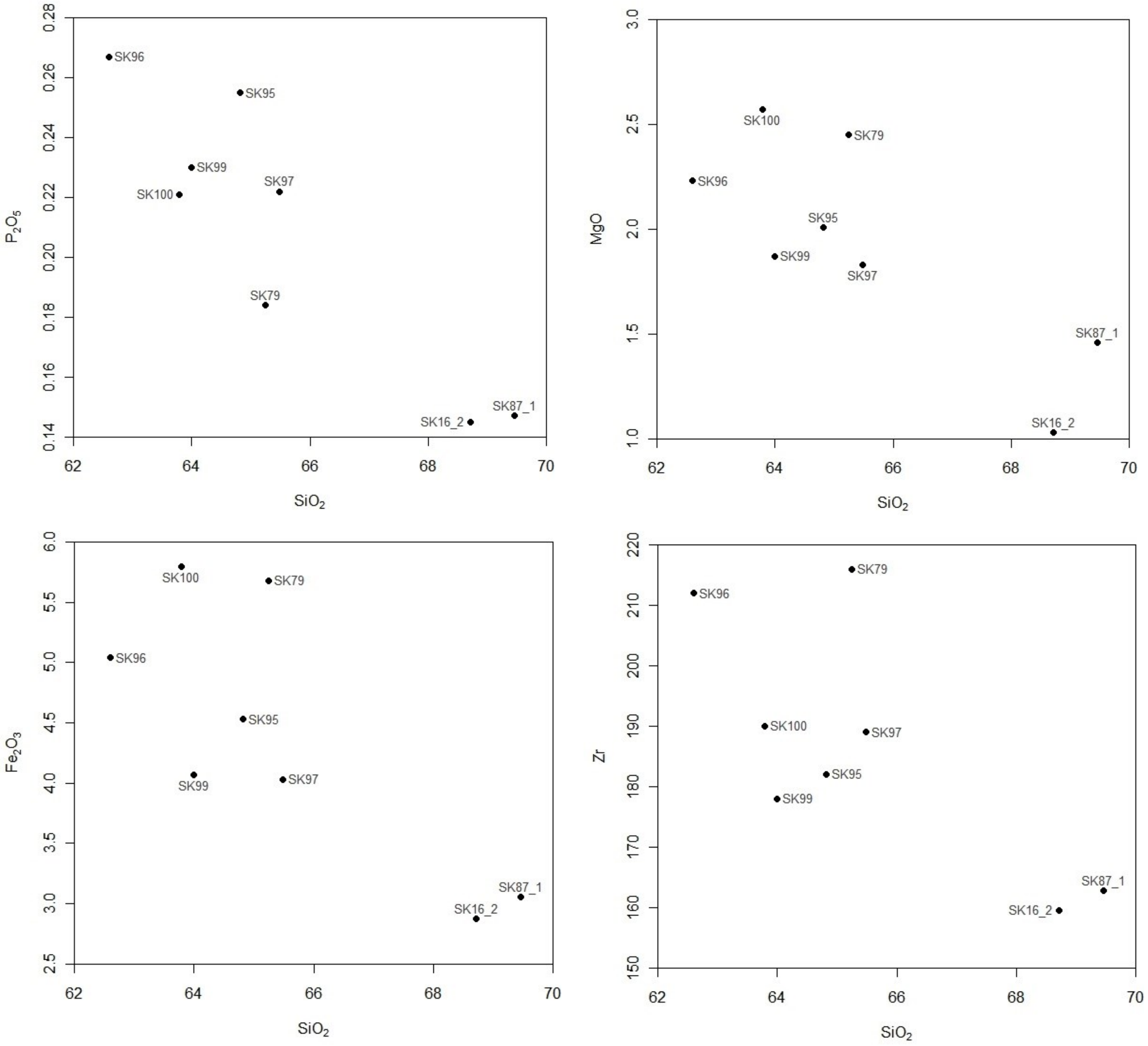

Fig. 68: Harker diagrams for samples used for zircon dating. Major elements in wt.%, trace elements in ppm.

Table 12: Newly evaluated samples of previous thesis (Eichelmüller & Schernitz, 2014). VAG = volcanic arc granite.

Sample	Rock type	Harris et al. (1986)	Batchelor et al. (1985)
ES15	Granite-Gneiss	VAG	Post-collision uplift
ES16	Granite-Gneiss	VAG	Pre-plate collision
ES17	Granodiorite-Gneiss	VAG	Post-collision uplift
ES18	Granite-Gneiss	VAG	Late-orogenic
ES42	Granite	VAG	Syn-collision
ES57	Granite-Gneiss	VAG	Pre-plate collision
ES58	Granite	VAG	Syn-collision
ES94	Granite-Gneiss	VAG	Late-orogenic
ES95	Granite-Gneiss	VAG	Pre-plate collision

5.4. Zircon Typology

The selection process for samples is based on lithology and a geochemical content minimum for the element Zr. The minimum has been set to 130 ppm to ensure a high amount of zircon minerals for each sample. Further, samples of each main orthogenetic lithology and at least one of each geotectonic position have been selected. Paragneisses were not selected. Also the geographical positions of the samples were taken into account, not to cross-path with already taken samples from colleagues. During the preparation process (see chapter 4) the amount of selected zircons decreased continuously. The scanning electronic microscope (SEM) revealed further cracks and provided the base to select certainly measurable zircons (Table 13). Already prepared, but unmeasured samples of a previous thesis (Eichelmüller & Schernitz, 2014) also have been selected, whereby due to the lack of scaling bares the selection process of these samples was rather difficult.

Table 13: Selected samples for radiometric dating of this thesis and the according amount of it, during varies stages of the previous described workflow design.

Sample	Zr in ppm	Rock type	Mounted	Polished	EM selection	Measured
SK16_2	159.5	Granite-Gneiss	41	37	16	0
SK79	215.8	Granodiorite-Gneiss	94	47	1	0
SK87_1	162.7	Granite-Gneiss	96	48	7	0
SK95	181.9	Granodiorite-Gneiss	77	77	6	0
SK97	188.7	Tonalite	79	79	3	0
SK96	211.8	Tonalite	114	57	1	0
SK99	178.3	Granodiorite-Gneiss	61	37	3	0
SK100	189.8	Granite-Gneiss	47	47	21	0

Table 14: Previous prepared samples of Eichelmüller & Schernitz (2014).

Sample	Zr in ppm	Rock type	Mounted	Polished	EM selection	Measured
ES15	153	Granite-Gneiss		13	0	0
ES16	177	Granite-Gneiss		13	8	0
ES17	185	Granodiorite-Gneiss		16	14	0
ES18	192	Granite-Gneiss		12	3	0
ES42	133	Granite		12	0	0
ES57	191	Granite-Gneiss		22	0	0
ES58	94	Granite		5	0	0
ES94	143	Granite-Gneiss		16	0	0
ES95	171	Granite-Gneiss		19	0	0

The location of the analysed samples is seen in (Fig. 69), further the exact coordinates and zircon content in ppm is stated in (Table 15).

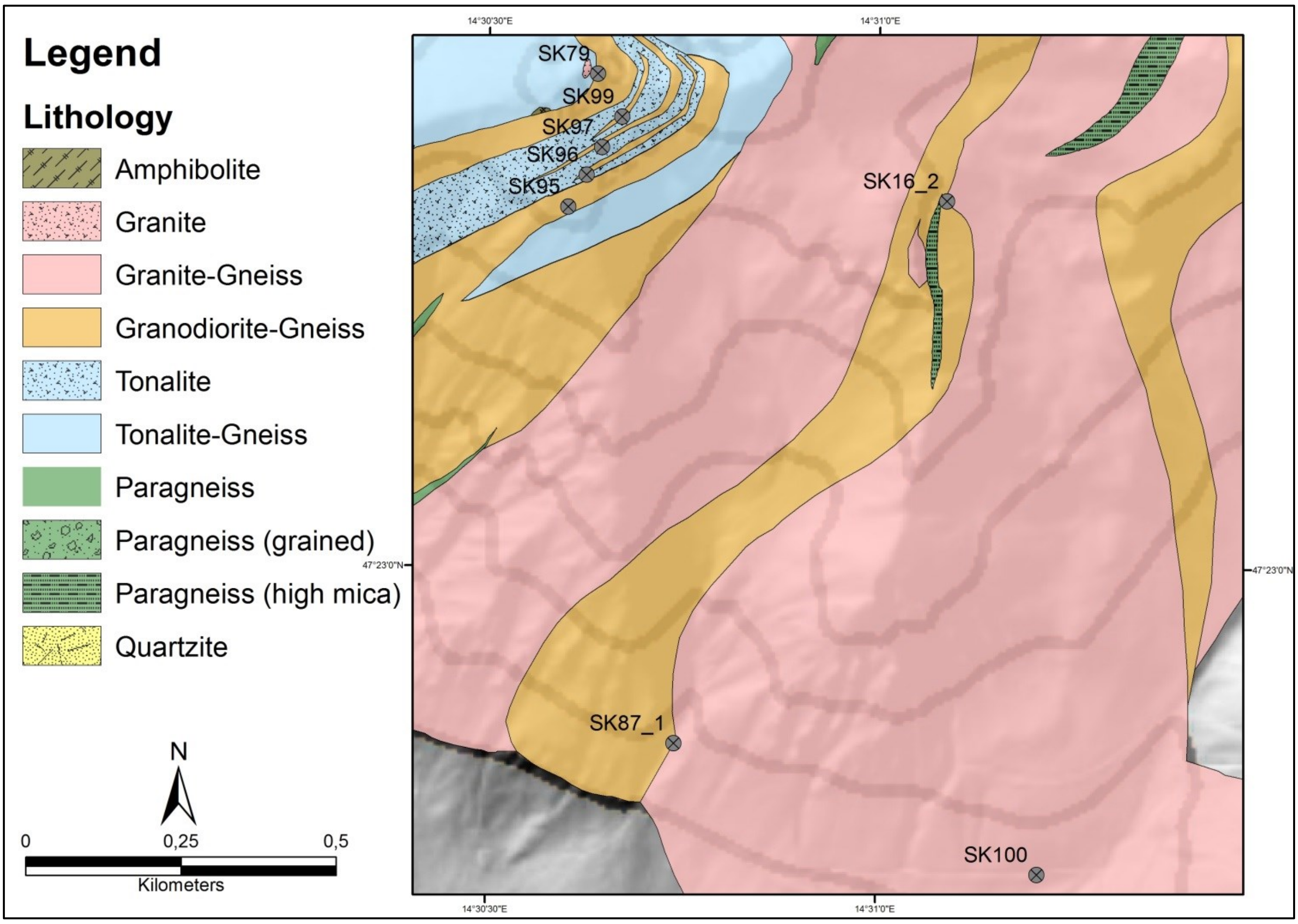

Fig. 69: Location of collected zircon samples.

Table 15: Supplementary details about the selected samples for radiometric dating.

Sample	Zr in ppm	Rock type	Latitude	Longitude	Elevation
SK16.2	159.5	Granite-Gneiss	N47° 23.319'	E14° 31.088'	1978 m
SK87.1	162.7	Granite-Gneiss	N47° 22.846'	E14° 30.741’	1554 m
SK100	189.8	Granite-Gneiss	N47° 22.733'	E14° 31.207'	1538 m
SK95	181.9	Granodiorite-Gneiss	N47° 23.313'	E14° 30.602'	2129 m
SK79	215.8	Granodiorite-Gneiss	N47° 23.429'	E14° 30.639'	2220 m
SK99	178.3	Granodiorite-Gneiss	N47° 23.392'	E14° 30.671'	2144 m
SK96	211.8	Tonalite	N47° 23.341'	E14° 30.626'	2126 m
SK97	188.7	Tonalite	N47° 23.365'	E14° 30.645'	2140 m

5.4.1. Electron Microscopy

The EM analysis has shown, that many inclusions, mostly apatite, are found within the zircons of all samples, they are also often cracked, or otherwise mechanically influenced whereby an often rounded core, e.g. SK100 (Fig. 70) or SK97 (Fig. 71), is visible in the centre of most zircons.

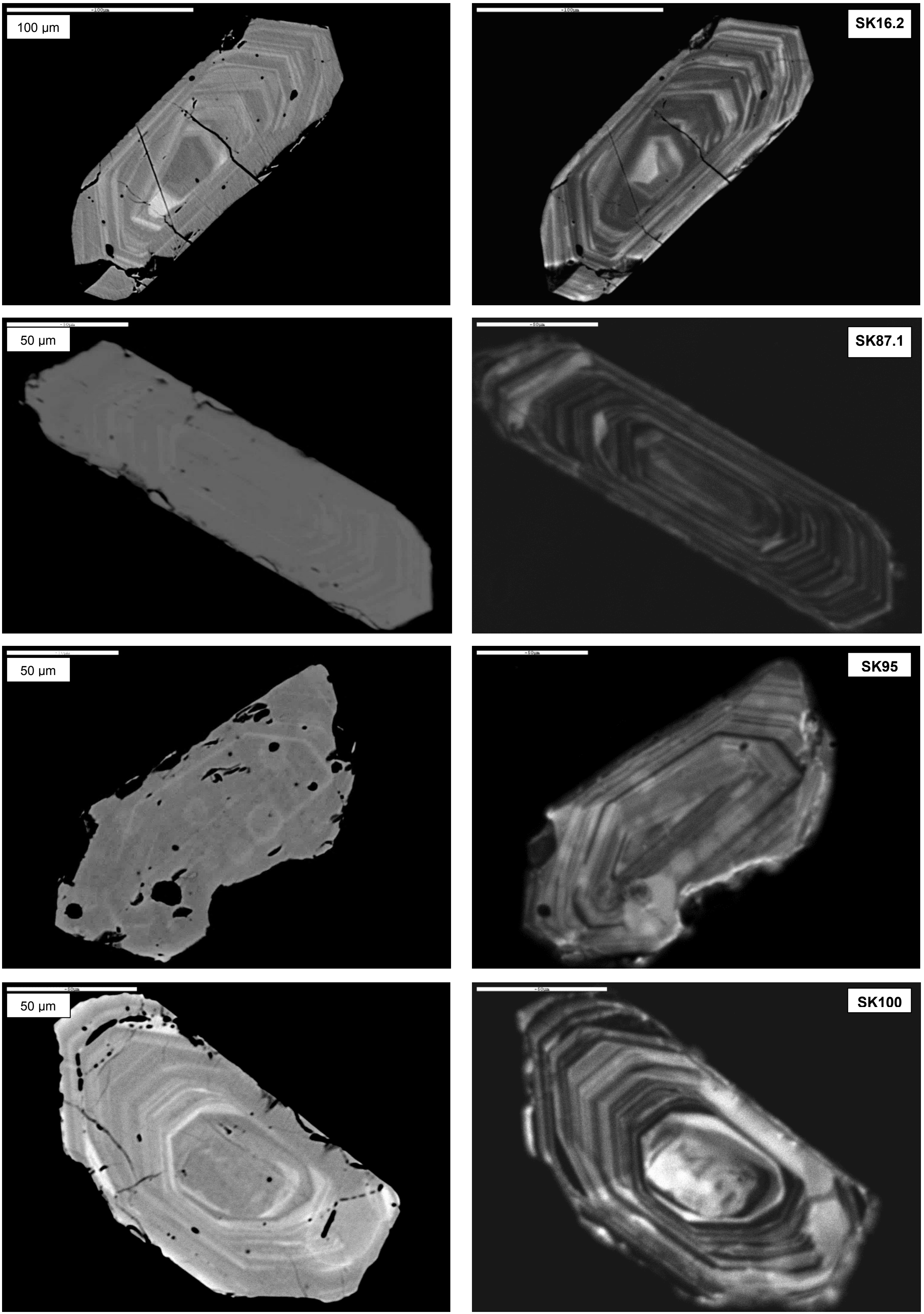

Fig. 70: Examples of high resolution photographs of zircons, BSE (left column) and CL (right column).

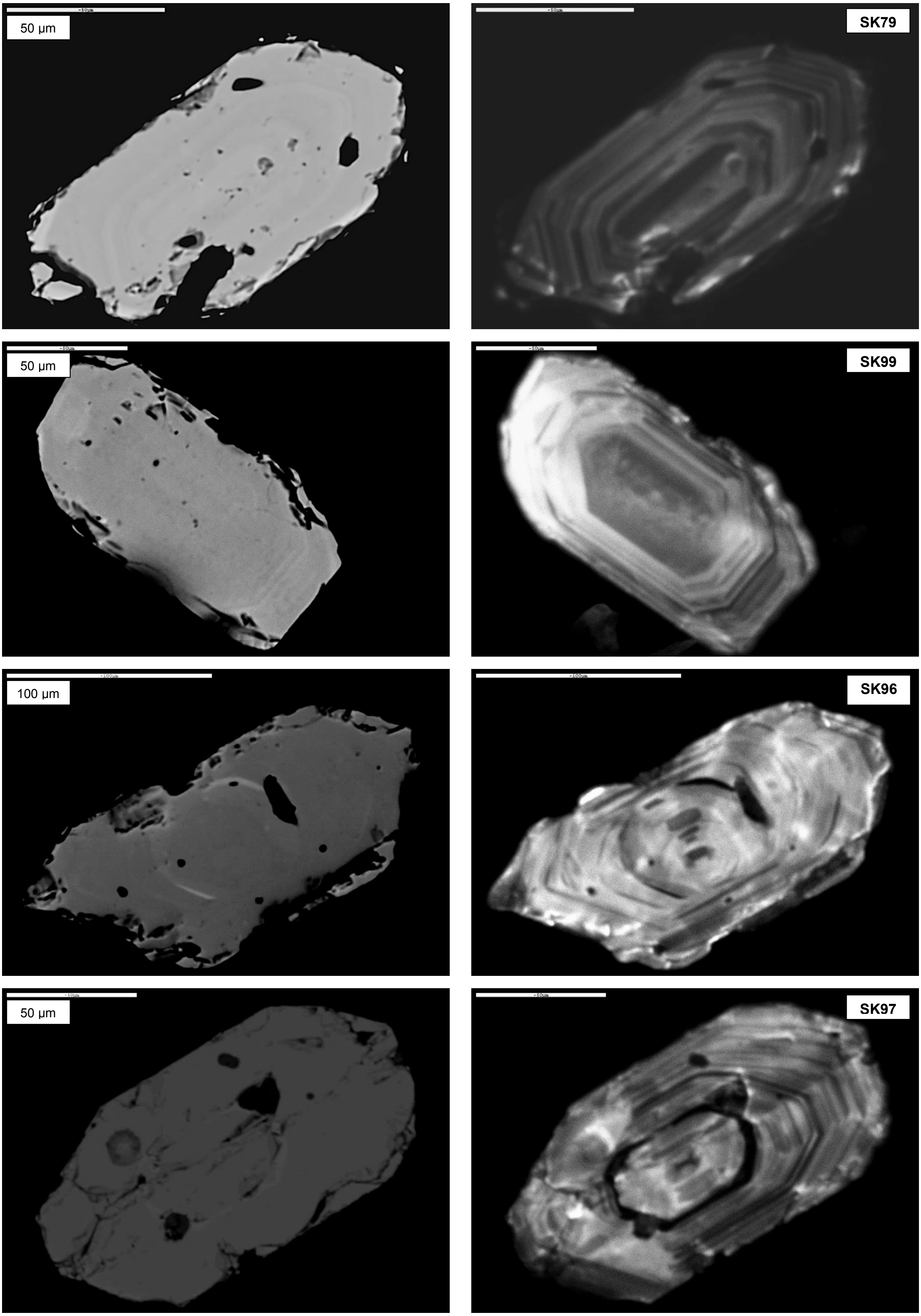

Fig. 71: Further examples of high resolution photographs, BSE (left column) and CL (right column).

5.4.2. Zonation of Zircons

Zircons of each analysed sample have been optically described regarding their habitus within their different layers. The categorization has been focused on the zonation (outer-shell, core mantles, core itself), whereby each where diversified into idiomorphic, rounded, broken and missing. The results are provided in the following (Fig. 72).

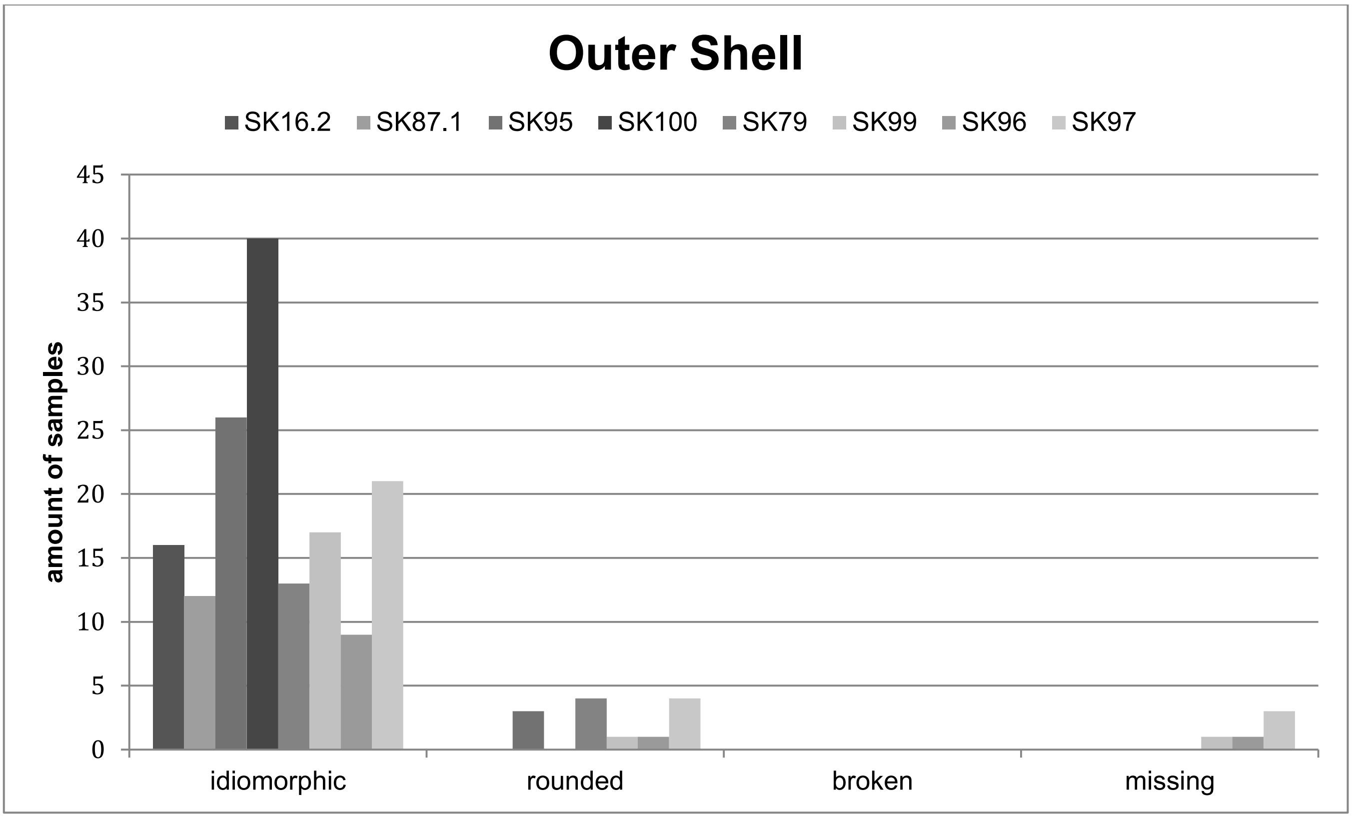

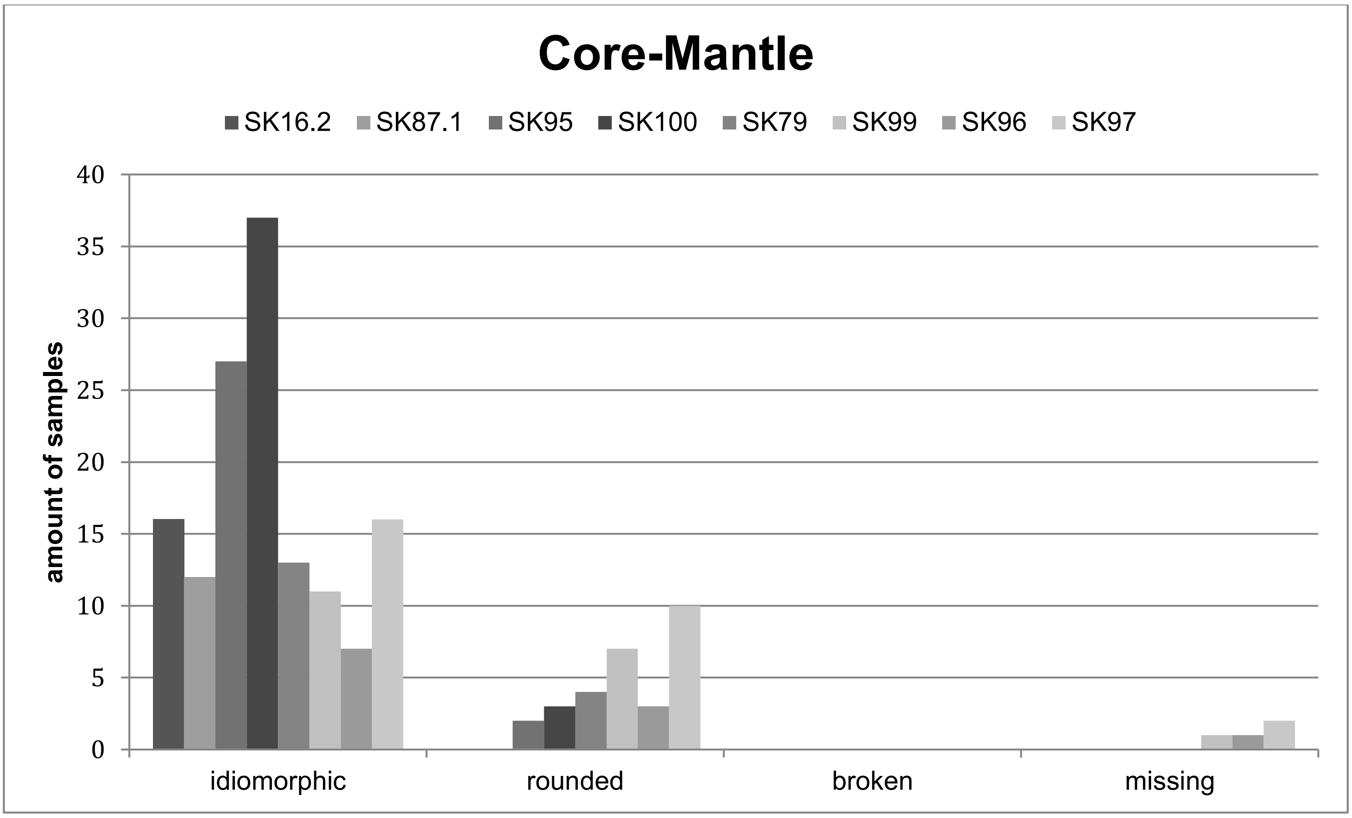

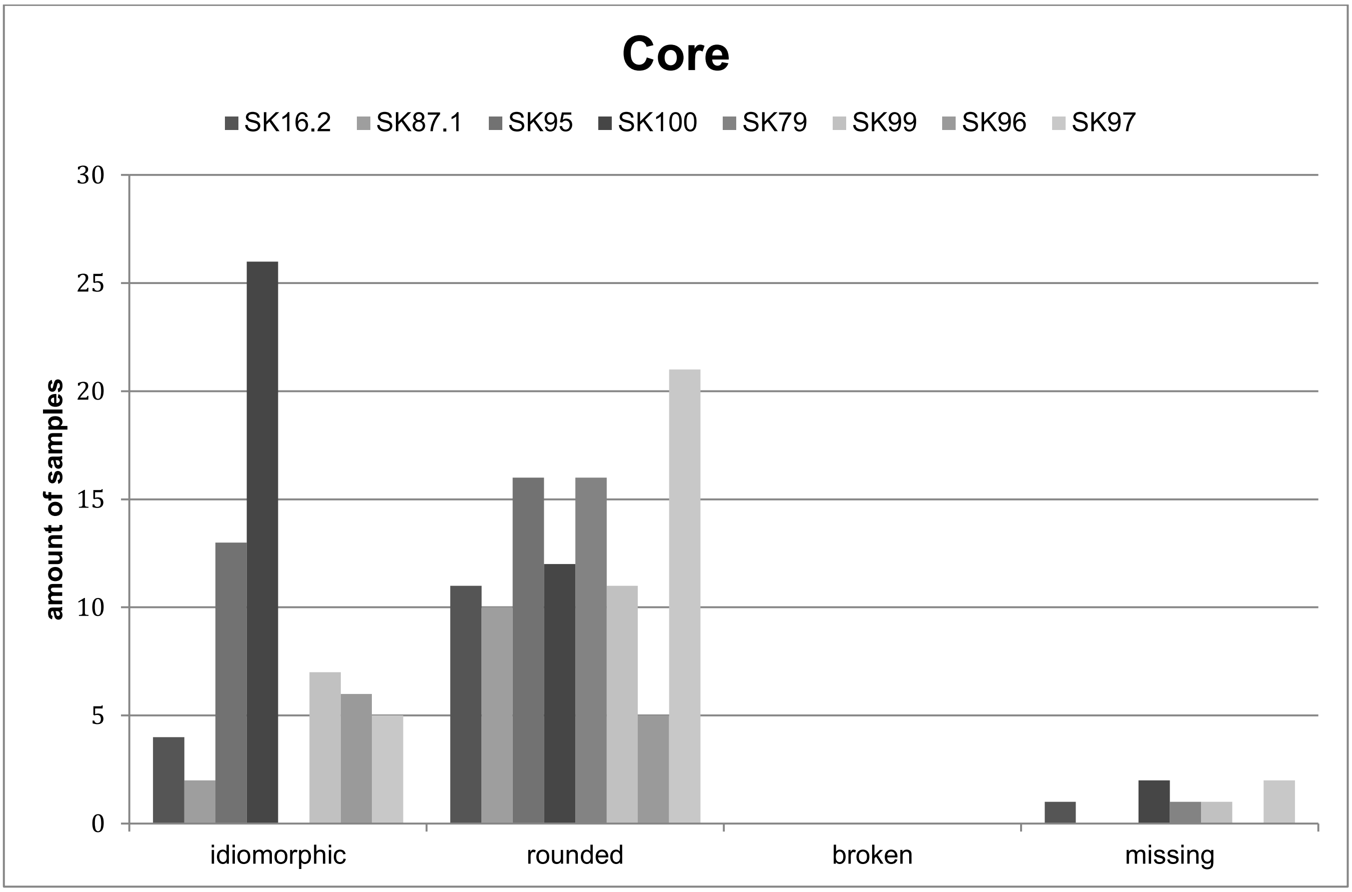

Fig. 72: Distribution of zircon habitus of outer shell, core-mantle and core.

The overall habitus of the zircons varies strongly between the core and the core-mantle. Most cores of the sample range are rounded but the outer-mantle and core-mantle are mostly characterized with an idiomorphic crystal shape. The weathered appearance and the inclusions of apatite occur irregularly and can also be found in different positions of the zircon independently if core or mantle. Because of technical difficulties no measurements with the LA-ICP-MS have been executed, therefore all samples remain unmeasured.

6. Discussion

The orientation of stretching lineation with its west-north-west (WNW) direction is conclusive with the Seckauer nappe stacking process as described previously (chapter 2 & 3). The estimated plane strain of the LPO analysis were also seen in field by elongated quartz bars (Fig. 34), which can be an indicator that there was no shortening or extension perpendicular to the stretching axes (lineation 280/25).

The observed north-west tending shear strain of most microscoped samples is throughout concordant with the stretching lineation which indicates that the development of normal faults was a brittle movement, as also the fault gouge shows (Fig. 36), and therefore concurs with a rather later development. Therefore the normal fault (page 56) in the western part of the study area must have occurred during a later stage and might be connected with the south-east (SE) directing movement of the central block between the Pöls and Palten fault (Fig. 17). The variation of the shear direction between the granite-gneisses and the paragneisses with about 40°, whereby the granodiorite-gneisses lie within those variation, can either be interpreted as division into different stages of development (e.g. fold), or just as margin of deviation. It is also noticeable that the general dipping angle is very low and varies mostly between 10° and 25°.

The temperature estimation of 300 °C to 400 °C by microscoping has been verified by LPO analysis and is concordant with the metamorphic grade (Fig. 24), quoted fluid inclusions (Schönegger, 2015), as well as with other previous theses (Eichelmüller & Schernitz, 2014). This temperature estimation is also conclusive with the T-t path of the Gleinalm and Seckauer Tauern during the Upper Cretaceous (Fig. 24 & Fig. 25).

The literature has already revealed that plagioclase rich orthogneisses (e.g. tonalites and granodiorites) occur together with biotite-plagioclase paragneisses (page 56). The mapping results do also correlate strongly with the literature based classification of different granitoids (Fig. 18) whereby the nomenclature is now according to Streckeisen (1974) and not discriminated as earlier (Fig. 20). Analysed samples show the same dominantly peraluminous and partly metaluminous character as previous theses (Eichelmüller & Schernitz, 2014; Schönegger, 2015) and other literature (Schermaier et al., 1997). The single amphibolite with its SiO_2 content of 44.527 wt.% (see Table 3 of appendix) can also be connected by literature (Neubauer & Raumer, 1993) with the tonalites which are often accompanied by ultramafic rocks.

The calc-alkaline melting series (Fig. 38) has a dominantly potassium-rich setting which is typical for continental arc and post-collisional settings (Roberts & Clemens, 1993) and is also typical for more mature arcs which are farther away from the trench. This calc-alkaline trend has also been evaluated south of the study area (Eichelmüller & Schernitz, 2014) (Fig. 1). Also the volcanic arc setting (Table 9) has been confirmed which is also certified by numerous researches (Eichelmüller & Schernitz, 2014; Pfingstl, 2013; Ratschbacher, 1986; Scharbert, 1981; Schermaier et al., 1997; Schönegger, 2015), and the literature based $^{87}Sr/^{86}Sr$ ratios (page 36) also indicate a highly evolved melt of a typical volcanic arc batholith core zone.

Further a correlation between lithology and geotectonic position can be assumed (Table 10 & Fig. 67). The tonalite and tonalite-gneiss together with the amphibolite are pre-plate collision, the granite, granite-gneiss and the paragneiss are summarized as syn-collision, and the granodiorite-gneiss is seen as late-orogenic to post-collision uplift, whereby the majority of pre-plate collision types are I-type granitoids and most of the syn-collision types are S-type granitoids.

By comparing these geochemical results with the presented palaeogeographic evolution (page 39) the study area can be positioned within a time span of 570 Ma to 480 Ma and probably identified as northern volcanic island arc and active continental margin of the Cadomian terranes north of Gondwana.

Regarding the geochronological evolution of the Seckau Complex the following has to be stated. No new zircon ages have been contributed but evaluated habitus of zircons have shown that most of them passed through several growing phases (Fig. 72), whereby the disruption of concentric oscillatory zoning (e.g. SK100; Fig. 70) is often seen as result of late and post-magmatic cooling, in addition needle shaped zircon crystals (e.g. SK87.1; Fig. 70) are typically for rapid crystallization e.g. sub-volcanic intrusion (Hanchar & Hoskin, 2003) and the prominent presence of {211} is another indication of the calc-alkaline trend (Pupin, 1980), and therefore the zircon study correlates strongly with the geochemical data and could probably substantiate the previous stated Cadomian theory through successful radiometric dating.

Also if some cores (e.g. SK97; Fig. 71) do inherit xenocrystic cores can only be distinct through differences in U-content between core and rims, this should be considered during future radiometric dating especially samples classified as S-typ. Further, the new geochronological overview of previous dated areas (chapter 3.2) provides a solid fundament to the future understanding of the development of the Seckauer Tauern.

Based on the collected literature the question if the Seckauer Tauern are part of the so called "Proto-Alps" (Heinrichs et al., 2012) or Cadomian terranes is more likely. Schaltegger et al. (1997) has already described the geodynamic scenario. His thesis is also applicable for the Seckauer Tauern because literature based dates vary between 745 Ma and 354 Ma (page 32).

The Speik Complex can be seen as the back-arc basin and the Amering and Seckau Complex can be interpreted as the volcanic arc of an active continental margin, where intrusions of gabbroic tonalitic melts (I-type) and collisional acid magmatism (S-type) could have been created around 600 Ma to 500 Ma (Fig. 26 & Fig. 27). Table 10 backs up this statement by assigning the rock types according to Chappell & White (2001) and showing that the granites have a higher affection to the S-type in contrary to the I-type which is mostly assigned to tonalites and granodiorites which are typical for active continental margins.

Of course the Variscan orogeny probably have had an impact on those units, therefore the less deformed pre-plate collision I-type granitoids are considered to be a secondary intrusion event related to the Variscan orogeny. The full extent of the Variscan importance within the Seckauer Tauern remains as an open question.

7. Conclusions

This thesis provides new maps, areal classifications and geochemical whole rock data of the Seckau Complex which contributes, together with the thorough literature summary of the Seckauer Tauern, to the overall understanding of a more detailed development of it. The stages of the Alpine evolution were captured within the Seckau Complex e.g. WNW nappe stacking, peak conditions during Late Cretaceous around 300 °C to 400 °C and supposedly normal fault(s) related to the SE directed fault system during younger stages. Further the volcanic arc setting and calc-alkaline trend based on the geochemical data correlate with the zircon habitus. Questions about the relation of the Seckau Complex and the Cadomian terranes have been raised again, whereby already prepared zircon samples are now waiting to be successfully measured (U/Pb) to substantiate the newly gathered indication.

List of References

Ahrens, L. H. (1955). Implications of the Rhodesia age pattern. *Geochim. Cosmochim*, *8*, 1–15.

Batchelor, R. a., & Bowden, P. (1985). Petrogenetic interpretation of granitoid rock series using multicationic parameters. *Chemical Geology*, *48*(1-4), 43–55. doi:10.1016/0009-2541(85)90034-8

Becker, L. P. (1981). Zur Gliederung des Obersteirischen Altkristallins (Muriden). *Geologische Bundesanstalt*, 3–17.

Beckhoff, B., Kanngießer, B., Langhoff, N., Wedell, R., & Wolff, H. (2006). *Handbook of Practical X-Ray Fluorescence Analysis* (p. 878). Springer.

Bernoulli, D. (2007). The pre-Alpine geodynamic evolution of the Southern Alps : a short, *12*(June), 3–10.

Blanckenburg, F., Villa, I. M., Baur, H., Morteani, G., & Steiger, R. H. (1989). Time calibration of a PT-path from the Western Tauern Window, Eastern Alps: the problem of closure temperatures. *Contrib. Mineral. Petrol.*, (101), 1–11.

Blenkinsop, T. G. (2000). *Deformation Microstructures and Mechanisms in Minerals and Rocks*.

Chappell, B. W., & White, A. (1974). Two contrasting granit types. *Pacific Geology*, *8*, 173–174.

Chappell, B. W., & White, A. J. T. (2001). Two contrasting granite types: 25 years later. *Australien Journal of Earth Sciences*, *48*, 489–499.

Collins, W. J., Beams, S. D., White, A. J. T., & Chappell, B. W. (1982). Nature and origin of A-type granites with particular reference to Southeastern Australia. *Contrib. Mineral. Petrol.*, *80*, 189–200.

Doe, B. R. (1970). *Lead Isotopes*. Springer.

Dunkl, I., Kuhlemann, J., Reinecker, J., & Frisch, W. (2005). Austrian Journal of Earth Sciences, volume 98 straints from apatite fission track age-provenance of, *98*.

Eichelmüller, S., & Schernitz, J. (2014). Petrologie , Geochemie und Geochronologie von Granitoiden der Seckauer / Triebener Tauern.

Faryad, S. W., & Hoinkes, G. (2001). Alpine Chloritoid and Garnet From the Hochgrössen Massif (Speik Complex, Eastern Alps), *146*, 387–396.

Faryad, S. W., Melcher, F., Hoinkes, G., Puhl, J., Meisel, T., & Frank, W. (2002). Relics of eclogite facies metamorphism È ssen in the Austroalpine basement , Hochgro (Speik complex), Austria, 49–73.

Faryad, S. W., Melcher, F., Hoinkes, G., Puhl, J., Meisel, T., & Frank, W. (2002). Relics of eclogite facies metamorphism in the Austroalpine basement, Hochgrössen (Speik complex), Austria. *Mineralogy and Petrology*, *74*(1), 49–73.

Faure, G., & Mensing, T. M. (2005). *Isotopes: Principles and Applicaitons* (Third Edit). Wiley.

Frank, W., Esterlus, M., Frey, I., Jung, G., Krohe, A., & Weber, J. Die Entwicklungsgeschichte von Stub- und Koralpenkristallin und die Beziehung zum grazer Paläozoikum (1983).

Frank, W., Klein, P., Nowy, W., & Scharbert, S. (1976). Die Datierung geologischer Ereignisse im Altkristallin der Gleinalpe (Steiermark) mit der Rb/Sr-Methode. *Tschermarks Mineralogische Und Petrographische Mitteilung*, *23*(3), 197–203. Retrieved from http://link.springer.com/article/10.1007%2FBF01134162

Frank, W., Kralik, M., Scharbert, S., & Thöni, M. (1987). *Geochronological Data from the Eastern Alps*. (H. W. Flügel & P. Faupl, Eds.) (Geodynamic, pp. 272–281).

Frisch, W., & Gawlick, H.-J. (2003). The nappe structure of the central Northern Calcareous Alps and its disintegration during Miocene tectonic extrusion?a contribution to understanding the orogenic evolution of the Eastern Alps. *International Journal of Earth Sciences*, *-1*(1), 1–1. doi:10.1007/s00531-003-0357-4

Frisch, W., Neubauer, F., Bröcker, M., Brückmann, W., & Haiss, N. (1987). interpretation of geochemical data from teh Caledonian basement within the Austroalpine basement complex. In; Flügel HW, Sassi FP, Grecula P (eds) Pre-Variscan and Variscan events in the Alpine-Mediterranean mountain belts. In *Alfa* (pp. 209–226).

Froitzheim, N. (1996). Kinematics of Jurassic rifting , mantle exhumation , and passive-margin formation in the Austroalpine and Penninic nappes (eastern Switzerland). *Geological Society of America Bulletin*, *108*(1), 1120–1133.

Froitzheim, N. (2011). *Geology of the Alps Part 1 : General remarks; Austroalpine nappes.*

Froitzheim, N., Plasienka, D., & Schuster, R. (2008). *The geology of Central Europe* (pp. 1141–1232).

Gasser, F. D., Gusterhuber, J., Krische, O., Puhr, B., Scheucher, L., Wagner, T., & Stüwe, K. (2009). Geology of Styria : An overview, 5–36. Retrieved from http://retro.seals.ch/digbib/view?pid=smp-001:1988:68::358

Goldstein, J. L., & Newbury, D. E. (1997). *Scanning Electron Microscopy and X-Ray Microanalysis;* (2nd ed.). Kluwer Academic Publishers.

Golonka, J., & Gawęda, A. (2012). Plate Tectonic Evolution of the Southern Margin of Laurussia in the Paleozoic.

Grassler, F. (1984). Alpenvereinseinteilung der Ostalpen. *Berg, 108*, 215–224.

Haiss, N. (1991). *Untersuchungen zur Genese von Plagioklasgneisen im Basiskristallin der Ostalpen (Gleinalm-, Ötztal und Silvrettakristallin.*

Hanchar, & Hoskin. (2003). Zircon. *Reviews in Mineralogy & Geochemistry*, *53*.

Handler, R., Dallmeyer, R. D., & Neubauer, F. (1997). Ar / Ar ages of detrital white mica from Upper Austroalpine units in the Eastern Alps , Austria : Evidence for Cadomian and contrasting Variscan sources, 69–80.

Handler, R., Neubauer, F., Hermann, S., & Dallmeyer, R. D. (1999). Silurian - devonian 40 Ar/ 39 Ar mineral ages from the kaintaleck nappe: evidence fro mid-paleozoic tectonothermal activity in upper austroalpine basement units of the eastern alps (Austria), (June).

Harris, N., Pearce, J., & Tindle, A. (1986). Geochemical characteristics of collision-zone magmatism. *Geological Society London Special Publicaion*, *19*, 67–81.

Heinrichs, T., Siegesmund, S., Frei, D., Drobe, M., & Schulz, B. (2012). Provenance signatures from whole-rock geochemistry and detrital zircon ages of metasediments from the austroalpine basement south of the tauern window (eastern Tyrol, Austria). *Geo.Alp*, *9*, 156–185.

Hejl, E. (1984). Geochronologische un dpetrologische Beiträge zur Gesteinsmetamorphose der Scladminger Tauern. *Berichte Der Geologischen Bundesanstalt1*, *30/31*, 289–318.

Hejl, E. (1997). ' Cold spots ' during the Cenozoic evolution of the Eastem Alps : thermochronological interpretation of apatite fission-track data, *1*(1993).

Imeokparia, E. G. (1981). Ba/Rb and Rb/Sr ratios as indicators of magmatic fractionation, postmagmatic alteration and mineralization - Afu Younger Granite complex, Northern Nigeria. *Geochemical Journal*, *15*, 209–219.

Irvine, T., & Barager, W. (1971). A guide to the chemical classificaitno of the common volcanic rocks. *Canadian Journal of Earth Sciences*, *8*, 523–548.

Janoschek, W. R., & Matura, A. (1980). Outline of the Geology of Austria. *Abhandlung Geologische Bundesanstalt*, *34*, 7–98.

Janousek, V., Farrow, C. M., & Erban, V. (2006). Interpretation of Whole-rock Geochemical Data in Igneous Geochemistry: Introducing Geochemical Data Toolkit (GCDkit). *Journal of Petrology*, *47*(6), 1255–1259. doi:10.1093/petrology/egl013

Koller, F., Götzinger, M., Neumayer, R., & Niedermayer, G. (1983). Beiträge zur Mineralogie und Geochemie der Pegmatite des St. Radegunder Kristallins und der Gleinalpe. *Archief Für Lagerstättenforschung Der GEologsichen Bundesanstalt*, 47–65.

Kroner, U., & Romer, R. L. (2013). Two plates — Many subduction zones: The Variscan orogeny reconsidered. *Gondwana Research*, *24*(1), 298–329. doi:10.1016/j.gr.2013.03.001

Kurz, W., & Fritz, H. (2003). Tectonometamorphic Evolution of the Austroalpine Nappe Complex in the Central Eastern Alps — Consequences for the Eo-Alpine Evolution of the Eastern Alps. *International Geology Review*, *45*, 1100–1127.

Lide, D. R., & Frederikse, H. P. R. (1995). *Handbook of chemistry and Physics*.

Lister, G. ., & Hobbs, B. . (1980). The simulation of fabric development during plastic deformation and its application to quartzite: the influence of deformation history. *Journal of Structural Geology*, *2*(3), 355–370. doi:10.1016/0191-8141(80)90023-1

Lister, G. S. (1977). Discussion: Crossed-girdle c-axis fabrics in quartzites plastically deformed by plane strain and progressive simple shear. *Tectonophysics*, *39*(1-3), 51–54. doi:10.1016/0040-1951(77)90087-7

Mandl, M., Kurz, W., Pfingstl, S., Schuster, R., Hauzenberger, C., & Fritz, H. (2014). Geological Evolution of the Austroalpine Seckau Complex (Eastern Alps). In *PANGEO Austria*.

Melcher, F. (2004). A Metamorphosed Early Cambrian Crust-Mantle Transition in the Eastern Alps, Austria. *Journal of Petrology*, *45*(8), 1689–1723. doi:10.1093/petrology/egh030

Metz, K. (1962). Das ostalpine kristallin der niederen tauern im bauplan der ne-alpen. *1International Journal of Earth Sciences*, *52*(7), 210–226.

Metz, K. (1965). Das ostalpine Kristallin im Bauplan der östlichen Zentralalpen. *Akademie Der Wissenschaften Wien*, 230–274.

Metz, K. (1976a). Der geologische Bau der Seckauer und Rottenmanner Tauern, (November).

Metz, K. (1976b). Der geologische Bau der Seckauer und Rottenmanner Tauern. *Jahrbuch Der Geologischen Bundesanstalt*, *119*(2), 151–205.

Metz, K. (1978). Bruchsysteme und Westbewegungen in den östlichen Zentralalpen, *Mitteilungen Der Oesterreichischen Geologischen Gesellschaft*, *69*, 27–47.

Metz, V. K. (1971). Die Gaaler Schuppenzone als Südgrenze der Seckauer Masse.

Miller, C., & Thöni, M. (1997). Origin of eclogites from the Austoalpine Ötztal basement (Tirol, Austria): geochemistry and Sm-Nd vs. RB-Sr isotope systematics. *Chem. Geol.*, (137), 283–310.

Miyashiro, A. (1974). volcnaic rock sreis in island arcs and active continental margins. *American Journal of Science*, *274*, 321–355.

Nagl, V. H. (1976). Die Raum - Zeit Verteilung der Blockgletscher in den Niederen Tauern und die eiszeitliche Vergletscherung der Seckauer Tauern.

Neubauer, F. (1988a). Bau und Entwicklungsgeschichte des Rennfeld-Mugel ud des gleinalm-Kristallins (Ostalpen). *Geologische Bundesanstalt*, *42*, 1–127.

Neubauer, F. (1988b). The Variscan orogeny in the Austroalpine and Southalpine domains of the Eastern Alps. *Schweiz. Mineral. Petrogr. Mitt.*, *68*(3), 339–349. doi:http://dx.doi.org/10.5169/seals-52072 Detailed information

Neubauer, F. (1989). The leptinite-amphibolie complexes - a key for correlation of mid-European Variscides? In *Athens/GA July 21-22* (pp. 79–82).

Neubauer, F. (2002). Evolution of late Neoproterozoic to early Paleozoic tectonic elements in Central and Southeast European Alpine mountain belts: review and synthesis. *Tectonophysics*, *352*(1-2), 87–103. doi:10.1016/S0040-1951(02)00190-7

Neubauer, F. (2014). Gondwana-Land goes Europe, *1*.

Neubauer, F., Dallmeyer, R. D., & Schirnik, D. (1995). Late Cretaceous exhumation of the metamorphic Gleinalm dome , Eastern Alps " kinematics , cooling history and sedimentary response in a sinistral wrench corridor a a Munich Vienna, *242*, 79–98.

Neubauer, F., & Frisch, W. (1993). The Austro-Alpine Metamorphic Basement East of the Tauern Window. In *Pre-Mesozoic Geology in the Alps* (pp. 515–536).

Neubauer, F., Frisch, W., & Hansen, B. (2002). Early Palaeozoic tectonothermal events in basement complexes of the eastern Greywacke Zone (Eastern Alps): evidence from U-Pb zircon data. *International Journal of Earth Sciences*, *91*(5), 775–786. doi:10.1007/s00531-001-0254-7

Neubauer, F., Frisch, W., & Hansen, B. T. (1993). The pre-Alpine tectonothermal evolution of the Rennfeld region, Eastern Alps: a U-Pb zircon study. *Lithos*.

Neubauer, F., Frisch, W., & Tauber Hansen, B. (2003). Early Paleozoic and Variscan Events in the Austroalpine Rennfeld Block (Eastern Alps): A U-Pb Zircon Study. *Jahrbuch Der Geologischen Bundesanstalt*, *143*(4), 567–580.

Neubauer, F., Genser, J., & Handler, R. (2000). The Eastern Alps : Result of a two-stage collision process, (1994).

Neubauer, F., Handler, R., Hermann, S., & Paulus, G. (1994). Revised Lithostratigraphy and Structure of the Eastern Graywacke Zone (Eastern Alps) mckskmned tectonics, *86*(1993).

Neubauer, F., Hoinkes, G., Sassi, F. P., Handler, R., Höck, V., Koller, F., & Frank, W. (1999). Pre-Alpine metamorphism in the Eastern Alps. *Schweiz. Mineral. Petrogr. Mitt.*, (79), 41–62.

Neubauer, F., & Raumer, J. F. (1993). *Pre-Mesozoic Geology in the Alps* (pp. 515–536).

Norman, M. D., & Leeman, W. P. (1992). Granites and Rhyolites from the northwestenr USA: temporal variation in magmatic processes and relations to tectonic setting. *Transaction of Teh Royal Society of Edinburgh: Earth Sciences*, *83*(1-2), 71–81.

Ortner, H., Aichholzer, S., Zerlauth, M., Pilser, R., & Fügenschuh, B. (2015). Geometry, amount, and sequence of thrusting in the Subalpine Molasse of western Austria and southern Germany, European Alps. *Tectonics*, *34*(1), 1–30. doi:10.1002/2014TC003550

Passchier, C. W. (1983). The reliability of asymmetric c-axis fabrics of quartz to determine sense of vorticity. *Tectonophysics*, *99*, T9–T18.

Passchier, C. W., & Trouw, R. A. j. (2005). *Microtectonics* (p. 366).

Pearce, J. A., Harris, N. B. W., & Tindle, A. G. (1984). Trace Element Discrimination Diagrams for the Tectonic Interpretation of Granitic Rocks. *Department of Earth Sciences, The Obpen University, Milton Keynes, MK76AA, Bucks, England*, 957–983.

Peccerillo, A., & Taylor, S. R. (1976). Geochemistry of eocene calc-alkaline volcanic rocks from the Kastamonu area, northern Turkey. *Contributions to Mineralogy and Petrology*, *56*, 63–81.

Pfingstl, S. (2013). Tektonische und metamorphe Entwicklung des Seckauer Kristallins.

Pfingstl, S., Kurz, W., Schuster, R., & Hauzenberger, C. (2015). Geochronological constraints on the exhumation of the Austroalpine Seckau Nappe (Eastern Alps). *Austrian Journal of Earth Sciences*, *108*(1), 172–185. doi:10.17738/ajes.2015.0011

Pleuger, J., Roller, S., Walter, J. M., Jansen, E., & Froitzheim, N. (2006). Structural evolution of the contact between two Penninic nappes (Zermatt-Saas zone and Combin zone, Western Alps) and implications for the exhumation mechanism and palaeogeography. *International Journal of Earth Sciences*, *96*(2), 229–252. doi:10.1007/s00531-006-0106-6

Pupin. (1980). Zircon and granite petrology. *Contributions to Mineralogy and Petrology*, *73*, 207–220.

Ratschbacher, L. (1986). Kinematics of Austro-Alpine Cover Nappes: Changing Trnaslation Path due to Transpression. *Tectonophysics*, *125*, 335–356.

Ratschbacher, L. (1987). Stratigraphy, tectonics and paleogeography of the Veitsch nappe (Graywacke zone , Eastern Alps, Austria): A rearrangement. In *Pre-Variscan and Variscan Events in the alpine mediterranean mountain belts Edited by Flügel, Sassi and Grecula* (pp. 407–414).

Ratschbacher, L., Frisch, W., Linzer, H.-G., & Merle, O. (1991). Lateral extrusion in the eastern Alps, PArt 2: Structural analysis. *Tectonics*, *10*(2), 257–271. doi:10.1029/90TC02623

Raumer, J. F., Bussy, F., Schaltegger, U., Schulz, B., & Stampfli, G. M. (2013). Pre-Mesozoic Alpine basements—Their place in the European Paleozoic framework. *Geological Society of America Bulletin*, *125*(1-2), 89–108. doi:10.1130/B30654.1

Raumer, J. F., & Stampfli, G. M. (2008). The birth of the Rheic Ocean — Early Palaeozoic subsidence patterns and subsequent tectonic plate scenarios. *Tectonophysics*, *461*(1-4), 9–20. doi:10.1016/j.tecto.2008.04.012

Reed, S. (2010). *Electron Microsprobe Analysis and Scanning Electron Microscopy in Geology*. Cambridge University Press. Retrieved from http://www.amazon.de/Electron-Microprobe-Analysis-Scanning-Microscopy/dp/052114230X/ref=sr_1_3?ie=UTF8&qid=1433408390&sr=8-3&keywords=scanning+electron+microscopy

Roberts, M. P., & Clemens, J. D. (1993). Origin of high-potassium, calc-alkaline, I-type granitoids. *Geology*, *21*, 825–828.

Schaltegger, U., Nägler, T. F., & Corfu, F. (1997). A Cambrian island arc in the Silvretta nappe : constraints from geochemistry and geochronology. *Schweiz. Mineral. Petrogr. Mitt.*, *77*(3), 337–350.

Scharbert, S. (1981). Untersuchung zum Alter des Seckauer Kristallins. *Mitt. Ges. Geol.Bergbaustu. Österreich*, *27*, 173–188.

Schedl, A. (1981). *Geologsiche, geochemische und lagerstättenkundliche Untersuchungen im ostalpinen Kristallin der Schladminger Tauern.*

Schermaier, A., Haunschmid, B., & Finger, F. (1997). Distribution of Variscan I- and S-type granites in the Eastern Alps: a possible clue to unravel pre-Alpine basement structures. *Tectonophysics*, *272*(2-4), 315–333. doi:10.1016/S0040-1951(96)00265-X

Schermaier, A., Haunschmid, B., Schubert, G., Frasl, G., & Finger, F. (1992). Diskriminierung von S-typ und I-typ graniten auf der basis zirkontypologischer untersuchungen. *Frankf Geiwiss Arb Serie A*, *11*, 149–153.

Schmid, S. M., Fügenschuh, B., Kissling, E., & Schuster, R. (2004). Tectonic map and overall architecture of the Alpine orogen. *Eclogae Geologicae Helvetiae*, *97*(1), 93–117. doi:10.1007/s00015-004-1113-x

Schönegger, M. (2015). *Die tektonische und geochemische Entwicklung in den Seckauer Tauern im Bereich des Gaalgrabens - Sommertörls (Steiermark)*

Schulz, B. (2008). Basement of the Alps. In *Geology of Central Europe, Volume 1: Precambrian and Paleozoic* (pp. 79–83). McCanne; T. Retrieved from http://www.amazon.de/Geology-Central-Europe-Precambrian-Palaeozoic/dp/1862392463/ref=sr_1_fkmr0_2?ie=UTF8&qid=1431949454&sr=8-2-fkmr0&keywords=Geology+of+central+Europe+Precambrian+and+Paleozoic

Schuster, R. (2013). *Einführung in die regionale Geologie Europas - Geologie von Österreich*.

Schuster, R., Koller, F., Hoeck, V., Hoinkes, G., & Bousquet, R. (2004). Metamorphic Structure of the Alps Metamorphic Evoluiton of the Eastern Alps. *Mitteilungen Der Österreichischen Mineralogischen Gesellschaft*, *149*, 175–199.

Schuster, R., Scharbert, S., Abart, R., & Frank, W. (2001). Permo-Triassic extension and related HT/LP metamorphism in the Austroalpine - Southalpine realm. *Mitt. Geol. Bergbau Stud. Österr.*, (44), 111–141.

Schuster, V. R., & Stüwe, K. (2010). Die Geologie der Alpen im Zeitraffer, 5–22.

Shand, S. J. (1943). *The Eruptive Rocks* (2nd ed., p. 444). New York.

Stamp, G. M., & Borel, G. D. (2002). Paleozoic evolution of pre-Variscan terranes : From Gondwana to the Variscan collision, 263–280.

Stampfli, G. M., Raumer, J. ., & Wilhem, C. (2011). The distribution of Gondwana-derived terranes in the Early Paleozoic, 567–574.

Steiger, R. H., & Jäger, E. (1977). Subcomission on Geochronology: Conventions on the use of decay constans in geo- and cosmochronology. *Earth Planet*, *Sci.Letter*, 359–362.

Streckeisen, A. (1974). Classification and nomenclature of plutonic rocks recommendations of the IUGS subcommission on the systematics of Igneous Rocks. *Geologische Rundschau*, *63*(2), 773–786. doi:10.1007/BF01820841

Sylvester, P. J. (1989). Post-Collisional Alkaline Granites. *The Journal of Geology*, *97*(3), 261–280.

Taylor, H. E. (2001a). Chapter 3 - Inductively Coupled Plasmas. In H. E. Taylor (Ed.), *Inductively Coupled Plasma-Mass Spectrometry* (pp. 15–27). San Diego: Academic Press. doi:http://dx.doi.org/10.1016/B978-012683865-7/50003-X

Taylor, H. E. (2001b). *Inductively Coupled Plasma-Mass Spectrometry*. *Inductively Coupled Plasma-Mass Spectrometry* (pp. 7–13). Elsevier. doi:10.1016/B978-012683865-7/50002-8

Tollmann, A. (1977). *Geologie von Österreich* (pp. 190–211, 279–308, 212).

Toy, V. G., Prior, D. J., & Norris, R. J. (2008). Quartz fabrics in the Alpine Fault mylonites: Influence of pre-existing preferred orientations on fabric development during progressive uplift. *Journal of Structural Geology*, *30*, 602–621. doi:10.1016/j.jsg.2008.01.001

Wallbrecher, E. (2012). Fabric 8 Geologische Softare. Graz.

Werner, C. D. (1987). Saxonian granulites - a contribution to the geochemical diagnosis of original rocks inhigh-metamorphic complexes. *Geophysik*, *96*(3/4), 271–290.

Wetherill, G. W. (1956). Discordant uranium-lead ages. *Trans. Am. Geochys. Union*, *37*, 320–326.

Wetherill, G. W. (1963). Discordant uranium-lead ages - Pt 2; discordant ages resulting from diffusion of lead and uranium. *J. Geophys. Res.*, *68*, 2957–2965.

Whalen, J., Curri, K., & Chappell, B. (1987). A-type granites: Geochemical characteristics, discrimination and petrogenesis. *Contributions to Mineralogy and Petrology1*, *95*, 407–419.

White, W. M. (2015). *Isotope Geochemistry* (p. 496).

Wilson, C. J., Russel-Head, D. S., Kunze, K., & Viola, G. (2007). The analysis of quartz c-axis fabric using modified optical microscope. *Journal of Microscopy*, *227*, 30–41.

8. Appendix

Table 1: Coordinates of the sampling sites.

Sample	Latitude		Longitude		Altitude
SK1	N	47.3975	E	14.5200	1,688 m
SK1.1	N	47.3977	E	14.5199	1,695 m
SK1.2	N	47.3978	E	14.5191	1,722 m
SK2	N	47.3978	E	14.5191	1,722 m
SK3	N	47.3907	E	14.5239	1,959 m
SK4	N	47.3911	E	14.5220	1,946 m
SK5	N	47.3911	E	14.5224	1,944 m
SK7	N	47.3911	E	14.5210	1,976 m
SK8	N	47.4022	E	14.5235	1,680 m
SK9	N	47.4064	E	14.5206	1,812 m
SK9.1	N	47.4065	E	14.5206	1,810 m
SK10	N	47.4027	E	14.5216	1,752 m
SK11	N	47.4025	E	14.5214	1,752 m
SK12	N	47.3893	E	14.5210	1,936 m
SK13	N	47.3886	E	14.5215	1,905 m
SK14	N	47.3885	E	14.5214	1,899 m
SK15	N	47.3885	E	14.5211	1,904 m
SK16	N	47.3889	E	14.5185	1,965 m
SK16.1	N	47.3887	E	14.5182	1,974 m
SK16.2	N	47.3887	E	14.5181	1,979 m
SK17	N	47.3887	E	14.5178	2,008 m
SK17.1	N	47.3887	E	14.5177	2,005 m
SK17.2	N	47.3885	E	14.5178	2,011 m
SK18	N	47.3885	E	14.5177	2,004 m
SK18.1	N	47.3884	E	14.5176	2,012 m
SK19	N	47.3881	E	14.5175	2,015 m
SK20	N	47.3885	E	14.5181	1,984 m
SK21	N	47.4020	E	14.5213	1,712 m
SK22	N	47.4019	E	14.5211	1,727 m
SK23	N	47.4018	E	14.5205	1,743 m
SK24	N	47.4017	E	14.5205	1,730 m
SK24	N	47.4016	E	14.5205	1,736 m
SK25	N	47.4016	E	14.5204	1,735 m
SK25.1	N	47.4016	E	14.5201	1,757 m
SK26	N	47.4014	E	14.5199	1,841 m
SK26	N	47.4015	E	14.5193	1,776 m
SK26.1	N	47.4016	E	14.5196	1,693 m
SK26.2	N	47.4018	E	14.5197	1,764 m
SK27	N	47.3906	E	14.5096	2,217 m
SK28	N	47.3900	E	14.5094	2,202 m
SK29	N	47.3897	E	14.5252	1,892 m
SK30	N	47.3896	E	14.5252	1,882 m
SK31	N	47.3896	E	14.5247	1,893 m
SK32	N	47.3894	E	14.5244	1,900 m
SK33	N	47.3891	E	14.5242	1,882 m
SK34	N	47.3891	E	14.5241	1,880 m
SK35	N	47.3890	E	14.5239	1,885 m
SK36	N	47.3888	E	14.5238	1,883 m
SK37	N	47.3888	E	14.5234	1,885 m
SK38	N	47.3888	E	14.5232	1,898 m
SK39	N	47.3887	E	14.5231	1,897 m
SK40	N	47.3888	E	14.5227	1,902 m
SK41	N	47.3878	E	14.5217	1,861 m
SK42	N	47.3872	E	14.5195	1,903 m
SK43	N	47.3871	E	14.5193	1,917 m
SK44	N	47.3870	E	14.5191	1,918 m
SK45	N	47.3867	E	14.5182	1,968 m
SK46	N	47.3864	E	14.5179	1,975 m
SK46	N	47.3864	E	14.5179	1,983 m
SK48	N	47.3870	E	14.5178	2,007 m
SK49	N	47.3902	E	14.5146	2,140 m
SK50	N	47.3907	E	14.5148	2,147 m
SK51	N	47.3911	E	14.5151	2,139 m
SK52	N	47.3918	E	14.5172	2,104 m
SK53	N	47.3918	E	14.5177	2,101 m
SK54	N	47.3911	E	14.5217	1,970 m
SK55	N	47.3905	E	14.5247	1,965 m
SK56	N	47.3980	E	14.5188	1,721 m
SK56.1	N	47.3982	E	14.5187	1,746 m
SK57	N	47.3981	E	14.5182	1,772 m

SK58	N	47.3981	E	14.5180	1,779 m
SK59	N	47.3983	E	14.5168	1,842 m
SK60	N	47.3981	E	14.5163	1,870 m
SK61	N	47.3951	E	14.5162	1,966 m
SK62	N	47.3949	E	14.5163	1,984 m
SK64	N	47.3913	E	14.5141	2,087 m
SK65	N	47.3909	E	14.5133	2,100 m
SK66	N	47.3908	E	14.5127	2,114 m
SK67	N	47.3910	E	14.5123	2,105 m
SK68	N	47.3910	E	14.5118	2,097 m
SK69	N	47.3909	E	14.5109	2,154 m
SK70	N	47.3903	E	14.5115	2,176 m
SK71	N	47.3903	E	14.5137	2,165 m
SK72	N	47.3915	E	14.5155	2,127 m
SK73	N	47.3939	E	14.5078	2,058 m
SK74	N	47.3926	E	14.5085	2,091 m
SK75	N	47.3895	E	14.5065	2,148 m
SK76	N	47.3890	E	14.5059	2,130 m
SK77	N	47.3890	E	14.5059	2,133 m
SK78	N	47.3906	E	14.5104	2,227 m
SK79	N	47.3905	E	14.5107	2,221 m
SK80	N	47.3904	E	14.5109	2,198 m
SK81	N	47.3903	E	14.5112	2,187 m
SK81	N	47.3903	E	14.5110	2,191 m
SK82	N	47.3903	E	14.5126	2,160 m

SK83	N	47.3908	E	14.5146	2,150 m
SK84	N	47.3921	E	14.5160	2,134 m
SK85	N	47.3799	E	14.5117	1,510 m
SK86	N	47.3802	E	14.5116	1,569 m
SK87	N	47.3809	E	14.5124	1,565 m
SK87.1	N	47.3808	E	14.5124	1,555 m
SK88	N	47.3811	E	14.5127	1,583 m
SK89	N	47.3816	E	14.5128	1,606 m
SK90	N	47.3819	E	14.5134	1,628 m
SK91	N	47.3822	E	14.5135	1,632 m
SK92	N	47.3802	E	14.5118	1,535 m
SK93	N	47.3890	E	14.5095	2,145 m
SK94	N	47.3885	E	14.5096	2,115 m
SK95	N	47.3886	E	14.5100	2,130 m
SK96	N	47.3890	E	14.5104	2,126 m
SK97	N	47.3894	E	14.5108	2,140 m
SK98	N	47.3896	E	14.5110	2,129 m
SK99	N	47.3899	E	14.5112	2,144 m
SK100	N	47.3789	E	14.5201	1,539 m
SK101	N	47.3774	E	14.4858	1,268 m
SK102	N	47.3778	E	14.4856	1,270 m
SK103	N	47.3778	E	14.4854	1,295 m
SK104	N	47.3771	E	14.4839	1,313 m
SK105	N	47.3768	E	14.4830	1,326 m
SK106	N	47.3766	E	14.4822	1,350 m

SK107	N	47.3762	E	14.4809	1,393 m
SK108	N	47.3760	E	14.4806	1,406 m
SK109	N	47.3759	E	14.4800	1,428 m
SK111	N	47.3768	E	14.4789	1,481 m
SK112	N	47.3824	E	14.4759	1,378 m

Table 2: Calculations of the loss of ignition (LOI). N1 = weight of ceramic crucible, N2 = weight of ceramic crucible and sample material (~1 g), after drying in the drying oven at 105 °C and cooling for 24 h in a desiccator, N3 = weight of the ceramic crucible and sample material after the annealing for 1 h at 1,200 °C and cooling for 1 h in a desiccator. The LOI ratio is calculated the following 100 x (N2-N3)/(N2-N1).

Sample	N1	N2	N3	LOI
SK3	17.40197	18.50678	18.49754	0.83634
SK4	19.60118	20.94135	20.92704	1.06777
SK6	17.20467	18.32511	18.30338	1.93942
SK7	19.64902	21.09685	21.08241	0.99735
SK8	18.49450	19.59504	19.57865	1.48927
SK8.2	22.81800	24.08671	24.07030	1.29344
SK8_2	24.81786	26.01265	25.99382	1.57601
SK9	19.24678	20.45861	20.44644	1.00427
SK10.1	17.91469	19.00529	18.99808	0.66110
SK11	17.40116	18.62764	18.61540	0.99798
SK12.1	18.49423	19.75618	19.74612	0.79718
SK13.1	19.24748	20.26618	20.25203	1.38903
SK15.1	19.24630	20.32687	20.31331	1.25489
SK16	18.49914	19.58298	19.57407	0.82208
SK16.1	17.20515	18.23053	18.21493	1.52139
SK16.2	17.47657	18.51624	18.50503	1.07823
SK17.3	17.81547	19.02320	19.00688	1.35130
SK18.1	19.55593	20.78543	20.77322	0.99309
SK18.1	19.64885	20.76021	20.74792	1.10585
SK19.1	17.81585	18.92524	18.91652	0.78602
SK20	19.24697	20.46923	20.45522	1.14624
SK21.1	26.03666	27.04557	27.03238	1.30735
SK22.1	24.29282	25.30002	25.28827	1.16660
SK26.1	18.49881	19.53132	19.51472	1.60773
SK28	26.03607	27.11637	27.09596	1.88929
SK57	24.29211	25.31861	25.30021	1.79250
SK58	24.60330	25.61548	25.60152	1.37920
SK69	19.64906	20.74481	20.71600	2.62925
SK73	18.49827	19.52830	19.51026	1.75141
SK771	24.37930	25.49305	25.47801	1.35039
SK78	24.60295	25.61706	25.60279	1.40715
SK79	21.00396	22.00450	21.98377	2.07188
SK82	18.49435	19.50554	19.48666	1.86711
SK85	19.06166	20.81093	20.78612	1.41831
SK87	18.49483	19.51567	19.50161	1.37730
SK87.1	22.81869	23.99424	23.97588	1.56182
SK90	19.55570	20.57338	20.56260	1.05927
SK93	22.00909	23.07257	23.05485	1.66623
SK94	17.20438	18.26590	18.25127	1.37821
SK95	24.81840	25.82928	25.81378	1.53332
SK96	25.85007	26.91425	26.89615	1.70084
SK97	22.81888	23.84085	23.82400	1.64878
SK99	22.00830	23.18868	23.16382	2.10610
SK100	24.38009	25.38603	25.37335	1.26051

Table 3: Geochemical data of the analysed samples. Major oxides in wt.%.

Sample	SiO_2	TiO_2	Al_2O_3	Fe_2O_3	MnO	MgO	CaO	Na_2O	K_2O	P_2O_5	LOI	Sums
SK3	73.384	0.224	13.373	2.008	0.044	0.673	1.249	3.626	3.646	0.102	0.836	99.570
SK4	71.569	0.349	14.016	2.313	0.053	0.995	1.230	4.039	3.411	0.117	1.068	99.520
SK6	68.939	0.442	15.643	2.475	0.041	1.242	0.893	3.297	4.115	0.154	1.939	99.520
SK7	73.458	0.415	13.262	2.225	0.045	1.038	0.941	4.280	2.555	0.103	0.997	99.580
SK8	84.278	0.219	9.283	0.939	0.005	0.823	0.038	0.048	3.526	0.032	1.418	100.910
SK8_2	67.033	0.580	14.732	3.765	0.068	1.499	3.080	3.703	2.662	0.218	1.576	99.280
SK8.2	82.214	0.218	8.805	0.514	0.003	0.472	0.028	0.058	3.837	0.033	1.293	97.770
SK9	71.609	0.283	14.628	2.188	0.040	0.933	0.967	4.069	3.422	0.100	1.004	99.550
SK10_1	74.593	0.183	13.296	1.663	0.025	0.435	0.588	3.763	3.906	0.071	0.661	99.550
SK11	74.410	0.200	13.444	1.554	0.030	0.476	0.804	3.954	3.477	0.075	0.998	99.740
SK12_1	71.744	0.388	13.902	2.470	0.062	1.244	1.224	4.283	2.861	0.127	0.797	99.450
SK13_1	66.973	0.666	15.317	3.709	0.079	1.680	1.928	4.363	3.265	0.190	1.389	99.910
SK15_1	70.802	0.404	14.330	2.785	0.059	1.420	1.101	4.296	2.885	0.139	1.255	99.760
SK16	71.056	0.399	14.235	2.631	0.055	1.008	1.929	4.462	2.481	0.131	0.822	99.590
SK16_1	70.607	0.352	14.955	2.332	0.055	1.023	1.451	4.463	3.421	0.120	1.521	100.810
SK16_2	68.706	0.412	15.697	2.874	0.069	1.030	2.412	4.234	3.263	0.145	1.078	100.430
SK17_3	70.488	0.305	15.098	2.120	0.039	1.145	1.084	4.154	3.331	0.111	1.351	99.560
SK18	71.474	0.292	14.557	2.189	0.034	0.983	0.878	4.449	3.190	0.098	1.106	99.580
SK18_1	71.860	0.300	14.601	2.080	0.042	0.959	0.652	4.345	3.505	0.100	0.993	99.720
SK19_1	71.832	0.290	14.501	2.076	0.037	0.900	0.890	4.296	3.419	0.088	0.786	99.460
SK20	68.022	0.528	14.714	3.492	0.070	1.312	2.546	3.827	2.889	0.195	1.146	99.080
SK21_1	72.612	0.242	14.157	1.838	0.032	0.691	0.469	3.801	3.768	0.081	1.307	99.280
SK22_1	72.295	0.286	13.969	2.084	0.033	0.738	0.846	4.029	3.317	0.080	1.167	99.190

Sample	SiO_2	TiO_2	Al_2O_3	Fe_2O_3	MnO	MgO	CaO	Na_2O	K_2O	P_2O_5	LOI	Sums
SK26_1	74.340	0.192	12.494	1.804	0.028	0.815	0.690	3.321	3.486	0.076	1.608	99.180
SK28	44.527	2.601	14.260	13.321	0.197	8.082	10.558	2.006	0.548	0.417	1.889	98.620
SK57	65.565	0.585	15.383	3.704	0.084	2.259	1.490	4.434	3.330	0.223	1.792	99.210
SK58	72.183	0.292	13.889	2.010	0.029	0.856	0.420	3.832	3.933	0.096	1.379	99.200
SK69	65.004	0.538	14.231	4.410	0.095	2.683	2.352	2.416	4.269	0.189	2.629	99.100
SK73	68.369	0.483	14.904	3.434	0.063	1.386	1.179	3.370	3.930	0.189	1.751	99.310
SK77_1	64.128	0.795	15.772	5.777	0.100	2.222	2.517	3.518	2.573	0.152	1.350	99.160
SK78	70.751	0.374	14.173	3.063	0.054	1.112	1.443	4.238	2.453	0.050	1.407	99.390
SK79	65.239	0.795	13.879	5.678	0.097	2.449	1.476	2.844	3.970	0.184	2.072	99.020
SK82	66.760	0.472	15.104	4.395	0.063	2.067	0.596	4.117	3.292	0.179	1.867	99.220
SK85	68.833	0.357	14.857	2.229	0.051	1.081	2.089	5.443	2.097	0.123	1.418	98.870
SK87	65.160	0.625	15.765	3.869	0.133	1.750	3.225	3.709	2.754	0.230	1.382	98.980
SK87_1	69.457	0.477	15.085	3.055	0.060	1.458	1.290	4.386	3.133	0.147	1.562	100.570
SK90	74.193	0.086	13.468	0.806	0.017	0.297	0.589	4.864	3.591	0.021	1.059	99.240
SK93	63.729	0.637	15.555	4.680	0.077	1.874	3.919	3.630	2.678	0.263	1.743	99.150
SK94	64.078	0.703	15.339	4.650	0.080	2.033	3.321	3.587	3.153	0.255	1.378	98.930
SK95	64.824	0.679	14.943	4.533	0.081	2.005	3.546	3.424	2.940	0.255	1.533	99.110
SK96	62.603	0.676	15.802	5.041	0.093	2.228	3.909	3.474	2.834	0.267	1.701	99.020
SK97	65.481	0.603	15.008	4.032	0.086	1.831	3.151	4.013	2.620	0.222	1.649	99.070
SK99	63.988	0.621	15.620	4.072	0.071	1.868	2.750	3.472	3.786	0.230	2.106	99.010
SK100	63.789	0.609	15.263	5.798	0.065	2.568	1.450	4.051	3.765	0.221	1.255	99.140

Table 4: Geochemical data of the analysed samples. Trace elements in ppm.

Sample	Ba	Ce	Cr	Cs	Cu	Ga	La	Nb	Nd	Ni	Pb	Rb	Sc	Sr	Th	U	V	Y	Zn	Zr
SK3	1158.4	45.5	<20	<20	<20	17.8	46.6	<20	25.3	<20	<20	100.5	<20	299.8	<20	<20	28.4	<20	28.8	114.5
SK4	1207.7	57.9	<20	<20	<20	16.7	71.3	<20	51.8	<20	<20	81.6	<20	294.4	<20	<20	34.4	<20	41.7	121.7
SK6	757.3	117.5	<20	19.8	<20	22.2	75.2	<20	37.3	<20	<20	133.6	<20	149.7	<20	<20	54.6	<20	89.5	142.4
SK7	708.5	69.0	<20	<20	<20	14.7	58.1	<20	46.1	<20	<20	75.4	<20	188.9	<20	<20	35.2	20.4	28.6	119.6
SK8	192.1	19.5	<20	<20	<20	11.6	26.3	<20	<20	<20	<20	124.9	<20	<20	<20	<20	20.4	<20	<20	79.2
SK8_2	1126.2	47.9	<20	<20	<20	21.3	47.1	<20	31.3	<20	<20	75.4	<20	552.6	<20	<20	68.2	<20	58.8	168.8
SK 8.2	256.7	101.7	<20	<20	<20	13.0	101.1	<20	21.7	<20	<20	113.0	<20	10.3	<20	<20	20.7	<20	<20	63.4
SK9	767.0	58.2	<20	<20	<20	18.7	40.9	<20	20.7	<20	<20	99.5	<20	287.7	<20	<20	30.8	<20	34.5	112.3
SK10_1	896.5	46.9	<20	23.3	<20	16.8	47.1	<20	22.6	<20	22.4	107.7	<20	143.8	<20	<20	<20	22.1	<20	78.4
SK11	791.4	38.7	<20	<20	<20	17.6	55.5	<20	19.5	<20	<20	99.4	<20	164.1	<20	<20	<20	24.3	<20	78.7
SK12_1	963.5	90.2	<20	23.0	<20	16.3	74.4	<20	34.7	<20	<20	78.8	<20	319.8	<20	<20	35.9	<20	52.9	140.1
SK13_1	1064.2	119.9	<20	<20	<20	20.6	95.2	<20	58.2	<20	20.3	98.4	<20	369.4	<20	<20	65.1	30.2	78.6	162.4
SK15_1	959.0	53.5	<20	<20	<20	15.1	49.4	<20	34.0	<20	<20	76.8	<20	278.1	<20	<20	47.5	<20	54.4	134.3
SK16	936.4	51.8	<20	28.0	<20	15.3	40.7	<20	36.1	<20	<20	64.9	<20	449.2	<20	<20	45.5	<20	44.9	130.8
SK16_1	1276.2	84.0	<20	<20	<20	17.1	47.6	<20	32.0	<20	<20	79.7	<20	285.2	22.4	<20	45.9	<20	39.3	106.9
SK16_2	995.0	52.2	<20	34.2	<20	20.0	52.3	<20	<20	<20	20.2	86.4	<20	481.0	<20	<20	44.3	<20	49.1	159.5
SK17_3	810.5	47.9	<20	<20	<20	21.8	64.8	<20	33.7	<20	<20	112.8	<20	210.0	<20	<20	21.8	<20	36.7	135.7
SK18	821.3	60.5	<20	<20	<20	18.0	52.2	<20	<20	<20	<20	87.5	<20	208.4	<20	<20	24.5	<20	26.1	118.6
SK18_1	637.0	78.3	<20	<20	<20	18.9	51.0	<20	<20	<20	<20	113.2	<20	175.0	<20	<20	26.1	<20	38.2	108.8
SK19_1	696.1	40.5	<20	<20	<20	19.0	37.5	<20	<20	<20	<20	100.3	<20	272.1	<20	<20	26.8	<20	45.1	105.6
SK20	972.8	84.3	32.1	<20	<20	19.7	65.5	<20	30.0	<20	<20	75.9	<20	592.7	<20	<20	58.0	36.6	42.1	196.0
SK21_1	716.3	59.7	<20	<20	<20	21.9	75.6	<20	27.5	<20	<20	121.9	<20	125.9	<20	<20	<20	23.8	19.8	84.9
SK22_1	591.1	85.4	<20	<20	<20	19.8	56.5	<20	<20	<20	<20	116.9	<20	212.0	21.3	<20	<20	20.5	30.1	105.4

Sample	Ba	Ce	Cr	Cs	Cu	Ga	La	Nb	Nd	Ni	Pb	Rb	Sc	Sr	Th	U	V	Y	Zn	Zr
SK26_1	660.8	70.0	<20	<20	151.1	17.2	59.5	<20	<20	<20	<20	111.9	<20	121.9	<20	<20	28.7	<20	23.3	70.9
SK28	134.9	47.1	263.5	<20	33.9	26.2	78.4	20.4	41.1	102.8	<20	20.6	32.4	289.5	<20	<20	278.6	35.2	137.7	224.1
SK57	1243.3	78.6	<20	<20	<20	21.1	69.4	<20	45.0	<20	<20	99.4	<20	275.7	<20	<20	67.0	<20	106.6	172.1
SK58	812.8	74.0	<20	26.2	<20	17.0	42.9	<20	28.8	<20	<20	109.6	<20	137.4	<20	<20	30.5	<20	23.4	130.4
SK69	911.3	109.2	24.3	<20	<20	19.0	104.2	<20	52.1	<20	<20	142.1	<20	228.7	<20	<20	78.3	23.8	61.4	155.2
SK73	784.6	92.9	<20	29.5	<20	19.9	57.6	<20	28.2	<20	<20	124.4	<20	230.4	21.1	<20	58.6	27.4	26.0	131.6
SK77_1	480.7	51.8	66.2	26.7	22.2	18.4	61.9	<20	<20	<20	<20	97.5	<20	274.2	<20	<20	108.6	23.4	71.3	176.8
SK78	486.2	119.0	<20	<20	<20	16.9	66.9	<20	43.1	<20	<20	78.0	<20	214.4	37.9	<20	50.7	<20	44.6	130.0
SK79	600.4	83.2	36.6	<20	<20	22.7	58.1	19.7	<20	<20	<20	163.4	<20	217.3	31.6	<20	98.0	<20	114.7	215.8
SK82	770.9	30.5	<20	<20	<20	22.4	33.5	<20	<20	<20	<20	108.5	<20	108.0	23.9	<20	61.9	21.8	38.8	157.7
SK85	680.1	71.5	<20	23.9	<20	16.6	62.4	<20	<20	<20	<20	58.7	<20	317.5	<20	<20	34.6	<20	34.1	109.7
SK87	814.7	81.6	20.6	<20	<20	22.4	87.3	<20	33.2	<20	<20	97.4	<20	512.0	<20	<20	69.3	21.3	85.1	170.3
SK87_1	969.1	104.6	<20	20.5	<20	18.0	73.4	<20	46.3	<20	<20	90.3	<20	324.7	23.4	<20	56.7	25.0	41.0	162.7
SK90	412.8	38.2	<20	<20	<20	16.9	46.1	<20	<20	<20	<20	91.2	<20	110.3	<20	<20	<20	<20	<20	43.0
SK93	707.3	69.3	29.6	<20	<20	19.6	60.1	<20	26.8	<20	23.0	90.5	<20	572.2	<20	<20	78.7	<20	61.7	225.0
SK94	1055.2	118.5	25.5	26.9	<20	21.2	66.3	<20	47.3	<20	20.8	96.7	<20	556.5	<20	<20	88.1	21.3	59.0	193.0
SK95	873.6	137.4	23.7	<20	<20	18.1	91.0	<20	39.0	<20	<20	91.3	<20	534.6	<20	<20	90.1	22.3	75.6	181.9
SK96	686.7	117.2	25.1	<20	<20	23.1	93.4	<20	38.4	<20	<20	107.9	<20	580.6	27.4	<20	93.1	<20	77.3	211.8
SK97	896.3	33.3	23.9	<20	<20	18.7	52.2	<20	21.6	<20	22.4	83.0	<20	511.7	<20	<20	83.4	20.2	70.7	188.7
SK99	1126.2	52.9	23.6	<20	22.7	22.6	42.4	<20	26.6	<20	<20	107.5	<20	377.5	<20	<20	71.6	<20	56.0	178.3
SK100	1128.4	116.5	<20	<20	<20	18.0	88.8	<20	50.2	<20	<20	131.1	<20	301.8	<20	<20	60.3	30.3	54.4	189.8

Table 5: Orientation data of granite-gneiss.

Dip-Direction	Dip-Angle
261	25
255	35
275	25
255	35
290	25
242	35
260	35
280	25
280	20
270	35
290	20
290	15
275	35
275	30
280	30
260	20
290	25
290	40
280	30
265	25
240	30
235	30
230	30
350	25
045	45
040	35
045	45
60	60
335	10
245	35
300	30
280	30
275	30
270	25
300	25
295	25
315	35
315	25
310	10
310	20
285	30
300	35
275	15
270	20
265	40
265	50
290	30
290	30
310	20
265	35
080	85
270	35
230	35
255	25
255	25
270	15
265	30
260	35
265	30
260	35
270	30
285	15
290	25
270	30
285	25
295	30
275	25
285	20
285	15
310	40
250	50
260	20
260	20
250	30
240	30
245	35
240	30
250	30
240	30
245	30
230	35
250	35
230	30
240	35
245	25
320	25
232	30
358	35
356	10
250	10
250	10
310	5

Table 6: Orientation data of granodiorite-gneiss.

Dip-Direction	Dip-Angle
240	30
310	30
275	20
295	15
300	25
300	10
300	20
330	45
325	35
325	35
265	25
315	25
350	40
280	35
340	30
010	30
000	15
262	40
250	35
270	25
248	40
262	20
220	30
244	25
228	25
314	10
296	10
290	10
290	10
345	25
288	20
285	15
235	40
250	35
245	40
285	30
290	25
310	15
282	16
290	20
288	25
312	25
292	30
284	15
286	15
268	65
280	75
268	85
268	60
320	40
330	40
315	35
226	40
240	42
226	42
265	35

Table 7: Orientation data of quartz-veins.

Dip-Direction	Dip-Angle
60	30
75	70
60	35
280	30
265	25
230	68
285	70

Table 8: Orientation data of par-agneiss

Dip-Direction	Dip-Angle
245	50
265	20
255	25
295	15
225	50
235	40
260	35
250	40
265	30
250	35
250	35
250	35
275	30
290	20
285	15
280	10
300	15
300	10
280	10
260	20

Table of Figures

Table of Tables

Table of Appendix Tables